

# Destabilization of Alfvén Eigenmodes by Fast Particles in W7-AS

INAUGURALDISSERTATION

zur

Erlangung des akademischen Grades eines

doctor rerum naturalium (Dr. rer. nat.)

an der Mathematisch-Naturwissenschaftlichen Fakultät

der

Ernst-Moritz-Arndt-Universität Greifswald

vorgelegt von

Stefan Zegenhagen

geboren am 7. 7. 1974

in Ueckermünde

Greifswald, im Februar 2006

Dekan: Prof. Dr. Klaus Fesser

1. Gutachter: Prof. Dr. Thomas Klinger

2. Gutachter: Prof. Dr. Kazuo Toi

Tag der Promotion: 5. 7. 2006

# Contents

<b>1</b>	<b>Introduction</b>	<b>1</b>
<b>2</b>	<b>Principles of magnetic plasma confinement</b>	<b>5</b>
2.1	Magnetic Field Topology . . . . .	6
2.1.1	Magnetic Field Lines . . . . .	6
2.1.2	Magnetic Field Line Curvature, Pressure and Tension . . . . .	6
2.1.3	Flux Surfaces . . . . .	7
2.1.4	Magnetic Flux Coordinates . . . . .	9
2.2	Particle Dynamics in Fusion Plasmas . . . . .	12
2.2.1	Radial Particle Drifts . . . . .	13
2.2.2	Trapped and Passing Particles . . . . .	16
2.3	Magnetohydrodynamics . . . . .	18
2.3.1	MHD equilibria . . . . .	19
2.3.2	Stability of MHD Equilibria . . . . .	22
<b>3</b>	<b>Alfvén Waves, -continua and Eigenmodes</b>	<b>25</b>
3.1	Alfvén Waves and Alfvén Continua . . . . .	26
3.1.1	Waves in an infinite, homogeneous plasma . . . . .	26
3.1.2	Inhomogeneous plasma slab . . . . .	28
3.1.3	Shear Alfvén Continuum in Cylindrical Geometry . . . . .	29
3.1.4	Continuous Spectrum in Toroidal Geometry . . . . .	31
3.2	Alfvén Eigenmodes . . . . .	34
3.2.1	Global Alfvén Eigenmodes (GAEs) . . . . .	34
3.2.2	Gap Modes . . . . .	35

3.3	Beyond Ideal MHD . . . . .	36
3.3.1	Wave Drive and Damping . . . . .	36
3.3.2	Wave-Induced Transport . . . . .	43
3.3.3	Kinetic Modifications of the Alfvén Wave Spectrum . . . . .	45
<b>4</b>	<b>Experimental and numerical tools</b>	<b>47</b>
4.1	The W7-AS device . . . . .	47
4.2	Diagnostics . . . . .	50
4.2.1	Mirnov Diagnostic . . . . .	52
4.2.2	Plasma parameter diagnostics . . . . .	56
4.2.3	Fast Ion Loss Detector . . . . .	60
4.3	Mirnov Data Analysis . . . . .	61
4.3.1	Continuous wavelet transform . . . . .	62
4.3.2	Lomb periodogram analysis . . . . .	64
4.4	Numerical codes . . . . .	73
4.4.1	Equilibrium reconstruction and magnetic coordinate transforms	73
4.4.2	Alfvén continuum calculation . . . . .	74
4.4.3	Calculation of the fast ion distribution function . . . . .	74
4.4.4	Growth rate calculation . . . . .	76
<b>5</b>	<b>Experimental Results</b>	<b>79</b>
5.1	Data Analysis . . . . .	79
5.1.1	Data Availability . . . . .	82
5.1.2	Equilibrium reconstruction . . . . .	83
5.1.3	Mode Number Analysis . . . . .	85
5.1.4	Eigenmode Identification . . . . .	89
5.1.5	Ion Distribution Function . . . . .	89
5.1.6	Growth Rates and Fast Ion Losses . . . . .	92
5.2	Discharge Scan . . . . .	94
5.2.1	Discharge Classification . . . . .	95
5.2.2	Eigenmode Classification . . . . .	97
<b>6</b>	<b>Discussion and Conclusions</b>	<b>109</b>

6.1	Equilibrium Reconstruction . . . . .	109
6.2	Mirnov Data Analysis . . . . .	111
6.3	Alfvén Eigenmodes and their Stability . . . . .	112
6.3.1	GAEs . . . . .	113
6.3.2	TAEs . . . . .	114
6.3.3	EAEs and High-Frequency Eigenmodes . . . . .	115
6.3.4	Unidentified Eigenmodes . . . . .	116
6.4	Alfvén Eigenmodes and Fast-Ion Losses . . . . .	117
6.5	Conclusions . . . . .	118
<b>7</b>	<b>Summary</b>	<b>121</b>
<b>A</b>	<b>Differential Geometry</b>	<b>125</b>
A.1	Reciprocal sets of vectors . . . . .	125
A.2	Curvilinear Coordinates . . . . .	126
A.3	Co- and Contravariant Components . . . . .	127
A.4	Tensors . . . . .	130
A.5	Important Vector Identities . . . . .	131
<b>B</b>	<b>Boozers magnetic coordinates</b>	<b>135</b>
B.1	Covariant <b>B</b> Components . . . . .	135
B.2	Boozer Coordinates . . . . .	137
<b>C</b>	<b>List of Discharges and AEs</b>	<b>141</b>
C.1	Discharges . . . . .	141
C.2	Observed Alfvén Instabilities . . . . .	145
C.2.1	GAEs . . . . .	145
C.2.2	TAEs . . . . .	146
C.2.3	EAEs . . . . .	147
C.2.4	NAE, HAE and MAE Modes . . . . .	148
C.2.5	Unidentified Alfvén Eigenmodes . . . . .	148



# Chapter 1

## Introduction

Controlled nuclear fusion of hydrogen isotopes in a plasma promises to provide a nearly inexhaustible source of energy and high environmental safety as compared to nuclear fission. The most favourable fusion reaction is the one between deuterium and tritium



which provides the highest yield of energy. In order to reach ignition conditions, where the fusion born  $\alpha$ -particles heat the plasma sufficiently strong to compensate for the heat losses, the plasma must be heated up to temperatures of  $T \geq 10 \text{ keV}$  and must be confined long enough to satisfy the Lawson criterium [1]

$$n\tau_E > 1.5 \times 10^{20} \text{ s/m}^3,$$

where  $\tau_E$  is the energy confinement time (the ratio of heating power to energy loss rate) and  $n$  the plasma density.

The most advanced approach towards the achievement of relevant fusion reactor parameters is the confinement of the plasma in a closed, toroidal magnetic field with twisted, helical field lines. Two different concepts are currently pursued that differ in the way the magnetic field is created. The *Tokamak* is an axisymmetric device that creates a strong toroidal field with large external coils. The necessary poloidal field component is generated by toroidal currents induced by a transformer, with the plasma forming the secondary winding. This does not allow steady-state operation because of the alternating current requirement in the transformer. Intense research is performed on alternative schemes to drive current in Tokamak plasmas. The second class of magnetic confinement devices is the *Stellarator*, where the helical magnetic field is generated completely by external coils. Stellarators are therefore independent of permanently flowing plasma currents, but, in contrast to tokamaks, they are not axisymmetric.

The performance of todays fusion experiments is not only limited by technical constraints. The sources of free energy available in bounded plasmas with strong gradients are commonly tapped by instabilities that degrade the confinement of particles

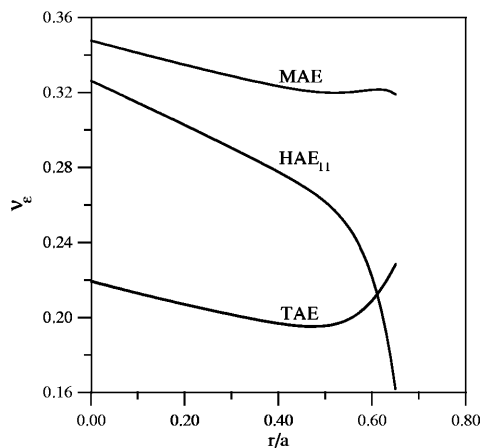


Figure 1.1: Prediction of the fraction of redistributed energetic  $\alpha$  particles caused by Alfvén eigenmodes in optimized stellarators. Taken from Ref [11].

and energy. One of the most important type of instabilities are Alfvén eigenmodes, which are still subject to extensive studies.

Alfvén waves were discovered by Hannes Alfvén in the 1940's, a pioneer in the physics of charged fluids [2, 3]. Besides being observed in astronomical and laboratory plasmas, they dominate much of the low-frequency dynamics in fusion plasmas. The Alfvén wave describes a basic oscillation between plasma kinetic energy and magnetic field energy. The most familiar example is the shear Alfvén wave, characterized by "field line bending", that is analogous to a wave travelling along a massive string. It propagates along the magnetic field lines at the Alfvén velocity,

$$v_A = \frac{B}{\sqrt{\mu_0 \rho}},$$

where  $\rho$  is the plasma mass density and  $B$  the magnetic field strength. Alfvén waves in fusion plasmas constitute a continuous spectrum of stable waves [4] that were originally not considered to be a threat. This changed suddenly when it was realized that the continuous spectrum has gaps [5, 6] in which discrete, only weakly damped eigenmodes can exist [7–9]. The gap formation is caused by the symmetry breaking associated with magnetic field inhomogeneities over a magnetic surface. Because stellarators, in contrast to tokamaks, do not have toroidal symmetry, an even larger number of gaps exists here [10].

The high Alfvén velocity of  $v_A \sim 10^6$  m/s allows resonant interaction with Alfvén eigenmodes only for energetic particles created either by plasma heating sources or by fusion reactions. Destabilization of Alfvén eigenmodes by fast ions was predicted and observed in fusion plasmas [9, 12–14] as well as enhanced transport and, eventually, energetic particle losses [11, 15, 16]. The latter is of special importance because the energetic particles are needed to heat the bulk plasma. Their premature removal can cause a significant degradation of the plasma performance. A rough estimate of the expected fraction of fusion born  $\alpha$  particles that are radially redistributed by resonant



interaction with Alfvén eigenmodes, which is based on worst case arguments, predicts that more than 35% can be transported away from the resonance region (Fig. 1.1). There it was assumed that all particles, which are in resonance with the wave, are immediately redistributed. On the other hand, in a fusion reactor a controlled wave-particle interaction could provide a way to remove the helium "ash" from the plasma after the  $\alpha$  particles have slowed down.

This thesis intends to study Alfvén eigenmodes in neutral beam heated, high-density and low-temperature discharges of the W7-AS stellarator, that was operated successfully from 1988 – 2002 [17, 18]. Studies of Alfvénic instabilities have been done previously [19–24]. In these studies, the common appearance of the so-called Global Alfvén Eigenmodes with frequencies of 15 – 40 kHz in the presence of neutral beam injection (NBI) heating was reported. The eigenmode structure was mostly inferred from a tomographic reconstruction of the soft X-Ray emissions from the plasma [21], or by analyzing the phase differences between spatially distribution magnetic pickup (Mirnov) coils [25]. In order to obtain growth rates and saturation levels, numerical simulations were performed using Tokamak codes and toroidally averaged equilibria. Since that time, W7-AS was upgraded a lot. Noteworthy are e.g. the installation of an island divertor, the change from balanced to unbalanced NBI and permanent diagnostic improvements. These changes paved the way towards stable discharges with increased density and plasma energy. It seems therefore necessary to revisit the properties of Alfvén eigenmodes under the new discharge conditions.

One goal of the present thesis is to rigorously identify Alfvén instabilities in as many different discharges as possible. The identification will be done by direct comparison of observed mode numbers and frequencies to the shear Alfvén spectrum, the mode numbers will be inferred from the Mirnov diagnostic that allows one to obtain information about both, poloidal *and* toroidal mode number simultaneously. The parameter scan should reveal parameter limits and instability thresholds for the various types of Alfvén eigenmodes. A second goal of this thesis is to look for correlations between eigenmodes and fast ion losses to uncover the most dangerous instabilities.

The thesis is structured as follows: Chapter 2 presents a review of the most important topics of stellarator theory, including magnetic field topology, single particle dynamics and the ideal magnetohydrodynamic (MHD) fluid model. Chapter 3 intimately describes the ideal MHD spectrum of Alfvén waves and eigenmodes, ending with the inclusion of kinetic effects to describe wave-particle interactions and modifications of the ideal MHD spectrum. In Chapter 4 the W7-AS device is presented. An overview is given of the diagnostic setup and the numerical tools that have been used in this thesis. A special focus is put on the newly developed tool to analyze the Mirnov data with high accuracy and sensitivity. Chapter 5 presents the analysis procedure applied to each observed Alfvén eigenmode, using one of the studied discharges as example. This is followed by the collected results of all analyzed cases. In Chapter 6 the results are discussed and conclusions are drawn, Chapter 7 gives a summary.



## Chapter 2

# Principles of magnetic plasma confinement

This chapter is to review some aspects of the theory of plasmas in strong magnetic fields, especially in toroidal fusion devices. The physical aspects in these devices can be described quite conveniently if one is able to hide the complexity of the magnetic field structure in those devices behind a special choice of curvilinear coordinate systems in which the magnetic field lines appear as straight lines. The topology of the magnetic field in toroidal fusion devices can be conveniently described in those coordinates, so they are presented first.

After having laid these foundations, the particle behaviour in magnetic fusion devices is addressed. The particle-orbit theory is an excellent tool to derive the forces on particles and corresponding drifts and can be used to explain the classical and neoclassical radial transport of particles and energy. To handle the whole plasma as a many-body system kinetic theory needs to be applied. It describes the plasma as ensembles of particle species in terms of their distribution functions. The evolution of the distribution functions is governed by a kinetic equation. The kinetic theory, however, is too complex to be conveniently used to derive global plasma parameters which are obtained as velocity moments of the distribution functions. A set of simpler fluid equations are obtained by taking the moments of the kinetic equation, the magnetohydrodynamic (MHD) equations. They are commonly used to self-consistently calculate magnetic fields and radial plasma profiles. This MHD equilibrium is described in another section of this chapter.

## 2.1 Magnetic Field Topology in Toroidal Fusion Devices

### 2.1.1 Magnetic Field Lines

A magnetic *field line* is, by definition, a curve whose tangent is in every point parallel to the magnetic field vector  $\mathbf{B}$ . This definition can be cast in mathematical form. Let  $\mathbf{R}$  be a position vector from the origin to a point on the field line,  $\mathbf{R}$  follows the curve. Then  $d\mathbf{R}$  is a vector that is tangent to the field line. The *equation of a magnetic field line* is:

$$\mathbf{B} = c d\mathbf{R} \iff \frac{B^1}{du^1} = \frac{B^2}{du^2} = \frac{B^3}{du^3} = c \iff \mathbf{B} \times d\mathbf{R} = 0, \quad (2.1)$$

where  $c$  is a constant. In the expression in the middle of Eq. (2.1) both vectors,  $\mathbf{B}$  and  $\mathbf{R}$ , have been expanded in contravariant components. If the field line is considered to be parameterized by the length  $l$  along the curve where  $l$  is assumed to increase in the direction in which  $\mathbf{B}$  points,  $d\mathbf{R}/dl$  is a unit vector parallel to the magnetic field, denoted by  $\mathbf{b} = \mathbf{B}/B$ . A comparison with (2.1) yields  $c = B/dl$  for the constant and the equation of a magnetic field line reads to be

$$\frac{B}{dl} = \frac{B^1}{du^1} = \frac{B^2}{du^2} = \frac{B^3}{du^3} = \frac{\mathbf{B} \cdot \nabla u^1}{du^1} = \frac{\mathbf{B} \cdot \nabla u^2}{du^2} = \frac{\mathbf{B} \cdot \nabla u^3}{du^3}. \quad (2.2)$$

### 2.1.2 Magnetic Field Line Curvature, Pressure and Tension

Consider the dot product of  $\mathbf{b}$  with itself. Because  $\mathbf{b}$  is a unit vector,  $\mathbf{b} \cdot \mathbf{b} = 1$ . Hence,

$$\frac{d(\mathbf{b} \cdot \mathbf{b})}{dl} = \frac{d\mathbf{b}}{dl} \cdot \mathbf{b} + \mathbf{b} \cdot \frac{d\mathbf{b}}{dl} = 0$$

which can only be satisfied if  $\mathbf{b} \cdot (d\mathbf{b}/dl) = 0$  and, therefore,  $d\mathbf{b}/dl$  is perpendicular to the tangent vector  $\mathbf{b}$ . The curvature vector  $\boldsymbol{\kappa}$  is defined by the relation

$$\left. \frac{d\mathbf{b}}{dl} \right|_{\text{along } \mathbf{b}} \equiv \kappa \hat{\mathbf{n}} \equiv \frac{1}{R_c} \hat{\mathbf{n}} \equiv \boldsymbol{\kappa}. \quad (2.3)$$

Here,  $\hat{\mathbf{n}}$  is the unit vector normal to the field line that points towards the center of the curvature,  $\kappa$  is the curvature and  $R_c$  is the local curvature radius. The directional derivative  $d/dl|_{\text{along } \mathbf{b}}$  is equal to the dot product of  $\mathbf{b}$  with  $\nabla$ :

$$\left. \frac{d}{dl} \right|_{\text{along } \mathbf{b}} \equiv \mathbf{b} \cdot \nabla \equiv \frac{\partial}{\partial l} \quad (2.4)$$

By comparing the last two expressions, one finds another expression for  $\boldsymbol{\kappa}$  which is commonly used:

$$\boldsymbol{\kappa} = (\mathbf{b} \cdot \nabla) \mathbf{b} = \mathbf{b} \cdot \nabla \mathbf{b} \quad (2.5)$$

which is the dot product of a vector  $\mathbf{b}$  with a dyad  $\nabla\mathbf{b}$

In a current carrying medium in the presence of a magnetic field, the force density (force per unit volume) is given by:

$$\mathbf{f} = \frac{d\mathbf{F}}{dV} = \mathbf{J} \times \mathbf{B}.$$

However, since the current density  $\mathbf{J}$  can be written as the curl of the magnetic field,  $\mu_0\mathbf{J} = \nabla \times \mathbf{B}$ , the force density can be recast in terms of  $\mathbf{B}$  only:

$$\mathbf{f} = \frac{1}{\mu_0}(\nabla \times \mathbf{B}) \times \mathbf{B} = \frac{1}{\mu_0}(\mathbf{B} \cdot \nabla)\mathbf{B} - \frac{1}{2\mu_0}\nabla B^2. \quad (2.6)$$

In (2.6) the first term in the last expression,  $\mathbf{B} \cdot \nabla\mathbf{B}/\mu_0$ , is related to the field line curvature via

$$\mathbf{f}_{\text{tension}} = \frac{1}{\mu_0}(\mathbf{B} \cdot \nabla)\mathbf{B} = \frac{B^2}{\mu_0}\boldsymbol{\kappa}. \quad (2.7)$$

It represents a force on the field line that is directed to the center of the curvature and thus tries to reduce field line bending. Due to this force the field line behaves like an elastic chord that is subject to a tension  $B^2/\mu_0$ . Therefore this force is called *magnetic tension*. The second term,  $-\nabla B^2/2\mu_0$ , can be identified with a pressure force density  $-\nabla p$  where the *magnetic pressure* is given by

$$p_{\text{mag}} = \frac{B^2}{2\mu_0}. \quad (2.8)$$

### 2.1.3 Flux Surfaces

The motion of charged particles in magnetic fields is governed by the electromagnetic force

$$\mathbf{F} = q(\mathbf{E} + \mathbf{v} \times \mathbf{B}),$$

where  $\mathbf{E}$  and  $\mathbf{B}$  are the electric and magnetic field, respectively,  $q$  is the particle charge and  $\mathbf{v}$  is the particle velocity. If no electric field is present, the only force on the particle is  $q(\mathbf{v} \times \mathbf{B})$ . The resulting acceleration is perpendicular to both, the magnetic field direction and the current particle velocity. The particle orbit is described by the equation of motion. For simplicity, cartesian coordinates and  $\mathbf{B} = (0, 0, B)^T$  are assumed.

$$\ddot{x} = \frac{qB}{m}\dot{y} = \omega_L\dot{y} \quad \ddot{y} = -\frac{qB}{m}\dot{x} = -\omega_L\dot{x} \quad \ddot{z} = 0 \quad (2.9)$$

As can be seen easily, in homogeneous fields the particle will move in a circle (or *gyrate*) around the field line in the plane perpendicular to the magnetic field with the *cyclotron*,

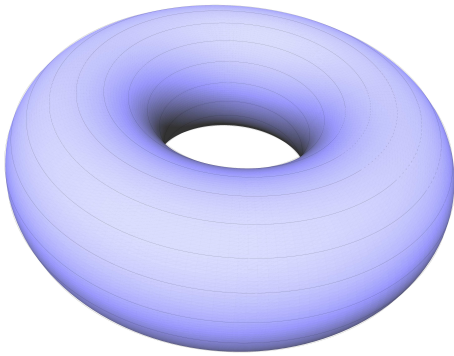


Figure 2.1: Simple toroidal field without rotational transform. Black lines indicate magnetic field lines.

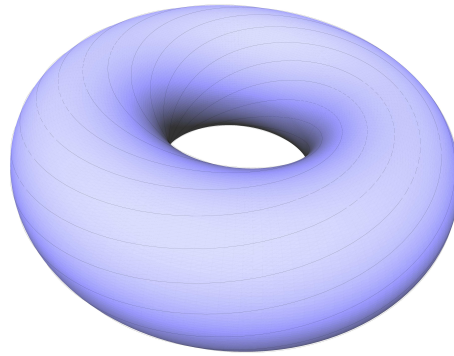


Figure 2.2: Toroidal field with rotational transform. Black lines indicate magnetic field lines.

*gyro* or *Larmor frequency*  $\omega_L = q|\mathbf{B}|/m$ . The radius of this circle, the *Larmor radius*  $r_L = m|\mathbf{v}_\perp|/q|\mathbf{B}|$ , depends on the speed of the particle perpendicular to the magnetic field.

The work done on the particle by the magnetic field is

$$W = \int \mathbf{F} \cdot d\mathbf{x} = q \int (\mathbf{v} \times \mathbf{B}) \cdot d\mathbf{x} = q \int (\mathbf{v} \times \mathbf{B}) \cdot \mathbf{v} dt \equiv 0$$

because  $\mathbf{F} \perp \mathbf{v}$ . Consequently, the particle energy stays constant. We can summarize the findings in the following picture: Charged particles in a homogeneous magnetic field move with constant velocity along the field lines while they gyrate around them.

This leads one to a simple idea to confine a plasma inside a magnetic field: If one would take a homogeneous, cylindrical magnetic field and bend that into a torus as shown in Fig. 2.1, the result is a finite volume from which no open field lines escape. Any particle following the field lines should stay confined within the magnetic field. The real situation is, however, not quite as simple since the magnetic field in such a toroidal configuration is not homogeneous. As will be shown in chapter 2.2, the gyration of a particle in a magnetic field gradient gives rise to a drift  $\mathbf{v}_{\nabla B}$  and the motion along bent field lines causes another drift  $\mathbf{v}_\kappa$  of the guiding centers out of the confinement region. An additional poloidal field component solves the problem. It lets the field lines "spiral" around the torus as indicated in Fig. 2.2 and the particles will pass alternating regions where the drift points into and out of the confinement region, respectively, and cancels in average.

The slope of the field lines is measured by the *rotational transform*  $\iota$ . Approximately, it equals the number of poloidal transits  $m$  of the field line around the torus divided by the number of toroidal transits  $n$  before the field line closes upon itself. A more rigorous definition will be given later. But usually, the field lines are not closed. Instead, they ergodically cover a twodimensional surface. Any such surface that is ergodically traced out by a field line is called a *magnetic surface*, also called an irrational surface because

on these surfaces,  $\iota$  approaches an irrational value in the limit  $n \rightarrow \infty$ . Let  $d\mathbf{S}$  be a surface element of a magnetic surface. Due to the construction of the surface,  $d\mathbf{S} \cdot \mathbf{B} = 0$  is satisfied everywhere on the surface. An important consequence of this relation is that the magnetic flux enclosed by the magnetic surface is constant. This is the reason for another synonym for magnetic surfaces, namely *flux surfaces*.

The magnetic field in toroidal fusion devices consists of a set of nested flux surfaces, each traced out by non-closing field lines. Between these magnetic surfaces one can define surfaces that contain field lines that close upon themselves after several transits around the torus. Because  $\iota$  is a rational number on these surfaces, they are called *rational* magnetic surfaces. The innermost flux surface has a zero volume and is degenerate. It is called the *magnetic axis*.

The existence of nested flux surfaces can be guaranteed in devices with a symmetry axis, i.e. axisymmetric tokamaks and helically symmetric stellarators. Strictly speaking, it must be possible to find a set of canonical coordinates with an ignorable coordinate. The equation of a field line (2.2) can be cast in Hamiltonian form and Kolmogorov-Arnold-Moser (K.A.M.) theory assures the existence of perfect, closed and nested flux surfaces. K.A.M. theory also guarantees the existence of a set (of non-zero measure) of invariant surfaces in the presence of small perturbations (i.e. manufacturing errors) [26, 27]. Between these "good surfaces" exists a possibly dense set of surfaces which open up into ergodic regions or magnetic islands, where field lines behave chaotically and ergodically fill an entire non-zero volume. However, even these regions are absolutely confined if they have a good K.A.M. surface on either side.

### 2.1.4 Magnetic Flux Coordinates

The magnetic field topology suggests a certain choice of curvilinear coordinates. By convention, the first (radial) coordinate labels the magnetic surfaces. The other two coordinates span a coordinate mesh that completely covers the flux surface and are usually, though not always, associated with angles.

Any quantity  $\rho$  that satisfies  $\mathbf{B} \cdot \nabla \rho = 0$  and is strictly monotonically increasing away from the magnetic axis can be used as radial coordinate. The first condition simply states that  $\rho = \text{const}$  spans a surface that is parallel to  $\mathbf{B}$  everywhere. The second condition is necessary to have the coordinate single-valued and that the coordinate system is right-handed. The constraint  $\nabla \rho = 0$  at the magnetic axis can be used to ensure that  $\rho$  is well behaved and continuous at the magnetic axis. There are four quantities that are commonly used:

1. the enclosed volume  $V$ ,
2. the enclosed toroidal flux  $\Psi_{tor}$ ,
3. the normalized (toroidal) flux  $s = \Psi_{tor}/\Psi_{tor}^a$  that is zero at the magnetic axis and equals unity at the plasma boundary, and

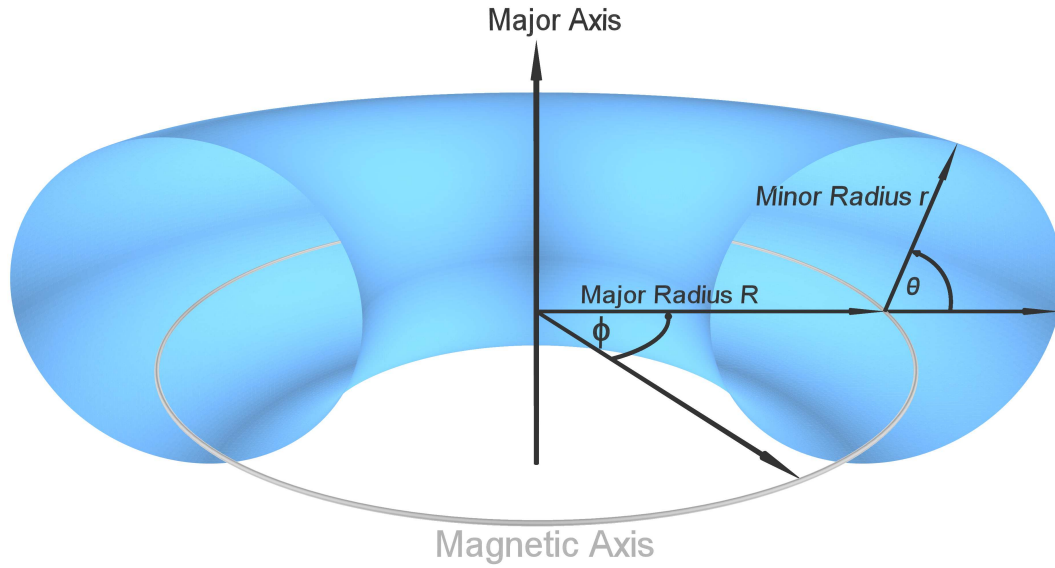


Figure 2.3: Simple toroidal coordinates  $r, \theta, \phi$ . Here,  $r$  is a flux surface label,  $\theta$  is the poloidal angle and  $\phi$  is the toroidal angle.

4. the effective radius  $r = a\sqrt{s}$ , where  $a$  is the effective minor radius.

Though the ideal MHD force balance,  $\nabla p = \mathbf{J} \times \mathbf{B}$ , ensures that  $\mathbf{B} \cdot \nabla p = 0$ , the plasma pressure cannot be used as flux surface label because it need not be single valued, as in the case of hollow pressure profiles, and it generally increases towards the magnetic axis which would result in a left-handed coordinate system.

Toroidal flux coordinates are a set of poloidal and toroidal angles  $\theta_f$  and  $\phi_f$  chosen such that the equation of a field line is the equation of a straight line in those coordinates. It is common to say that magnetic field lines appear as straight lines in  $(\theta_f, \phi_f)$ . To locate a point in space it is sufficient to identify the flux surface on which the point lies and then to construct coordinate curves on that flux surface with the required properties. This, however, does not yet describe a coordinate system. As stated in Appendix A.2, it is necessary to know the coordinate surfaces completely which in turn requires that  $\mathbf{B}$  is known everywhere. One usually starts by constructing a simple, or elementary, coordinate system  $(\rho, \theta, \phi)$  as seen in Fig. 2.3. It is assumed that  $\mathbf{B} = \mathbf{B}(\rho, \theta, \phi)$  is known as a function of the elementary angle coordinates. The functions  $\theta(\mathbf{R})$  and  $\phi(\mathbf{R})$  are multiple-valued functions because a certain point on a flux surface is described the angle coordinates  $\theta + 2\pi m$  and  $\phi + 2\pi n$  where  $m, n$  are arbitrary integers. The gradients, however, must be single-valued functions and therefore periodic in  $\theta$  and  $\phi$ .

When  $\mathbf{B}$  is written in its contravariant components,  $\mathbf{B} = B^\rho \mathbf{e}_\rho + B^\theta \mathbf{e}_\theta + B^\phi \mathbf{e}_\phi$  with  $B^i \equiv \mathbf{B} \cdot \nabla u^i$ , it can be seen immediately that  $B^\rho = \mathbf{B} \cdot \nabla \rho \equiv 0$  because  $\mathbf{B}$  lies in the



flux surface. Hence,

$$\mathbf{B} = B^\theta \mathbf{e}_\theta + B^\phi \mathbf{e}_\phi = \sqrt{g} B^\theta (\nabla \phi \times \nabla \rho) + \sqrt{g} B^\phi (\nabla \rho \times \nabla \theta) \quad (2.10)$$

where  $\sqrt{g} = [\nabla \rho \cdot (\nabla \theta \times \nabla \phi)]^{-1}$  is the Jacobian which is supposed to be a known, single-valued function of  $(\rho, \theta, \phi)$ . The two components  $B^\theta$  and  $B^\phi$  are not independent of each other, as can be seen from  $\nabla \cdot \mathbf{B} = 0$ :

$$\frac{\partial}{\partial \theta}(\sqrt{g} B^\theta) + \frac{\partial}{\partial \phi}(\sqrt{g} B^\phi) = 0, \quad (2.11)$$

which suggests that  $B^\theta$  and  $B^\phi$  are derived from a single function  $\nu = \nu(\rho, \theta, \phi)$ :

$$B^\theta = -\frac{1}{\sqrt{g}} \frac{\partial \nu}{\partial \phi}, \quad B^\phi = \frac{1}{\sqrt{g}} \frac{\partial \nu}{\partial \theta}. \quad (2.12)$$

The gradient of  $\nu$  is given by  $\nabla \nu = (\partial \nu / \partial \rho) \nabla \rho + (\partial \nu / \partial \theta) \nabla \theta + (\partial \nu / \partial \phi) \nabla \phi$ . Remembering that  $\nabla \rho \times \nabla \rho \equiv 0$ , Eq. (2.10) can be rewritten as

$$\begin{aligned} \mathbf{B} &= \sqrt{g} B^\theta (\nabla \phi \times \nabla \rho) + \sqrt{g} B^\phi (\nabla \rho \times \nabla \theta) \\ &= \nabla \rho \times \left( \frac{\partial \nu}{\partial \theta} \nabla \theta + \frac{\partial \nu}{\partial \phi} \nabla \phi \right) \\ &= \nabla \rho \times \nabla \nu. \end{aligned} \quad (2.13)$$

This equation can be used to determine which form  $\nu$  must have. The dependence of  $\nu$  on  $\rho$  is not important because the cross product with  $\nabla \rho$  cancels this term.  $\mathbf{B}$  is a physical quantity and thus must be periodic in  $(\theta, \phi)$  to be single-valued. It is not required that  $\nu$  is single-valued, but  $\nabla \rho \times \nabla \nu$  must be. If  $\nu$  is periodic in  $\theta$  and  $\phi$ ,  $\nabla \nu$  and  $\nabla \rho \times \nabla \nu$  will be as well. The only non-periodic (secular) terms that  $\nu$  may have must be linear in  $\theta$  and  $\phi$ , otherwise  $\nabla \nu$  would contain terms containing  $\theta$  or  $\phi$  which remain after the cross product with  $\nabla \rho$ . The most general form for  $\nu$  is

$$\nu(\rho, \theta, \phi) = a(\rho) \theta + b(\rho) \phi + \tilde{\nu}(\rho, \theta, \phi). \quad (2.14)$$

Here,  $\tilde{\nu}$  is the periodic part of  $\nu$ . Because  $B^\theta$ ,  $B^\phi$  and  $\sqrt{g}$  are known functions of  $\rho$ , the dependence of  $\nu$  on  $\rho$  is fixed. The  $\rho$  dependence of  $a(\rho)$  and  $b(\rho)$  can be found from (2.14) by looking at the toroidal flux and the poloidal ribbon flux inside the flux surface

$$\Psi_{tor} = \frac{1}{2\pi} \iiint_V \mathbf{B} \cdot \nabla \phi \, d^3 R, \quad \Psi_{pol}^r = \frac{1}{2\pi} \iiint_V \mathbf{B} \cdot \nabla \theta \, d^3 R, \quad (2.15)$$

where  $d^3 R = \sqrt{g} \, d\rho \, d\theta \, d\phi$ . The derivative with respect to  $\rho$  is

$$\begin{aligned} \dot{\Psi}_{tor} = \frac{d\Psi_{tor}}{d\rho} &= \frac{1}{2\pi} \int_0^{2\pi} d\theta \int_0^{2\pi} d\phi \sqrt{g} \mathbf{B} \cdot \nabla \phi = \frac{1}{2\pi} \int_0^{2\pi} d\theta \int_0^{2\pi} d\phi \frac{\partial \nu}{\partial \theta} \\ &= \frac{1}{2\pi} \int_0^{2\pi} d\theta \int_0^{2\pi} d\phi \left( a(\rho) + \frac{\partial \tilde{\nu}}{\partial \theta} \right) = 2\pi a(\rho) \end{aligned} \quad (2.16a)$$

$$\begin{aligned}\dot{\Psi}_{pol}^r = \frac{d\Psi_{pol}^r}{d\rho} &= \frac{1}{2\pi} \int_0^{2\pi} d\theta \int_0^{2\pi} d\phi \sqrt{g} \mathbf{B} \cdot \nabla \theta = \frac{1}{2\pi} \int_0^{2\pi} d\theta \int_0^{2\pi} d\phi \frac{\partial \nu}{\partial \phi} \\ &= \frac{1}{2\pi} \int_0^{2\pi} d\theta \int_0^{2\pi} d\phi \left( -b(\rho) + \frac{\partial \tilde{\nu}}{\partial \phi} \right) = -2\pi b(\rho)\end{aligned}\quad (2.16b)$$

Here, (2.12) and (2.14) have been used as well as the fact that the integrals containing  $\partial \tilde{\nu} / \partial \theta$  and  $\partial \tilde{\nu} / \partial \phi$  vanish because  $\tilde{\nu}$  is periodic in  $\theta$  and  $\phi$ . Hence,  $\nu$  becomes

$$\nu(\rho, \theta, \phi) = \frac{1}{2\pi} (\dot{\Psi}_{tor} \theta - \dot{\Psi}_{pol}^r \phi) + \tilde{\nu}(\rho, \theta, \phi). \quad (2.17)$$

If  $\tilde{\nu}$  happens to be constant on a flux surface (or zero), the coordinates  $(\theta, \phi)$  are already flux coordinates because in this case the equation of a field line (2.2) in these coordinates is the equation of a straight line,  $\dot{\Psi}_{tor} \theta - \dot{\Psi}_{pol}^r \phi = \text{const.}$  Otherwise one can perform a change of variables to eliminate  $\tilde{\nu}$ :

$$\theta_f = \theta + \frac{2\pi \tilde{\nu}}{\dot{\Psi}_{tor}}, \quad \phi_f = \phi \quad \text{or} \quad (2.18a)$$

$$\phi_f = \phi - \frac{2\pi \tilde{\nu}}{\dot{\Psi}_{pol}^r}, \quad \theta_f = \theta. \quad (2.18b)$$

The contravariant components of  $\mathbf{B}$  in the new coordinates are given by  $B^\rho = 0$ ,  $B^{\theta_f} = \dot{\Psi}_{pol}^r / 2\pi \sqrt{g_f}$  and  $B^{\phi_f} = \dot{\Psi}_{tor} / 2\pi \sqrt{g_f}$ . With these relations given, the rotational transform  $\iota$  can be rigorously defined as the slope of the field lines in flux coordinates:

$$\iota(\rho) = \frac{d\theta_f}{d\phi_f} = \frac{B^{\theta_f}}{B^{\phi_f}} = \frac{\dot{\Psi}_{pol}^r}{\dot{\Psi}_{tor}}. \quad (2.19)$$

The new angle coordinates  $(\theta_f, \phi_f)$  are not uniquely determined. If  $(\theta'_f, \phi'_f)$  are supposed to be given by

$$\theta'_f = \theta_f + \dot{\Psi}_{pol}^r G(\rho, \theta_f, \phi_f), \quad \phi'_f = \phi_f + \dot{\Psi}_{tor} G(\rho, \theta_f, \phi_f), \quad (2.20)$$

where  $G$  is an arbitrary periodic function, these coordinates are proper straight field line coordinates, too, as can be shown by substitution. This freedom can be used to further deform the angle coordinates to make expressions look simpler. Boozer [28] uses the freedom to form a set of magnetic coordinates that have the property that the Jacobian is a function of  $\sqrt{g} \sim 1/B^2$ , where the proportionality factor is a constant on flux surfaces. This simple Jacobian has made Boozer's coordinates very popular. They are explained in detail in Appendix B.

## 2.2 Particle Dynamics in Fusion Plasmas

In high-temperature fusion plasmas the mean free path for collisions between particles is very large and the orbits in between the collisions are subject to the forces of averaged

magnetic and electric fields only, generated by external sources and by long-range interactions between the particles. In order to understand the plasma confinement in magnetic fields it is necessary to first understand the unperturbed orbits of charged particles. The orbits are described by the equation of motion:

$$\mathbf{F} = \frac{d\mathbf{p}}{dt} = q(\mathbf{E} + \mathbf{v} \times \mathbf{B}) + \mathbf{K}_{ext}. \quad (2.21)$$

Here,  $\mathbf{p}$  is the particle momentum,  $\mathbf{E}$  and  $\mathbf{B}$  are the electric and magnetic field, respectively,  $\mathbf{v}$  is the particle velocity and  $\mathbf{K}_{ext}$  is an external force. In a homogeneous magnetic field, without electric field and external force, the particle moves freely and with constant speed along the field lines and gyrates around them in the plane perpendicular to the magnetic field. For many applications it is sufficient to neglect the gyrational motion and assume that the particle moves along a virtual line in the center of the gyro-orbit, the *guiding center*.

The circulating charged particle produces a small current and therefore an additional magnetic field. This field is opposite to the external magnetic field and weakens it. The effect is characterized by the *magnetic moment* of the particle

$$\boldsymbol{\mu} = -\frac{mv_{\perp}^2}{2B}\mathbf{b} = -\frac{1}{2}mv_{\perp}^2\frac{\mathbf{B}}{B^2} \quad (2.22)$$

The magnetic moment grows linearly with the particle energy perpendicular to the magnetic field, is independent of the particle charge, and is directed opposite to the external magnetic field. It is important to note that without collisions the magnetic moment is conserved if the magnetic field  $B$  varies slowly along the particle orbit compared to the oscillatory gyrational motion, in other words, the magnetic moment is an adiabatic invariant. In magnetic fusion devices the magnetic moment can be considered as a constant for thermal particles in nearly all cases of interest because the strong magnetic field makes the gyro-radii so small that the field variation over the gyro-radius is negligible.

### 2.2.1 Radial Particle Drifts

A charged particle is confined in a magnetic field if it is not subject to drifts perpendicular to the magnetic field. At first a general expression for the drift velocity caused by a force is derived. Starting from eq. (2.21), acceleration terms due to electric fields and the particle gyration are neglected, the particle is taken to be force-free,  $\mathbf{F} = \mathbf{0}$  and only the components  $\perp \mathbf{B}$  are considered:

$$0 = \mathbf{K}_{\perp} + q(\mathbf{v}_D \times \mathbf{B})_{\perp}. \quad (2.23)$$

Here,  $\mathbf{K}$  is an accelerating force. This equation describes the drift velocity  $\mathbf{v}_D$  of the guiding center of particles caused by force  $\mathbf{K}$ , which is perpendicular to  $\mathbf{K}$  and  $\mathbf{B}$ :

$$\mathbf{v}_D = \frac{\mathbf{K} \times \mathbf{B}}{qB^2} \quad (2.24)$$

This equation states that only forces with a component perpendicular to  $\mathbf{B}$  can cause cross-field drifts and that the direction of the drift can be different for electrons and ions.

### 2.2.1.1 $\mathbf{E} \times \mathbf{B}$ drift

Charged particles are accelerated in electric fields which exert a force  $\mathbf{F}_E = q\mathbf{E}$  on the particle. If the electric field is purely parallel to the magnetic field,  $\mathbf{E} \parallel \mathbf{B}$ , the particle will be accelerated along the magnetic field and no cross-field drift occurs. If the electric field is perpendicular to the magnetic field, eq. (2.24) can be used to determine the  $\mathbf{E} \times \mathbf{B}$  drift velocity  $\mathbf{v}_{E \times B}$ :

$$\mathbf{v}_{E \times B} = \frac{\mathbf{E} \times \mathbf{B}}{B^2}. \quad (2.25)$$

This drift does not depend on mass or charge of the particles and is therefore the same for ions and electrons.

### 2.2.1.2 Drift in Inhomogeneous Magnetic Fields

The orbit of a gyrating particle has a constant curvature if it moves in a homogeneous field, it moves on a closed circle in the plane  $\perp \mathbf{B}$ . If the magnetic field in which the particle moves has gradients perpendicular to the field direction,  $\nabla B \perp \mathbf{B}$ , the curvature of the gyro-orbit depends on the gyro angle and is no longer constant. The orbit is not closed anymore and in average, the particle drifts into a direction which is perpendicular to both,  $\nabla B$  and  $\mathbf{B}$ , as indicated in Fig. 2.4. The drift velocity can be approximated if we replace the gyrating particle by a dipole magnet with the same magnetic moment  $\mu$ . In inhomogeneous fields, this magnet experiences a force  $\mathbf{K}_{\nabla B} = \mu \nabla_{\perp} B$  which is substituted into Eq. (2.24):

$$\mathbf{v}_{\nabla B} = \frac{\mathbf{K}_{\nabla B} \times \mathbf{B}}{qB^2} = -\mu \frac{\nabla_{\perp} B \times \mathbf{B}}{qB^2} = \frac{mv_{\perp}^2}{2B} \cdot \frac{\mathbf{B} \times \nabla_{\perp} B}{qB^2}. \quad (2.26)$$

This drift depends on particle mass and particle charge. In a magnetic field without rotational transform electrons and ions drift vertically away into different direction, producing charge separation and a strong electric field, which will in turn cause a radial  $\mathbf{E} \times \mathbf{B}$ -drift across the magnetic field and out of the confinement region.

### 2.2.1.3 Curvature Drift

If the particle moves along bent magnetic field lines it will experience a centrifugal force caused by particle inertia and the field line curvature  $\kappa$  given by eq. (2.5). The force depends on the velocity parallel to the magnetic field,  $\mathbf{K}_{\kappa} = -mv_{\parallel}^2 \kappa$ . The expression

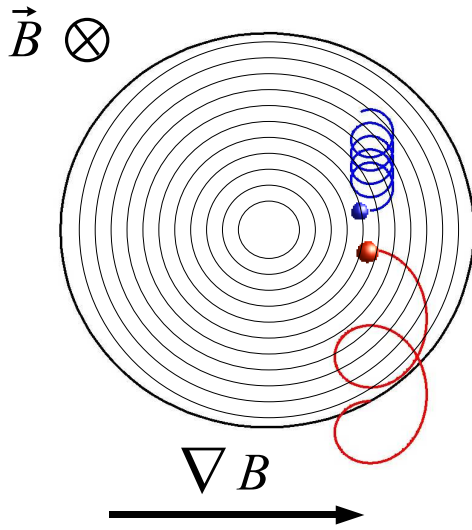


Figure 2.4: Effect of gradients  $\nabla B \perp \mathbf{B}$ : gyration orbits are not closed anymore, ions (red) and electrons (blue) start drifting in opposite directions.

— Flux Surface  
— Drift Surface

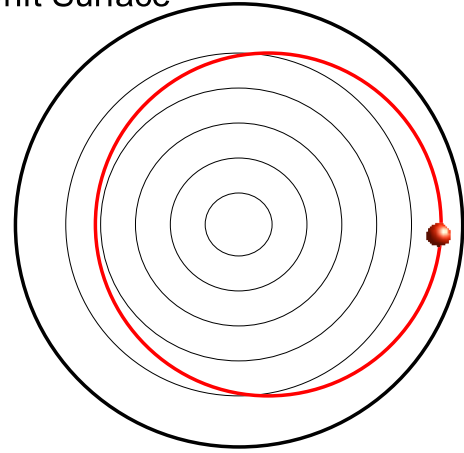


Figure 2.5: Drift orbit of charged particles in a helical field. The displacement is caused by permanent  $\nabla B$  and  $\kappa$  drifts which cancel in average.

for  $\kappa$  can be further modified to give  $\kappa = (\mathbf{b} \cdot \nabla) \mathbf{b} = \nabla b - \mathbf{b}(\mathbf{b} \cdot \nabla b) = \nabla_{\perp} b = \nabla_{\perp} B/B$ . Inserting this expression into eq. (2.24) yields

$$\mathbf{v}_{\kappa} = \frac{\mathbf{K}_{\kappa} \times \mathbf{B}}{qB^2} = \frac{mv_{\parallel}^2}{B} \cdot \frac{\mathbf{B} \times \nabla_{\perp} B}{qB^2}. \quad (2.27)$$

Again, this vertical drift depends on particle mass and charge, leads to charge separation and produces electric fields. The resulting  $\mathbf{E} \times \mathbf{B}$  drift will transport the particles radially out of the confinement region.

#### 2.2.1.4 Drift Surfaces

Because of the curvature and the  $\nabla B$  drifts, a simple toroidal magnetic field does not confine a plasma. It was soon discovered that the addition of a poloidal field component can stop the particles from drifting away. This makes the field lines spiral helically around the torus and the particles are led alternately through regions where the vertical drift points into and out of the confinement region, respectively. Thus the particles stay confined on poloidally and toroidally closed surfaces. Due to the permanent drift, however, the *drift surface* is displaced with respect to the magnetic surface as indicated in Fig. (2.5). The displacement is of the order [29]

$$\delta_D \sim \frac{r}{R} \cdot r_{L,\theta} = \epsilon \cdot r_{L,\theta}, \quad (2.28)$$

where  $\epsilon = r/R$  is the local inverse aspect ratio whereas the *poloidal Larmor radius*  $r_{L,\theta}$  is defined as:

$$r_{L,\theta} = \frac{mv}{|q|B_\theta}$$

The drift surface displacement  $\delta_D$  depends on the particle energy via  $r_{L,\theta}$ . For thermal particles  $\delta_D$  is usually small enough to be neglected, but for highly energetic particles that are born near the plasma boundary the displacement can become so large that these are lost during their first orbit.

### 2.2.2 Trapped and Passing Particles

The energy of a charged particle  $\mathcal{E} = m(v_\parallel + v_\perp)^2/2$  is conserved along its orbit, the magnetic moment  $\mu = mv_\perp^2/2B$  is an adiabatic invariant which will be taken to be constant in the following. One can now consider the effect of a gradient of  $B$  parallel to the magnetic field. If the particle moves into regions with higher field, the conservation of the magnetic moment requires that the velocity perpendicular to  $\mathbf{B}$  grows accordingly

$$\frac{v_\perp^2}{B} = \text{const.}$$

Conservation of energy requires that  $(v_\parallel + v_\perp)^2 = \text{const.}$  Hence, the particle will be accelerated perpendicular to  $\mathbf{B}$  and slowed down along the field. If  $B$  becomes so strong that  $\mathcal{E} - \mu B = 0$ , all particle energy is transferred to the gyration and the particle motion along the magnetic field stops and is reversed. This is called the magnetic mirror effect.

Assuming a simple magnetic field

$$\mathbf{B} = \begin{pmatrix} 0 \\ B_\theta(r) \\ B_0 \end{pmatrix} \cdot \left(1 - \frac{r}{R} \cos \theta\right)$$

in the elementary toroidal coordinates introduced in Fig. (2.3), it is easily seen that all particles for which  $\mathcal{E}/[B_0(1 + r/R)] < \mu < \mathcal{E}/[B_0(1 - r/R)]$  holds are mirrored at some poloidal angle  $\theta_m$ . They cannot perform a full poloidal transit around the torus and remain in the range  $-\theta_m \leq \theta \leq \theta_m$ . Such particles are referred to as *trapped particles*, and on any magnetic surface  $r = \text{const}$  they constitute a fraction  $\sim \sqrt{2r/R}$  of all particles of an isotropic distribution. All other particles, referred to as *passing particles*, circulate around the torus poloidally as well as toroidally, with a parallel velocity  $v_\parallel$  being modulated by the magnetic field variation but which does not change sign. Fig. 2.6 shows the orbit of a trapped particle, a so called "banana orbit". Trapped particles stay indeed confined on the low field side of the torus where they are mirrored between points with the same field strength. The slow precession in toroidal direction is also caused by the drifts. The width of the banana is an important parameter in

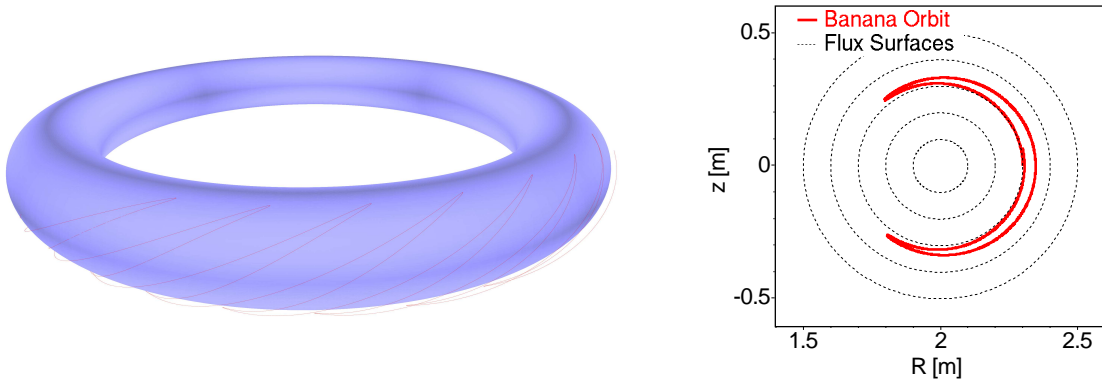


Figure 2.6: "Banana" orbit of a trapped particle in 3D and a projection onto the poloidal  $(r, z)$ -plane. The particle is being reflected at a certain magnetic field strength. The drifts cause the excursions from the flux surface and the toroidal precession of the particle.

neoclassical transport theory because it determines the step size in a random walk model. It is approximately given by [29]

$$\delta_B \sim \sqrt{\epsilon} \cdot r_{L,\theta}. \quad (2.29)$$

A comparison with Eq. (2.28) yields that the banana width is a factor  $\sqrt{\epsilon}$  larger than the drift surface displacement. As in the case of the drift surface displacement for passing particles, the banana width of trapped particles depends on the particle energy. This means of course that energetic trapped particles are more easily lost than passing particles.

In stellarators the magnetic field strength also varies toroidally. If a particle is trapped in a narrow toroidal mirror, it stays at approximately the same poloidal position and cannot profit from the drift "compensation" due to the helical field. Hence, these *deeply trapped particles* are lost almost immediately. In velocity space  $(v_{\parallel}, v_{\perp})$  the region from which the particles are lost forms a cone, accordingly named loss cone.

While the kinetic energy of a particle is a constant of motion, its associated magnetic moment is an adiabatic invariant, which is also well conserved in fusion plasmas. From these two constants, a parameter can be derived that describes whether a particle is trapped or not. Remembering that  $\mu B \equiv \mathcal{E}_{\perp}$  is the particles perpendicular kinetic energy, passing particles have

$$\mathcal{E} - \mu B_{max} \equiv \mathcal{E}_{\parallel} > 0$$

at the point of the highest magnetic field along their orbit. Trapped particles are reflected before this point and  $\mathcal{E} - \mu B_{max} = 0$  describes the trapping boundary. A different parameter that is commonly used is the pitch  $\chi = v_{\parallel}/v$ . A particle with a small pitch  $\chi \approx 0$  has small parallel velocity compared to the perpendicular velocity  $v_{\perp} = \sqrt{1 - p^2} \cdot v$  and is likely to be trapped. The trapping boundary again depends on  $B_{max}$ . This definition, however, is not exact and suffers from  $v_{\parallel}$  and therefore the

pitch not being a constant of motion. It is meaningful only after averaging along the particle orbit.

## 2.3 Magnetohydrodynamics

A complete description of a fusion plasma as a many-particle system can in general be done using kinetic theory. In this framework, the plasma is described in terms of distribution functions  $f_i = f_i(\mathbf{x}, \mathbf{p})$  which measure the number of particles of species  $i$  at position  $\mathbf{x}$  having the momentum  $\mathbf{p}$ . All macroscopic quantities (pressure, currents, temperatures, densities, ...) of species  $i$  can be calculated as velocity moments of the distribution function  $f_i$ . The evolution of the distribution function is described by a kinetic equation, in the case of plasma physics the *Vlasov equation* is used:

$$\frac{\partial f}{\partial t} + \mathbf{v} \cdot \frac{\partial f}{\partial \mathbf{x}} + \frac{q}{m}(\mathbf{E} + \mathbf{v} \times \mathbf{B}) \cdot \frac{\partial f}{\partial \mathbf{v}} = 0. \quad (2.30)$$

It is obtained by inserting the Lorentz force directly into Boltzmann's equation. This general approach provides a fairly complete description of collisionless plasmas, but inherits a vast complexity.

A fusion plasma has several properties that make it possible to describe it approximately with much simpler models:

- quasineutrality:  $n_e = \sum_i n_i Z_i$  in each volume much larger than the Debye sphere;
- the bulk plasma on a flux surface is in thermal equilibrium;
- the plasma is strongly magnetized, i.e., the particles can move freely only along magnetic field lines and the gyro-radii are much smaller than typical scale lengths;
- the plasma has almost no electrical resistivity.

The local thermal equilibrium guarantees that the plasma can be suitably described by macroscopic plasma parameters such as density, pressure, and average velocity which are obtained as the moments of the distribution function. Relations between these quantities can be obtained by taking the moments of the Vlasov equation accordingly. This procedure is shown in many textbooks on plasma physics, e.g. [30], and is not repeated here. Upon taking the zeroth-order moment, the equation of continuity is obtained. The first-order moment results in a force balance equation that describes the conservation of momentum. One usually stops after taking the second-order moment, from which the conservation of energy is derived. The set of equations is not closed: Each equation contains quantities which have to be derived from the next higher-order moment. In fact, the set of equations has to be closed at some point by using an approximation for the missing quantity.



The moment equations have a form similar to the equations which describe a conducting fluid immersed in a magnetic field. Consequently, the described approach is known as "magnetohydrodynamic" (MHD) description. Quasineutrality relates the ion- and electron density to each other and allows one to consider the plasma as a single fluid. In the approximation of infinite conductivity the "ideal MHD" equations read

$$\begin{aligned}
\frac{\partial \rho}{\partial t} + \nabla \cdot (\rho \mathbf{v}) &= 0 & (\text{mass continuity}) \\
\rho \frac{d\mathbf{v}}{dt} + \nabla p - \mathbf{J} \times \mathbf{B} &= 0 & (\text{force balance}) \\
\mathbf{E} + \mathbf{v} \times \mathbf{B} &= 0 & (\text{ideal Ohm's law}) \\
\frac{d}{dt} \left( \frac{p}{\rho^\gamma} \right) &= 0 & (\text{adiabatic eq. of state}) \\
\nabla \cdot \mathbf{B} &= 0 & (\text{no magnetic monopoles}) \\
\nabla \times \mathbf{B} - \mu_0 \mathbf{J} &= 0 & (\text{Ampère's law}) \\
\nabla \times \mathbf{E} + \frac{\partial \mathbf{B}}{\partial t} &= 0 & (\text{Faraday's law})
\end{aligned} \tag{2.31}$$

Here,  $p$  is the pressure,  $\rho$  the mass density,  $\mathbf{v}$  the fluid velocity,  $\gamma$  the adiabaticity index,  $\mathbf{J}$  the current density, and  $d/dt = \partial/\partial t + (\mathbf{v} \cdot \nabla)$  is the convective derivative. The electric and magnetic fields,  $\mathbf{E}$  and  $\mathbf{B}$ , consist of externally applied fields and averaged internal fields arising from long-range interactions between the plasma particles.

A lot of physics has been discarded in the derivation of the ideal MHD equations. Due to the assumptions made, these equations are not valid on time and length scales where the single particle motion becomes important. The requirements on the collisionality of the plasma are quite strict: the plasma has to be collisional enough to ensure a local thermal equilibrium and uncollisional enough that electric resistivity is negligible. Still, the ideal MHD model provides a powerful framework to describe global properties of the plasma and is used to determine the equilibrium and its linear stability.

### 2.3.1 MHD equilibria

The ideal MHD model is commonly employed to calculate a selfconsistent solution of the model (2.31) at finite plasma pressures, called *equilibrium*. This is needed because, according to the force balance equation, the presence of pressure gradients generates currents flowing in the plasma which modify the vacuum magnetic field until a stable configuration is obtained. One is usually interested in stationary equilibria where  $\mathbf{v} = 0$  because these are most stable. Any equilibrium flow is an additional source of energy which may be tapped by instabilities. The magnetostatic equations are found from

(2.31) by setting  $\mathbf{v} = 0$ . One obtains

$$\begin{aligned}\mathbf{J} \times \mathbf{B} &= \nabla p \\ \nabla \times \mathbf{B} &= \mu_0 \mathbf{J} \\ \nabla \cdot \mathbf{B} &= 0\end{aligned}\tag{2.32}$$

For axisymmetric toroidal equilibria it is possible to derive an equilibrium equation that must be satisfied by any such plasma. A suitable choice of coordinates is the cylindrical  $(R, \phi, z)$ -coordinate system where  $\phi$  is the toroidal angle,  $R$  is the radius and  $z$  the height along the major axis of the torus. Writing out  $\nabla \cdot \mathbf{B}$  in these coordinates yields

$$\nabla \cdot \mathbf{B} = \frac{1}{R} \frac{\partial(RB_R)}{\partial R} + \frac{\partial B_z}{\partial z} + \frac{1}{R} \frac{\partial B_\phi}{\partial \phi} = 0.\tag{2.33}$$

$\partial/\partial\phi = 0$  due to axisymmetry and hence  $\mathbf{B} = \mathbf{B}(R, z)$  only and within a poloidal plane the components of  $\mathbf{B}$  can be written in terms of a flux function  $\Psi$

$$RB_R = \frac{\partial \Psi}{\partial z}, \quad RB_z = -\frac{\partial \Psi}{\partial R} \quad \text{or} \quad \mathbf{B} = \frac{1}{R} \nabla \Psi \times \hat{\mathbf{e}}_\phi + B_\phi \hat{\mathbf{e}}_\phi.\tag{2.34}$$

The plasma current can now be calculated using Ampère's law and the obtained magnetic field

$$\mu_0 \mathbf{J} = \frac{1}{R} \nabla(RB_\phi) \times \hat{\mathbf{e}}_\phi - \frac{1}{R} \Delta^* \Psi \hat{\mathbf{e}}_\phi,\tag{2.35}$$

where  $\Delta^*$  is the Laplace operator in these coordinates. The force balance equation  $\mathbf{J} \times \mathbf{B} = \nabla p$  states that  $\mathbf{B} \cdot \nabla p = 0$  and therefore magnetic field lines lie on isobaric surfaces, or  $p = p(\Psi)$ . Furthermore,  $\mathbf{J} \cdot \nabla p = 0$  from which can be derived that  $\mathbf{J} = \mathbf{J}(\Psi)$  alone. After some further manipulation one obtains the *Lüst-Schlüter-Grad-Shafranov equation* as

$$\Delta^* \Psi = -\mu_0 R^2 \frac{dp(\Psi)}{d\Psi} - \mu_0^2 F(\Psi) \frac{dF(\Psi)}{d\Psi}\tag{2.36}$$

where  $F(\Psi) \equiv RB_\phi/\mu_0$ . This is a second order elliptic partial differential equation for calculating the equilibrium in terms of the magnetic flux. To find a solution, the pressure  $p$  and the current function  $F$  have to be prescribed as some physically reasonable distribution of the flux  $\Psi$  along with suitable boundary conditions. After having determined the spatial distribution of the magnetic flux  $\Psi(R, z)$ , the other quantities like poloidal and toroidal magnetic field, current and pressure can be found as functions of  $R$  and  $z$ . Shafranov has given a simple solution of this equation starting from the linear ansatz  $p(\Psi) \sim \Psi$  and  $F(\Psi) = F_0$ :

$$\Psi(R, z) = \frac{R^2}{R_0^4} (2R_0^2 - R^2 - 4a^2 z^2),$$

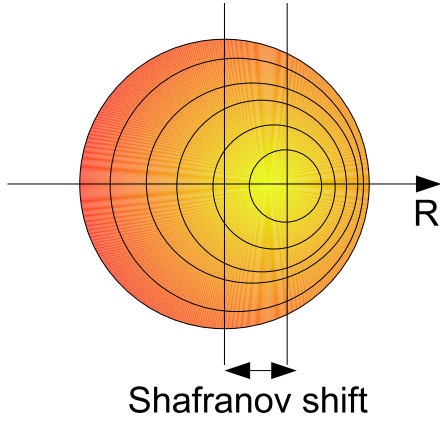


Figure 2.7: Solution of an axisymmetric toroidal equilibrium with circular cross sections including Shafranov shift

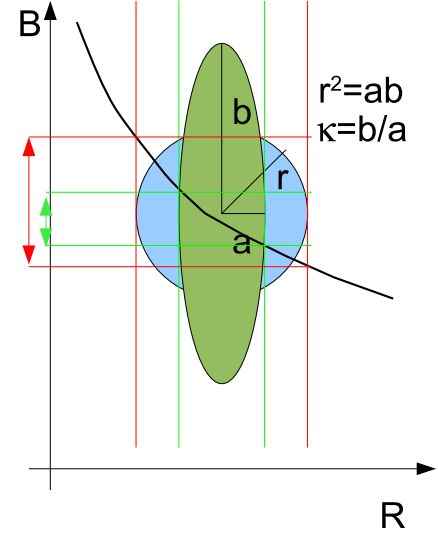


Figure 2.8: Plasma elongation to reduce the Shafranov shift

where  $R_0$  and  $a$  are constants. An example gives Fig. 2.7 where contours of constant  $\Psi$  are shown which correspond to flux surfaces. This figure also indicates the so-called *Shafranov shift*, a general property of toroidal equilibria. The shift of the inner flux surfaces w.r.t. the outer ones is generated by equilibrium currents in the following way: The equilibrium current density  $\mathbf{J}$  can be written in components parallel and perpendicular to  $\mathbf{B}$ ,

$$\mathbf{J} = \mathbf{J}_{\parallel} + \mathbf{J}_{\perp} = (\mathbf{J} \cdot \mathbf{B}) \frac{\mathbf{B}}{B^2} - \frac{\nabla p \times \mathbf{B}}{B^2}.$$

The perpendicular component  $\mathbf{J}_{\perp}$  is called the diamagnetic current and depends on the pressure gradient. The parallel current is called Pfirsch-Schlüter current and is linked to the diamagnetic current via  $\nabla \cdot \mathbf{J} = \nabla \cdot (\mathbf{J}_{\parallel} + \mathbf{J}_{\perp}) = 0$ . From this one obtains:

$$\nabla \cdot \mathbf{J}_{\parallel} = -\nabla \cdot \mathbf{J}_{\perp} = 2\mathbf{J}_{\perp} \cdot \nabla \ln B. \quad (2.37)$$

Eq. (2.37) states that the Pfirsch-Schlüter currents are determined by two factors: firstly by the diamagnetic currents that depend on the pressure gradient, and secondly by the poloidal variation of  $B = |\mathbf{B}|$ . The toroidal component of the Pfirsch-Schlüter currents has a different sign on high-field side and low-field side of the torus and creates an additional magnetic field that shifts the inner flux surfaces towards the low-field side. The Shafranov shift limits the stability of the equilibrium towards high central plasma pressures. In order to reduce the Shafranov shift,  $\Delta B = B_{\max} - B_{\min}$  has to be reduced. By observing that  $B \sim 1/R$  for toroidal magnetic fields, one way to achieve this goal is a non-circular shaping of flux surfaces as in Fig. 2.8. This is the reason why in most magnetic fusion devices, tokamaks as well as stellarators, the flux surfaces have elliptic or D-shaped cross sections.

For general three-dimensional equilibria it is not possible to find a simplified equilibrium condition such as Eq. (2.36). The common way to calculate an equilibrium in this case is to employ a variational principle. Besides the prescription of pressure and current profiles, an initial value for the spatial distribution of the magnetic flux  $\Psi(R, \phi, z)$  is needed as well. This configuration is then varied until the residual MHD forces vanish or the MHD energy functional is minimized. An example of a W7-AS equilibrium is shown in Fig. 2.9

### 2.3.2 Stability of MHD Equilibria

Another purpose for which the ideal MHD model is commonly utilized is to test whether an equilibrium is stable to small perturbations, and hence to determine whether the equilibrium will persist or ultimately be destroyed. The MHD model allows only perturbations that grow exponentially or stable waves that propagate through the plasma.

The MHD equations are nonlinear partial differential equations. In order to make them more amenable to stability analysis, it is reasonable to linearize them about a stationary equilibrium by writing all quantities  $Q$  as  $Q(\mathbf{x}, t) = Q_0(\mathbf{x}) + \epsilon \tilde{Q}(\mathbf{x}, t)$ , where the subscript 0 denotes the equilibrium value,  $\tilde{Q}$  is the perturbation and  $\epsilon$  a smallness parameter. All terms of order  $\epsilon^2$  and higher are neglected. The linearized equations are obtained by setting  $\epsilon = 1$ . It is customary to introduce the fluid displacement vector  $\boldsymbol{\xi}$  defined by

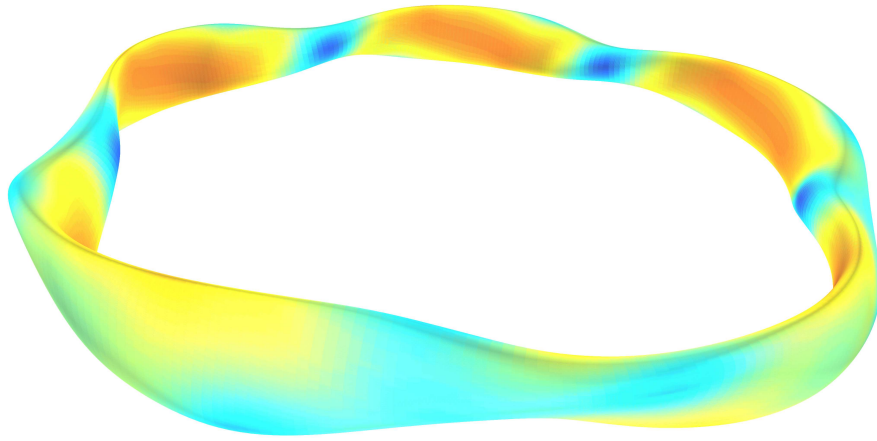
$$\mathbf{v} = \frac{\partial \boldsymbol{\xi}}{\partial t}.$$

Because a stationary equilibrium was assumed ( $\mathbf{v}_0 = 0$ ),  $\boldsymbol{\xi}$  clearly is a first order quantity in  $\epsilon$ . The linearized set of ideal MHD equations then reads

$$\begin{aligned} \frac{\partial \tilde{p}}{\partial t} + \nabla \cdot (\rho_0 \tilde{\mathbf{v}}) &= 0 \\ \rho_0 \frac{\partial^2 \boldsymbol{\xi}}{\partial t^2} + \nabla \tilde{p} - \tilde{\mathbf{J}} \times \mathbf{B}_0 - \mathbf{J}_0 \times \tilde{\mathbf{B}} &= 0 \\ \tilde{\mathbf{E}} + \tilde{\mathbf{v}} \times \mathbf{B}_0 &= 0 \\ \frac{\partial \tilde{p}}{\partial t} + \tilde{\mathbf{v}} \cdot \nabla p_0 + \gamma p_0 \nabla \cdot \tilde{\mathbf{v}} &= 0 \\ \nabla \cdot \tilde{\mathbf{B}} &= 0 \\ \nabla \times \tilde{\mathbf{B}} - \mu_0 \tilde{\mathbf{J}} &= 0 \\ \nabla \times \tilde{\mathbf{E}} + \frac{\partial \tilde{\mathbf{B}}}{\partial t} &= 0 \end{aligned} \tag{2.38}$$

The linearized Ohm's and Ampère's law can be used to eliminate  $\tilde{\mathbf{J}}$  and  $\tilde{\mathbf{E}}$ . The resulting equations can be used to eliminate  $\tilde{\mathbf{B}}$  and  $\tilde{p}$  from the force balance equation. The result is a equation of motion for the fluid displacement vector  $\boldsymbol{\xi}$ :

$$\rho_0 \frac{\partial^2 \boldsymbol{\xi}}{\partial t^2} = \mathbf{F}(\boldsymbol{\xi}), \tag{2.39}$$



(a) Variation of  $|\mathbf{B}|$  (blue: small, red: high fields).

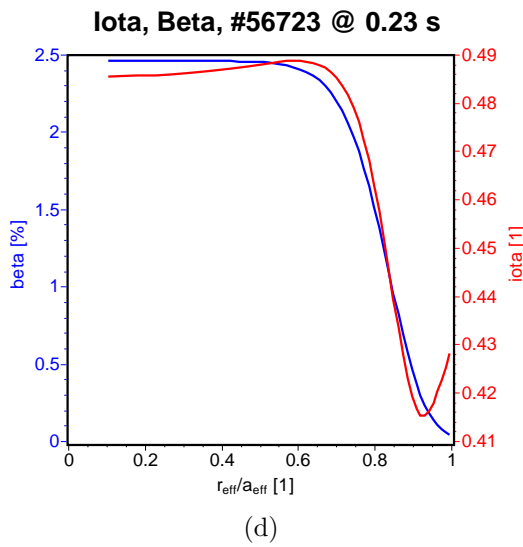
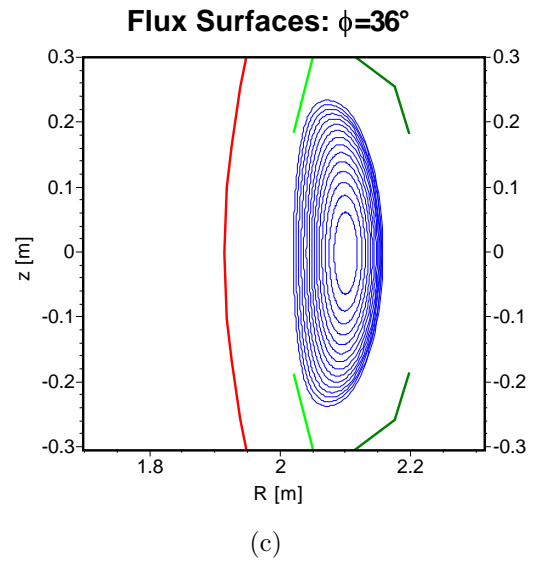
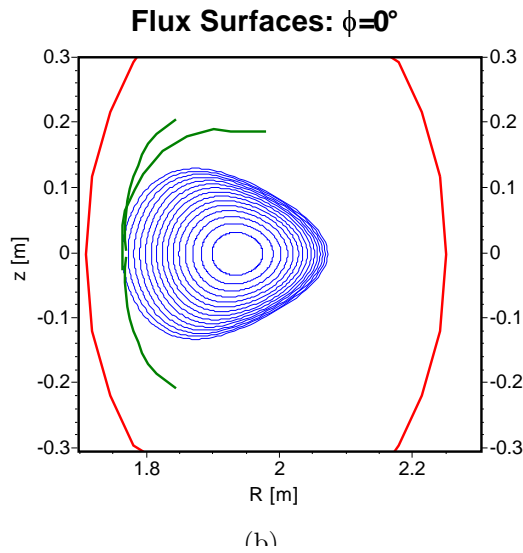


Figure 2.9: MHD equilibrium for W7-AS shot #56723 at  $t = 0.230$ s. (a) shows the variation of the magnetic field strength on the flux surface, (b) and (c) show the toroidal variation of the plasma cross section along with the vessel (red) and in-vessel components (green), and (d) shows the radial distribution of  $\beta$  and  $\iota$ .

where  $\mathbf{F}(\boldsymbol{\xi})$  is the MHD force operator

$$\begin{aligned} \mathbf{F}(\boldsymbol{\xi}) \equiv & \nabla(\gamma p_0 \nabla \cdot \boldsymbol{\xi} + \boldsymbol{\xi} \cdot \nabla p_0) \\ & + \frac{1}{\mu_0} \{(\nabla \times \nabla \times (\boldsymbol{\xi} \times \mathbf{B}_0)) + (\nabla \times \mathbf{B}_0) \times [\nabla \times (\boldsymbol{\xi} \times \mathbf{B}_0)]\}. \end{aligned} \quad (2.40)$$

The stability analysis can be done in several ways using this force operator. The first method is the application of the energy principle: If the equilibrium is stable, the change in potential energy due to a displacement of the plasma by  $\boldsymbol{\xi}$  should be positive. If the equilibrium is unstable, the potential energy of the plasma can be lowered by displacing it. The change in potential energy can be calculated from the work required to displace the plasma:

$$\delta W = -\frac{1}{2} \int \boldsymbol{\xi} \cdot \mathbf{F}(\boldsymbol{\xi}) d\tau.$$

If  $\delta W$  is positive for *all* allowable displacements, the equilibrium is stable. If  $\delta W$  is negative for *some* allowable displacements, the equilibrium is unstable.

A different way of analyzing the stability of an equilibrium is the normal mode method. Here the ansatz  $\boldsymbol{\xi}(\mathbf{x}, t) = \boldsymbol{\xi}(\mathbf{x}) \cdot \exp(-i\omega t)$  is made for the displacement. Doing a Fourier transform of eq. (2.39) in time, an eigenvalue equation is obtained

$$-\rho_0 \omega^2 \boldsymbol{\xi} = \mathbf{F}(\boldsymbol{\xi})$$

with  $\omega^2$  as eigenvalue and  $\boldsymbol{\xi}$  as eigenfunction.  $\mathbf{F}$  is a hermitian as well as self-adjoint operator and hence, all eigenvalues  $\omega^2$  are real. The square root of  $\omega^2$  can be written as a complex number:  $\sqrt{\omega^2} = \omega_r + i\gamma$ , where  $\omega_r$  is the eigenfrequency and  $\gamma$  the growth rate of the perturbation. The condition  $\omega^2 = 0$  marks the transition between stable, purely propagating waves with  $\gamma = 0$  and unstable, purely growing solutions with  $\omega_r = 0$ . A mixture of both, e.g. growing or damped oscillations, is not possible. In addition to the frequency or growth rate, the eigenfunction and therefore the structure of the perturbation is known as well.

## Chapter 3

# Alfvén Waves, -continua and Eigenmodes

Alfvén waves and Alfvén eigenmodes constitute the marginally stable part of the spectrum, e.g.  $\omega^2 > 0$ , of the ideal MHD force operator  $\mathbf{F}$ , Eq. (2.40). In ideal MHD, they correspond to purely oscillating phenomena,  $\text{Re}(\omega) > 0$ , with constant amplitude,  $\text{Im}(\omega) = 0$ , which can roughly be divided into compressional and uncompressional waves. This chapter reviews the properties of the spectrum of uncompressional shear Alfvén waves in fusion devices. Due to the enormous amount of literature available on this topic, the focus is put on selected issues only.

It is the complexity of  $\mathbf{F}$  that makes it very difficult to analyze the force operator directly. Resolving the Alfvén wave spectrum in full detail in three-dimensional geometry requires to employ numerical codes. It is therefore common to investigate the properties of the spectrum in several approximations with increasing complexity, making analytical progress wherever possible – a procedure that gives insight into the physical origin of various aspects even if the derived expressions describe the situation only qualitatively.

This chapter follows the same procedure. Sec. 3.1 reviews the continuous Alfvén wave spectrum. At first, the dispersion relations of compressional and uncompressional Alfvén waves are derived in an infinite, homogeneous and magnetized plasma. Following this, the influence of plasma inhomogeneities and symmetry breaking in toroidal geometries on the shear Alfvén wave spectrum will be shown. Besides the continuous spectrum of localized waves, the ideal MHD force operator also contains a discrete spectrum of extended shear Alfvén eigenmodes in bounded plasmas that are considered in section 3.2.

As outlined above, the ideal MHD equations are obtained as velocity moments of the kinetic Vlasov equation. Consequently, details of the particle motion and the particle distribution functions that describe the energy exchange between plasma particles and waves have been averaged out, resulting in the prediction that Alfvén eigenmodes are marginally stable in ideal MHD theory. Section 3.3 deals with the implications

of reintroducing kinetic effects. The perturbative extension of the ideal MHD model to include the self-consistent evolution of the particle distribution function under the influence of an electromagnetic wave (i.e. a shear Alfvén eigenmode) results in expressions from which the growth and damping rates of ideal MHD instabilities can be inferred. The topic of enhanced radial particle transport caused by shear Alfvén eigenmodes is treated only qualitatively, mainly because detailed theoretical studies are still missing. Apart from rough estimates based on worst case assumptions, numerical simulations for three-dimensional geometry are currently being developed. Finally, the modification of the shear Alfvén wave spectrum in the presence of kinetic effects is illustrated.

## 3.1 Alfvén Waves and Alfvén Continua

### 3.1.1 Waves in an infinite, homogeneous plasma

The simplest case to consider is an infinite plasma without gradients. The configuration is described by the following equations:

$$\begin{aligned}\rho &= \rho_0, \\ \mathbf{v} &= 0, \\ p &= p_0, \\ \mathbf{B} &= \mathbf{B}_0 = B_0 \mathbf{e}_z, \\ \mathbf{J} &= 0,\end{aligned}$$

where  $\rho_0, p_0$  and  $B_0$  are constants. Upon substituting the above expressions into the linearized ideal MHD equations, Eq. (2.38), following the normal mode approach with  $f(\mathbf{x}, t) = f_0 \cdot e^{i(\mathbf{k} \cdot \mathbf{x} - \omega t)}$  for any generic perturbed quantity  $f$ , and solving for the components of the perturbed velocity  $\tilde{\mathbf{v}} = (\tilde{v}_x, \tilde{v}_y, \tilde{v}_z)$ , it follows that

$$\begin{aligned}(\omega^2 - k_{\parallel}^2 v_A^2) \tilde{v}_x &= 0, \\ (\omega^2 - k_{\perp}^2 v_s^2 - k^2 v_A^2) \tilde{v}_y &- k_{\perp} k_{\parallel} v_s^2 \tilde{v}_z = 0, \\ -k_{\perp} k_{\parallel} v_s^2 \tilde{v}_y &+ (\omega^2 - k_{\parallel}^2 v_s^2) \tilde{v}_z = 0,\end{aligned}\tag{3.1}$$

where  $v_A \equiv \sqrt{B_0^2 / \mu_0 \rho_0}$  is the Alfvén velocity,  $v_s \equiv \sqrt{\gamma p_0 / \rho_0}$  is the sound velocity, and  $k^2 = k_{\parallel}^2 + k_{\perp}^2$ . The dispersion relation  $\omega(k)$  is obtained solving this system of linear equations. One obtains three branches:

$$\omega^2 = \omega_A^2 = k_{\parallel}^2 v_A^2,\tag{3.2}$$

$$\omega^2 = \frac{1}{2} k^2 (v_A^2 + v_s^2) \left( 1 \pm \sqrt{1 - \alpha^2} \right),\tag{3.3}$$

with

$$\alpha^2 = \frac{4k_{\parallel}^2}{k^2} \frac{v_A^2 v_s^2}{(v_A^2 + v_s^2)^2}.$$



The first branch, Eq. (3.2), describes a wave known as *shear Alfvén wave*. It does not depend on  $k_{\perp}$  and corresponds to a purely transverse wave with the perturbed magnetic field being parallel to the perturbed velocity and perpendicular to the equilibrium magnetic field  $\mathbf{B}_0$ . The wave travels along the magnetic field lines with a velocity  $\mathbf{v}_A = v_A \cdot \mathbf{B}_0/B_0$ . The group velocity is equal to the phase velocity and the fluid element oscillates in phase with the magnetic field line that behaves as a massive string under tension. The motion is incompressible and, hence, density and pressure perturbations are zero. The shear Alfvén wave can be thought as an oscillation between perpendicular plasma kinetic energy and the potential energy required to bend the field lines.

The second and third branches, Eq. (3.3), are called *magneto-acoustic* or *magnetosonic waves*. They depend on both, parallel and perpendicular components of the wave vector, and produce a compression of the magnetic field and a pressure perturbation. Since  $0 < \alpha^2 < 1$ , each of the waves corresponds to a purely oscillating solution. The *fast magnetosonic wave* corresponds to the plus sign in front of the square root term in (3.3) and has a frequency  $\omega^2 = \omega_f^2$  which is always larger than the Alfvén frequency,  $\omega_A^2 < \omega_f^2$ . In the case  $\beta \ll 1$  it reduces to the *compressional Alfvén wave* with

$$\omega_f^2 \approx (k_{\perp}^2 + k_{\parallel}^2)v_A^2,$$

where the fluid oscillates almost perpendicular to the magnetic field and the compression is dominated by magnetic field compression.

The *slow magnetosonic wave* corresponds to the minus sign in eq. (3.3). The frequency  $\omega^2 = \omega_s^2$  is always less than the Alfvén frequency. In the limit  $\beta \ll 1$  it reduces to the *sound wave* with the dispersion relation

$$\omega_s^2 \approx k_{\parallel}^2 v_s^2.$$

Here, the oscillation is mostly parallel to the magnetic field and is dominated by fluid compression. It results from the balance between plasma inertia and the plasma compression in the force balance.

It can be shown that the incompressible shear Alfvén waves are the ones that are most easily driven unstable [31]. The work done by an arbitrary displacement of the plasma to compress the fluid is always positive, corresponding to an increase in potential energy which makes the plasma more stable. Another way to show the greater stability of compressional Alfvén waves is by interpreting the terms  $k_{\parallel}v_A$  and  $k_{\perp}v_A$  as effective spring constants, in analogy to a harmonic oscillator [32]. A larger spring constant implies a greater ability of the plasma to maintain its state under external perturbations. Because  $k_{\parallel} < \sqrt{k_{\parallel}^2 + k_{\perp}^2}$ , the shear Alfvén waves are easier to excite in the presence of sources of free energy than compressional Alfvén waves. Another important difference between both wave types is related to the group velocity, which is along  $\mathbf{B}_0$  for shear Alfvén waves and mostly across the magnetic field for the latter, because in the systems of interest  $k_{\parallel} \ll k_{\perp}$  always holds.

### 3.1.2 Inhomogeneous plasma slab

A confined plasma is always characterized by spatial inhomogeneities. In this section, the simplest case of an inhomogeneous plasma, a one-dimensional slab with a straight magnetic field is studied. The equilibrium quantities are assumed to vary only along the  $x$ -direction,  $\rho_0 = \rho_0(x)$ ,  $p_0 = p_0(x)$ ,  $\mathbf{B}_0 = \mathbf{B}_0(x) = B_{0,y}(x)\mathbf{e}_y + B_{0,z}(x)\mathbf{e}_z$ . The equilibrium condition can be found from the force balance using Ampère's law to substitute the current:

$$\frac{d}{dx} \left( p_0 + \frac{B_0^2}{2\mu_0} \right) = 0.$$

Any perturbed quantity is assumed to have the form  $f = f_0 \exp[i(k_y y + k_z z - \omega t)]$ . Moreover, it is convenient to choose a set of coordinates based on the directions parallel and perpendicular to  $\mathbf{B}_0$  by defining  $\mathbf{e}_\parallel \equiv \mathbf{B}_0/B_0$  and  $\mathbf{e}_\perp = \mathbf{e}_\parallel \times \mathbf{e}_x$ . In these coordinates,  $k_\parallel = (k_y B_{0,y} + k_z B_{0,z})/B_0$  and  $k_\perp = (k_y B_{0,z} - k_z B_{0,y})/B_0$ . After some manipulation it's possible to obtain the following wave equation for  $\xi_x$  [33]:

$$\frac{d}{dx} \left( \frac{B_0^2 D_A \alpha'}{\alpha' k_\perp^2 - D_A} \frac{d\xi_x}{dx} \right) - B_0^2 D_A \xi_x = 0. \quad (3.4)$$

Here,  $D_A \equiv \omega^2/v_A^2 - k_\parallel^2$  is the local shear Alfvén propagator and

$$\alpha' = 1 + \frac{\gamma\beta\omega^2}{2\omega^2 - \gamma\beta k_\parallel^2 v_A^2},$$

where  $\beta = 2\mu_0 p_0/B_0^2$  is the plasma beta. Eq. (3.4) again describes the three branches already studied in the previous section which are now coupled by equilibrium inhomogeneities. This equation and, hence, its solution is singular at points where  $B_0^2 D_A \alpha' = 0$ , corresponding to the appearance of two continuous spectra:

$$\omega^2 = \omega_A^2(x) = k_\parallel^2(x) v_A^2(x), \quad (3.5)$$

$$\omega^2 = \omega_s^2(x) = \frac{v_s^2(x) k_\parallel^2(x)}{1 + v_s^2(x)/v_A^2(x)}. \quad (3.6)$$

The origin of the singularities can be explained by a resonant excitation of the shear Alfvén waves [34]. Shear and compressional Alfvén waves are coupled in eq. (3.4). The compressional waves transport their energy mostly across the magnetic field and pile it up at positions where the shear Alfvén spectrum can be resonantly excited. The singularities are a signature of the breakdown of the ideal MHD model. In fact, it is the absence of an energy dissipation mechanism for shear Alfvén waves in ideal MHD that leads to the long-term singular behaviour of the shear Alfvén eigenfunctions.

Shear Alfvén waves become local plasma oscillations due to the plasma inhomogeneities. If one assumes a wave with a certain wave vector  $\mathbf{k}$ , the component  $k_\parallel$  parallel to  $\mathbf{B}_0(x)$  depends on  $x$  as does the Alfvén velocity  $v_A(x)$  and thereby the frequency  $\omega_A$  (see

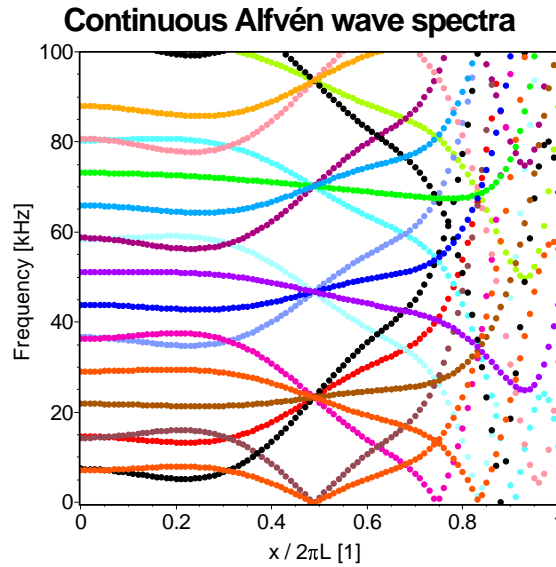


Figure 3.1: Continuous spectra of shear Alfvén waves. Colours indicate different wave branches, each having a distinct wave vector  $\mathbf{k}$ .

Fig. 3.1). This gives rise to an interesting damping mechanism called *phase mixing*: If the time-asymptotic behaviour of a spatially extended velocity perturbation  $\mathbf{v}(x)$  is studied [34], it is seen that the amplitude of the  $v_x$ -component decays as  $1/t$  whereas the other components oscillate with constant amplitude. Due to the inhomogeneities, each fluid element along the inhomogeneity oscillates at its own shear Alfvén frequency, losing coherence with the motion of the adjacent fluid elements. An initially smooth and extended perturbation changes in time and loses phase coherence along  $x$ , qualitatively explaining the name "phase mixing".

Finally, it has to be pointed out that the shear Alfvén wave spectrum is degenerate, which is a consequence of the fact that the dispersion relation depends on  $k_{\parallel}$  alone. At each position  $x$  it is possible to find waves with distinct  $\mathbf{k}_1 \neq \mathbf{k}_2$  that have  $k_{\parallel,1}(x) = \pm k_{\parallel,2}(x)$  and, therefore,  $\omega_{A,1}^2(x) = \omega_{A,2}^2(x)$ .

### 3.1.3 Shear Alfvén Continuum in Cylindrical Geometry

The simplest plasma equilibrium is a pressureless ( $p_0 = 0$ ) *screw pinch*. A screw pinch of length  $2\pi R_0$  is characterized by a magnetic field  $\mathbf{B}_0 = (0, B_{0\theta}(r), B_{0z}(r))^T$ , where  $(r, \theta, z)$  is a cylindrical coordinate system. It is an one-dimensional equilibrium similar to the sheared slab, the only new feature is the presence of a finite magnetic field curvature. It is mainly of relevance as an approximation to a large aspect-ratio tokamak.

From now on, sound and compressional Alfvén waves and their coupling to the shear Alfvén wave spectrum will be neglected, an assumption that allows some simplifica-

tions. Because shear Alfvén waves are purely transversal, magnetic field perturbation is perpendicular to the equilibrium field only,  $\tilde{B}_\parallel = 0$ , or in terms of the magnetic vector potential  $\tilde{\mathbf{A}}_\perp = 0$  which allows to write  $\tilde{\mathbf{A}} = \tilde{A}\mathbf{b}$ . In the ideal MHD limit, parallel electric fields are not allowed, i.e.  $\tilde{E}_\parallel = 0$ . Using these approximations, it is possible to express the perturbed electromagnetic field through a single, scalar potential  $\tilde{\Phi}$  (assuming that it varies as  $\exp(-i\omega t)$  in time):

$$\tilde{\mathbf{E}} = -\nabla_\perp \tilde{\Phi}, \quad \tilde{\mathbf{B}} = \nabla \times \tilde{\mathbf{A}} = \nabla \times (\tilde{A}\mathbf{b}) = \frac{1}{i\omega} \nabla \times (\nabla_\parallel \tilde{\Phi}\mathbf{b}). \quad (3.7)$$

Here, the definitions  $\nabla_\perp = \nabla - \mathbf{b}\nabla_\parallel$  and  $\nabla_\parallel = \mathbf{b} \cdot \nabla$  have been used.

The cylindrical geometry suggests to take shear Alfvén oscillations of the scalar potential in form of a suitable Fourier series:

$$\tilde{\Phi}(r, \theta, z, t) = \sum_{m,n} e^{i(m\theta - nz/R_0)} \cdot \tilde{\Phi}_{m,n}(r, t).$$

With these prerequisites the description of shear Alfvén waves reduces to an infinite set of uncoupled, second-order partial differential equations for individual  $(m, n)$ -branches [35]

$$\frac{1}{r^2} \frac{\partial}{\partial r} \left[ r^3 (m\iota - n)^2 + r^3 \frac{R_0^2}{v_A^2} \frac{\partial^2}{\partial t^2} \right] \frac{\partial}{\partial r} \left( \frac{\tilde{\Phi}_{m,n}(r, t)}{r} \right) = 0, \quad (3.8)$$

where  $\iota = \iota(r) = R_0 B_{0\theta}(r)/[r B_{0z}]$  is the rotational transform. The solutions of (3.8) are

$$\tilde{\Phi}_{m,n}(r, t) \sim \exp[-i\omega_A(r)t], \quad (3.9a)$$

$$\omega_A^2(r) \equiv \frac{v_A^2(r)(m\iota(r) - n)^2}{R_0^2} = v_A^2(r)k_\parallel^2(r), \quad (3.9b)$$

where  $k_\parallel \equiv (m\iota - n)/R_0$  has been defined. The solutions are similar to the sheared slab case, i.e. local plasma oscillations that form a frequency continuum. To see this, consider the dispersion relation (3.9b). For a fixed branch  $\tilde{\Phi}_{m,n}$ , the frequency  $\omega_A$  varies continuously with the radius due to the dependence of  $v_A$  and  $\iota$  on  $r$ .

The cylindrical spectrum is degenerate as well: The dispersion relation has two solutions at radial positions  $r_*$  where  $\iota(r_*)$  is a rational number. In this case it is always possible to solve the equation  $k_\parallel(m_1, n_1, r_*) = -k_\parallel(m_2, n_2, r_*)$  for integer values of  $m_1, m_2, n_1$  and  $n_2$ , respectively, which means that the dispersion relations of two different shear Alfvén wave branches  $\tilde{\Phi}_{m_1, n_1}$  and  $\tilde{\Phi}_{m_2, n_2}$  intersect at  $r_*$  as indicated in Fig. 3.2. For given mode numbers  $(m_1, n_1)$  and  $(m_2, n_2)$  the radial position  $r_*$  at which the branches intersect is determined by the condition

$$\iota_* = \iota(r_*) = \frac{n_1 + n_2}{m_1 + m_2}. \quad (3.10)$$

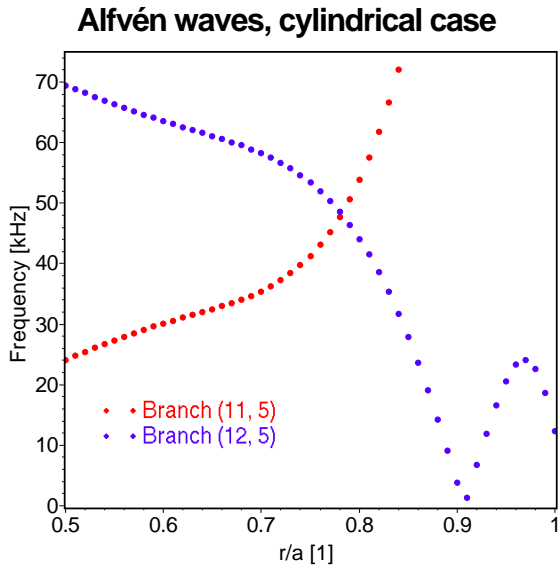


Figure 3.2: Two different Alfvén wave branches which cross at a radial position where the intersection condition Eq. (3.10) is satisfied.

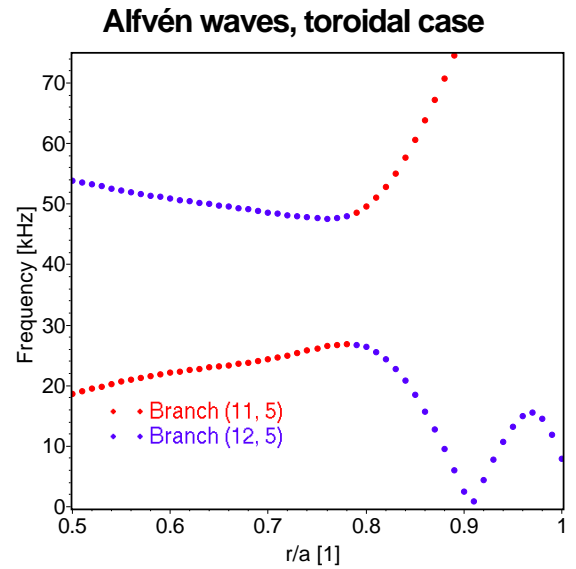


Figure 3.3: Alfvén wave branches which are coupled by toroidicity to break up and reconnect. Colors indicate the wave branch in the cylindrical limit  $\epsilon^{(10)} \rightarrow 0$ .

Hence, two shear Alfvén wave branches in cylindrical geometry will intersect if the corresponding value of  $t_*$  is reached at some radius inside the plasma. The frequency at the intersection point is given by a relation that does not depend on  $(m_1, n_1)$  and  $(m_2, n_2)$  individually, but only on their differences:

$$\omega_A(t_*) = |(m_2 - m_1)t_* - (n_2 - n_1)| \frac{v_A}{2R_0}. \quad (3.11)$$

### 3.1.4 Continuous Spectrum in Toroidal Geometry

In the cylindrical case the equilibrium was characterized by a constant magnetic field strength  $B = |\mathbf{B}|$  on a flux surface  $r = \text{const}$ . This cannot be achieved in toroidal geometry. Even in the simplest case of a toroidal equilibrium with circular cross sections, the toroidal magnetic field generated by the external coil set will vary as  $1/R$  inside the plasma, where  $R$  is the distance from the major axis of the torus. Consequently,  $B$  is not constant on any flux surface. Plasma shaping further complicates the symmetry properties of  $B$  by introducing additional variations. While tokamaks have axisymmetric equilibria (the toroidal angle is the ignorable coordinate) and there  $B = B(s, \theta)$  is a function of the poloidal angle variable  $\theta$  only, stellarators commonly have a variation of  $B$  in toroidal direction as well,  $B = B(s, \theta, \phi)$ . The symmetry-breaking leads to new features in the spectrum of shear Alfvén waves.

To proceed with the analysis, it is necessary to specify the equilibrium magnetic field strength in a form suitable for further treatment. It is common to expand the magnetic field strength in a series of the form

$$B = \bar{B}h, \quad h = 1 + \sum_{\mu, \nu} \epsilon_B^{(\mu\nu)}(s) \cos(\mu\theta - \nu N\phi). \quad (3.12)$$

Here,  $\bar{B}$  is the average magnetic field on the magnetic axis and  $\mu, \nu$  are integers.  $N$  is the number of identical field periods in stellarators, and  $(s, \theta, \phi)$  the magnetic coordinates with  $s = \Psi/\Psi_a$  being the normalized magnetic flux. It is possible to relate the Fourier coefficients in Eq. (3.12) to the flux surface shape. The  $(\mu, \nu) = (1, 0)$  harmonic is caused by toroidicity as explained above, the  $(2, 0)$  harmonic is caused by an overall vertical elongation (ellipticity) of the plasma, and the  $(3, 0)$  harmonic by triangularity. All other harmonics with  $\nu = 0$  are generated by additional deviations from circular plasma cross sections and are possible in tokamaks as well as in stellarators. In the latter, harmonics with  $\nu \neq 0$  are present as well: the  $(0, \nu > 0)$  are called mirror harmonics (purely toroidal variations), while the  $(\mu > 0, \nu > 0)$  terms are called helical harmonics.

If, again, perturbations of the form

$$\tilde{\Phi}(s, \theta, \phi, t) = \sum_{m, n} \Phi_{m, n}(s) \exp[i(m\theta - n\phi - \omega t)]$$

are assumed and a Fourier transform in  $\theta$  and  $\phi$  is applied, the resulting differential equations that describe  $\tilde{\Phi}_{mn}$  do no longer decouple. To show this, consider the following equation describing shear Alfvén waves in a current free, optimized stellarator in Boozer coordinates (neglecting the effects of plasma pressure on the equilibrium magnetic field), that has been derived in Ref. [10]:

$$\sum_{m, n} \left[ \hat{L} \frac{\partial}{\partial x^i} \left( g^{is} k'_{\parallel} + k_{\parallel} g^{ij} \frac{\partial}{\partial x^j} - i h k_{\parallel}^2 b^i \right) - \omega^2 R_0 \frac{\partial}{\partial x^i} \frac{1}{\bar{v}_A^2 h^4} \left( i g^{ij} \frac{\partial}{\partial x^i} + h b^i k_{\parallel} \right) \right] \cdot \tilde{\Phi}_{m, n} \exp[i(m\theta - n\phi - \omega t)] = 0.$$

Here,  $x^i = s, \theta, \phi$ ,  $g^{ij}$  are the contravariant metric coefficients, and  $\bar{v}_A = \bar{B}/\sqrt{\mu_0 \rho_0}$  is the mean Alfvén velocity. This equation is a three-dimensional equation. The dependence on  $\theta$  and  $\phi$  arises not only due to the Fourier coefficients of  $B$  (contained in  $h$ ), but also from the metric coefficients which are themselves functions of  $B$  and can be expanded in a Fourier series similar to (3.12), yielding coefficients  $\epsilon_g^{(\mu\nu)}$ . If furthermore the coupling parameters  $\epsilon$  are assumed to be small, the equation can be simplified to an infinite set

of coupled second-order differential equations similar to Eq. (3.8):

$$\begin{aligned}
0 = & \frac{\partial}{\partial r} r^3 \left( \frac{\omega^2}{\bar{v}_A^2} - k_{m,n}^2 \right) \frac{\partial E_{m,n}}{\partial r} + Q_{m,n} E_{m,n} \\
& + \sum_{\mu,\nu} \frac{\partial}{\partial r} r^3 \left[ \frac{\omega^2}{\bar{v}_A^2} \left( \frac{\epsilon_g^{(\mu\nu)}}{2} - 2\epsilon_B^{(\mu\nu)} \right) - k_{m,n} k_{m+\mu,n+N\nu} \frac{\epsilon_g^{(\mu\nu)}}{2} \right] \frac{\partial E_{m+\mu,n+N\nu}}{\partial r} \\
& + \sum_{\mu,\nu} \frac{\partial}{\partial r} r^3 \left[ \frac{\omega^2}{\bar{v}_A^2} \left( \frac{\epsilon_g^{(\mu\nu)}}{2} - 2\epsilon_B^{(\mu\nu)} \right) - k_{m,n} k_{m-\mu,n-N\nu} \frac{\epsilon_g^{(\mu\nu)}}{2} \right] \frac{\partial E_{m-\mu,n-N\nu}}{\partial r},
\end{aligned} \tag{3.13}$$

where

$$k_{m,n} = k_{\parallel}(m, n), \quad E_{m,n} = \frac{\tilde{\Phi}_{m,n}}{r}, \quad Q_{m,n} = r \left( \frac{\omega^2}{\bar{v}_A^2} - k_{m,n}^2 \right) (1 - m^2) + r^2 \frac{\partial}{\partial r} \left( \frac{\omega^2}{\bar{v}_A^2} \right),$$

and  $r \sim \sqrt{s}$ . If the cylindrical case is recovered by setting  $\epsilon_{g,B}^{(\mu\nu)} = 0$ , the equations (3.13) decouple and the cylindrical result is obtained that two different Alfvén wave branches  $(m, n)$  and  $(m + \mu, n + N\nu)$  intersect at radial positions  $r_*$  and at frequencies  $\omega$  where

$$t_* = t(r_*) = \frac{2n + N\nu}{2m + \mu}, \quad \omega_*^{(\mu\nu)} = \omega^{(\mu\nu)}(t_*) = |\mu t_* - N\nu| \frac{\bar{v}_A}{2R_0}. \tag{3.14}$$

The formerly independent  $(m, n)$  and  $(m + \mu, n + N\nu)$  branches split up in the presence of a finite  $\epsilon^{(\mu\nu)}$  and reconnect as indicated in Fig. 3.3. The frequency gap that appears has a minimum width of  $\sim \epsilon^{(\mu\nu)}$  near the intersection point. Because this happens simultaneously for all  $(m, n)$  at different radial locations, a radially extended frequency gap opens up. ( $t_*$  depends on  $m$  and  $n$  whereas  $\omega^{(\mu\nu)}$  does not!) The gap frequency  $\omega^{(\mu\nu)}$  varies with the plasma radius through  $t$  and  $v_A$ . However, no continuum branch can cross this gap because an arbitrary cylindrical branch  $\omega = \omega_{m,n}(t)$  will necessarily meet another branch  $\omega = \omega_{m \pm \mu, n \pm N\nu}(t)$  and reconnect. Consequently, the shear Alfvén dispersion relation  $\omega_A^2 = k_{\parallel}^2 v_A^2$  has no solution inside the gap.

If more than just one coupling coefficient is present, a gap opens for each of these. If the  $\epsilon^{(\mu\nu)}$  are not small, an interaction between different gaps is possible. This usually means that especially wide gaps shift the adjacent gaps in frequency. Also, the formation of secondary or higher order gaps is possible. Even if  $\epsilon^{(\mu\nu)} = 0$  the branches  $(m, n)$  and  $(m + \mu, n + N\nu)$  can be coupled provided that two (or more) other coupling parameters  $\epsilon^{(\mu_1\nu_1)}, \epsilon^{(\mu_2\nu_2)}$  are large, and  $\nu = \nu_1 + \nu_2$  and  $\mu = \mu_1 + \mu_2$ , respectively. Fig. 3.4 presents the Alfvén wave continuum calculated for a typical W7-AS discharge using the COBRA code (Sec. 4.4.2). Besides the usual  $(\mu, 0)$ -gaps known in tokamaks, the figure shows that in stellarators gaps with  $\nu \neq 0$  are possible and can even be significantly larger, e.g. the extremely wide helicity-induced  $(2, 1)$  gap which is caused by the rotating helicity of the plasma cross section.

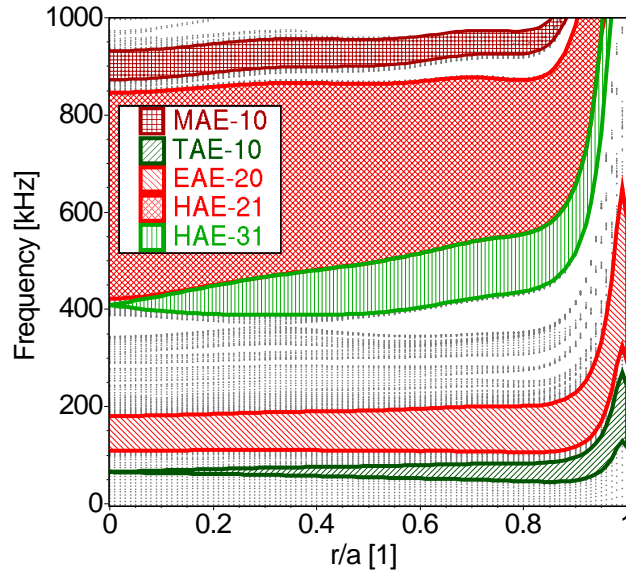


Figure 3.4: Alfvén continuum calculated numerically for a typical W7-AS discharge. The black dots indicate the Alfvén continuum calculated by a scan in  $k_{\parallel}$  and  $r/a$ . The absence of the dots is an indication for the formation of gaps. The most important gaps have been colored for better identification.

## 3.2 Alfvén Eigenmodes

In laboratory plasmas, Alfvén waves are difficult to excite because sufficient energy is needed to bend the field lines. Moreover, in a sheared magnetic field, Alfvén waves are characterized by a continuous spectrum and become highly localized oscillations at the flux surface where the local dispersion relation  $\omega^2 = k_{\parallel}^2 v_A^2$  is fulfilled. If any radially extended perturbation happens to excite the continuous shear Alfvén wave spectrum, it will suffer from strong continuum damping by the phase mixing phenomenon.

This is the reason that Alfvén instabilities were not considered to be a threat to fusion plasmas until it was discovered that the Alfvén continuum has gaps [5, 6, 12, 13]. It was soon realized that in these gaps a discrete spectrum of Alfvén instabilities with possibly well-behaved, non-singular radial eigenfunctions exists [7, 9], the so called *Alfvén Eigenmodes* (AEs). These AEs do not necessarily intersect the shear Alfvén continuum and therefore may be weakly damped.

### 3.2.1 Global Alfvén Eigenmodes (GAEs)

The existence of the GAE can already be established in cylindrical geometry with a sheared magnetic field as in the screw pinch (Sec. 3.1.3). A necessary condition for the existence of the GAE is that the dispersion relation of a continuum branch  $\omega_A^2(r)$  has a minimum at some radial position  $r_{ext}$ , where  $d\omega_A^2/dr = 0$  as indicated in Fig. 3.5.



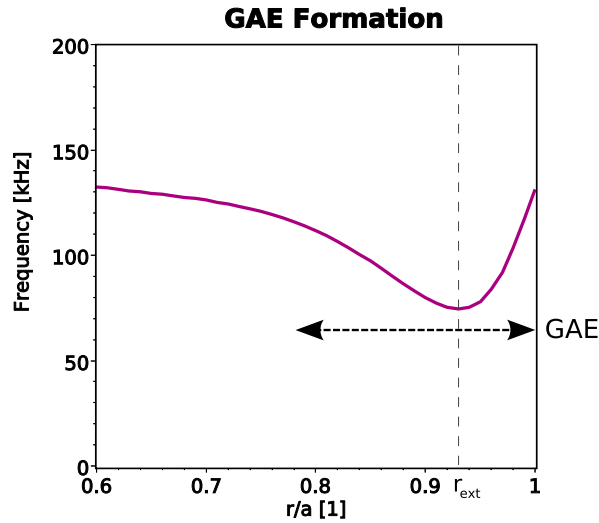


Figure 3.5: Alfvén continuum with an extremal point (minimum) at  $r_{ext}$ . Below the continuum Global Alfvén Eigenmodes can exist.

In Refs. [32, 36] it has been shown that by expanding the shear Alfvén wave equation around  $r_{ext}$  and applying a Fourier transform in  $r$ , a Schrödinger-like equation is obtained that supports bound as well as continuous solutions. The continuous solutions in Fourier space correspond to the strongly localized shear Alfvén waves, while the solutions that are localized in Fourier space correspond to radially extended solutions in real space.

The fact that these eigenmodes can extend over a large fraction of the plasma radius has earned them the name *Global Alfvén Eigenmodes* (GAEs). They have a frequency slightly below the minimum of the shear Alfvén continuum (cf. Fig. 3.5) and do not suffer from continuum damping. It should be noted that they do not, at no point in the plasma, obey the shear Alfvén dispersion relation. GAEs are difficult to excite in tokamaks because toroidicity and the relatively high magnetic shear  $\hat{s} = dt/dr$  have a stabilizing effect on these modes. They are, however, often observed in low-shear discharges as possible in W7-AS [21] in the presence of neutral beam heating.

### 3.2.2 Gap Modes

Near the degenerate intersection point  $\iota_*(m, n, \mu, \nu)$ , Eq. (3.14) of two cylindrical branches  $(m, n)$  and  $(m + \mu, n + \nu)$ , which is resolved by the coupling of these branches, the wave equations for both branches can be shown to have a new type of solution with discrete eigenvalues  $\omega^2$  that lie inside the  $(\mu, \nu)$ -gap in the continuous shear Alfvén wave spectrum. This was demonstrated for the first time in Ref. [8] in the high- $n$  and in Ref. [7] in the low- $n$  approximation for the toroidicity-induced coupling in tokamaks. Assuming only one dominant pair of coupling numbers  $(\mu, \nu)$ , the radial eigenfunctions are centered around the intersection point  $\iota_*$  and have a width  $|m\Delta\iota| \sim \epsilon^{(\mu, \nu)}$  [35],

where  $\Delta t = t(r) - t_*$ . Thus, the solutions become very localized around  $r_*$  for high  $m$ , but low shear can significantly enhance their width.

The new solution describes an eigenmode which is formed by the coupling of at least two harmonics inside the continuum gap (gap mode). The radial extension of the eigenmode can be further enhanced by the coupling to more harmonics according to the scheme  $(m, n) + (m + \mu, n + \mu) \rightarrow (m + \mu, n + \nu) + (m + 2\mu, n + 2\nu)$ . Whether or not this coupling is possible depends, among others, on the profile of  $t$  because it is required that the intersection points  $t_*(m, n, \mu, \nu)$  and  $t_*(m + \mu, n + \nu, \mu, \nu)$  are close enough to allow the radial eigenfunctions to overlap. This effectively limits the number of coupled harmonics in low-shear devices.

Historically, the gap modes were assigned names that indicate the geometric origin of their existence. The  $(1, 0)$  coupling is caused by toroidicity, hence the name *toroidicity-induced Alfvén eigenmode* (TAE), the continuum gap in which the mode exists is called *TAE gap*. Ellipticity causes the  $(2, 0)$  coupling and the corresponding gap mode is termed *ellipticity-induced Alfvén eigenmode* (EAE), giving the name EAE gap for the  $(2, 0)$  continuum gap. All other tokamak-like gap modes and continuum gaps with  $\nu = 0$  are named *noncircularity-induced* (NAE $_{\mu\nu}$ ). In stellarators,  $B$  varies in toroidal direction as well, creating additional gaps for which  $\nu \neq 0$ . In case of helical variations of  $B$  where both,  $\mu$  and  $\nu$  are  $\neq 0$  the name *helicity-induced* (HAE $_{\mu\nu}$ ) is used, whereas purely toroidal variations, which cause toroidal mirror fields, are named *mirror-induced* (MAE $_{0\nu}$ ).

Near the cylindrical intersection point  $r_*$ , the gap modes are inside the continuum gap but they are radially extended and have a constant frequency throughout the plasma. It can happen that at some other radial location  $r_0$ , they obey the local shear Alfvén wave dispersion relation  $\omega^2 = k_{\parallel}^2(r_0)v_A^2(r_0)$ . In this case they can resonantly excite the Alfvén continuum and suffer from strong continuum damping. Otherwise the gap modes are only weakly damped and can be destabilized by a suitable driving mechanism.

### 3.3 Beyond Ideal MHD

#### 3.3.1 Wave Drive and Damping

The power transfer between particles and electromagnetic waves is obtained by taking the time derivative of the work  $\mathcal{E} = \int \mathbf{F} d\mathbf{s}$  done on the particle by the Lorentz force:

$$\frac{d\mathcal{E}}{dt} = e(v_{\parallel} \cdot \tilde{\mathbf{E}}_{\parallel} + \mathbf{v}_{\perp} \cdot \tilde{\mathbf{E}}_{\perp}) + \boldsymbol{\mu}_p \cdot \frac{\partial \tilde{\mathbf{B}}}{\partial t}, \quad (3.15)$$

where  $\tilde{\mathbf{E}}$  and  $\tilde{\mathbf{B}}$  are the electric and magnetic field associated with the wave, respectively, and  $\mathcal{E}$  is the particle energy. Assuming that  $\tilde{\mathbf{E}}$  and  $\tilde{\mathbf{B}}$  vary as  $\sim \exp(i\mathbf{k} \cdot \mathbf{x} - i\omega t)$

and integrating (3.15), it is seen that in average a non-vanishing energy exchange between wave and particle is only possible if the resonance condition  $\mathbf{v} \approx \mathbf{v}_{ph}$  is satisfied ( $\mathbf{v}_{ph}$  is the phase velocity of the wave). Shear Alfvén waves and eigenmodes propagate along the magnetic field lines with the Alfvén velocity  $v_A$ , hence fast particles can resonantly interact with these waves if they have longitudinal velocities  $v_{\parallel}^{res} \approx v_A$ .

The parallel electric field is always  $\tilde{E}_{\parallel} = 0$  in the ideal MHD approximation. Even if kinetic effects such as finite resistivity are included, the ratio  $v_{\parallel} \tilde{E}_{\parallel} / (v_{\perp} \tilde{E}_{\perp}) \ll 1$  so that the term containing  $\tilde{E}_{\parallel}$  can be neglected [11]. If one considers only well circulating particles where  $v_{\parallel} \gg v_{\perp}$ , the third term in (3.15) can be neglected because  $\mu_p \rightarrow 0$  for these particles and usually  $\tilde{B}/B_0 < 10^{-3}$  for Alfvén eigenmodes. This leaves  $e \mathbf{v}_{\perp} \cdot \tilde{\mathbf{E}}_{\perp}$  as the dominant term. After averaging over the fast gyro-motion of the particle, retaining the guiding center drift only (see Sec. 2.2), and assuming vanishing radial transport, this becomes

$$\frac{d\mathcal{E}}{dt} = e \mathbf{v}_D \cdot \tilde{\mathbf{E}}_{\perp}.$$

Thus, the energy exchange between fast, circulating ions (as produced by the neutral beam injection at W7-AS) and AEs is dominated by the periodic cross-field drift velocity  $\mathbf{v}_D$ . There is a subtle implication in the dependence of the wave-particle interaction on the drift velocity: Because the particles are confined on drift surfaces, that are displaced from the flux surfaces to which the modes are aligned, the particle "feels" a periodic modulation of the wave amplitude and phase through which it can interact with the mode itself. This *sideband excitation* creates additional resonances which allow a significant wave-particle interaction even for particles with  $v_{\parallel} < v_A$  as seen in the modified resonance condition [11]:

$$\frac{v_{\parallel}^{res}}{v_A} = \left[ 1 \pm 2 \frac{\mu_D \ell - N \nu_D}{\mu \ell - N \nu} \right]^{-1} \text{sgn}(k_{mn}). \quad (3.16)$$

Here,  $\mu_D$  and  $\nu_D$  are the Fourier coefficients of  $\mathbf{v}_D$  which are related to the Fourier coefficients of the magnetic field,  $(\mu, \nu)$  are the coupling numbers of the AE, and  $k_{mn} = k_{\parallel}(m, n) = (m\ell - n)/R_0$  is the parallel wave number of one of the AE harmonics. If all dominant fourier harmonics  $(\mu_D, \nu_D)$  are substituted into (3.16) one after the other, the complete list of possible resonances is obtained.

The eigenvalues  $\omega^2$  of the ideal MHD force balance operator in the normal mode approach are real (see Sec. 2.3.2). Therefore all Alfvén waves are marginally stable in this theory. In order to derive an expression for the energy exchange between wave and particles, kinetic effects have to be included. In the following, two theoretical models are presented that perturbatively apply a kinetic correction to the ideal MHD model based on the drift-kinetic approximation, i.e., neglecting the fast gyro-motion of the particles and considering the drift of guiding centers only as described in section 2.2.

### 3.3.1.1 Perturbative, Local Approach

By identifying  $(e \mathbf{v})$  with a current carried by a particle, observing that in ideal MHD Alfvén waves are marginally stable, and neglecting  $\mu_p \partial \tilde{\mathbf{B}} / \partial t$ , Eq. (3.15) can be written as

$$\int d^3x \tilde{\mathbf{J}} \cdot \tilde{\mathbf{E}} = 0,$$

where the integral is taken over the entire plasma volume. This equation describes the energy exchange between the whole plasma and the wave in ideal MHD. Now, a perturbative approach is applied as described in [11]. Assuming that a small population of energetic particles  $\alpha$  is present, the current can be written as  $\tilde{\mathbf{J}} = \tilde{\mathbf{J}}^{MHD} + \tilde{\mathbf{J}}^\alpha$ . Here,  $\tilde{\mathbf{J}}^{MHD}$  is the wave-induced current in ideal MHD, and  $\tilde{\mathbf{J}}^\alpha$  is that of the energetic ions. Using the fact that for ideal-MHD Alfvén waves  $\tilde{E}_\parallel = 0$  and  $\tilde{B}_\parallel = 0$  one can write  $\tilde{\mathbf{A}}_\perp = 0$  and  $\tilde{\mathbf{E}} = -\nabla_\perp \tilde{\Phi}$  which is assumed to depend on time as  $\sim \exp(-i\omega t)$ . If the wave frequency  $\omega$  is presented as  $\omega = \omega_0 + \delta\omega$ , the equation

$$\int d^3x \tilde{\mathbf{J}}^{MHD} \cdot \nabla \tilde{\Phi} = 0$$

determines the ideal MHD eigenfrequency  $\omega_0$ . For the perturbative approach to be valid,  $\delta\omega \ll \omega_0$  should hold. For the growth rate  $\gamma = \text{Im } \omega$  is obtained

$$\gamma = -\text{Im} \frac{\int d^3x \tilde{\mathbf{J}}_\perp^\alpha \cdot \nabla_\perp \tilde{\Phi}}{\int d^3x (\partial \tilde{\mathbf{J}}^{MHD} / \partial \omega_0) \cdot \nabla \tilde{\Phi}}. \quad (3.17)$$

The energetic particle current is calculated from the distribution function of the fast particles, which can be calculated as the solution of the linearized Vlasov equation by the method of characteristics and be written as follows:

$$\tilde{f} = -\frac{e}{m_\alpha} \int_{t_0}^t d\tau \left( \tilde{\mathbf{E}} + \mathbf{v} \times \tilde{\mathbf{B}} \right) \cdot \frac{\partial f_0}{\partial \mathbf{v}}, \quad (3.18)$$

where  $f_0$  is the equilibrium distribution function and  $\mathbf{v}(t) = d\mathbf{r}(t)/dt$  are determined by the equation of motion of the particles. Instead of using spatial coordinates, it is more convenient to use the constants of motion of the particles as independent variables for the distribution function. Assuming only well circulating particles where  $v_\parallel \approx \text{const.}$  and neglecting the Larmor rotation, the constants of motion and adiabatic invariants are the particle energy  $\mathcal{E}$ , the magnetic moment  $\mu_p$ , and the toroidal canonical momentum. The additional assumption of small particle orbit width allows one to use the radial coordinate  $r$  instead of the toroidal canonical momentum. In many practical applications the particle trapping parameter  $\lambda = \mu_p \bar{B} / \mathcal{E}$ , related to the particle pitch by  $\lambda = 1 - \chi^2$ , is easier accessible than  $\mu_p$ . Here,  $\bar{B}$  is the averaged magnetic field on the magnetic axis. In these coordinates, considering only the resonance part of  $\tilde{f}$

and using the drift-kinetic approximation,  $\mathbf{v} = \mathbf{v}_\parallel + \mathbf{v}_D$ , Eq. (3.18) can be simplified to give:

$$\tilde{f}(t) = \frac{e}{m_\alpha} \hat{\Pi} f_0 \int_0^\infty dt' \mathbf{v}_D(t-t') \cdot \nabla \tilde{\Phi}(t-t'), \quad (3.19)$$

where  $\hat{\Pi}$  is a differential operator given by

$$\hat{\Pi} = m_\alpha \frac{\partial}{\partial \mathcal{E}} - \frac{m_\alpha \lambda}{\mathcal{E}} \frac{\partial}{\partial \lambda} + \frac{n}{\omega \omega_{ct}} \frac{1}{r} \frac{\partial}{\partial r} \quad (3.20)$$

and  $\omega_c$  is the particle gyro frequency. To proceed, all important quantities are expressed in Fourier series according to

$$\begin{aligned} \tilde{X} &= \sum_{m,n} X_{mn}(r) \exp(im\theta - in\phi - i\omega t), \\ B_0 &= \bar{B} \left[ 1 + \sum_{\mu,\nu} \epsilon_B^{(\mu\nu)}(r) \cos(\mu\theta - N\nu\phi) \right], \\ \mathbf{v}_D &= \sum_{p,s} \mathbf{u}_{p,s}(r) \exp(ip\theta + is\phi). \end{aligned}$$

All indices,  $m, n, \mu, \nu, p$  and  $s$  are integers. Assuming that the particle stays on flux surfaces allows the simplification  $r(t) = \text{const.}$  and the approximation of the time dependence of the particle position as

$$\theta(t') = \theta(t) + \omega_\theta \cdot (t' - t), \quad \phi(t') = \phi(t) + \omega_\phi \cdot (t' - t).$$

Here,  $\omega_\theta$  and  $\omega_\phi$  are the frequencies of the poloidal and toroidal particle rotation, respectively. This gives for the energetic ion distribution function:

$$\tilde{f}_{mn} = -\frac{ie}{m_\alpha} \hat{\Pi} f_0 \sum_{p,s} \frac{\mathbf{u}_{ps} \cdot \nabla \tilde{\Phi}_{mn}}{\Omega_{mn}^{ps}} \exp(ip\theta + is\phi), \quad (3.21)$$

where  $\Omega_{mn}^{ps} = \omega - (p+m)\omega_\theta - (s-n)\omega_\phi$ . Now the wave-induced energetic particle current is given as the velocity moment over the distribution function,

$$\mathbf{j}_{mn}^\alpha = e \int d^3v (\mathbf{v}_\parallel + \mathbf{v}_D) f_{mn}.$$

After some algebra and in the limit of well-localized modes and that only two essential harmonics are present, the authors of Ref. [11] arrive at the following expression for the growth rate:

$$\gamma = \frac{2\pi^2 e^2 v_A^2(r_*)}{m_\alpha} \int d^3v \hat{\Pi} f_0 \sum_{p,s} |u_{ps}|^2 \frac{\delta(v_\parallel - v_\parallel^{res})}{|k_{mn}^{ps}|}, \quad (3.22)$$

where  $r_*$  is the radius around which the mode is localized,

$$k_{mn}^{ps} = [(m + p)t - (n - s)]/R_0,$$

and the resonant longitudinal velocity is

$$v_{\parallel}^{res} = \omega/k_{mn}^{ps} \quad (3.23)$$

Eq. (3.22) contains the differential operator  $\hat{\Pi}$  which consists of three terms: The first term,  $m_{\alpha}\partial/\partial\mathcal{E}$ , is usually stabilizing because  $\partial f/\partial\mathcal{E}$  is usually negative. This collisionless damping is also known as *Landau damping*. However, if positive velocity gradients are present in the distribution function, they can strongly drive instabilities. Experiments performed in W7-AS with radial NBI indicate that if the positive gradients are strongly localized in space, they are likely to drive ion cyclotron instabilities with frequencies in the MHz range [37]. Only spatially extended positive velocity gradients are expected to contribute significantly to the mode drive via the term containing  $\partial f/\partial\mathcal{E}$ , but the creation of such gradients requires that the energetic particles cross a loss cone during their slowing-down. If the fast ion distribution function is isotropic, the second term of  $\hat{\Pi}$  vanishes but it can contribute to the growth rate of eigenmodes in case of strongly anisotropic NBI heating. The third term containing  $\partial/\partial r$  gives the largest contribution to the growth rate in most cases. It describes the influence of the spatial (radial) inhomogeneity of the distribution function on the stability of an eigenmode. The magnitude of the interaction is given by the ratio of the *diamagnetic drift frequency*  $\omega_{*\alpha}$  to the mode frequency:

$$\frac{\omega_{*\alpha}}{\omega_0} = \frac{nv_{\alpha}^2}{\epsilon r \omega_0 \omega_{c\alpha}} \cdot \frac{\partial \ln(n_{\alpha})}{\partial r}, \quad (3.24)$$

where  $n$  is the toroidal mode number,  $v_{\alpha}$  is the characteristic speed of the energetic particles,  $\omega_{c\alpha}$  is their cyclotron frequency, and  $\partial \ln(n_{\alpha})/\partial r$  is the density gradient scale length. This term describes both, damping and drive of a mode, depending on the sign of the mode numbers. Because the density decreases with  $r$ , modes with  $n < 0$  are destabilized if  $B > 0$ . When the field is reversed,  $\omega_*$  changes sign with  $\omega_{c\alpha}$ . The diamagnetic drift frequency grows linearly with  $n$  and therefore favours modes with large mode numbers.

In the derivation of Eq. (3.22) it was assumed that the mode is strongly localized around the surface  $r = r_*$ . This approximation is justified even for modes with a rather wide extend if the magnetic shear is small and the density profile is flat, which is usually the case in optimized stellarators. On the other hand, the authors of Ref. [11] admit that the applicability of the approximation of only two dominant harmonics is likely to be violated due to strong multimode coupling where more than just one  $\epsilon^{(\mu\nu)}$  is responsible for coupling of additional harmonics to the eigenmode. The approximation of energetic, well-circulating ions with  $v_{\parallel} \gg v_{\perp}$  that was explicitly made use of in the derivation of the growth rate further limits the applicability of the expression to cases with tangential NBI, which is, however, no restriction at W7-AS. If the same

formalism is employed to calculate the damping by the bulk plasma, only the Landau damping by electrons and ions which are in resonance with the mode is covered – the growth of the instability will probably be overestimated. Recently, the theory has been generalized to take into account the finite width of eigenmodes and the effects of finite Larmor radii and finite  $B_{\parallel}$  [38].

### 3.3.1.2 Kinetic MHD

The second approach generalizes the ideal MHD force balance to take into account kinetic effects and is described in Ref. [39]. The use of a scalar plasma pressure implies distribution functions that are isotropic on flux surfaces, dropping this assumption requires to represent the pressure with a tensor

$$\nabla \cdot \overleftrightarrow{\mathbf{P}} = -\rho \frac{d\mathbf{v}}{dt} + \mathbf{J} \times \mathbf{B}. \quad (3.25)$$

Respecting the privileged direction imposed by the magnetic field by expansion in components parallel and perpendicular to  $\mathbf{b} = \mathbf{B}/B$ , the pressure tensor can approximately be written as

$$\overleftrightarrow{\mathbf{P}} = p_{\perp} \overleftrightarrow{\mathbf{I}} + (p_{\parallel} - p_{\perp}) \mathbf{b}\mathbf{b}$$

with

$$p_{\parallel} = \sum_{x=e,i,\alpha} \int d^3v m_x v_{\parallel}^2 f_x, \quad p_{\perp} = \sum_{x=e,i,\alpha} \int d^3v \mu B f_x,$$

where  $f_x$  is the distribution of species  $x$ ,  $e$  stands for plasma electrons,  $i$  for thermal ions,  $\alpha$  for the fast particle species, and  $\mu B$  is the particle energy perpendicular to  $\mathbf{b}$ . After linearizing, the first-order part of  $\overleftrightarrow{\mathbf{P}}$  is given by

$$\overleftrightarrow{\mathbf{P}} = \sum_{x=e,i,\alpha} \int d^3v [\mu B \overleftrightarrow{\mathbf{I}} + (m_x v_{\parallel}^2 - \mu B) \mathbf{b}\mathbf{b}] \tilde{f}_x + [(m_x v_{\parallel}^2 - \mu B)(\tilde{\mathbf{b}}\mathbf{b} + \mathbf{b}\tilde{\mathbf{b}})] f_{0,x} \quad (3.26)$$

In the following, it is assumed that all perturbed quantities vary in time as  $\sim \exp(-i\omega t)$ . The energy change due to the perturbation can be calculated from the linearized, first-order force balance (3.25) by multiplying it with the complex conjugate of the displacement vector  $\xi$  and integrating over the plasma volume (only displacements perpendicular to the equilibrium magnetic field are allowed, in accordance with ideal MHD). The result can be written in terms of three individual contributions:

$$\delta W_{kin} = \delta W_{mag} + \delta W_p, \quad (3.27a)$$

where the individual contributions are given by:

$$\delta W_{kin} = \frac{\omega^2}{2} \int d^3x \rho |\xi_{\perp}|^2, \quad (3.27b)$$

$$\delta W_{mag} = \frac{1}{2} \int d^3x |\tilde{\mathbf{B}}|^2 - \tilde{\mathbf{B}} \cdot (\boldsymbol{\xi}_\perp^* \times \mathbf{J}_0), \quad (3.27c)$$

$$\delta W_p = \frac{1}{2} \int d^3x \boldsymbol{\xi}^* \cdot (\nabla \cdot \overleftrightarrow{\mathbf{P}}_e) + \boldsymbol{\xi}^* \cdot (\nabla \cdot \overleftrightarrow{\mathbf{P}}_i) + \boldsymbol{\xi}^* \cdot (\nabla \cdot \overleftrightarrow{\mathbf{P}}_\alpha). \quad (3.27d)$$

Here,  $\delta W_{kin}$  describes the change in the kinetic energy of the system due to the perturbation, the change in magnetic energy,  $\delta W_{mag}$ , is identical to the ideal MHD contribution to the perturbed magnetic energy, and all kinetic effects are embedded in  $\delta W_p$ . If this term is considered to be small, i.e.  $\delta W_p \ll \delta W_{mag}$ , the growth rate can be calculated perturbatively:

$$\Delta\omega + i\gamma \approx \frac{1}{2} \frac{\delta W_p(\omega_0)}{\delta W_{mag}} \cdot \omega_0 \quad (3.28)$$

In this approach, each particle species contributes separately to the growth and damping of the mode. The task is now to find an expression for the perturbed distribution function. The author of Ref. [39, 40] uses a drift-kinetic equation. Furthermore, only ideal MHD perturbations are assumed ( $E_\parallel = 0$ ) and radial particle drifts are neglected. In order to avoid following the 3D particle orbits explicitly, a technique developed by Rewoldt et al. [41] is used where the particles are assumed to move along field lines, feeling a bounce or transit averaged drift only. The resulting expressions give the perturbed distribution function  $\tilde{f}$  in terms of  $f_0$  and the perturbed fields – they are different for passing and trapped particles because of the integration over the different particle orbits. The resonance frequencies correspond to characteristic frequencies of the particle orbits: transit and bounce frequencies and their harmonics, and transit or bounce average drifts of the guiding centers including the sideband resonances given by eq. (3.16). In Boozer coordinates the contribution of a single particle species  $x$  to the energy integral (3.27) is found to be [40]

$$\begin{aligned} \delta W_x = & \frac{\pi}{m_x^2} \left\{ \begin{matrix} \sum_\sigma \\ 1 \end{matrix} \right\} \int ds \int d\phi \int d\mu d\mathcal{E} \left( - \int \frac{d\theta}{|v_\parallel|} \sqrt{g} B \right) \\ & \times \sum_{\substack{m,n \\ m',n'}} \sum_{p=-\infty}^{\infty} e^{-i\frac{2\pi}{N}(n'-n)\phi} \left( \frac{\partial f_{0,x}}{\partial \mathcal{E}} \right)_\mu \\ & \times \frac{\omega - 2\pi(\frac{n}{N}J - mI)\omega_*}{m \langle \omega_d^\theta \rangle + \frac{n}{N} \langle \omega_d^\phi \rangle + \left\{ \begin{matrix} \sigma(p+nq)\omega_t \\ p \omega_b \end{matrix} \right\} - \omega} \\ & \times \tilde{L}_{m'n'} \mathcal{M}_{pn}^{m'n'} \cdot \tilde{L}_{mn} \mathcal{M}_{pn}^{mn}, \end{aligned} \quad (3.29)$$

where the particle Lagrangian  $\tilde{L} = -(m_x v_\parallel^2 - \mu B) \boldsymbol{\xi}_\perp \cdot \boldsymbol{\kappa} + \mu B \nabla \cdot \boldsymbol{\xi}_\perp$  describes the particle guiding-center motion,

$$\mathcal{M}_{pn}^{m'n'} = \left\{ \begin{matrix} \langle \exp [2\pi i(m' + n'q)\theta'' - i(p + nq)\omega_t t''] \rangle \\ \langle e^{2\pi i(m' - n'q)\theta''} [\cos^2(\frac{\pi}{2}p) \cos(p\omega_b t'') - i \sin^2(\frac{\pi}{2}p) \sin(p\omega_b t'')] \rangle \end{matrix} \right\}$$



$q = \iota^{-1}$ ,  $\langle \dots \rangle$  denotes the transit or bounce average along particle orbits [ $t'' = t''(\theta'')$ ],  $p$  denotes the Fourier harmonics of bounce or transit frequencies,  $\omega_t$  ( $\omega_b$ ) is the transit (bounce) frequency for passing (trapped) particles,  $I$  and  $J$  are the toroidal and poloidal plasma current, respectively, and the upper term in  $\{\dots\}$  has to be used for passing particles whereas the lower term is suitable for trapped particles. The reduced diamagnetic drift frequency is given by

$$\omega_* = -\frac{1}{Ze\sqrt{g}B^2} \frac{\partial f_x / \partial s}{\partial f_x / \partial \mathcal{E}}.$$

Eq. (3.29) contains, similar to eq. (3.22), terms  $\sim \partial f / \partial s$  and  $\sim \partial f / \partial \mathcal{E}$  that are expected to behave equivalently. In contrast to the local approach, the particle motion is less approximate, a fact that leads to additional resonances at the particle transit or bounce frequencies that can enhance drive or damping.

Once the displacement  $\boldsymbol{\xi}(\mathbf{x})$ , the ideal MHD eigenfrequency of the mode  $\omega_0$  and the distribution functions  $f_0$  for all species are known, Eq. (3.28) can be solved numerically to obtain the effective growth rate of the instability. It includes the finite radial extend of eigenmodes as well as the different characteristics of the orbits of trapped and passing particles – providing a more profound description of the effective linear growth and damping rate than the local approach. Still, this approach is perturbative and, strictly speaking, valid only in the limit of small perturbations and energetic particle populations.

### 3.3.2 Wave-Induced Transport

Wave-particle interactions have been treated in a linear perturbative approach in the last section. This is useful to determine the linear growth rate which indicates whether an eigenmode is stable or unstable under given conditions. But it does not describe wave amplitude saturation or the radial redistribution of particles in the presence of a wave with finite amplitude, effects that are observed in all fusion experiments. Full non-linear and self-consistent calculations of wave-particle interactions are required to solve this task.

Due to the complexity of the problem, analytical predictions and simple numerical models of the effect of a wave on the particle distribution function result mostly in qualitative arguments. Numerical simulations of the full non-linear problem that describe the temporal evolution of particle distribution functions as well as mode amplitude and frequencies have been done for tokamaks and successfully compared to the experiment (e.g. [42, 43]). But excessive use of the axisymmetry of tokamak configurations had to be made to reduce the dimensionality of the problem and make it numerically tractable. Comparable simulations are just becoming available for stellarators due to increasing computing power and advanced numerical schemes [44, 45].

Because systematic non-linear studies of wave-particle interactions in stellarators are still lacking, the following discussion of wave-induced particle transport will only name

the most important physical effects that are expected. These effects can be roughly divided into two classes: (I) resonant transport that affects particles which move in resonance with the wave, and (II) non-resonant transport that affects other particles as well by perturbations of their orbital motion.

### 3.3.2.1 Resonant Transport

Particles that are in resonance with an instability can drive it if they provide a source of free energy that can be tapped by the instability. The most important are strong spatial gradients and deviations from a local Maxwellian distribution function. This implies, of course, that if energy is transferred from the particles to the wave, the energy source is drained until a stable configuration is achieved.

In case of instabilities driven by spatial gradients this means that the gradients are reduced. Steep radial gradients in the distribution of energetic particles are a common phenomenon in fusion devices. The effect of Alfvén eigenmodes on the distribution function is a radial redistribution of the resonant particles within the region where the mode is localized to reduce the local gradient. If the mode is localized near the plasma edge, the energetic ions can be expelled from the plasma.

An alternate mechanism for the resonant transport affects passing particles that are close to the trapping boundary. If they are in resonance with the mode and transfer parallel energy to it, they can become trapped and possibly leave the plasma on large banana orbits. In either case, the amount of particle losses is expected to scale linearly with the mode amplitude [15, 16].

### 3.3.2.2 Non-Resonant Transport

In contrast to the losses by resonant interaction with the instability, enhanced transport caused by Alfvén eigenmodes is also possible for particles that are not in resonance with the mode. Several responsible mechanisms can be identified [14]:

- The displacement of flux surfaces associated with the mode causes the fast ion to move radially by the same amount. This can potentially increase the step size in a random walk model of diffusion as in classical or neoclassical transport theory. However, this effect is considered to be negligible.
- Alfvénic activity can cause a stochastization of magnetic field lines (destruction of magnetic surfaces) if the amplitude of the perturbation is sufficiently strong. In this case the radial transport is caused by the parallel motion of particles along stochastic field lines. After the stochasticity threshold has been overcome, the particle transport is expected to scale as  $(\tilde{B}/B_0)^2$  [42].
- The periodic perturbation causes additional resonances between the complex orbital motion of the particle and the spatial structure of the mode field. Again, a

large amplitude perturbation of  $\tilde{B}/B \sim 10^{-3}$  is required for the effect to become important [16].

### 3.3.3 Kinetic Modifications of the Alfvén Wave Spectrum

#### 3.3.3.1 Kinetic Alfvén Waves

The singularities that appear in Eq. (3.4) are a sign that the ideal MHD model breaks down when very short scale perturbations are excited. On these short scales it is expected that charge separation effects and, hence, finite parallel electric field perturbations  $\tilde{E}_{\parallel}$  become important due to, e.g., finite ion Larmor radius effects, small but finite electron inertia, as well as finite plasma resistivity and viscosity. All these effects can be included in a finite, complex valued conductivity in Ohm's law which means dropping the ideal MHD assumption. In the presence of finite  $\tilde{E}_{\parallel}$ , additional effects can also be expected from wave-particle interactions such as viscous, collisional, or Landau damping of waves by electrons and ions. If such "kinetic" effects are included, it is possible to show that the wave equation is modified to include a fourth-order term like [34, 35]

$$4\omega^2 \nabla_{\perp} \rho_k^2 \nabla_{\perp} \xi_x, \quad (3.30)$$

where

$$\rho_k^2 = \rho_i^2 \left[ \frac{3}{4}(1 - i\delta_i) + \frac{T_e}{T_i}(1 - i\delta_e) \right].$$

$\delta_e$  and  $\delta_i$  are the electron and ion damping contributions, respectively, and  $\rho_i$  is the ion Larmor radius. This equation is valid provided the relations  $m_e/m_i \ll \beta_e \ll 1$  and  $k_{\perp}^2 \rho_i^2 \ll 1$  hold. The term containing the fourth-order derivative removes the singularities near the resonant layer. In fact, the modified wave equation describes the conversion of a long-wavelength shear Alfvén wave to a short-wavelength *kinetic Alfvén wave* (KAW) near the resonant layer, that transports the energy across the magnetic field away from the resonance and is eventually absorbed by the background plasma. The dispersion relation for KAWs is [46]:

$$\omega^2 = \begin{cases} k_{\parallel}^2 v_A^2 \left[ 1 + \left( \frac{3}{4} + \frac{T_e}{T_i} \right) k_{\perp}^2 \rho_i^2 \right] & k_{\perp}^2 \rho_i^2 \ll 1, \\ k_{\parallel}^2 v_A^2 \left( 1 + \frac{T_e}{T_i} \right) k_{\perp}^2 \rho_i^2 & k_{\perp}^2 \rho_i^2 \gg 1. \end{cases} \quad (3.31)$$

If the fourth order term is small, it dominates the wave equation only near the position where the second order term vanishes. If the kinetic effects become large, they can modify the Alfvén wave spectrum considerably. A possible consequence is a shift of the frequencies of shear Alfvén eigenmodes into the continuum.

The same considerations hold qualitatively in toroidal devices. In addition, due to KAW coupling, similar to shear Alfvén wave coupling, a countable infinity of new *Kinetic Alfvén Eigenmodes* (KAEs) emerges with frequencies just above the continuum

gaps [47] that replace the continuous spectrum. The granularity of the KAE spectrum becomes visible when observed with a resolution capable to detect kinetic effects. Recently, KAEs have been shown to exist in stellarators similar to the Wendelstein-line [48].

### 3.3.3.2 Energetic Particle Modes

In the presence of sufficiently strong fast-particle drive, yet another Alfvén eigenmode emerges that is, correspondingly, called *Energetic Particle Mode* (EPM). Their existence has been shown analytically for tokamaks [49–51] and requires that the energetic particle dynamics are included nonperturbatively, i.e. on the same footing as the bulk plasma dynamics. In stellarators, energetic particle modes are expected as well, with similar features as in tokamaks.

EPMs are predicted to emerge from the KAE dispersion relation as additional shear Alfvén instability if the fast-particle drive exceeds the local continuum damping. These modes can, therefore, be characterized as *forced oscillations* of the plasma with frequencies close to characteristic frequencies of the fast particle motion, e.g. transit, bounce or precession frequencies, and inside the shear Alfvén continuum. Consequently, the instability is characterized by a threshold. In the case of tokamaks it has been shown that the three types of shear Alfvén eigenmodes, ideal MHD gap modes, KAEs and EPMS, occur under different experimental conditions [49]. Gap modes are a threshold-less instability and can be destabilized by a perturbatively small population of energetic particles. They always constitute the most unstable shear Alfvén eigenmode if they do not suffer from continuum damping due to the variation of the gap frequency with the radial plasma profiles. If the drive by the energetic ions is sufficiently strong to overcome the continuum damping, EPMS are expected to be the strongest instability. KAEs become the most important instability only if the TAE is strongly damped by the continuum and the threshold for EPM excitation is not exceeded. However, KAEs are never strongly unstable, recalling that strongly driven KAEs merge into the EPM branch.

From linear analytical calculations [51, 52] as well as numerical simulations [53] of EPMS it is known that the real part of the EPM eigenfrequency strongly depends on detailed characteristics of the energetic ion distribution function. Frequency chirping and conversions between EPMS, KAEs and gap modes are expected in the presence of non-linear wave-particle interactions and changes in the background plasma. The radial eigenfunctions of the most unstable EPMS are localized at radial positions where the particle drive is strongest. Frequency chirping on slow time scales is associated with changes in the thermal bulk plasma and can happen for gap modes as well as for EPMS, while chirping on short time scales characteristic for fast-ion redistribution due to strong wave-particle interactions is predicted exclusively for EPMS. Frequencies inside the shear Alfvén continuum, the different radial localization as well as the frequency chirping are hints that sometimes allow to distinguish between gap modes and EPMS in experimental observations of Alfvénic activity.

# Chapter 4

## Experimental and numerical tools

### 4.1 The W7-AS device

The Wendelstein 7 - Advanced Stellarator was operated from 1988 to 2002 at the Institute for Plasma Physics (IPP) in Garching, Germany. It is a five-period stellarator. The enormous flexibility in the vacuum magnetic field configuration and plasma heating scenarios have made the device being a full success. The mission of W7-AS included: [54]

- demonstrate the generation of a confining magnetic field with modular coils,
- demonstrate the success of partial stellarator optimization,
- study the plasma confinement properties of a currentless stellarator,
- develop suitable heating scenarios,
- develop and study of the island divertor concept.

Several operation modes with improved plasma confinement were discovered at W7-AS:

**H-Mode in stellarators:** High confinement mode with edge transport barrier at the plasma boundary,

**OC-Mode:** Optimum Confinement mode with negative radial electric fields in the gradient region,

**HDH-Mode:** High Density H-Mode with good energy confinement and low impurity accumulation simultaneously at high densities.

Fig. 4.1 shows a picture of the W7-AS device surrounded by diagnostic and heating equipment. Tab. 4.2 lists some important device parameters.

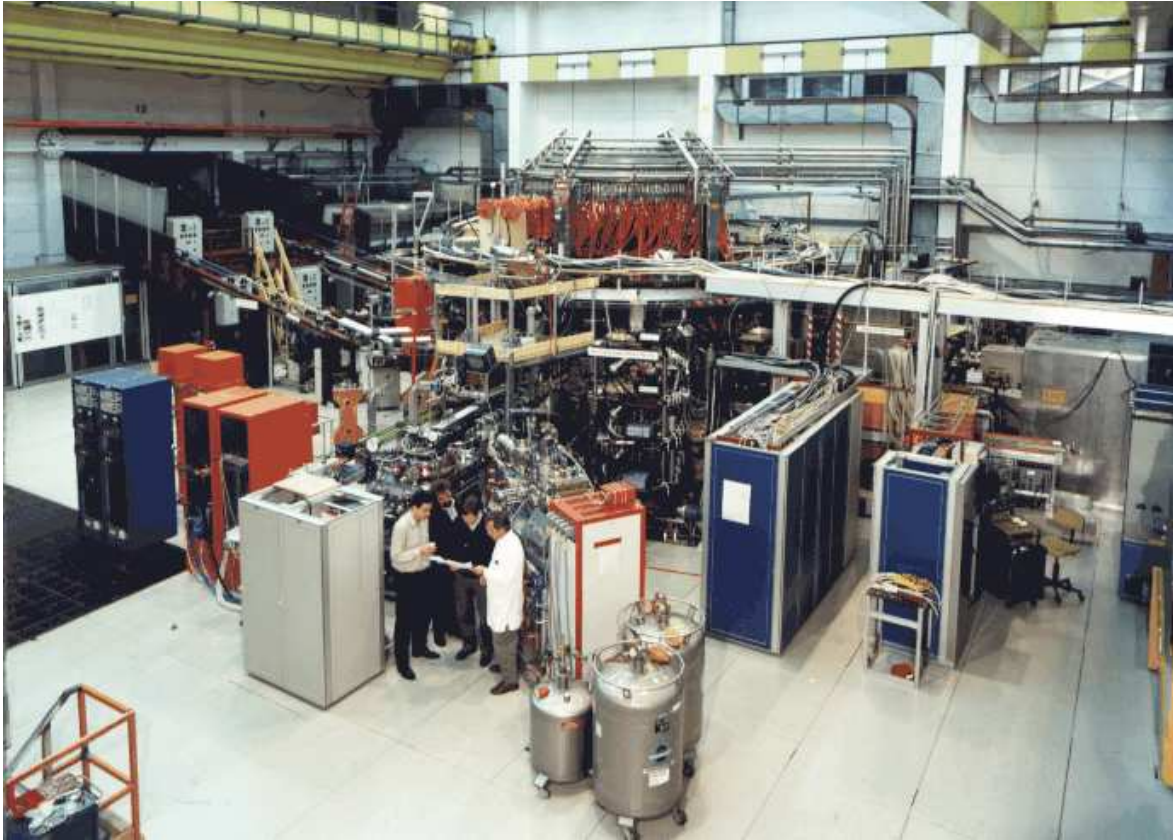


Figure 4.1: Photo showing the W7-AS stellarator and diagnostic/heating equipment.

The vacuum magnetic field in W7-AS is produced by coil systems shown schematically in Fig. 4.2. W7-AS is a partially optimized low shear stellarator with five identical field periods and is shaped like a pentagon. The main field is generated by non-planar modular field coils which generate toroidal and poloidal field components simultaneously. These coils alone produce a field of up to 2.5 Tesla with a fixed rotational transform  $\iota \sim 0.4$  and almost no magnetic shear  $d\iota/dr$ . Additional planar toroidal field coils are used to change  $\iota$  in the range from about  $0.3 \leq \iota \leq 0.6$ . At low  $\iota$ , the shear is slightly negative, at high  $\iota$  it becomes more and more positive. A small vertical field generated by the vertical field coils controls the horizontal position of the plasma column to compensate the Shafranov shift. The ohmic (OH) transformer is used to either compensate toroidal currents (such as the bootstrap current) to zero for a net current free operation, or to induce substantial tokamak-like currents in order to increase the magnetic shear and to study current-driven plasma instabilities. An additional set of larger non-planar coils located in the corners of the pentagon introduces even more flexibility. They allow to increase the magnetic field at the corners and modify the mirror ratio of the toroidal magnetic mirrors. Not shown in Fig. 4.2 are the control coils, two coils per period that were used to control the size of natural magnetic islands present in the vacuum magnetic field for large  $\iota$  values.

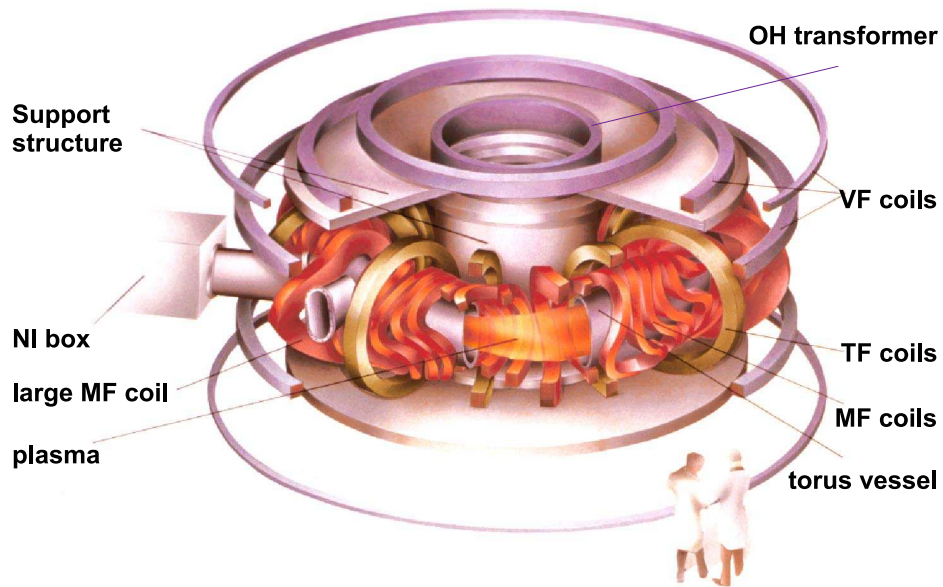


Figure 4.2: W7-AS magnetic field coils. MF: modular field, TF: toroidal field, VF: vertical field, OH: Ohmic heating, NI: neutral beam injection.

Diagnostic	Type	Quantities measured
Interferometers	optical, $\mu$ wave	line integrated electron density
Electron Cyclotron Emission (ECE)		electron temperature, fluctuations
Thomson Scattering	Ruby and Nd:YAG	electron density and temperature
Neutral Particle Analyzer (NPA)		ion concentrations and temperature, impurities
Bolometer		radiation power
Soft X-Ray Cameras		electron temperature, impurities, fluctuations, tomography
Spectrometers		densities, temperatures, impurities
H $_{\alpha}$ Camera		neutral gas density, particle fluxes, divertor strike lines
Diamagnetic Loop		plasma energy content
Rogowski Coil		plasma currents
Mirnov Probes		magnetic fluctuations
Ion Loss Probe (EFIP)		escaping energetic ions
Diagnostic Atom Beams	e.g. Lithium beam	edge plasma density
Langmuir Probes		plasma parameters and fluctuations in the divertor region

Table 4.1: Selection of diagnostics at W7-AS.

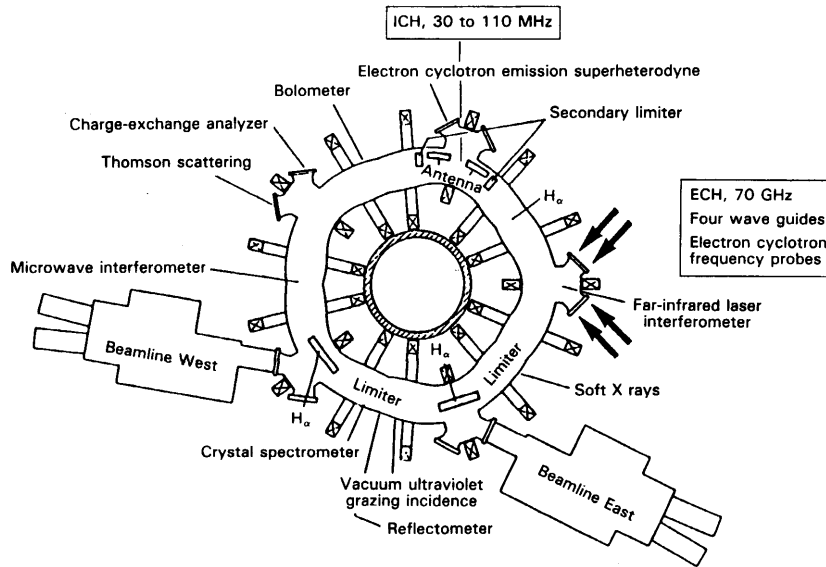


Figure 4.3: Heating and diagnostic systems installed at W7-AS. Not all available diagnostics are shown.

Several diagnostics were installed at W7-AS to monitor the plasma. Table 4.1 illustrates the diagnostic possibilities, even though it is not complete. For plasma heating, neutral beam injection (NBI) and electron cyclotron resonance heating (ECRH) were used. The NBI system consisted of two beamlines with four sources of 0.5 MW each that were set up for balanced (co- and counter) tangential injection. Later, the setup was changed for unbalanced injection (Fig. 4.4). The injected, highly energetic neutral particles are ionized either collisionally or by charge exchange reactions and heat the bulk plasma by thermalization. The ECRH system had five sources with 70/140 GHz and 0.5 MW power each. ECRH was used for (local) plasma heating, local electron cyclotron current drive (ECCD), and electron heat transport studies (by power modulation). Also, experiments using the OXB conversion to convert electron cyclotron waves to electrostatic Bernstein waves, for which no upper cutoff density exists, were performed.

## 4.2 Diagnostics

This section deals with diagnostics that were installed at W7-AS. The focus will only be on those diagnostics that have been used in the data analysis. After giving a short overview of the physical basis, the setup at W7-AS will be explained.



Device		
type		Advanced Stellarator
coil system		modular coils
symmetry		$m = 5$
rotational transform $t$	1	$0.3 \leq t \leq 0.6$
major radius $R$	m	2.0
minor radius $a$	m	$a \leq 0.2$
fuel gas		$^1\text{H}$ or $^2\text{H}$ (D)
first wall materials		TiC, tungsten, (boronized) carbon
wall conditioning methods		carbonization, boronization, He glow discharge
Magnetic field		
toroidal field at coils	T	3.5
toroidal field at axis	T	2.5
field ripple, $\Delta B/B$	1	0.09 on axis 0.3 on LCMS
magnetic well	1	$-0.015 \dots 0.01$
Heating		
ECRH	70 GHz	1 x 0.5 MW (3s)
	140 GHz	1 x 0.3 MW (1s)
	140 GHz	3 x 0.6 MW (1s)
NBI	tangential	8 x 0.5 MW ( $\leq 1\text{s}$ )
	radial	moderate power only

### Operational Limits

Quantity	Limit	$B_0$ [T]	$t_a$	$n_e$ [ $\text{m}^{-3}$ ]	$T_e$ [eV]	$P_{\text{NBI}}$ [MW]	$P_{\text{ECRH}}$
$n_e$	$4.0 \cdot 10^{20}$	2.5	0.55		350	2.4	
$T_e$	6.8 keV	2.5	0.34	$2.0 \cdot 10^{19}$			2 MW
$T_i$	1.8 keV	2.5	0.345	$5.0 \cdot 10^{19}$		1.3	
$\langle \beta \rangle$	3.4%	0.9	0.5	$2.0 \cdot 10^{20}$		2.8	
$\tau_E$	0.06s	2.5	0.345	$1.1 \cdot 10^{20}$		0.33	
$n_e T_i \tau_E$	$5.0 \cdot 10^{21}$ eVsm $^{-3}$	2.5	0.345	$1.1 \cdot 10^{20}$		0.33	

Table 4.2: Some important properties of the W7-AS device.

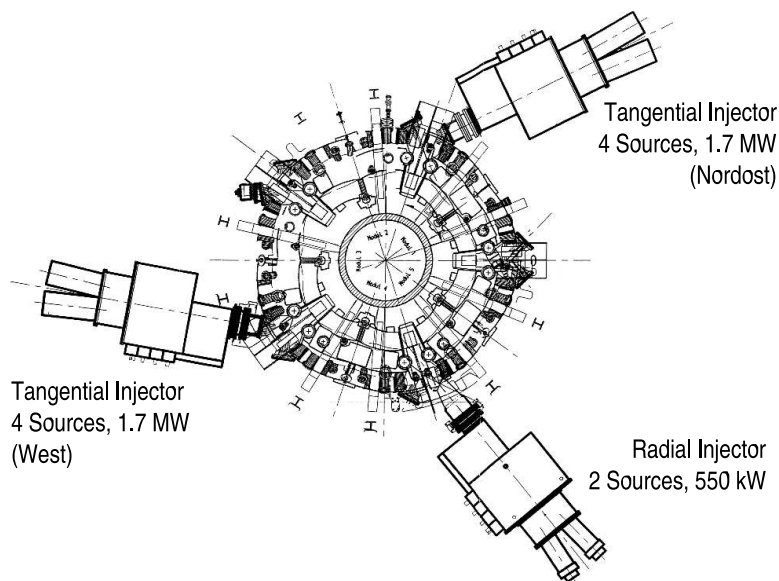


Figure 4.4: NBI beamline setup at the end of W7-AS operation. The former counter-injecting beamline was moved to perform co-injection as well. The radial injector was mainly used for diagnostic purposes.

Probes	Sample rate	Cross section [cm <sup>2</sup> ]	Length [cm]
MIR-1, Type 1	333 kHz	3.60	2.1
MIR-1, Type 2	333 kHz	3.20	3.2
MIR-1, Type 3	333 kHz	3.20	2.1
MIR-3, MIR-5	1 MHz	5.94	3.6

Table 4.3: Important properties of the Mirnov probes at W7-AS.

### 4.2.1 Mirnov Diagnostic

The Mirnov diagnostic consists of a set of spatially distributed coils that measure magnetic fluctuations  $dB/dt$ . The coils cannot be immersed into the hot plasma, they are usually mounted to the vessel wall. To shield the coils from stray radiation and hot particle fluxes, they are embedded in a steel tube.

The recorded time traces yield information about spatially extended, periodic magnetic field fluctuations in the plasma. At W7-AS, three poloidal arrays of MIRNOV probes were installed, called *MIR-1*, *MIR-3*, and *MIR-5*. Their spatial distribution is shown in Fig. 4.5 and some important properties are compiled in Tab. 4.3. All probes are setup to measure fluctuations of the poloidal field component. In the MIR-1 array, three different types of coils were used, all coils in arrays MIR-3 and MIR-5 are of the same type. The MIR-1 array could be operated independently of the fast probes in arrays MIR-3 and MIR-5.

The probes in the MIR-1 array have a good inductance  $L$  as well as a rather large

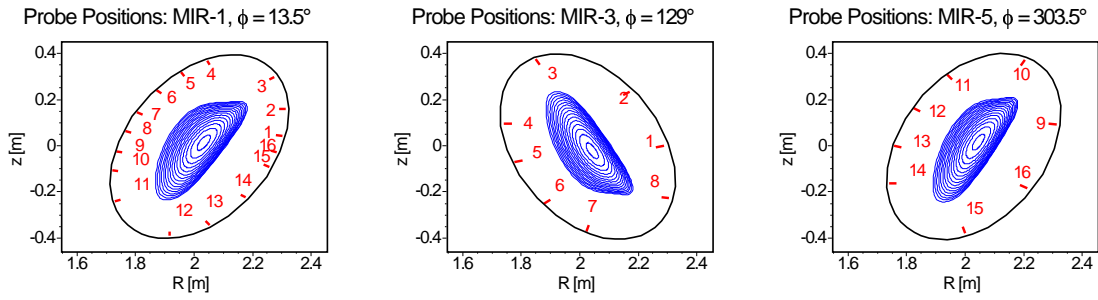


Figure 4.5: Mirnov probe setup at W7-AS. The black line indicates the vessel contour, the blue lines are flux surfaces from a sample configuration, the numbered probes are shown in red.

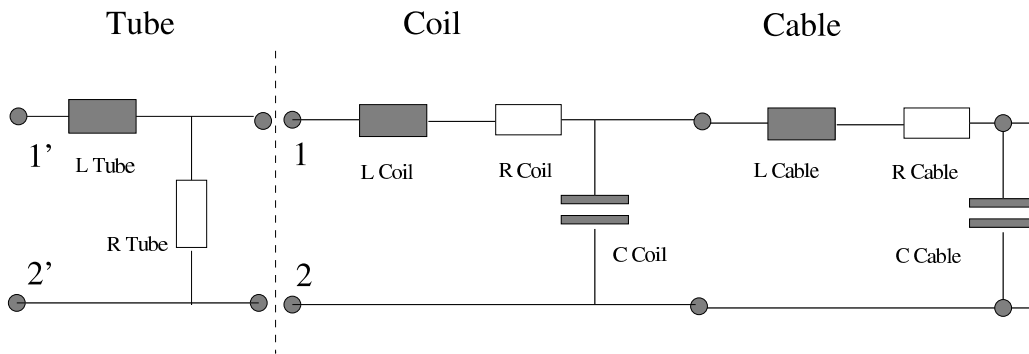


Figure 4.6: Equivalent circuit of the MIR-1 probe, connection cable, and housing tube to calculate the transfer function.

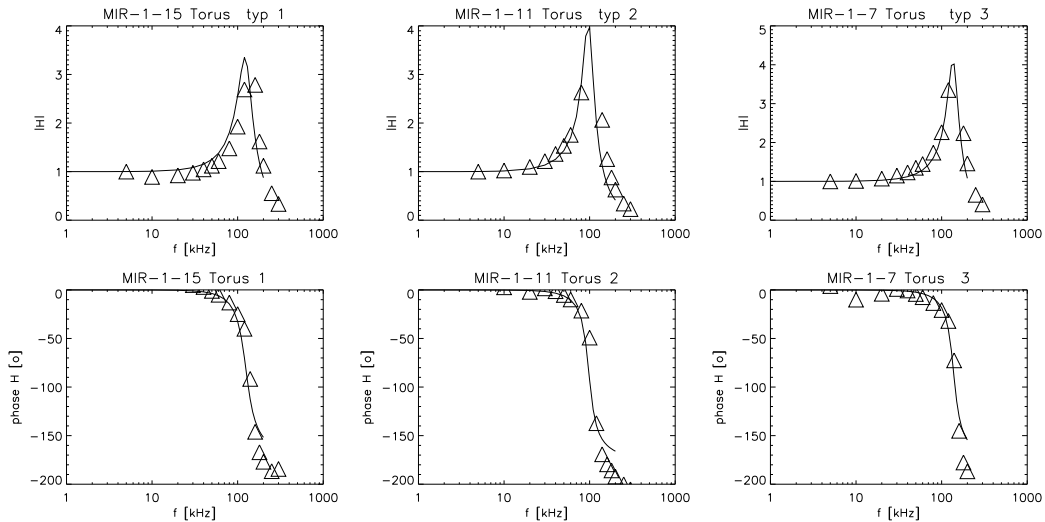


Figure 4.7: Comparison of analytical transfer function with the measured one for each type of MIR-1 probes. The top row shows the amplitude of the transfer function, the bottom row shows the phase shift. Solid line: analytical model according to the equivalent circuit. Triangles: measurements performed on 04. Aug. 1998.

capacity  $C$ . Therefore, they behave like LC resonance circuits with a resonance frequency near 200 kHz that is slightly different for each probe type. Furthermore, long connection cables without impedance converters shift the resonance frequency towards 70-120 kHz. Near the resonance frequency, the amplitude of the induced voltage increases significantly and the phase between exciting signal and induced voltage jumps gradually from 0 to  $\pm\pi$ . This phase shift can be corrected if the complex transfer function of the measurement setup is known. Earlier attempts to correct the data resulted in an analytical model for the transfer function, based on the equivalent circuit shown in Fig. 4.6, that agreed well with measurements performed while the vessel was opened for maintenance in 1998 as shown in Fig. 4.7.

In order to validate the phase and amplitude corrections, the inverse transfer function was applied to measured time traces containing broadband fluctuations that are commonly observed in ECRH heated plasmas. The same fluctuations, recorded by the fast Mirnov probes of the nearby MIR-5 array at equivalent poloidal positions, were taken as a reference. It was assumed that the spectral properties of the fluctuations are similar. Fig. 4.8 shows the FFT spectra of the MIR-1 data with and without corrections along with the reference MIR-5 spectra. The resonance is clearly seen in the uncorrected data. The spectra of phase and amplitude corrected probe signals show that the amplitude is overcompensated by orders of magnitude near the resonance (the analytical transfer function diverges at that point). Furthermore, there is a mismatch in the resonance frequencies between analytical model and plasma system for each coil type. Since the agreement between measurement and model is quite good without plasma, the only explanation is that the presence of the plasma shifts the resonance frequencies as well. This indicates that the plasma must be included in the equivalent circuit for the probe setup (Fig. 4.6). The simple assumption that the plasma acts as an additional mutual inductance does not result in a consistent compensation of the shift for all probes simultaneously. It therefore seems to be impossible to apply proper phase and amplitude corrections to the MIR-1 array. Moreover, because the resonance frequencies differ in the range from 70 - 120 kHz between the probe types, the time traces measured with different probe types will have a different phase shift in this frequency range. This renders the MIR-1 probes useless for a proper eigenmode analysis in the frequency range beyond 70 kHz.

There were discharges where the plasma in W7-AS was created by a 900 MHz HF source instead of ECRH. In those cases, the MIR-3 time traces show occasional data losses for at least some of the MIR-3 probes which are mounted near the HF launcher. This problem is probably related to HF pickup and a corresponding failure of the DAC hardware. It could be improved but not fully avoided by the installation of HF filters. Affected are the time traces before  $t \approx 0.25$  s, a manual inspection of the time traces is required if eigenmodes in this time range are analyzed.

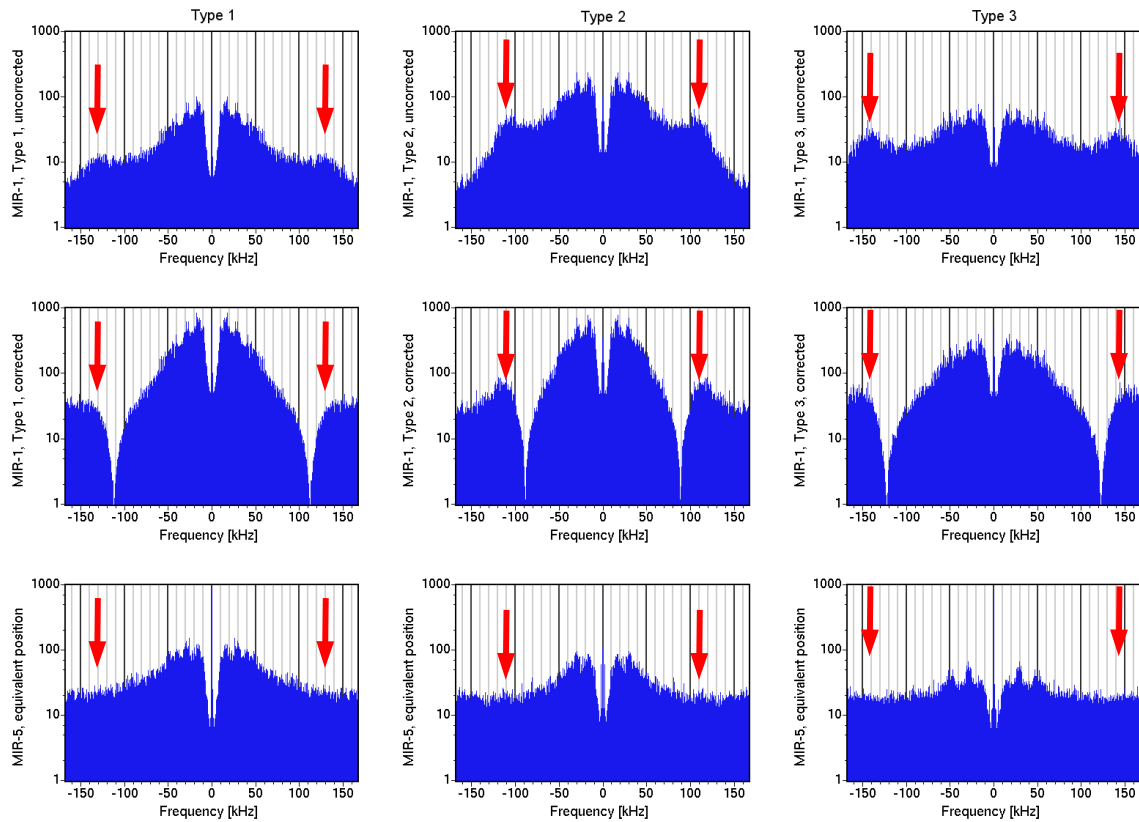


Figure 4.8: Application of the inverse transfer function to measured fluctuations for a probe of each type in the MIR-1 probe array. Top row: FFT of unmodified data; middle row: FFT of corrected data using the inverse transfer function; bottom row: spectrum of nearby fast probes at equivalent poloidal positions.

## 4.2.2 Plasma parameter diagnostics

The spatial temperature and density profiles of the plasma species are of great importance for any attempt to understand the plasma. In the following section an overview of the diagnostics is given which were used to obtain and validate the profiles.

### 4.2.2.1 Thomson Scattering

When a strong, linearly polarized, monochromatic electromagnetic wave is incident on a charged particle, the electric field of the wave exerts a force on the particle and sets it in motion. Since the field of the wave is periodic in time, so is the motion of the particle. Thus, the particle is permanently accelerated and, consequently, emits radiation. This process can be interpreted as a scattering of the incident wave. If the charged particle in question is an electron, the process is called Thomson scattering. If the particle is in rest, the frequency of the scattered wave is the same as that of the incident wave. Otherwise, the Doppler effect will detune the emitted frequency. This can be used to infer the electron velocity distribution function from the spectral shape of the scattered light, the intensity of the scattered light is proportional to the electron density. The Thomson scattering cross section

$$\sigma_{\text{Thomson}} = \frac{8\pi}{3} \left( \frac{e^2}{4\pi\epsilon_0 m_e c^2} \right)^2 = 6.65 \cdot 10^{-29} \text{m}^2$$

is very small. To gain a usable signal amplitude in measurements, enormous wave amplitudes (as those of intense laser beams) are needed.

At W7-AS, two Thomson scattering systems were installed. One system was equipped with a Ruby laser that could emit a single pulse per discharge. For time resolved electron density and temperature profiles, a second system using a Nd:YAG laser with a pulse length of 10ns and a repetition rate of 20ms was installed. The experimental setup is shown in Fig. 4.9. The laser light is chosen to traverse the plasma vertically near the elliptical plane to gain high spatial resolution with respect to the flux surfaces. 16 sight lines observe scattering volumes with a vertical extend of  $\delta z = 2.5\text{cm}$ . The vertical separation between the observation volumes is  $\Delta z = 4.0\text{cm}$ . The scattered light is projected onto polychromators that split the light into three frequency components. Each spatial channel is equipped with its own polychromator box. Basically one polychromator box consists of three interference filters that allow the scattered light to transmit in a certain wavelength range. The electron temperature can be estimated by fitting a Maxwellian velocity distribution integrated over the spectral sensitivity of each polychromator channel through these three points. At W7-AS, Bayesian probability theory is used to evaluate the electron temperature and density from the measurements including forward modelling of measured data and calibration measurements [55].

The spectral sensitivity of the polychromator channels was optimized for an electron temperature in the keV range. Most of the discharges that were analyzed in the

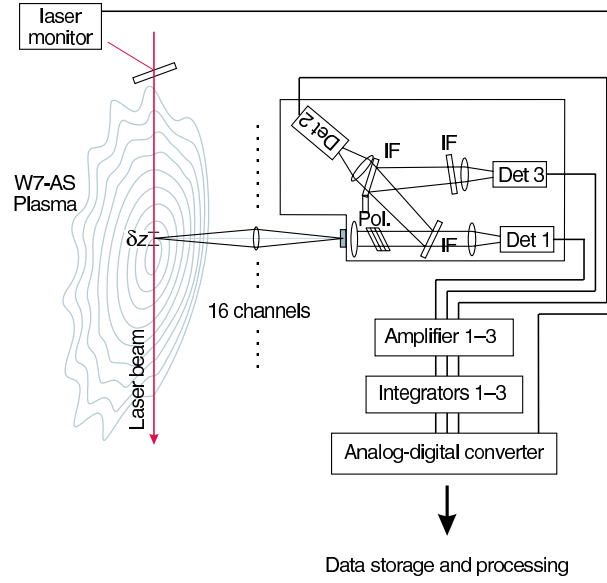


Figure 4.9: The Nd:YAG Thomson scattering system at W7-AS, including signal detection and processing. IF: interference filter, Det: detector (avalanche diode), Pol: polarizer.  $\delta z$  is the extend of the scattering volume.

scope of the present thesis, however, have electron temperatures well below 1 keV. For low temperatures, the signal of at least the outmost spectral channel becomes very small and the reconstructed temperature has a large uncertainty. Systematic errors in the calibration further complicate the situation. While the profile shape is well reproduced, the magnitudes of density and temperature are not. Therefore, the estimated profiles need to be further validated with other diagnostics that are known to produce reasonable results.

#### 4.2.2.2 Diamagnetic loop

The diamagnetic loop serves to measure the energy content of the plasma. It consists of a loop surrounding the plasma poloidally and the induced voltage is a measure for the change of the toroidal magnetic flux. One or more "compensation loops" measure the change of toroidal flux outside the plasma. The difference between them is the change of flux induced by the plasma, which is related to the energy content of the plasma. This change is usually negative which indicates that the plasma reduces the toroidal magnetic flux, i.e., the plasma is diamagnetic, hence the name of the diagnostic. For a screw pinch of length  $2\pi R$  and radius  $a$ , the total change in toroidal magnetic flux by the plasma energy and toroidal currents is given by [56]

$$\Delta\Phi_{tor} = -\frac{\mu_0 W}{3\pi R B_0} + \frac{\mu_0^2 I_{tor}^2}{8\pi B_0} + \frac{\pi\mu_0 t_{vac}}{R} \int_0^a j_{tor}(r) r^3 dr, \quad (4.1)$$

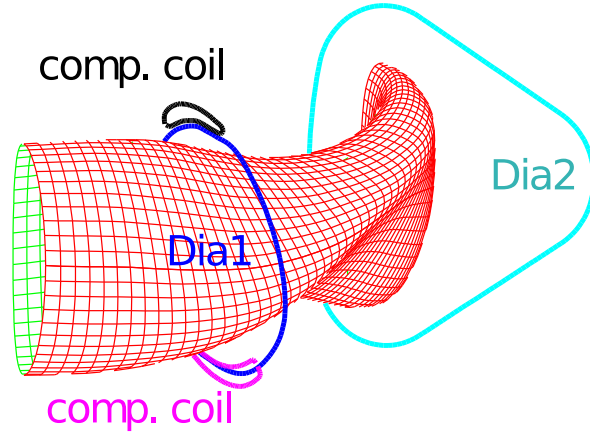


Figure 4.10: Diamagnetic loops at W7-AS. The loop named Dia1 is located in the  $\phi = 15^\circ$  plane, the second loop in the  $\phi = 36^\circ$  plane.

where  $W = 4\pi^2 R \cdot 3/2 \int r \cdot p(r) dr$  is the total plasma energy,  $I_{tor}$  the net toroidal current and  $j_{tor}(r)$  the toroidal current density. The last term describes the influence of the current density profile. Due to the factor  $r^3$  inside the integral, only the current densities near the plasma edge contribute significantly. If the net toroidal plasma current and the current density profile are known, the kinetic energy of the plasma can be reconstructed from the measured diamagnetic energy.

Fig. 4.10 shows the setup of the diamagnetic loops at W7-AS. The loop named "Dia1" is accompanied by two compensation coils, all three are installed inside the vessel. The second loop has no compensation coils and is mounted to the outside of the torus. The three-dimensional geometry of W7-AS has an influence on the probe signals such that Eq. (4.1) does not hold. Interpretation of measured data is, nevertheless, possible by forward modelling of the probe signals based on the full 3D geometry in the form of free-boundary MHD equilibria [57].

#### 4.2.2.3 Soft X-ray electron temperature measurements

At W7-AS, a set of three different soft X-Ray diagnostics was installed [58]. The first diagnostic system with two cameras was equipped with a huge variety of different filters for the incident photon energy and was used to measure line radiation emitted by impurity ions to determine the effective charge number  $Z_{eff}$  and to trace the radial impurity transport. The second system with a lower number of sight lines was used as a monitor for the electron temperature. The third system named "MiniSoX" consists of a total of 320 sight lines covering the whole discharge cross section. It allows for tomographic reconstruction of the plasma equilibrium and even the radial and poloidal mode structure of low-frequency Alfvén- and MHD Eigenmodes. Fig. 4.11 shows schematics of all three camera systems.

There are three major contributions to the total soft X-Ray emission of a hot plasma.



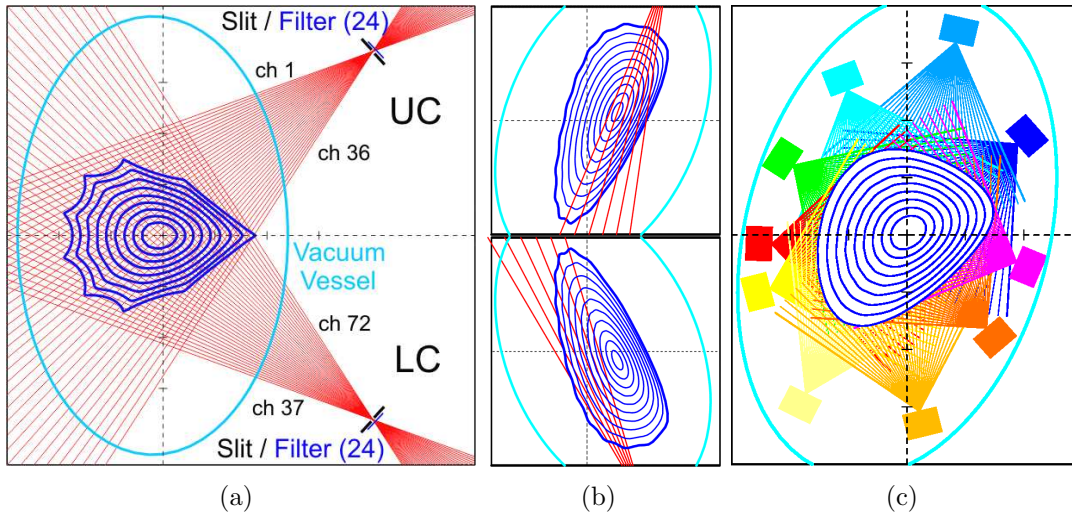


Figure 4.11: The three soft X-Ray diagnostic systems installed at W7-AS: (a) flexible impurity monitoring system; (b)  $T_e$  monitor system; (c) MiniSoX system for tomographic reconstructions.

The first component is the bremsstrahlung that is emitted by electrons that are accelerated in the Coulomb field of the ions. The spectral power density depends on the electron temperature as  $dP/d\omega \sim \exp(-\hbar\omega/k_B T_e)$ . The second important part is the radiation emitted by electron-ion recombination processes. The free electrons that are captured into bound states have no discrete energy spectrum, the recombination emission forms a continuous spectrum as well. The third component is the discrete line radiation emitted by plasma impurities.

The dependence of the spectral power density of the bremsstrahlung on the electron temperature can be used to derive electron temperature from soft X-Ray emission measurements. Two detectors with different absorber foils that are opaque for photons below a certain energy observe the electromagnetic radiation of the same plasma volume in the spectral ranges  $\omega_1 \dots \infty$  and  $\omega_2 \dots \infty$ , respectively. The ratio of the intensities measured in both spectral ranges is compared to model calculations to deduce the electron temperature. Line radiation by low- $Z$  impurities (e.g. boron, carbon) is suppressed by choosing appropriate filters that absorb these photons. The remaining intensity is weak due to the  $\exp(-\hbar\omega/k_B T_e)$  decay, but this can partially be compensated by choosing larger detectors and reducing the spatial resolution. Line radiation by medium- $Z$  impurities like iron or tungsten can be included into the model if the impurity species mix is known from spectroscopic measurements. In W7-AS, the central electron temperatures by X-Ray analysis usually agree well to ECE measurements. X-Ray analysis is especially valuable in the high density regime where ECE is in the cut-off regime.

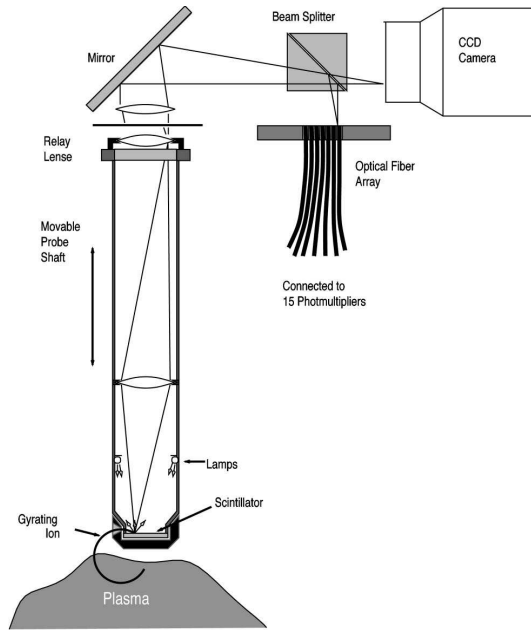


Figure 4.12: Schematic of the fast ion loss detector.

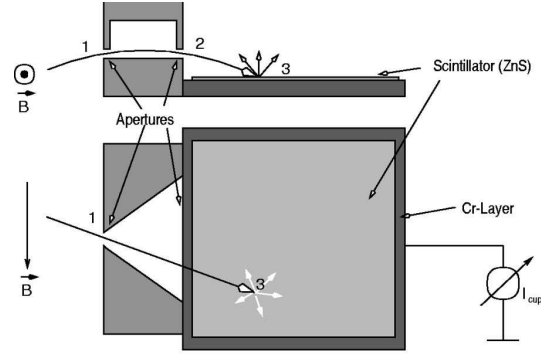


Figure 4.13: Schematic of side and top view of the probe operation. The gyro-radius (energy) of a particle determines if it can pass the two apertures 1 and 2, and how far from aperture 2 it will strike the scintillator in point 3. The pitch angle determines where the particle will strike along the orthogonal direction of the scintillator.

### 4.2.3 Fast Ion Loss Detector

A fast ion loss probe, called EFIP (Escaping Fast Ion Probe), based on a ZnS scintillator plate was installed on W7-AS, too [59]. The schematic of the diagnostic setup is shown in Fig. 4.12. The probe is located at a position where, according to guiding-center calculations, the largest flux of energetic ions is expected. It was mounted to a manipulator that allows the probe to be varyingly positioned from 27 cm below the midplane to 40 cm below the midplane (the location of the vessel wall).

Energetic ions that are able to enter the probe through two apertures (see Fig. 4.13) strike the scintillator at a position that is determined by their gyro radius (energy) and their pitch  $\chi = v_{\parallel}/v$ . The image of the light pattern on the scintillator is transferred through an optical system to a set of detectors that allow the spatial distribution and the total intensity of the light to be recorded. The details of the light pattern excited by the ions depends on the dimensions of the apertures, their position relative to the scintillator, and the orientation of the probe with respect to the ambient magnetic field. The W7-AS probe has, in fact, two sets of entrance apertures that allow one to measure co- and counterpassing ion losses simultaneously.

Interpretation of the spatial light pattern is possible by numerical simulation for a given magnetic field configuration. The striking points of particles on the scintillator are determined by the gyro radius and pitch angle only, which allows the generation of a mapping between  $(\mathcal{E}, \chi)$  and locations on the scintillator as shown in Fig. 4.14. The light was simultaneously recorded by a CCD camera, which gives an output image of

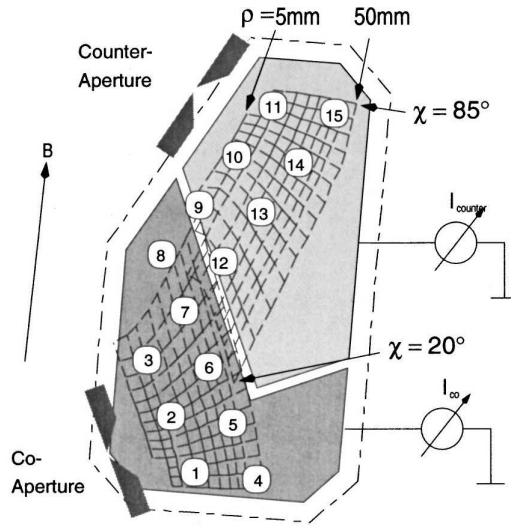


Figure 4.14: Pitch angle and energy maps for typical W7-AS discharge conditions. Shown is the scintillator outline, the aperture sets and the maps for co- and counter-passing ions. Only the counter coordinate grid is annotated with values. The numbered circles indicate regions on the scintillator to which the PMTs are sensitive.

128 × 128 pixels each 100 ms, and a set of 15 photomultipliers (PMTs) that observe different regions on the scintillator and are digitized with a rate of 4 kHz.

### 4.3 Mirnov Data Analysis

In this section, the tools for analyzing the Mirnov probe data are discussed. It covers advanced tools for harmonic analysis of one- and multidimensional datasets to obtain time-resolved frequency spectra as well as time-resolved frequency-mode number spectra from the sampled data.

The best way to check if some interesting coherent mode activity is present in the data is to look at the time-resolved frequency spectrum of the signals measured by individual probes. These can be calculated very fast with great accuracy by means of continuous wavelet transform.

All the standard tools for multi-dimensional harmonic analysis fail in the case of Mirnov data obtained on W7-AS and many other stellarators, mainly because the probes cannot be evenly spaced. Even worse, the probes at W7-AS are sampled with different sample rates. Thus the temporal datapoint spacing is uneven as well as the spatial spacing between probes. The mode number analysis is done using a newly developed technique based on the Lomb periodogram. It basically is a straightforward, multi-dimensional extension of Lomb's original periodogram definition [60]. It is well suited for the case of unevenly sampled datapoints. Like multi-dimensional Fourier transform, it analyses the available temporal and spatial data at the same time – giving maximum

confidence in the analysis results.

### 4.3.1 Continuous wavelet transform

The history of wavelet analysis started early in the 20th century. The goal was to develop a tool for highly time-resolved spectral analysis of datasets. Several applications exist: Signal coding, data compression and reconstruction, data filtering, or time-resolved frequency and power spectra. The term "wavelet" is due to Morlet and Grossman in the early 1980s. They used the french word "ondelette" which means "little wave". Wavelet transforms have become a standard technique in signal processing and this topic is covered in many text books [61–63].

Wavelet transform refers to the representation of a signal in terms of a finite length (or fast decaying), oscillatory waveform called the "mother wavelet". This waveform is scaled and translated in time and "compared" to the signal. Wavelet transforms are broadly classified into discrete wavelet transform (DWT) and continuous wavelet transform (CWT). Basically the difference between these two is that the continuous wavelet transform operates over all possible translations and scales, whereas the discrete wavelet transform uses only a specific subset of scales and translations that make the resulting wavelets bi-orthogonal. Every wavelet transform can be considered as a frequency-time representation of the signal and therefore is related to harmonic analysis. Furthermore, the continuous wavelet transform is subject to Heisenberg's uncertainty principle. In the following, only the CWT will be presented.

#### 4.3.1.1 The Mother Wavelet

The mother wavelet function  $\psi(t)$  must be continuous and has to satisfy the following conditions:

1.  $\int |\psi(t)|^2 dt = 1$  normalized
2.  $\int |\psi(t)| dt < \infty$  bounded
3.  $\int \psi(t) dt = 0$  zero mean
4.  $\int t^M \psi(t) dt = 0$   $M$  vanishing moments

The last condition is useful in many applications. For the application, the mother wavelet is scaled by a factor  $a$  (frequency) and translated by a shift  $b$  in time to give

$$\psi_{a,b}(t) = \frac{1}{\sqrt{a}} \cdot \phi\left(\frac{t-b}{a}\right).$$

Given the conditions above and this scaling rule, it can be shown that the wavelets  $\psi_{a,b}(t)$  are localized in both, time and frequency domain. The width of the wavelet in

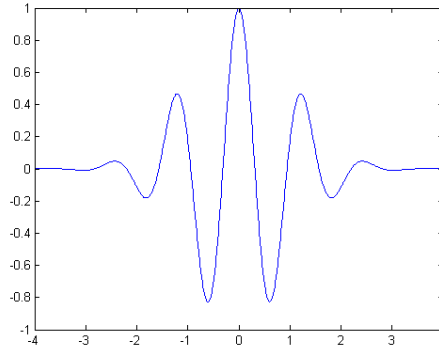


Figure 4.15: The Morlet wavelet.

frequency domain,  $\Delta f$ , and in time domain,  $\Delta t$ , satisfies the condition  $\Delta f \cdot \Delta t \geq C$ , which is Heisenberg's uncertainty principle. Several mother wavelets exist with different properties. For a frequency analysis, Morlet's wavelet is the best to one use.

#### 4.3.1.2 The Morlet Wavelet

The Morlet wavelet, named after Jean Morlet, was introduced by Goupillaud, Grossmann and Morlet in 1984 [64, 65]. It is a constant  $\kappa_\sigma$  subtracted from a plane wave and multiplied with a Gaussian window, as shown in Fig. 4.15.

$$\begin{aligned}\psi_\sigma(t) &= \frac{C_\sigma}{\pi^{1/4} e^{-t^2/2}} \cdot (e^{i\sigma t} - \kappa_\sigma) \\ \kappa_\sigma &= e^{-\sigma^2/2} \\ C_\sigma &= \frac{1}{\sqrt{1 + e^{-\sigma^2} - 2e^{-3\sigma^2/4}}}\end{aligned}\tag{4.2}$$

By the Gaussian envelope, this wavelet is well localized in both, time and frequency domain. The additional parameter  $\sigma$  specifies the number of harmonic oscillations within the window and allows a tradeoff between frequency and time resolution. Conventionally,  $\sigma > 5$  is used to avoid problems due to the small temporal extend at very low  $\sigma$ . The frequency uncertainty becomes very large at such small  $\sigma$ .

#### 4.3.1.3 Calculation of the Wavelet Transform

When calculating a complete wavelet transform, one first has to define a grid in time-frequency space on which the transform is to be calculated. The number of output points in frequency and time domain can be freely chosen. The ranges are, however, limited by the available data. The scanning frequency should not exceed the Nyquist frequency  $f_{Ny} = 1/2f_s$  where  $f_s$  is the sample frequency. For each point  $(t_i, f_j)$  in the output array, the wavelet at appropriate scale  $a = 1/2\pi f$  and time shift  $b = t_i - t_0$

is calculated and convolved with the data. The convolution can be done in two ways: Either, the convolution is calculated directly in the time domain. This can be quite efficient if one remembers that the wavelet is localized in time. Most of the wavelet will be (nearly) equal to zero and can safely be neglected. Then the convolution covers only a moderate amount of datapoints which is further reduced with increasing scanning frequency because of the better localization in time domain. Another acceleration can be achieved when the data is evenly sampled. Then the wavelet needs to be calculated only once for each scanning frequency, the shift in time can be done by simply shifting the indices. On the other hand, the convolution theorem can be used:

$$a \otimes b = \int a(t - \tau) \cdot b(\tau) d\tau = \mathcal{F}^{-1}(\mathcal{F}(a) \cdot \mathcal{F}^*(b))$$

where  $\mathcal{F}$  denotes the Fast Fourier Transform (FFT) and  $\mathcal{F}^*$  is the complex conjugate of  $\mathcal{F}$ . This procedure requires the data to be evenly sampled because the FFT algorithm is used. At each scanning frequency, three fourier transforms of the size of the dataset have to be calculated.

### 4.3.2 Lomb periodogram analysis

The harmonic analysis of unevenly sampled data can be done by evaluating the discrete version of the fourier integral explicitly (periodogram analysis, see e.g. [66]), but this has several drawbacks: First of all, it includes numerous computationally expensive evaluations of sine and cosine functions. And secondly, the obtained spectrum has no well-defined statistical properties. The latter means that if a peak is observed in the spectrum, it is impossible to tell whether the peak results from a periodic signal in the data at that frequency, or is caused by a signal at a different frequency due to spectral leakage or noise in the data. In the case of evenly spaced datapoints the sampling theorem along with the orthogonality of different frequency components (in infinitely sampled datasets) guarantees the relevance of any given peak in the spectrum. Nevertheless, the periodogram analysis is a good approximation to the spectrum that would have been obtained by least-squares fitting sine and cosine waves to the data.

In 1976, the Australian astronomer Lomb proposed a slight modification to the classical periodogram definition that makes the statistical behaviour of the periodogram equal to that obtained in the case of evenly spaced data [60]. The Lomb periodogram  $P$  for a dataset  $(t_i, y_i), i = 1 \dots N$  gives a power spectrum and is defined as

$$P(\omega) = \frac{1}{2\sigma^2} \left\{ \frac{[\sum_i (y_i - \bar{y}) \cos \omega(t_i - \tau)]^2}{\sum_i \cos^2 \omega(t_i - \tau)} + \frac{[\sum_i (y_i - \bar{y}) \sin \omega(t_i - \tau)]^2}{\sum_i \sin^2 \omega(t_i - \tau)} \right\} \quad (4.3)$$

where  $\omega$  is the scanning frequency,  $\sigma$  is the standard deviation, and  $\bar{y}$  the mean value of the dataset. The parameter  $\tau$  makes the periodogram invariant to time translations and is given by

$$\tau : \tan(2\pi\tau) = \frac{\sum_i \sin 2\omega t_i}{\sum_i \cos 2\omega t_i} \quad (4.4)$$

Lomb has shown that his periodogram is exactly equivalent to a least-squares fit of the data to the model

$$y = a \sin(\omega t - \tau) + b \cos(\omega t - \tau) + \varepsilon_i.$$

However, the spectrum is no direct measure for the amplitude of a periodic signal [67]. At each frequency  $\omega$ , a sine and cosine wave are fitted to the data  $y_i$  yielding coefficients  $a(\omega)$  and  $b(\omega)$  such that the sum of squared residuals  $\sum \varepsilon_i^2$  is minimized. Quantities proportional to the variances of the amplitude coefficients  $\text{var}(a)$  and  $\text{var}(b)$  are also computed. The periodogram (4.3) can be written as

$$P(\omega) = \frac{a^2 + b^2}{\text{var}(a^2 + b^2)} = \frac{a^2}{\text{var}(a)} + \frac{b^2}{\text{var}(b)},$$

which states that  $P$  is a relative measure of the signal amplitude compared to the variance of that amplitude. The covariance  $\text{cov}(a, b)$  can be omitted because the time shift  $\tau$  renders the sine and cosine functions orthogonal over time domain so that  $a$  and  $b$  are uncorrelated.

The statistical properties of the Lomb periodogram have been thoroughly investigated [67, 68]. For evenly spaced datapoints  $P(\omega)$  is proportional to the spectrum obtained by discrete fourier transform (DFT) or Welch's periodogram. For unevenly spaced datapoints it was shown [69] that for a peak of height  $z$  the "false alarm probability" (the probability that a peak of height  $z$  could be caused by pure gaussian noise) is

$$P(> z) = 1 - (1 - e^{-z})^M \approx M e^{-z} \quad (4.5)$$

where  $M$  is the number of independent frequencies scanned. It is very difficult to actually calculate  $M$  for a given datapoint distribution. Numerical simulations show that  $M$  is nearly identical with the number of datapoints  $N$  if the datapoints are evenly spaced and  $N$  frequencies in the Nyquist range are scanned [70]. The equivalent of the Nyquist set of frequencies  $\{\omega_k\}$  for  $N$  non-evenly spaced datapoints can be defined as the set of frequencies obtained by a discrete Fourier analysis of  $N$  evenly spaced datapoints between  $t_1$  and  $t_N$ , where the zero frequency component  $\omega_0$  is usually excluded in periodogram analysis. Therefore,  $\{\omega_k\} = \{\pm 2\pi k / (t_N - t_1) ; k = 1 \dots N/2 - 1\}$ . Equivalently, the Nyquist frequency is given by  $\omega_{k=N/2}$ . For uneven spacing and a random datapoint distribution, the number of independent frequencies is not much different from the case of even spacing.  $M$  may differ significantly, however, if the datapoints are "clumped" in groups of nearly regular size.

Several enhancements result from uneven datapoint spacing. Aliasing effects are reduced which makes it possible to detect frequencies well above the Nyquist frequency without significant alias peaks below. Oversampling, that means scanning additional frequencies between the ones given by the Nyquist set of frequencies, could also make sense. Quantitatively, the enhancements depend on the datapoint distribution – the best results are obtained for truly random spacing.

### 4.3.2.1 Multidimensional extension of the Lomb periodogram

The most general ansatz for a (possibly weakly nonlinear) propagating wave pattern is a series expansion in plane-wave basis functions:

$$f(\mathbf{x}, t) = \sum_j A_j \exp[i(\mathbf{k}_j \mathbf{x} - \omega t)] \quad (4.6)$$

Now consider a system that is topologically equivalent to a two-dimensional torus. Periodic boundary conditions suggest a change of space to angle coordinates and a parameterization of the wave vector by mode numbers. In poloidal direction we use  $\theta$  and  $m$  for the angle coordinate and the corresponding mode number, respectively, while in toroidal direction these quantities will be called  $\phi$  and  $n$ . Rewriting Eq. (4.6) with this choice of variables yields

$$f(\theta, \phi, t) = \sum_{m,n} A_{m,n} \exp[i(m\theta - n\phi - \omega t)]. \quad (4.7)$$

The signs in front of the spatial terms in the phase argument of the exponential function depend on the definition of the positive propagation directions in the experiment under consideration. Note that for strongly nonlinear modes, the series expansion (4.7) may not converge sufficiently fast. Then the number of harmonics required to correctly resemble the mode structure can become larger than the number of harmonics that can be unambiguously identified in experiment.

One can now consider a number of probes at positions  $(\theta_j, \phi_j)$  that yield the data points  $(t_{ij}, y_{ij})$ , where  $i$  is the time index and  $j$  denotes a probe number, respectively. We make no assumptions about the probe spacing or the sample rates of individual probes. It is then possible to use the Lomb periodogram to check for the probability that a certain harmonic with mode numbers  $(m, n)$  at frequency  $\omega$  is present in the measured data. This can be done by replacing all occurrences of  $\omega t_i$  in (4.3, 4.4) by the more complex phase argument

$$p_{ij} = m\theta_j - n\phi_j - \omega t_{ij}. \quad (4.8)$$

We then have

$$P_{3d}(m, n, \omega) = \frac{1}{2\sigma^2} \left\{ \frac{\left[ \sum_{i,j} (y_{ij} - \bar{y}) \cos(p_{ij} - \omega\tau) \right]^2}{\sum_{i,j} \cos^2(p_{ij} - \omega\tau)} + \frac{\left[ \sum_{i,j} (y_{ij} - \bar{y}) \sin(p_{ij} - \omega\tau) \right]^2}{\sum_{i,j} \sin^2(p_{ij} - \omega\tau)} \right\} \quad (4.9)$$

It is important to note that this straightforward extension does not change the statistical properties of the Lomb periodogram. In addition to that, because a single,



spatio-temporal model is fitted to all available data, resulting advantages are effective reduction of noise and maximum confidence in the obtained power spectra.

Experimentally observed eigenmodes are often non-stationary. Effects that are commonly observed include frequency sweeping and bursting modes. Thus it is vital to have a time-resolved analysis method at hand. In order to introduce time resolution to the Lomb periodogram, the same technique known from wavelet analysis is used. A window with a frequency-dependent width is applied to the dataset to reduce the analysis to a narrow time interval only. Time resolution is achieved by moving this window over the dataset. The impact of window functions and data weights on the Lomb periodogram has been discussed by Scargle [69]. The window is a two parameter family of functions  $W_{t_0, \omega}(t)$  with the analysis frequency and time as parameters. The time-resolved Lomb periodogram is given as:

$$P_{4d}(m, n, \omega, t_0) = \frac{1}{2\sigma^2 \cdot \sum_{i,j} W_{\omega, t_0}(t_{ij})} \times \left\{ \frac{\left[ \sum_{i,j} y_{ij}^*(\omega, t_0) \cos(p_{ij} - \omega\tau) \right]^2}{\sum_{i,j} \cos^2(p_{ij} - \omega\tau)} + \frac{\left[ \sum_{i,j} y_{ij}^*(\omega, t_0) \sin(p_{ij} - \omega\tau) \right]^2}{\sum_{i,j} \sin^2(p_{ij} - \omega\tau)} \right\} \quad (4.10)$$

where

$$y_{ij}^*(\omega, t_0) = (y_{ij} - \bar{y}) \cdot W_{\omega, t_0}(t_{ij}).$$

The window function should have the same translation and scaling properties as a mother wavelet. It has to be kept in mind that the window function can influence the spectral properties. Suitable windows are well localized in both, frequency and time domain. Choosing a non-localized window can lead to spectral leakage and thereby the formation of side lobes in the spectrum. Tests with a gaussian and a rectangular window have been performed to study the impact of the window shape. No significant spectral leakage could be observed in tests with the rectangular window and a realistic datapoint distribution. Hence, it seems reasonable to employ the rectangular window in all subsequent analyses.

In order to apply the mode number analysis to W7-AS Mirnov data, it is required that the probe positions are given in magnetic coordinates. The mapping procedure is discussed in section 5.1.3.

#### 4.3.2.2 Sensitivity studies with surrogate data

The extended Lomb periodogram has been subject to extensive tests which address two purposes. On one hand, it has to be made sure that the extended Lomb periodogram

Probe	Pol. mode number range	Tor. mode number range
MIR-1	$m = -7 \dots 7$	-
MIR-35	$m = -4 \dots 4$	$n$ : even/uneven
MIR-1 + MIR-35	$m = -7 \dots 7$	$n = -2 \dots 2$

Table 4.4: Effective Nyquist mode numbers calculated for the W7-AS Mirnov probe setup

gives the expected results. This can be done by studying the response to well known input data. On the other hand, no such relationship like the Nyquist theorem exists between datapoint spacing and mode number resolution of the harmonic analysis. The performance of the periodogram analysis has to be studied numerically for any situation considered. The following tests were performed with artificially generated datasets for the Mirnov probe setup at W7-AS.

**Effective Nyquist mode numbers:** In order to determine the effective Nyquist mode numbers for the Mirnov probe setup at W7-AS, test datasets with a wave having increasing mode number were prepared and analyzed until an alias peak with a smaller mode number was found. At W7-AS, the fast Mirnov probes (arrays MIR-3 and MIR-5, 1 MHz) have been used routinely only in a late stage of the experiment and for a long time, only the poloidal MIR-1 array was available. Therefore, the Nyquist mode number analysis has been done for MIR-1 and MIR-35 separately as well as combined. The test function used was:

$$f_{m,n,\omega}(\theta, \phi, t) = \sin(m\theta - n\phi - \omega t)$$

The effective Nyquist mode numbers that have been found are summarized in Tab. 4.4.

**Resolution of multiple harmonics:** Test datasets containing more than one harmonic have been prepared. Three different situations were studied: Different frequencies and mode numbers, same mode structure but different frequencies, and same frequency but different mode numbers. The test function used was:

$$f(\theta, \phi, t) = f_{m_1, n_1, \omega_1}(\theta, \phi, t) + f_{m_2, n_2, \omega_2}(\theta, \phi, t) + \dots$$

All the test cases could be correctly analyzed with all input harmonics resolved individually. An example is shown in Fig. 4.16. There, five different harmonics have been prepared which are all correctly resolved and separated from each others. This example contains harmonics at the same frequency but with different mode numbers, and such with the same mode numbers but different frequencies.

**Effect of noise:** The effect of noise on the analysis results has been tested with two different noise models. The first model is the well known additive or *amplitude noise*

$$f_{m,n,\omega}(\theta, \phi, t) = R + \sin(m\theta - n\phi - \omega t),$$

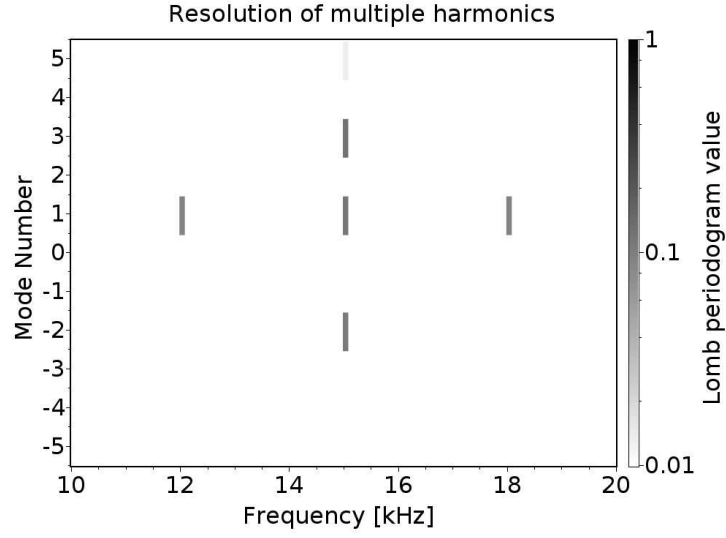


Figure 4.16: Resolution of multiple harmonics within a single signal. Five input harmonics were prepared, slightly asymmetrical in the mode numbers, which are all resolved unambiguously.

the second noise model used is *phase noise*

$$f_{m,n,\omega}(\theta, \phi, t) = \sin(m\theta - n\phi - \omega t + R).$$

The noise term  $R$  represents white noise (gaussian random variate with zero mean and a standard deviation  $\sigma$  that equals the noise amplitude).

In Fig. 4.17 the magnitude of the expected peak in the spectrum is shown as a function of the noise amplitude for both noise models. Higher noise amplitudes result in lower detection amplitudes which is equivalent to an increase of the probability that this peak could be caused by the gaussian noise present in the data. The exponential decay in case of the amplitude noise fits nicely to the statistical model given by Eq. (4.5).

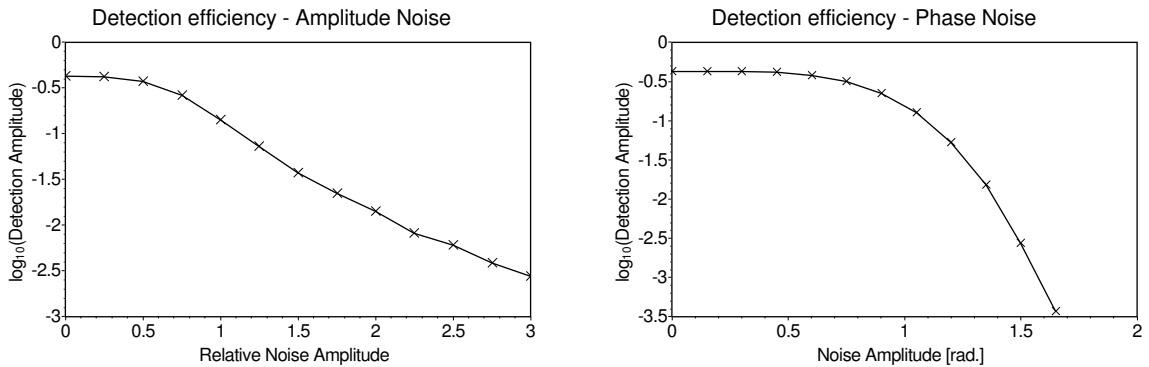


Figure 4.17: Effect of the noise level on the magnitude of an expected peak in the spectrum for both noise models.

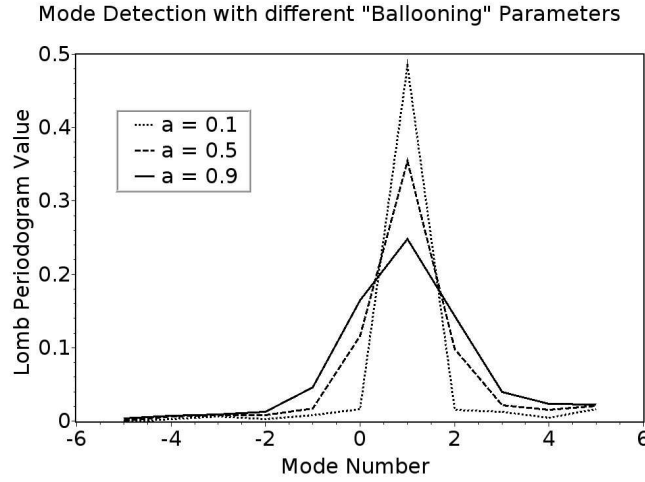


Figure 4.18: Effect of ballooning on the spectrum obtained by the Lomb periodogram.

The deviation from an exponential decay seen in the case of phase noise results from the fact that the noise term enters in a non-linear fashion.

**Effect of ballooning:** Ballooning is an effect that is frequently observed in toroidal fusion devices. It means that the amplitude of a perturbation on the inside of the torus (high field side) is much smaller than on the outside (low field side). To study how ballooning effects the obtained spectrum, the following test function was used:

$$f_{m,n,\omega}(\theta, \phi, t) = 10^{g(\theta)} \cdot \sin(m\theta - n\phi - \omega t)$$

where

$$g(\theta) = \frac{-a \sin^2 \theta / 2}{1 - a \sin^2 \theta / 2}$$

It has been found that the peak amplitude drops slowly due to the ballooning effect (cf. Fig. 4.18) and that with increasing "ballooning parameter"  $a$  the mode number peak is broadened. Still, the broadening is significant only for large values of  $a$ .

#### 4.3.2.3 Tests with experimental data

Having shown that the extended Lomb periodogram works as expected for artificial data, the capability of handling real experimental data still remains to be proved.

In some W7-AS shots, low-frequency MHD activity is observed that strongly affects large parts of the plasma. These pressure driven Eigenmodes induce large amplitude Mirnov signals with almost no noise. Thus they can easily and reliably be analyzed with other techniques. The goal is to determine the mode numbers with alternate methods and to compare the results to the Lomb periodogram.

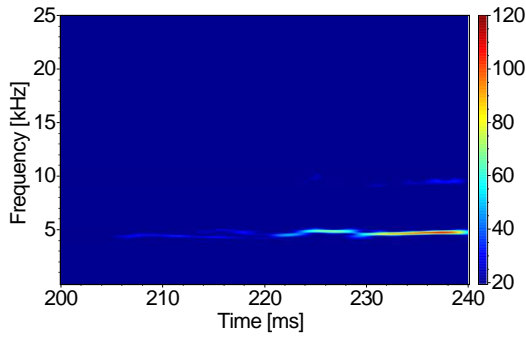


Figure 4.19: Wavelet analysis of W7-AS discharge #56723 at  $t \approx 0.24s$

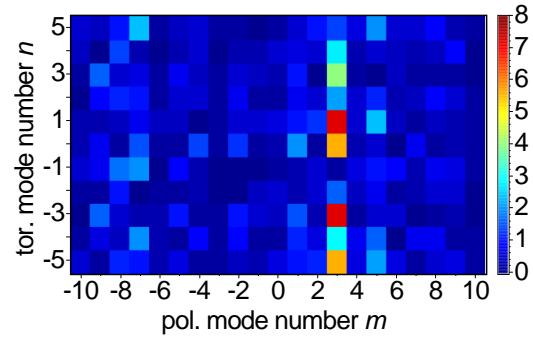


Figure 4.20: Mode number spectrum obtained by Lomb periodogram analysis for #56723,  $t = 0.24 - 0.25$ .

W7-AS discharge #56723 contains strong Mirnov activity at a frequency of about 4.5kHz (see Fig. 4.19). The Lomb periodogram analysis Fig. 4.20 predicts mode numbers  $(m, n) = (3, 1)$  for the observed activity. The equally strong peak observed at  $(m, n) = (3, -3)$  is due to spatial aliasing in  $n$ . Fig. 4.21 shows a part of the corresponding (low-pass filtered) raw data recorded by the MIR-1 array. The space-time diagram displays the time evolution of the amplitude measured by the MIR-1 probes along a poloidal circumference. The average slope of the wavefronts indicates a  $m = 3$  mode structure, explicitly exposed in the polar diagram. The same data inspection yields a toroidal mode number  $n = 1$ . The visible result is further supported by a phase difference analysis. Here, cross correlation functions for adjacent probes have been calculated. Using the known frequency it is possible to translate the time lag at the point of maximum correlation to a phase difference between the probes. The sum of all phase differences along a circumference equals the number of wave periods and the mode was estimated to be  $(m, n) = (3, 1)$  within numerical accuracy.

The origin of the discontinuities of the phase fronts in Fig. 4.21 can be explained by a forward simulation of the expected probe data. A dense set of helical current filaments with the same helicity as the eigenmode to simulate is put on the corresponding flux surface. The current distribution between the filaments is chosen to match a plane wave with the eigenmodes mode numbers  $(m, n)$  in magnetic coordinates, and Biot-Savart's law is used to calculate the perturbed magnetic field where needed. As time progresses, the current distribution is updated to simulate mode propagation and frequency. The magnetic field vector at the probe position is projected onto the probes normal direction of the probe cross-section and the time derivative of the projection gives the simulated probe signal. Fig. 4.22 shows the simulation result for W7-AS discharge #56723. The shape of the wave fronts is fairly well reproduced, including the sudden phase jumps near  $\theta = 2$  and  $\theta = 4$ . These are found to originate from the top and bottom regions of the plasma where the strong curvature deforms the eigenmodes magnetic field. It can also be seen that the poloidal magnetic angle  $\theta$  is compressed on the inside of the torus and expanded on the outside.

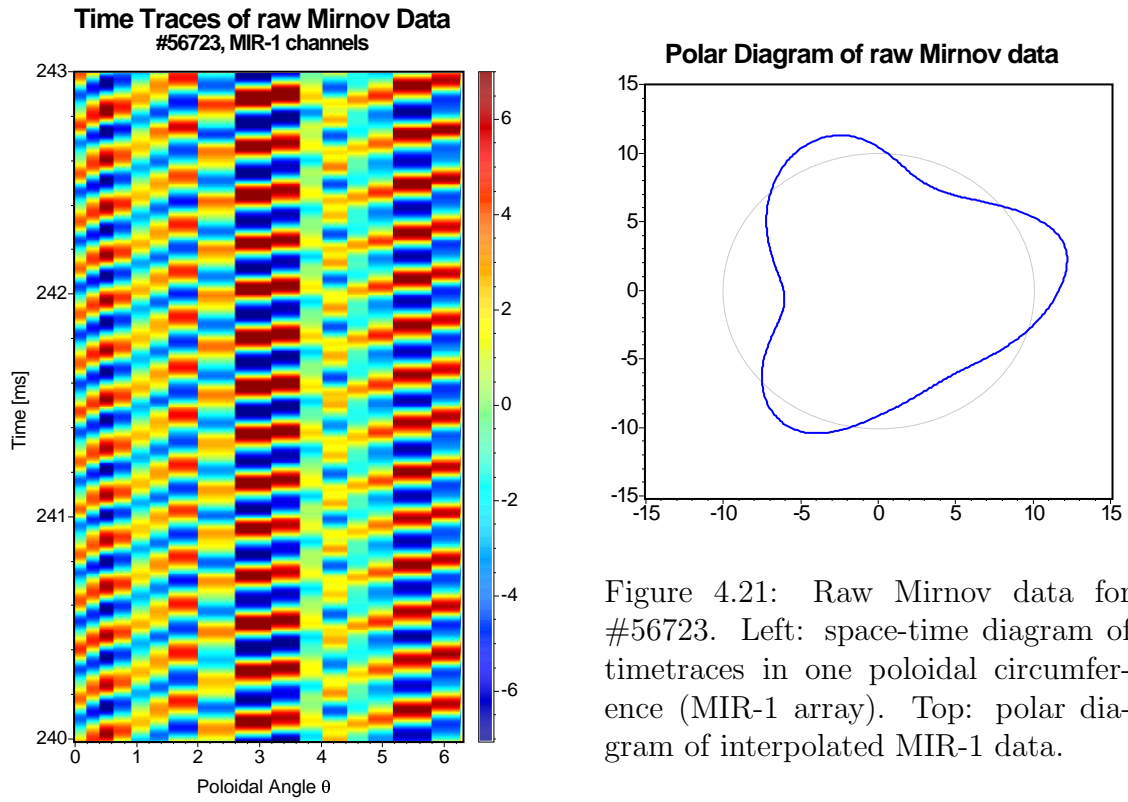


Figure 4.21: Raw Mirnov data for #56723. Left: space-time diagram of timetraces in one poloidal circumference (MIR-1 array). Top: polar diagram of interpolated MIR-1 data.

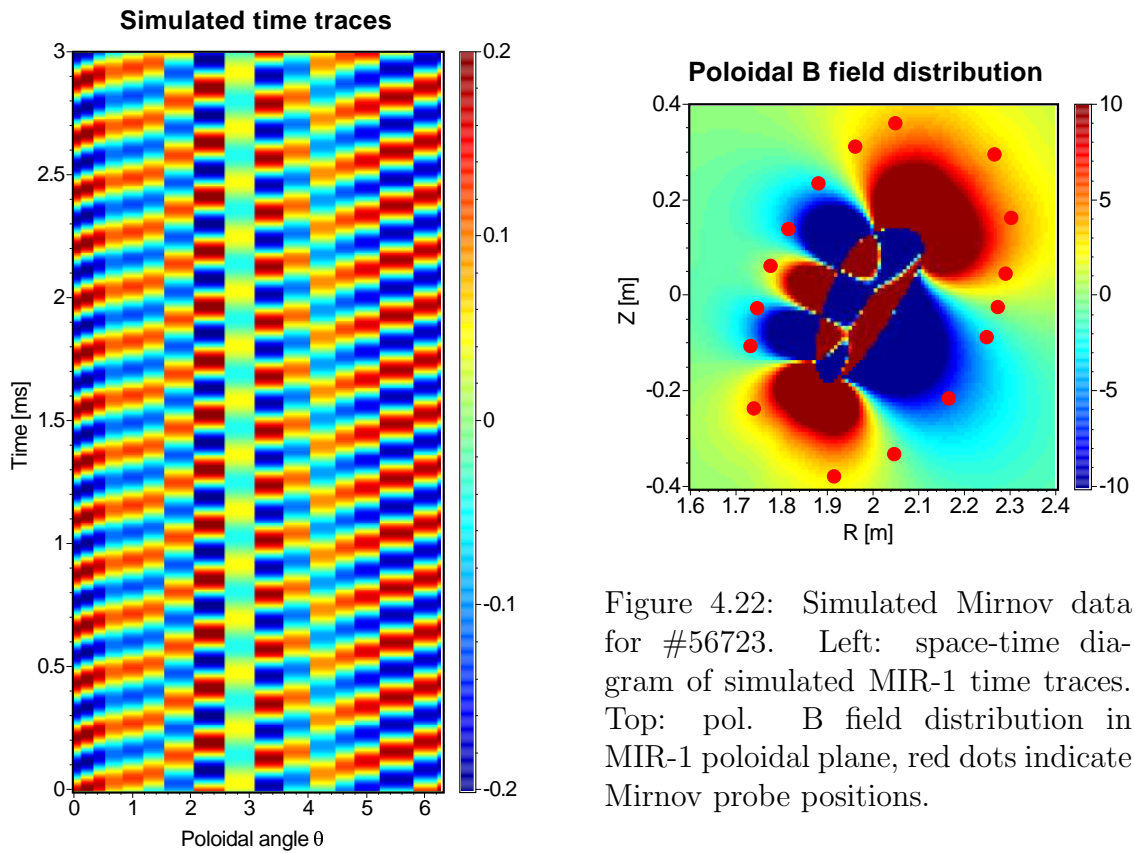


Figure 4.22: Simulated Mirnov data for #56723. Left: space-time diagram of simulated MIR-1 time traces. Top: pol. B field distribution in MIR-1 poloidal plane, red dots indicate Mirnov probe positions.

## 4.4 Numerical codes

### 4.4.1 Equilibrium reconstruction and magnetic coordinate transforms

For reconstructing the plasma equilibrium, the VMEC2000 code (Variational Moments Equilibrium Code) is used [71, 72]. It is a full 3D, free boundary code that solves for a plasma equilibrium by minimizing the MHD energy functional

$$W_p = \int_V \left( \frac{B^2}{2\mu_0} + p \right) dV.$$

The VMEC code requires the vacuum magnetic field, experimentally determined pressure and current profiles, and an initial guess of magnetic axis and the last closed flux surface (LCFS) as input parameters. It starts by building suitable magnetic surfaces in the vacuum magnetic field and in each iteration the geometry of the flux surfaces is varied until the resulting MHD force on the surfaces drops to zero within specified accuracy.

From the resulting plasma equilibrium, VMEC writes the Fourier coefficients of the magnetic flux surfaces and  $\mathbf{B}$  components in VMEC coordinates to an output file along with radial profiles of important plasma parameters like  $\beta$  and  $\iota$ . The resulting equilibrium is not yet suitable in many cases. Manual variation of certain free parameters between different VMEC runs is often required to make the equilibrium consistent with other experimental boundary conditions. This task is solved automatically by the STELLOPT code [73]. It takes the boundary conditions and uses VMEC iteratively in a nonlinear least-squares solver of Levenberg-Marquardt type to adopt the equilibrium to the boundary conditions. In VMEC runs for W7-AS, the usual requirements are that the plasma extends to the limiting structures (divertor) and that kinetic energy of the plasma is consistent with the measured diamagnetic energy. The plasma size can be controlled by changing the toroidal magnetic flux inside the LCFS which is a free parameter to VMEC2000. Furthermore, STELLOPT rescales the pressure profile to vary the plasma energy.

VMEC coordinates are no magnetic coordinates, an additional transformation is required to get these. In all subsequent calculations, Boozer coordinates [28] are used. The transformation is done using two separate tools for different purposes. Most theory codes use output of the "Mapping90" code [74] that provides the Fourier coefficients of flux surfaces, metric coefficients and other quantities in Boozer coordinates. On the other hand, simple transforms between Boozer and real space coordinates can be done with less information. The BOOZ\_XFORM program, that is a part of STELLOPT, provides the Fourier coefficients of flux surfaces and  $|\mathbf{B}|$  much faster.

The coordinate transform between Boozer and real space coordinates is done using the MCONF (Magnetic CONFiguration) package by Turkin [75]. Transforms from Boozer coordinates to real space coordinates are quite fast. The Fourier coefficients of the

real space variables with respect to the Boozer coordinate angles are given. Only the evaluation of a Fourier series for each spatial coordinate is needed. The back transform is not given explicitly and, therefore, more difficult – it is done by solving for those magnetic coordinates that, transformed to real space, match the given ones. This is efficiently implemented in MCONF using Newton’s method.

#### 4.4.2 Alfvén continuum calculation

The code COBRA (COntinuum BRanches of Alfvén waves) [10] is intended for calculations of the Alfvén continuum in tokamaks and stellarators. It solves the following equation of the Alfvén continuum in Boozer coordinates, which is derived from Eq. (3.13)

$$\hat{L} \left( g^{ss} \hat{L} \Phi \right) + \frac{\omega^2}{\omega_{A_0}^2} g^{ss} \tilde{g} \Phi = 0 \quad (4.11)$$

where  $\Phi$  is the wave function,  $\omega$  is the frequency,  $g^{ss} = g^{ss}(s, \theta, \phi) = |\nabla \Psi|^2$  is a component of the contravariant metric tensor in Boozer coordinates  $(s, \theta, \phi)$ ,  $\Psi$  is the toroidal magnetic flux,  $\hat{L} = \frac{\partial}{\partial \phi} + \iota \frac{\partial}{\partial \theta}$  is a differential operator along magnetic field lines,  $\tilde{g} = g(s, \theta, \phi)/g_0$  is the metric tensor determinant,  $g_0 = \langle \sqrt{g(s=0)} \rangle^2$ ,  $\langle \dots \rangle = \oint d\phi(\dots)/2\pi$ ,  $\omega_{A_0}$  is the characteristic Alfvén frequency at the magnetic axis. This equation describes a local Alfvén resonance on an isolated flux surface. It only includes differentiation within the flux surface with the radial coordinate  $s$  as parameter. As  $s$  is varied, the Alfvén continuum branches appear.

The code uses Fourier expansion of the problem. Rewriting (4.11) with Fourier coefficients for  $\Phi$ ,  $g^{ss}$ ,  $\tilde{g}g^{ss}$  and truncating the Fourier expansion yields a finite-dimensional generalized eigenvalue problem that is solved by the code. A significant amount of the work done by the code deals with minimization of the truncation effects on the obtained solution.

The code has three modes of operation. The first mode is a simple continuum scan in the  $(r, \omega)$  plane by solving the eigenvalue problem at several radial positions for many different values of the wave vector  $\tilde{k}$  in a certain interval  $\tilde{k}_1 \leq \tilde{k} \leq \tilde{k}_2$ . Thus the user obtains a general picture of the Alfvén continuum with all important gaps and continuum regions at once. The second mode calculates the boundaries of a continuum gap determined by the user by specifying the coupling numbers. This mode is important because it easily enables the user to identify the origin of gaps. The third mode of operation calculates the frequency  $\omega(s)$  for a continuum branch characterized by the mode numbers  $(m, n)$ .

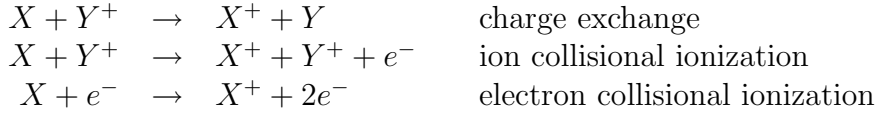
#### 4.4.3 Calculation of the fast ion distribution function

Fast ions can provide a drive for Alfvén eigenmodes. In W7-AS, fast ions are produced by the heating systems of which NBI is capable of creating non-Maxwellian fast ion



populations. To recover the fast ion distribution as best as possible, two steps are necessary – the first step is the determination of the "birth profile", in a second step the "slowing down" distribution is calculated.

As the energetic neutral particles traverse the plasma, a certain fraction of them is ionized. The most important reactions are ( $X$  and  $Y$  denote atomic species):



The NEUTRALBEAM code by Werner [76] uses Monte-Carlo techniques to simulate the ionization of test particles. The ionization reactions are modelled with measured plasma profiles and realistic atomic cross section data. It is assumed that plasma temperature and density are constant on flux surfaces and that the bulk plasma species have Maxwellian distribution functions. The code is capable of handling realistic particle source and vessel geometries. It was extended to also include equilibrium magnetic fields. As a result one obtains radially resolved power deposition and birth profiles. The birth profiles are further resolved by the ions orientation to the magnetic field, i.e. the pitch  $\chi$ . Typically,  $10^5 \dots 10^6$  injected particles are needed for smooth profiles.

In order to get the fast ion distribution function, the thermalization process of the newly born fast ions (slowing down) needs to be modelled. The routine DFNBI by Maßberg [77] is used for this purpose. It calculates the full (thermal + fast) ion distribution function, both the particle and energy balance are taken into account. More than one background ion component may be specified. Charge exchange losses are calculated in the presence of a neutral gas density. The code assumes an isotropic background plasma and hence cannot be used to model a global slowing down distribution function. It is, however, a suitable approximation to the slowing down on an isolated flux surface. The routine will be used to calculate a local slowing down distribution on each flux surface using the radially resolved birth profiles obtained from Monte-Carlo ionization.

The isotropic part of the distribution is calculated using the linearized Fokker-Planck equation (FPE) with NBI source, charge exchange and thermal loss term. The particle balance is satisfied iteratively in the first inhomogeneous solution of the FPE. Then the power transfer to the background plasma components is estimated in the second inhomogeneous solution to satisfy the energy balance. Finally, a homogeneous solution is added to give the specified beam particle density. The anisotropic contribution is estimated using Maxwellians for Rosenbluth's potentials. Legendre polynomial expansion is used for the distribution function, the corresponding differential equations in velocity are solved independently. The velocity grid has the highest resolution for very small velocities as well as close to the three injection energies.

The result of this calculation is a stationary distribution function  $f(s, v, \chi)$  for all, thermal and fast ions, that is isotropic in space on any given flux surface but anisotropic in velocity. Once the full ion distribution function is calculated, the usual statistical tools (moments of the distribution function) can be used to extract macroscopic quantities

like temperature, density, pressure, current, ... The loss terms have the side-effect of modifying the thermal background distribution, making it slightly non-Maxwellian. Consequently, no clear separation between thermal and fast ion distribution functions is possible. If a Maxwellian thermal background is subtracted from the full ion distribution function, the resulting fast ion distribution function is not positive-semidefinite anymore. In order to proceed it is, nevertheless, assumed that the thermal ion distribution is Maxwellian and statistical fast-ion quantities determined by velocity moments  $M(n, f) = \int \mathbf{v}^n f(\mathbf{v}) d^3v$  of the distribution function are assumed in the form:

$$M(n, f_{\text{fast}}) = M(n, f_{\text{full}}) - M(n, f_{\text{th}}) = M(n, f_{\text{full}} - f_{\text{th}}),$$

where  $f_{\text{th}}$  is a Maxwellian distribution function for temperature  $T$  and density  $n$  of the thermal bulk ions.

#### 4.4.4 Growth rate calculation

To get an estimate of the linear growth rate of a gap mode, the local perturbative model, Eq. (3.22), has been implemented in the LGRO code (Local GROWth) by Könies [40]. The code considers only two coupled harmonics, the radial location of the eigenmode as well as the frequency are taken as given by Eq. (3.14). For convenience, the Fourier harmonics of the periodic drift velocity,  $u_{ps}$ , are expressed as functions of the magnetic field strength,  $B_{\mu\nu}$ . Experience shows that only the largest  $B_{\mu\nu}$  coefficients need to be considered to obtain the most unstable eigenmodes. The inclusion of more coefficients leads to additional resonances between wave and particles with the side effect of destabilizing an increasing number of eigenmodes.

The code carries out the velocity integral for electrons, thermal ions and fast ions separately to highlight the contributions of each particle species. It is noted again that the local model was derived assuming well-circulating particles only and that trapped particle effects are neglected. Thermal electrons and ions are taken to be analytical Maxwellian distributions with densities and temperatures given by the equilibrium reconstruction. The fast particle contribution is calculated using the NBI slowing down distribution, where a Maxwellian thermal ion distribution is subtracted. Bicubic splines are used to represent the numerical data and obtain smooth derivatives inside the flux surface, whereas linear interpolation in the radial coordinate is found to be sufficient.

In addition, a code named CAS3D-K solving the global, kinetic MHD approach, Eqs. (3.28, 3.29), exists [40]. Besides the distribution functions of electrons, thermal and fast ions, it requires knowledge of the radial eigenfunctions of all coupled harmonics that form the eigenmode. These can be calculated with codes like CAS3D3 [78, 79] or BOA [10]. At the time of writing, CAS3D-K does not yet take advantage of the anisotropic distribution functions obtained from slowing-down modelling. However, previous results assuming an isotropic distribution of fast particles indicate that both models give qualitatively similar results for W7-AS [80]. The magnitudes of linear growth and damping rates obtained from LGRO are very approximate due to the

---

various approximations in the theoretical model and show large differences compared to CAS3D-K results, but the relative magnitudes of the various contributions are fairly well reproduced.



# Chapter 5

## Experimental Results

### 5.1 Data Analysis

The identification of Alfvén eigenmodes in stellarators is a complex issue and requires the incorporation of data from different diagnostics as well as the employment of different numerical codes. The main topics of this thesis can be cast in three questions: (I) Which modes are observed? (II) Is their instability predicted by current 3D models of wave-particle interaction? (III) Is confinement degradation observed? The scheme that was applied for data analysis and mode identification to answer these questions is shown in Fig. 5.1. Once the MHD equilibrium is reconstructed from discharge parameters and measured data, the calculation of the Alfvén continuum is straightforward. It is needed for the identification of experimentally observed AE instabilities and involves comparing predicted gap modes to observed mode numbers and frequencies. The next step is to model the fast ion distribution function as a pre-requisite for the calculation of the theoretically predicted growth rate of the instability. The second goal of this thesis is to study of AE-induced energetic particle losses. The time traces of EFIP photomultipliers are compared to the evolution of the wave amplitude for this purpose.

The reconstruction of the MHD equilibrium is an essential step in the analysis and all subsequent steps depend on it. This has several reasons:

- The equilibrium describes the magnetic topology and thus determines the magnetic flux coordinates.
- The radial profiles of important plasma parameters, e.g.  $\beta(r), t(r)$ , are determined by the MHD equilibrium. The structure of the Alfvén continuum, from which the mode numbers and frequencies of expected Alfvén eigenmodes are derived, depends sensitively on the shape of these profiles.
- The MHD equilibrium describes the variation of the magnetic field strength on flux surfaces that affects the structure of the Alfvén continuum and the expected resonances between waves and particles.

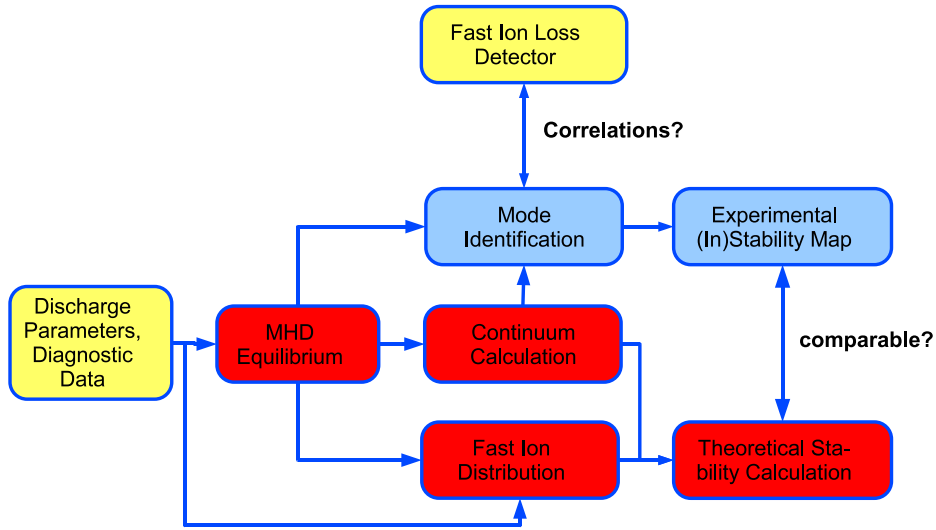


Figure 5.1: Data analysis scheme used for mode identification and stability prediction. Yellow indicates measured data stored in databases and shotfiles, red indicates that the use of numerical codes is involved.

- Information about the magnetic field direction, the shape of flux surfaces as well as radial density and temperature profiles of the bulk plasma are required to model the radially resolved, anisotropic velocity distribution function of the energetic particle population.

Due to the importance of the MHD equilibrium, special care is needed in this step. It is a consequence of the success of W7-AS operation that regimes of plasma parameters were achieved that have not been thought of in its design phase. This is especially true for the experiments close to the beta limit in the late phase of the experiments, from which all of the considered discharges are taken. In these regimes, the diagnostics are operating at their very limits and suffer from large uncertainties [81], making a careful data validation necessary.

In the remainder of this section, the data analysis procedure is explained in more detail using W7-AS discharge #54154 as example. This shot is from the high- $\beta$  program at half the possible magnetic field strength  $B = -1.25$  T and is one of the few studied discharges with uncompensated plasma current. It has been chosen because it gives insight into typical problems that appear. Some Mirnov activity occurs during the startup phase, but no Mirnov data besides the monitor signal is available in the time range  $t = 100 \dots 150$  ms where the activity is strongest and correlated with changes in the NBI power. Another mode is present at  $t \approx 200$  ms. Fig. 5.2 shows the time traces of the most important plasma parameters, while in Fig. 5.3 the frequency spectrum in the time window where the activity occurs is seen.

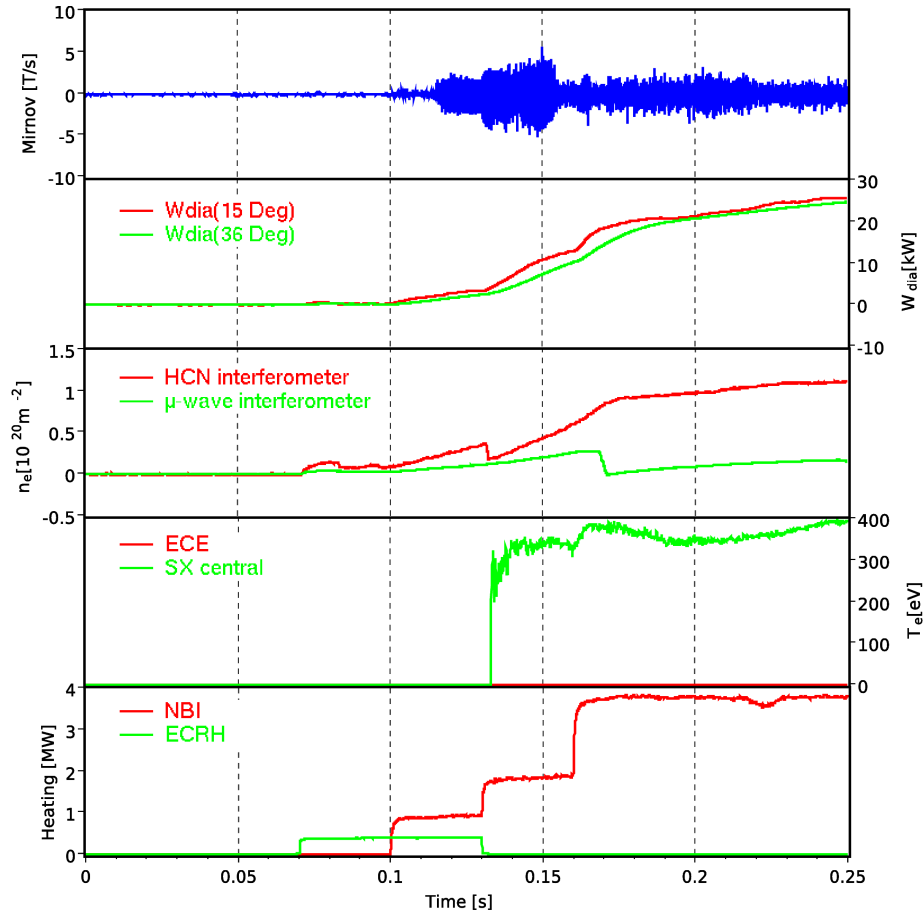


Figure 5.2: Time traces of Mirnov amplitude, plasma energy, line-integrated density, electron temperature, and heating power for W7-AS shot #54154.

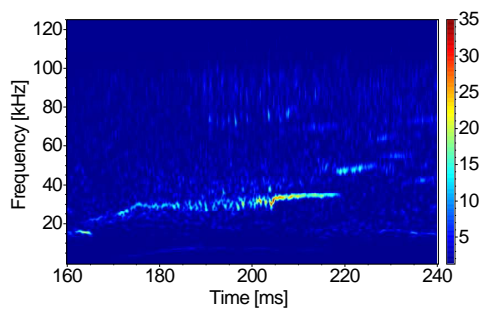


Figure 5.3: Wavelet transform of the Mirnov monitor signal for W7-AS shot #54154.

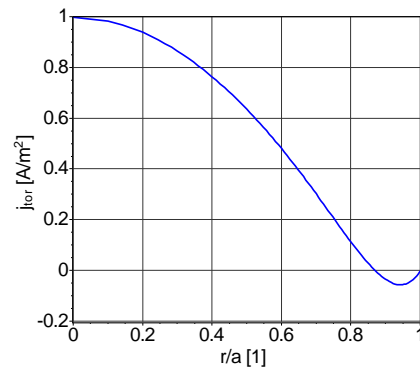


Figure 5.4: Default current density profile used for the equilibrium reconstruction.

### 5.1.1 Data Availability

The presence of Mirnov data from different poloidal and toroidal positions is required for a successful analysis of poloidal and toroidal mode numbers. Due to the resonances in the MIR-1 probes, they can only be used for frequencies below  $\approx 70$  kHz. The activity observed in shot #54154 is near 40 kHz, so it is possible to include MIR-1 data in the mode number analysis which is available from  $t = 0.20 \dots 0.53$  s. The other poloidal probe arrays, MIR-3 and MIR-5, have continuously sampled data in the time range  $t = 0.21 \dots 0.27$  s. Data loss in MIR-3 time traces due to the 900 MHz startup heating is not observed. The available Mirnov data allows a mode number analysis only for the tail of the mode in the time range  $t = 0.21 \dots 0.22$  s.

Besides the Mirnov data, the plasma parameters are of major importance for the equilibrium reconstruction. The shape of the density and temperature profiles is determined from the Nd:YAG Thomson scattering diagnostic that delivers the profiles with a repetition rate of 50 ms. The nearest time points for shot #54154 are  $t_1 = 0.18$  s and  $t_2 = 0.23$  s. The raw profiles for both time instants are shown in Fig. 5.5. Usually, the density and temperature profiles are interpolated in time to be able to reconstruct the equilibrium at a time where the Mirnov indicates the presence of an eigenmode is present. The density profile at  $t = 0.18$  s erroneously vanishes at  $z = -22$  cm and has an invalid value at  $z = 26$  cm, such that after dropping these values, no information about the density and, consequently, the pressure near the plasma edge remains. Therefore, only the profile at  $t = 0.23$  s can be used in the equilibrium reconstruction.

Due to the calibration error in the YAG Thomson system [55], a manual validation of the profiles is required. On W7-AS, several optical and microwave interferometers were installed, all with different lines of sight. Depending on the chord length inside the plasma and the plasma density, the interferometers suffer from fringe jumps and cut-offs and cannot be used reliably for the density calibration, as seen in Fig. 5.2. The innermost channel of the soft X-ray diagnostic provides a reliable estimate of the central electron temperature  $T_e^{SX}$  that can be used to calibrate YAG Thomson temperature profile. The density calibration is done afterwards, using the diamagnetic energy  $W_{dia}(\phi = 36^\circ)$  as reference for the kinetic energy stored in the plasma. Both diagnostics,  $T_e^{SX}$  and  $W_{dia}^{36}$  were available at the required time.

None of the diagnostics at W7-AS is capable of providing the radial profile of the toroidal plasma current density, only the net toroidal current can be measured. For shot #54154 at  $t = 0.23$  s the toroidal net current is approximately 7 kA. In principle, it is possible to obtain the current density profile by a careful transport analysis, but this is very sensitive to the input parameters, i.e. density and temperature profiles, power deposition profiles, and impurity concentrations. Because these suffer from large error bars in most discharges, a reconstruction has been attempted in the past only for selected W7-AS discharges. Taking these difficulties into account, it was decided to use a default current density profile (Fig. 5.4) for the equilibrium reconstructions. The default current density profile is plausible and is finally justified by the consistency of the analysis. But clearly such a choice means a significant hypothesis.



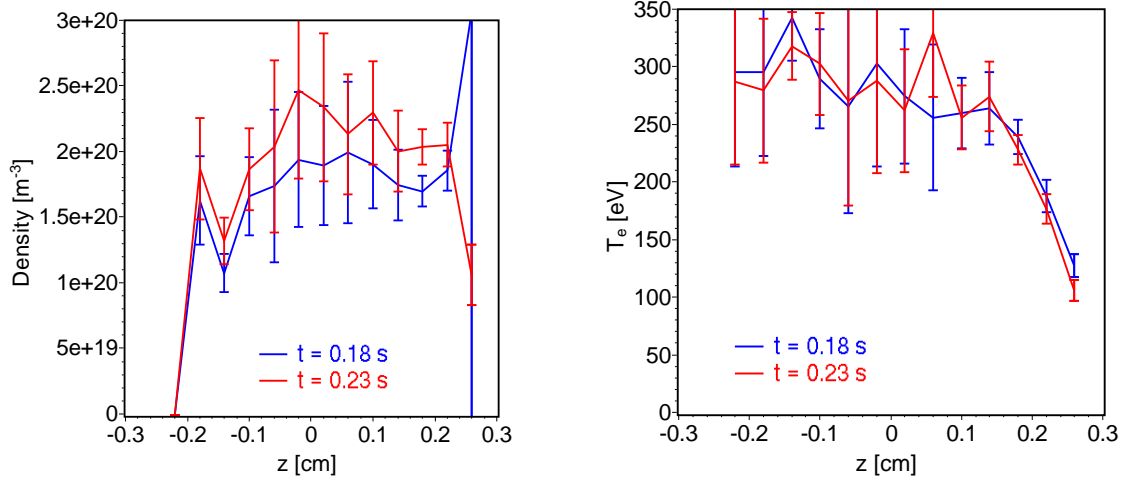


Figure 5.5: Density and temperature profiles obtained by Nd:YAG Thomson scattering for shot #54154 where  $z$  is the vertical coordinate in the cylindrical  $(R, \phi, z)$  coordinate system,  $z = 0$  corresponds to the horizontal midplane of W7-AS.

### 5.1.2 Equilibrium reconstruction

The MHD equilibrium reconstruction requires, as described in section 2.3.1, the prescription of the spatial distribution of plasma current and plasma pressure as a function of the flux label. Since the mapping between cylindrical coordinates  $(R, \phi, z)$ , which are independent of the plasma, and magnetic coordinates  $(s, \theta, \phi)$  is not known in advance, an iterative procedure needs to be applied.

Attempts to use the measured density and temperature profile directly results in unreasonable equilibria. The reason for this is that VMECs internal representation of the pressure profile as a polynomial  $p(s) = \sum_{n=0}^{10} a_n s^n$  has approximately the same number of free parameters as there are points in the measured profile. As a result, this representation of the profile will follow the measured points exactly and, despite the large error bars, no smoothing takes place. This problem can be circumvented by representing the data with a parametric model of the profile with less free parameters, where the analytical form of the model constrains the possible profile shapes. The following model has been used in most of the W7-AS analyses:

$$f(s) = \frac{a_0(1 - \beta s)}{1 + (s/s_0)^\alpha}, \quad (5.1)$$

where  $a_0$  is the central value,  $s_0$  determines the gradient region,  $\alpha$  the steepness of the gradient, and  $\beta$  the hollowness ( $\beta < 0$ : hollow profiles,  $\beta > 0$ : peaked profiles). After mapping the profile points to magnetic coordinates, the parameters  $a_0$ ,  $s_0$ ,  $\alpha$  and  $\beta$  are determined for density and temperature separately by a least-squares fit to the data, using the errorbars as weights. The pressure profile is then calculated using the ideal gas law:  $p = 2n_e k_B T_e$ , where  $n_e = n_i$  ( $Z_{eff} = 1$ ) and  $T_e = T_i$  has been assumed.

Ref. [81] describes a way to perform an integrated data analysis (IDA) that includes

data from different diagnostics using the Bayesian probability theory (BPT) to improve the accuracy of the Nd:YAG Thomson scattering profiles at W7-AS. While it is favourable to use IDA based on BPT, it is a lengthy calculation and the correct assessment of random and systematic errors of diagnostics at W7-AS is a complicated task for which no appropriate solution exists. To be able to proceed with the data analysis, a simplified validation procedure is used: It is assumed that the shape of density and temperature profiles are well reproduced. After outliers have been filtered out and the profiles are mapped to magnetic coordinates, spatial smoothing is achieved by fitting the profiles to the model function. Validation is then achieved by rescaling the profiles to make them consistent with other diagnostics. At first, the electron temperature profile is rescaled by a factor  $\alpha_t$  to reproduce the central electron temperature obtained from SX diagnostic. The next step is to calculate the pressure profile and, from that, the kinetic energy content of the plasma by integration over the plasma volume:

$$W_{kin} = \int p dV = \int_0^1 p \cdot \frac{dV}{ds} ds. \quad (5.2)$$

Comparing this to the measured diamagnetic energy gives the factor  $\alpha_n$  by which the density profile has to be rescaled. This has been embedded into the automated equilibrium reconstruction process. Looking at the posterior PDFs for the Nd:YAG Thomson scattering system in Ref. [81], it is observed that electron density and temperature given by this diagnostic are anti-correlated, while the plasma pressure should be well reproduced. One can therefore expect that the density and temperature corrections behave as  $\alpha_t \approx \alpha_n^{-1}$ . This was not observed for all discharges. Cases with both,  $\alpha_n > 1$  and  $\alpha_t > 1$ , or with corrections  $\alpha > 1.5$  were resolved manually.

The iterative procedure applied throughout this thesis to the equilibrium reconstruction is as follows:

1. The equilibrium reconstruction is performed for a pressure profile  $p(s) = p_0 - p_0 \cdot s$  that is linear in  $s$  and parabolic in  $r$ , with the constraints that the kinetic plasma energy matches the measured diamagnetic energy and that the plasma extends to the limiting structures (divertor or baffles). The equilibrium obtained this way should have the same size and shape of the last closed flux surface as the final result. The Shafranov shift is expected to be comparable; only the shape and relative position of the inner flux surface is expected to vary noticeably.
2. The equilibrium obtained in the last step is used to map the density and temperature profile points to magnetic coordinates. Afterwards they are fitted to the profile model and calibrated as described above. Then, the pressure profile is calculated from density and pressure profiles and the equilibrium reconstruction is repeated with the obtained pressure profile and the same constraints as before, keeping the plasma energy and the plasma size constant.

The second step can be repeated until profile mapping and equilibrium are converged. Further iterations turn out to not lead to additional accuracy because the uncertainties

in the pressure profile exceed the uncertainties in the mapping. Fig. 5.6 displays the reconstructed plasma parameter profiles and the shape of flux surfaces for the ideal MHD equilibrium for shot #54154.

### 5.1.3 Mode Number Analysis

The choice of coordinates in the mode number analysis naturally affects the obtained mode numbers  $(m, n)$  via the definition of the angle coordinates  $(\theta, \phi)$ . All calculations, to which the results are compared, are done in Boozer coordinates, hence the same coordinates have to be used in the mode number analysis. This requires to express the probe coordinates in Boozer coordinates. The mapping is not trivial because Boozer coordinates are not defined outside the last closed magnetic surface (LCMS). In order to derive a suitable mapping procedure, it should be noticed that only those eigenmodes which are localized near the plasma boundary can be observed by the Mirnov diagnostic. Core localized modes with vanishing displacement near the plasma boundary cannot cause magnetic perturbations visible from the outside of the plasma, thus allowing to restrict the mapping to the outer flux surfaces. In addition, the Mirnov probes do not allow to determine the radial eigenfunctions, not even the localization region of the mode due to the reason explained above. It is therefore necessary to *assume* the radial localization of the eigenmode. The mapping of Mirnov probe positions to magnetic coordinates is equivalent to determining the magnetic coordinates of the volume element inside the plasma from which the Mirnov probes observe the fluctuations. Two different mapping procedures have been tested.

- Using the approximation that the observation volume of a probe is a narrow cone directly in front of it and choosing a fixed flux surface  $s = s_0$  near the plasma boundary, the mapping reduces to finding the point  $\mathbf{R}(s_0, \theta_p, \phi_p)$  on the surface that is closest to the probe position  $\mathbf{R}_p$ , where  $\mathbf{R}$  is the position vector:

$$(s_0, \theta_p, \phi_p) : \quad \min |\mathbf{R}(s_0, \theta, \phi) - \mathbf{R}_p|. \quad (5.3)$$

- Secondly, forward modelling of the eigenmode using helical current filaments on the surface  $s_0$  and the law of Biot-Savart to calculate the perturbed field at the probe position has been implemented. The current filaments for a  $(m, n)$  eigenmode follow the path  $\theta = \theta_0 + \phi \cdot (n/m)$  in magnetic coordinates, where  $\theta_0$  is the poloidal start angle at  $\phi = 0$ . Using the approximation that the cylindrical toroidal angle  $\phi_c$  almost coincides with Boozers toroidal angle, the equivalent probe position in magnetic coordinates given by this "impulse response" mapping is  $\theta_p = \theta_0^{(max)} + \phi_c \cdot (n/m)$ , where  $\theta_0^{(max)}$  is the poloidal start angle of the current filament that gives the largest contribution to the simulated probe signal.

Both mapping procedures give comparable results, a weak dependency of the mapped coordinates on the mode numbers is observed using the second procedure. In Fig. 5.7

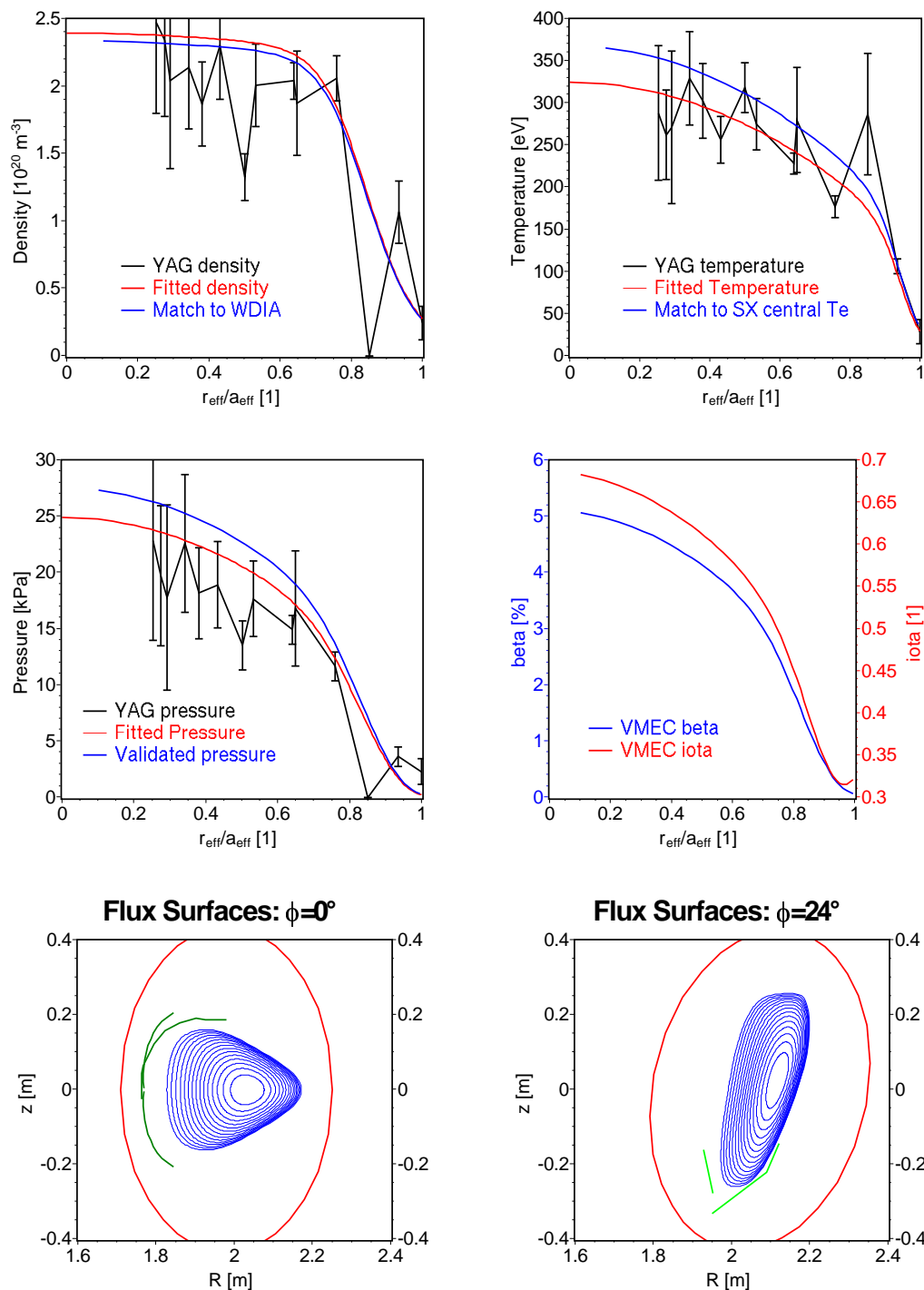


Figure 5.6: Equilibrium data for shot #54154: density, temperature and pressure profiles (black: measured data, red: fit to profile shape, blue: rescaled profiles) used as input as well as the resulting  $\beta$  and  $\iota$  profiles. Additionally, flux surfaces in two cross sections ( $\phi = 0^\circ$  and  $\phi = 24^\circ$ ) are shown along with the vessel outline and plasma facing in-vessel components.

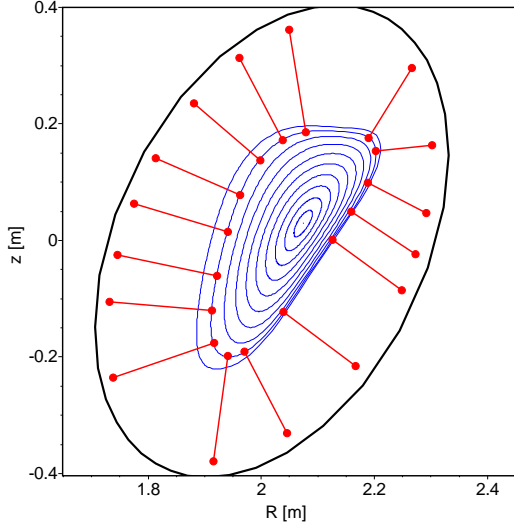


Figure 5.7: Mapping of probe coordinates to magnetic coordinates for W7-AS shot # 54154.

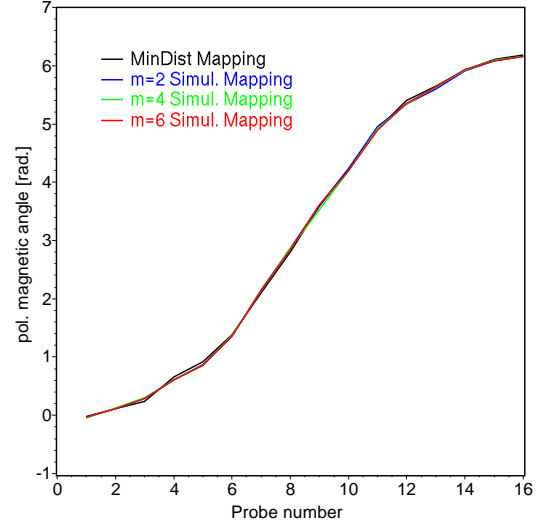


Figure 5.8: Comparison of minimum distance mapping and impulse response mapping for different  $m$ ,  $n = 2$  is used in all cases.

the result of the mapping is shown, while Fig. 5.8 depicts a comparison between both mapping procedures.

After having mapped the probe coordinates, the mode number analysis is straightforward using the extended Lomb periodogram (section 4.3.2) to scan a suitable parameter space in  $f, m, n$  and  $t$ . The result of this scan for shot #54154 is given in Fig. 5.9. The mode number spectrum shows a response at  $m = 0$  and  $m \approx 6/7$  for various  $n$ . The  $m = 0$  contribution can probably be attributed to a beginning far-field effect, a phenomenon that can be explained as follows: Assuming a multipole structure of the perturbed poloidal magnetic field that decays as  $\tilde{B}_{pol}(r) \sim \tilde{B}_{pol}(r_0) \cdot |r - r_0|^{-(m+1)}$ , the fine structure of the perturbed field in poloidal direction vanishes some distance away from  $r_0$ , especially for high  $m$ . The resulting "far field" has approximately the same phase everywhere along a poloidal circumference.

The other contributions in the mode number spectrum at  $m \approx 6/7$  suffer from spatial aliasing in  $n$  due to the low number of different probe positions in toroidal direction. To find the correct value of  $n$ , one can consider the shear Alfvén wave dispersion relation  $\omega_A^2 = k_{\parallel}^2 v_A^2 = (m\epsilon - n)^2 v_A^2 / R_0^2$ . A necessary condition to obtain low-frequency waves is that  $|k_{\parallel}| = \omega_A^2 / v_A^2 \ll 1$ , corresponding to  $(m\epsilon - n) \approx 0$ . Near the plasma boundary,  $\epsilon$  is approximately  $1/3$  as seen from Fig. 5.6, resulting in the inter-relationship  $n/m \approx 1/3$  and allowing to exclude cases with  $\text{sgn}(m) \neq \text{sgn}(n)$  from shear Alfvén eigenmode considerations. The only peak in the mode number spectrum that fulfills the necessary condition to be shear Alfvén is  $m \approx 6/7, n = 2$ .

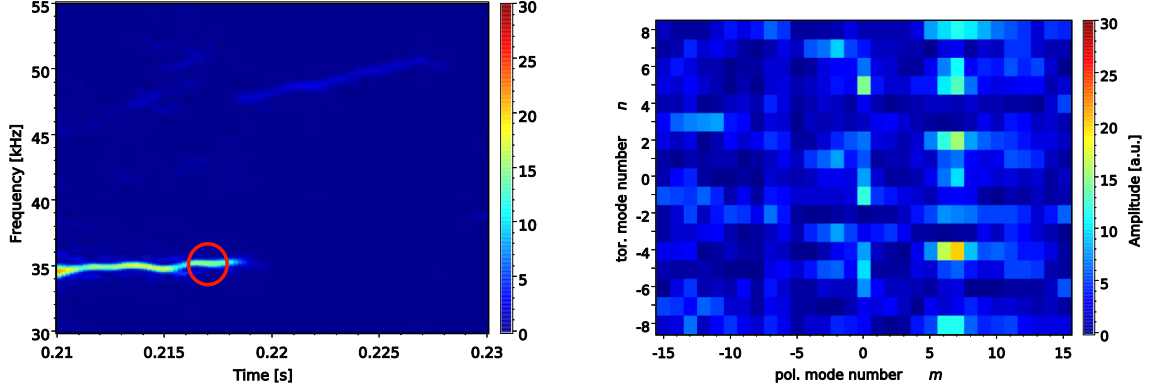


Figure 5.9: Results of the mode number scan for shot #54154,  $t = 0.21 \dots 0.23$ s. The left panel displays the time-resolved frequency spectrum for mode numbers  $(m, n) = (6, 2)$ , while in the right panel the complete mode number spectrum is given at the point indicated by the center of the red circle in the left panel.

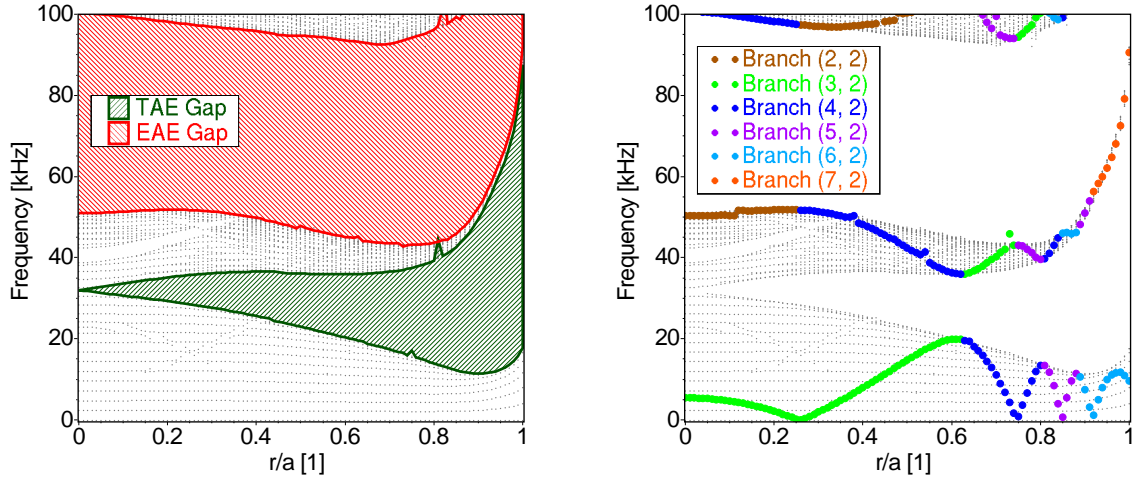


Figure 5.10: Shear Alfvén continuum calculated for W7-AS shot #54154,  $t = 0.23$ s. The left panel shows the continuum where individual continuum gaps have been coloured for identification. The right panel shows the same continuum and, additionally, the dispersion relations for selected continuum branches.

### 5.1.4 Eigenmode Identification

The next step on the way to identify an observed Mirnov activity as shear Alfvén eigenmode is to compare determined mode numbers and frequencies to the Alfvén continuum. It is calculated using the COBRA code (section 4.4.2) and requires the reconstructed density profile, the ideal MHD equilibrium as well as the set of Boozer coordinates for that equilibrium as input. The continuum is shown in Fig. 5.10, it can be seen in the left panel that the TAE gap extends over the whole plasma radius at  $f \approx 35$  kHz, the frequency of the eigenmode. The gap does not close near the plasma boundary, it is expected that the eigenmode will not suffer from continuum damping.

In the right panel of Fig. 5.10 the same continuum is shown in conjunction with a selection of relevant continuum branches. Different colours indicate the dominant poloidal harmonic of the coupled branches, i.e. to which cylindrical continuum branch a point would belong in the limit of vanishing coupling coefficients  $\epsilon^{(\mu\nu)}$ . The figure indicates that for a TAE with  $n = 2$  the following couplings could contribute to observed harmonics:  $m = 3, 4$ ,  $m = 4, 5$ , and  $m = 5, 6$ . A coupling between  $m = 6$  and  $m = 7$  is not expected from the shear Alfvén continuum. In Fig. 5.9, only a weak  $m = 5, n = 2$  harmonic is found, the strongest contributions are  $m = 6$  and  $m = 7$ . The weakness of the  $m = 5$  harmonics could result from a localization closer to the plasma core, in that case the radial eigenfunction could have diminished near the plasma boundary and is difficult to detect due to the low amplitude (the maximum of the radial eigenfunction of a harmonic does not necessarily coincide with the radial location of the branch crossing point in the Alfvén continuum). It must be noted that the equilibrium is calculated at  $t = 0.23$ s while the eigenmode terminates at  $t = 0.22$ s. In between the plasma profiles vary slightly (c.f. Fig. 5.2), so neither the mode number analysis nor the continuum calculation that are based on the equilibrium reconstruction are sufficiently precise to definitely exclude  $m = 5$  or  $m = 7$  as possible eigenmode harmonics. The required value of  $t$  for a  $m = 6, 7$  coupling inside the plasma can be estimated using Eq. (3.14) and the result is  $t_* = 0.308$ . The minimum  $t$  in Fig. 5.6 is  $t_{min} = 0.316$ , the difference of  $\delta t = 0.008$  is small compared to the uncertainties introduced by the unknown current density profile and the pressure profile and considering the large shear in this discharge.

Finally it can be concluded that the observed activity can be identified as TAE with  $n = 2$  and  $m = 5, 6, 7$  harmonics which is consistent with shear Alfvén continuum calculations.

### 5.1.5 Ion Distribution Function

The ion distribution function is an important ingredient in the calculation of the growth and damping rates of AEs and allows to extract statistical quantities describing the particle number densities and energy of fast ions. The tools for calculating the ion distribution function in the presence of a Maxwellian bulk plasma and NBI heating are described in Sec. 4.4.3.

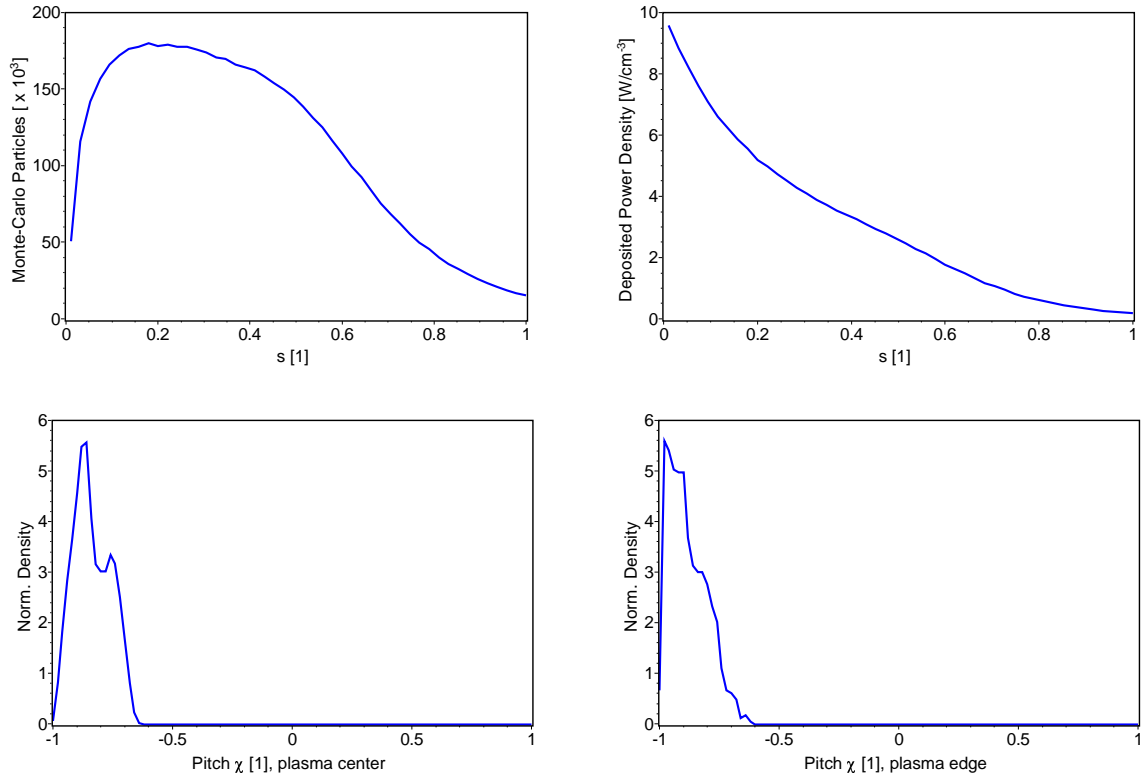


Figure 5.11: Birth profiles for W7-AS shot #54154,  $t = 0.23\text{s}$ , 3.4 MW NBI power. Radial profiles of deposited Monte-Carlo particle numbers and power density (top), and typical pitch profiles in the plasma core and at the plasma edge (bottom). The pitch profiles are normalized so that the integral  $\int_{-1}^1 f(\chi) d\chi \equiv 1$ .

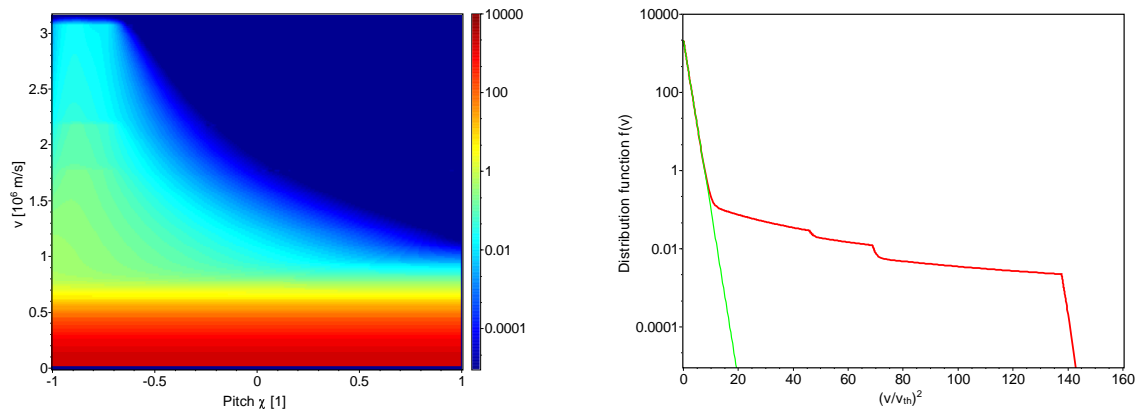


Figure 5.12: Full ion velocity distribution function for W7-AS shot #54154,  $t = 0.23\text{s}$ , 3.4 MW NBI power on a flux surface near the plasma core. Left graph:  $f(s_0, v, \chi)$ , right graph: pitch averaged distribution  $f(s_0, v)$ .



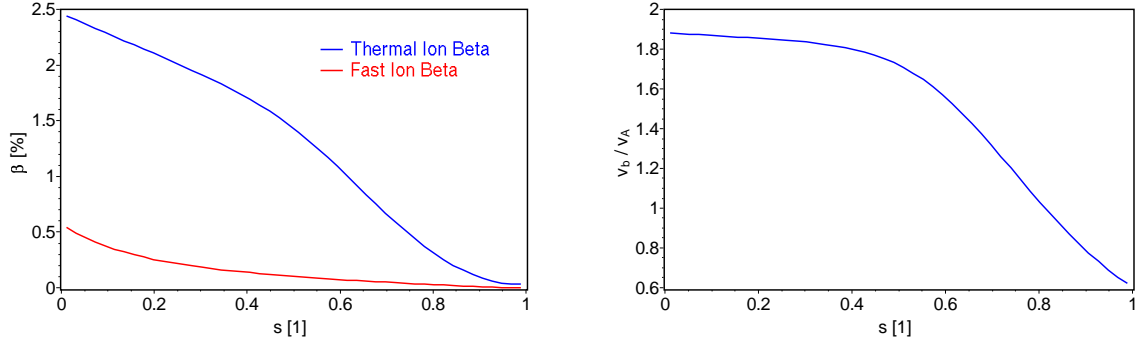


Figure 5.13: Radial profiles of  $\beta_{th}$ ,  $\beta_{fast}$ , and  $v_b/v_A$  for W7-AS shot #54154,  $t = 0.23$ s, 3.4 MW NBI power.

	$n_{th} \text{ [m}^{-3}\text{]}$	$n_{fast} \text{ [m}^{-3}\text{]}$	$\beta_{th} \text{ [%]}$	$\beta_{fast} \text{ [%]}$	$\beta_{fast}/\beta_{th}$	$v_b/v_A$
$s = 0$	$2.23 \cdot 10^{20}$	$1.01 \cdot 10^{18}$	2.45	0.55	0.22	1.89
$s = 1$	$2.77 \cdot 10^{19}$	$3.91 \cdot 10^{16}$	0.04	0.01	0.20	0.61
Vol. Avg.	$1.66 \cdot 10^{20}$	$3.55 \cdot 10^{17}$	1.31	0.16	0.12	1.36

Table 5.1: Statistical quantities obtained from the velocity distribution function calculated for W7-AS shot #54154,  $t = 0.23$ s, 3.4 MW NBI power.

In shot #54154 at  $t = 0.23$ s, both NBI beamlines with four ion sources per beamline were switched on, delivering a total heating power of 3.4 MW. Here a hydrogen beam was injected into a hydrogen plasma. In the ionization modelling with  $10^6$  test particles per beamline, the total deposited power was estimated to be 3.18 MW (93.6%). Prompt losses of injected particles are neglected in both, ionization and slowing down calculations. The birth profile is shown in Fig. 5.11, where it can be seen that the deposited power density peaks towards the plasma center, whereas most of the particles are ionized at intermediate radii. The pitch distributions are strongly anisotropic and reflect the unbalanced injection used for the later W7-AS discharges.

The velocity distribution functions obtained after the slowing-down calculation, Fig. 5.12, retain the velocity anisotropy near the injection energy. As expected, the fast particles become isotropic during thermalization. In the right graph of Fig. 5.12 the three injection energies  $\mathcal{E} = 55$  keV,  $\mathcal{E}/2$  and  $\mathcal{E}/3$  can be identified. Table 5.1 lists some important statistical quantities that were calculated using the ion distribution function. In Fig. 5.13 the radial profiles of  $\beta_i$ ,  $\beta_{fast}$  and  $v_b/v_A$  are depicted where  $v_b$  is the beam velocity and  $\beta_i$  is the thermal ion beta. When  $\beta_{fast}$  is compared to the power deposition profile in Fig. 5.11 and  $v_b/v_A(s)$  to the density profile in Fig. 5.6, one finds that the variation of  $\langle B_0 \rangle(s)$  is too small to influence the profile shape significantly.

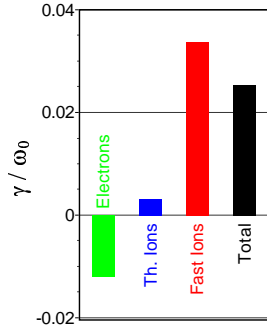


Figure 5.14: Growth rate for the  $(5/6, 2)$  TAE in #54154.

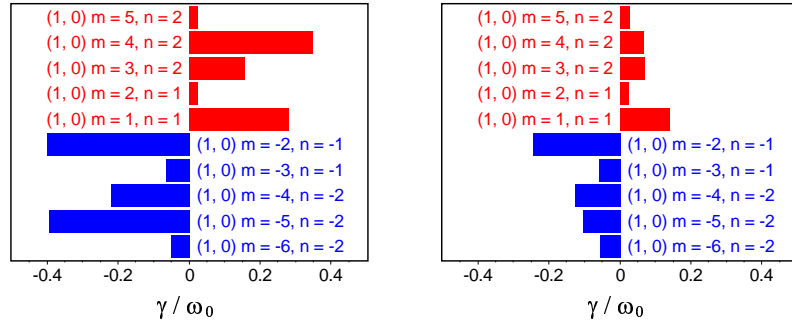


Figure 5.15: Effective growth rates several TAE modes for W7-AS shot #54154 using the anisotropic (left) or an equivalent isotropic distribution function (right).

### 5.1.6 Growth Rates and Fast Ion Losses

The LGRO code (Sec. 4.4.4) is used to calculate the growth rate of the identified  $m = 5/6, n = 2$  TAE instability based on the equilibrium reconstruction and the slowing-down distribution function. It is found that the electron Landau damping has a stabilizing effect on the mode (Fig. 5.14). The spatial inhomogeneity of the electron distribution function does also contribute, but this term is significantly smaller compared to the Landau damping. The thermal ions are slightly destabilizing. This is attributed to the localization of the mode in the gradient region of the plasma, where the density gradient is strong enough to drive the mode via the ions diamagnetic drift. The required small resonance velocities are provided by the non-axisymmetric  $\epsilon^{\mu\nu}$  coupling coefficients with  $\nu \neq 0$ .  $B$  is negative, and therefore  $\omega_{*,i}$  should be destabilizing for positive  $n$ . The thermal ion drive is not strong enough to overcome the electron damping and without the additional fast-particle drive the mode would be stable. In total, the effective growth rate is positive and the mode is predicted to be unstable, driven mainly by fast particles.

Fig. 5.15 shows a comparison of the effective growth rates of all TAEs with  $n = -2 \dots 2$  using the LGRO code, once with an anisotropic velocity distribution of the fast particles, and once with an equivalent isotropic distribution having the same  $\beta_{fast}$  and  $n_{fast}$ . The possible values of  $m$  and  $n$  are determined by the equilibrium  $t$ -profile according to eq. (3.14). This figure highlights that the fast-ion drive is directional. Only those eigenmodes whose harmonics have mode numbers with a certain sign are driven by the fast ions. A second fact can be derived from Fig. 5.15: The most unstable mode is not the one identified in experiment. The local model neglects the radial extension of the modes and therefore any continuum damping which can additionally stabilize some of the eigenmodes. Finally, the figure shows the difference between the isotropic and anisotropic distribution of fast ions. Some TAEs are selectively driven more unstable by the anisotropic velocity distribution while for others the drive reduces, depending on the number of fast ions that fulfill the resonance condition (3.23).

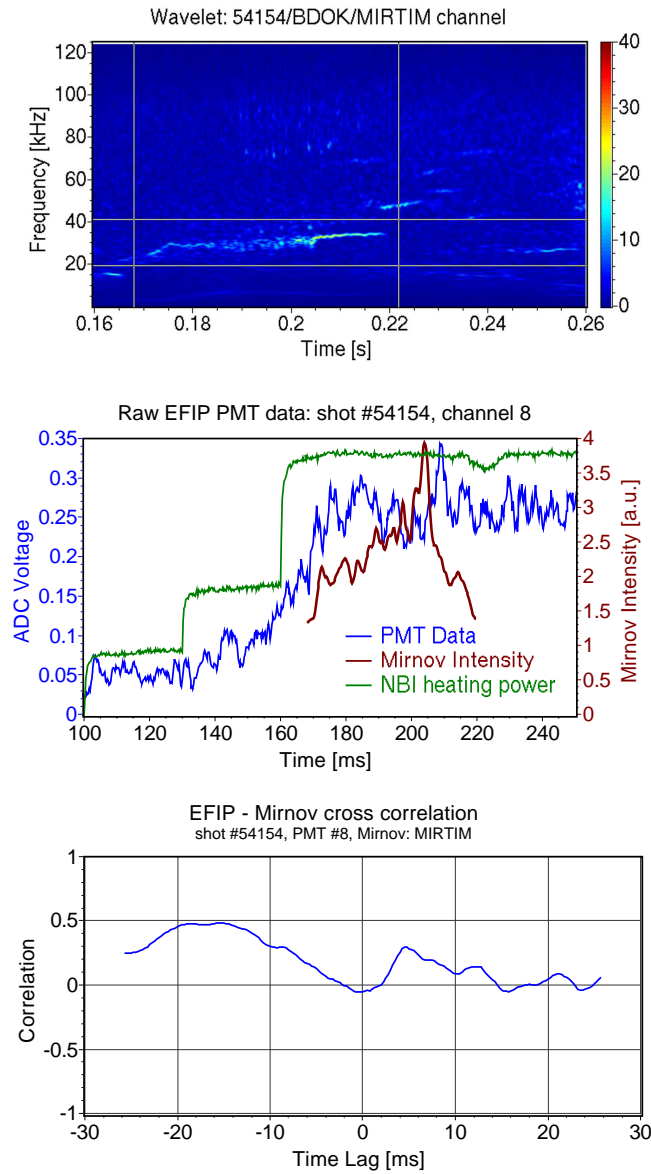


Figure 5.16: Procedure to identify resonant fast ion losses in W7-AS discharge #54154. Top: From the wavelet transform of a suitable Mirnov channel the spectral and temporal range of the observed eigenmode is selected, indicated by the rectangle. Center: Time traces of Mirnov intensity, calculated by integrating over frequency in the selected area, NBI power and an EFIP PMT signal. Bottom: Cross correlation function between Mirnov intensity and PMT data. Positive time lags indicate that the particle losses follow the Mirnov intensity.

As stated in Sec. 3.3.2, the fast ions losses by resonant wave-particle interaction are expected to scale linearly with the wave amplitude. Consequently, this allows one to look for correlations between the temporal evolution of the wave amplitude and fast ion losses to identify resonant losses. When calculating the wave amplitude, it has to be kept in mind that multiple activity at different frequencies is often observed. The time trace of the wave amplitude is therefore calculated by integrating the time-resolved frequency spectrum as obtained from wavelet transform in the spectral band where the mode exists, shown in Fig. 5.16. Additionally, the NBI power needs to be monitored to exclude changes in the fast ion loss signals that are caused by changes in the heating power. Finally, the (normalized) cross correlation functions between the EFIP PMT time traces and the Mirnov intensity are calculated. For the discharge #54154 and the discovered TAE instability, no significant correlation between Mirnov intensity and ion loss data could be established for any of the photomultipliers. The small positive correlation in PMT #8 at  $\Delta t \approx 5$  ms is hardly above the noise level. This is also supported by the value of the cross correlation function which is below 0.3.

## 5.2 Discharge Scan

In the course of the present work, in total of 133 Alfvénic activities are being studied along the line described in the last section. Discharge numbers range from 54009 to 56936. The discharges have been selected according to the following criteria:

**High  $\beta$ :** Usually, the high beta phase of these discharges is quiescent, but strong Alfvénic activity is frequently observed during the startup phase. In addition, the assumption  $T_e = T_i$  is well justified, the impurity content is low, the NBI driven toroidal current is almost always compensated, and the natural edge islands are usually suppressed to increase the plasma volume [82]. This is especially important enable the equilibrium reconstruction based on VMEC alone, because VMEC does not handle magnetic islands and ergodic regions.

**NBI heating, no ECRH:** This is required to have a fast ion distribution function and to have thereby a significant fast particle drive of Alfvén instabilities. Mixed H/D discharges have been avoided because of difficulties to determine the relative abundances of hydrogen and deuterium. Especially, experiments performed shortly after a change of the fuel gas are not considered because the hydrogen or deuterium inventory in the carbon-containing, plasma facing components in W7-AS can cause a significant pollution of the plasma. A period of several days is required until the inventory has decayed.

**Data availability:** It is required that YAG Thomson data is available to allow an equilibrium reconstruction based on measured density and temperature profiles. In addition, Mirnov data should be available for all probe arrays to determine both mode numbers,  $m$  and  $n$ , of the harmonics of the observed instability.

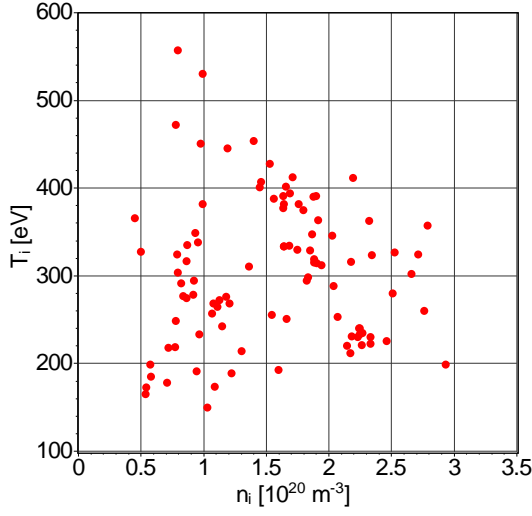


Figure 5.17: Thermal ion temperatures and densities covered by the discharges.

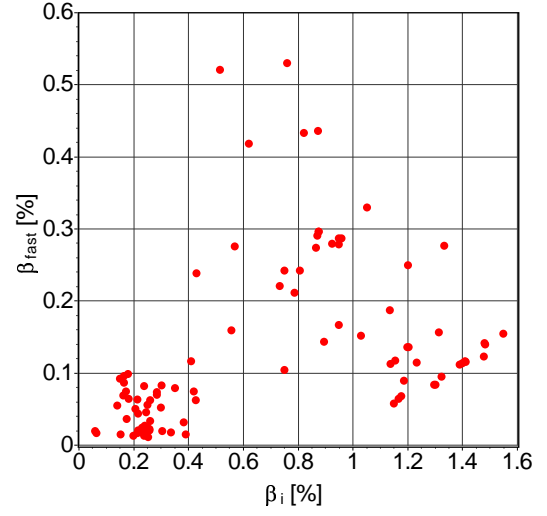


Figure 5.18: Comparison of the volume averages of fast and thermal ion beta.

These criteria effectively limit the number of suitable discharges. Those that have been identified stem from a few experimental campaigns as seen in Appendix C.1. In discharges where both, ECRH and NBI are listed as heatings, the ECRH heating starts after the analyzed time period and does not interfere with the Alfvén eigenmode analysis. The same holds for experiments dedicated to the study of electron Bernstein waves (EBW) and their applicability for plasma heating by OXB conversion. In the following, some statistical information about the different discharges that have been studied will be given to show the covered parameter range. Afterwards, the identified Alfvén eigenmodes are presented.

### 5.2.1 Discharge Classification

The studied discharges are collected from several experimental campaigns and cover a wide range of different plasma parameters. The experiments were conducted at magnetic field strengths of  $B_0 = -0.9$  T,  $-1$  T,  $-1.25$  T (half field) and  $-2.5$  T (full field). Both, hydrogen and deuterium discharges are present in the list of shots. Fig. 5.17 illustrates the variation of central ion density and temperature throughout the different discharges. The density ranges from  $n_i(0) \approx 5 \cdot 10^{19} \text{m}^{-3}$  to  $3 \cdot 10^{20} \text{m}^{-3}$ , while the ion temperature varies from  $T_i(0) \approx 150$  eV, in the early startup phase of some discharges, up to 550 eV. Although the density of fast ions is always small compared to the thermal bulk ion density,  $n_{fast}/n_i < 10^{-2}$ , they can carry a significant fraction of the total plasma energy. This is indicated in Fig. 5.18 which displays the volume-averaged fast ion beta  $\langle \beta_{fast} \rangle$  as a function of the thermal ion beta  $\langle \beta_i \rangle$ . The total thermal plasma beta  $\beta_{th} = \beta_i + \beta_e = 2\beta_i$ , because  $n_e = n_i$  and  $T_e = T_i$  were assumed. Discharges with  $\beta_{fast} \approx \beta_i$  as well as with  $\beta_{fast} < \beta_i$  are present. There is no obvious correlation between  $\beta_{fast}$  and  $\beta_i$ , they can be considered as independent variables.

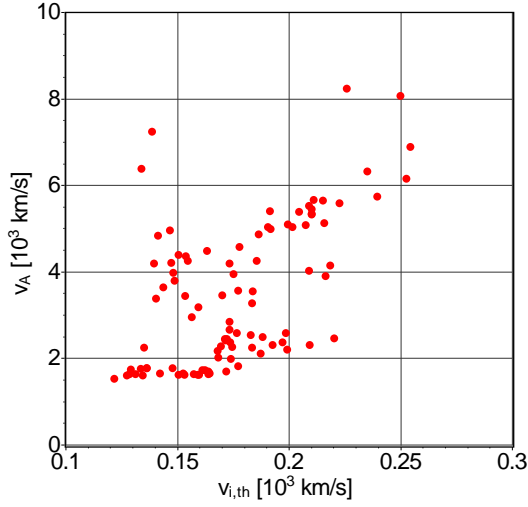


Figure 5.19: Comparison of the volume averaged thermal ion speed to the Alfvén velocity.

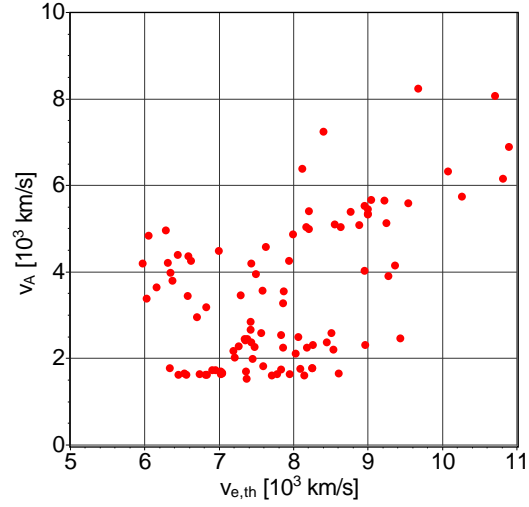


Figure 5.20: Comparison of the volume averaged thermal electron speed to the Alfvén velocity.

Figure 5.19 shows the comparison between the volume averages of two characteristic velocities, the thermal ion speed and the Alfvén velocity. It is found that the Alfvén velocity is always larger by a factor of at least 10. This is different for the electrons, Fig. 5.20, which have thermal velocities of the same order as the Alfvén velocity due to the low temperature and the high densities. It is expected that the electrons can interact resonantly with Alfvén eigenmodes and stabilize them via Landau damping.

Fig. 5.21 shows the variation of the ratio of NBI beam velocity  $v_b$  to the Alfvén velocity  $v_A$ , ranging from  $0.3 \leq v_b/v_A \leq 2.1$ . This figure also highlights the correlation between  $v_A$  and  $\beta_i$ :

$$\frac{v_b}{v_A} = \frac{\sqrt{2\mathcal{E}_{inj}/m_i}}{B/\sqrt{\mu_0 m_i n_i}} \sim \frac{\sqrt{n_i}}{B}, \quad \beta_i \sim \frac{n_i T_i}{B^2}.$$

The NBI injection energy was not varied and since the ratio  $v_b/v_A$  is independent of the particle mass, the deviation from a square root curve in Fig. 5.21 is a result of the temperature variation.

Two important parameters that determine the possibility of fast particle drive for Alfvén eigenmodes have already been mentioned. One is the ratio  $v_b/v_A$  which describes through which resonances the injected particles can interact with the eigenmodes. The other important parameter is the ratio  $\beta_{fast}/\beta_i$  that gives a comparison between the energy content in the destabilizing fast ion population and the potentially stabilizing thermal bulk plasma. Fig. 5.22 shows the data arranged this way. It should be noted that the volume averaged values displayed there are not significant unless the instability drive is effective over a large fraction of the plasma radius. For eigenmodes that are strongly localized in the gradient region, the picture may change qualitatively.

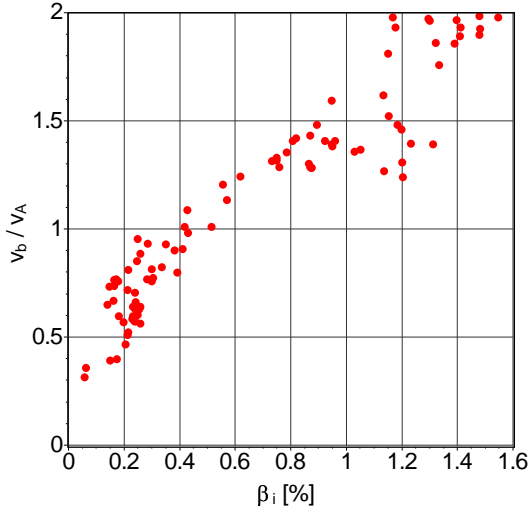


Figure 5.21: Variation of volume averaged  $v_b/v_A$ .

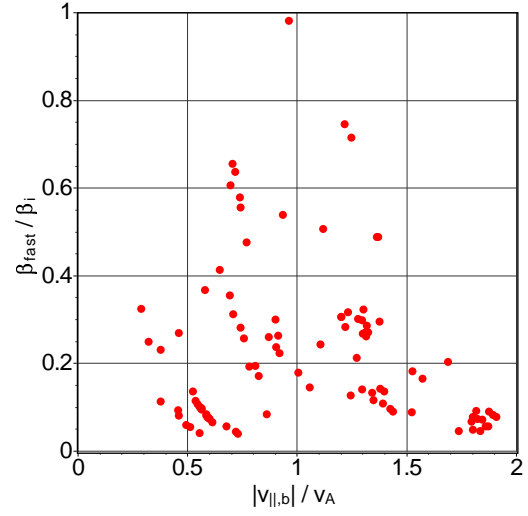


Figure 5.22: Volume averaged  $\beta_{fast}/\beta_i$  as a function of  $\langle v_b/v_A \rangle$ .

### 5.2.2 Eigenmode Classification

The results of the eigenmode identification of the 133 studied Alfvén instabilities can be summarized as follows:

**GAEs:** 19 (14.3%),

**TAEs:** 47 (35.3%),

**EAEs:** 8 identified + 13 with frequencies inside the EAE gap, total: 21 (15.8%),

**NAE<sub>30</sub>:** possibly 1,

**MAE<sub>01</sub>:** possibly 1,

**HAE<sub>21</sub>:** possibly 3,

**Unidentified:** 41 (30.8%).

A complete list of all discharges and AEs is given in Appendix C. The mode numbers and the frequency of the NAE<sub>30</sub> eigenmode are in agreement with the Alfvén continuum calculation, but the continuum gap is closed towards the plasma boundary and the mode is predicted to suffer from continuum damping. It is, therefore, not possible to be sure that the observed eigenmode is indeed the NAE<sub>30</sub> suggested by the mode numbers. The identification of the high-frequency MAE and HAE modes is not uniquely possible with the probe setup at W7-AS because (a) the MIR-1 array is unsuitable for frequencies larger than 70 kHz – this leaves only two different toroidal positions at which information about the mode structure is available; and (b) these modes involve

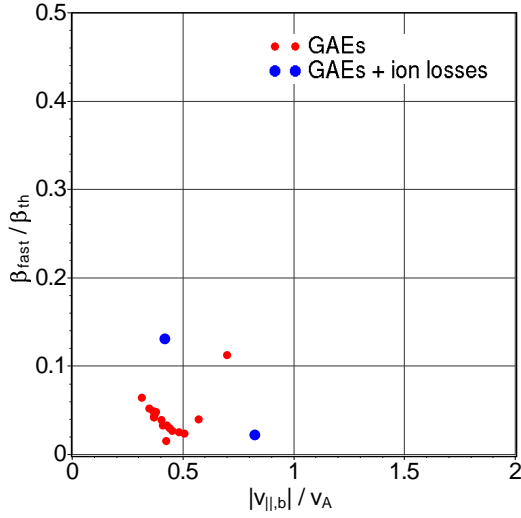


Figure 5.23:  $\beta_{fast}/(\beta_e + \beta_i)$  over  $v_b/v_A$  for GAEs. All quantities have been evaluated at  $s = s_0$ , the location of the minimum of the Alfvén continuum.

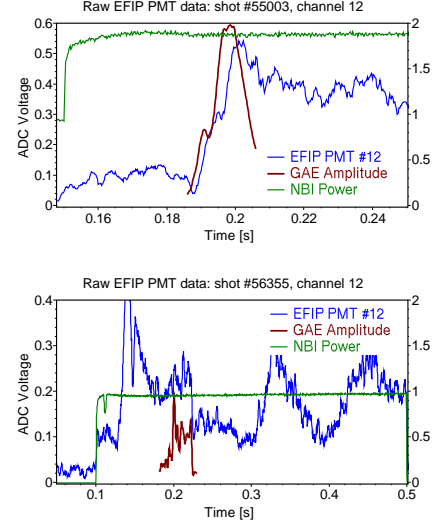


Figure 5.24: Fast ion losses seen by PMT #12 for GAEs in shot #55003 and #56355.

harmonics  $(m, n)$  and  $(m + \mu, n + N\nu)$  with  $n$ 's differing by the number of field periods  $N = 5$ . To summarize, for high-frequency modes the mode numbers are basically unknown, but in the cases mentioned above, the frequencies of the eigenmodes lies inside the continuum gaps and one possible harmonic could be found on the mode number spectra.

The unidentified AEs, which constitute one third of all studied AEs, could not be assigned to either of GAEs and gap modes, or have  $m = 0$  or  $n = 0$  as only dominant harmonic in the mode number spectrum. In the following, more details are given about the GAEs, TAEs, EAEs and the unidentified AEs.

### 5.2.2.1 GAEs

The GAEs (see Appendix C.2.1) were observed in low-shear discharges,  $t_{max} - t_{min} < 0.03$ , in the vicinity of but not including  $t = 0.5$  which is consistent with earlier studies [21, 83]. With the exception of shot #55003, #55480 and #56355, all GAEs were found in discharges of the same experimental program which is reflected by the similar discharge parameters in Fig. 5.23. In this series, the GAEs appeared reproducibly in the density ramp-up with comparable frequencies and the same high mode numbers  $(m, n) = (-14, -7)$ , which were found by studying the aliasing in the mode number spectrum. No ion or energy losses are associated with these GAEs.

The other three discharges are from different experimental programs. The activity observed in #55480 has no clear eigenfrequency and occupies the whole frequency band between 22 kHz and 32 kHz, but it can be assigned clear mode numbers  $(m, n) =$



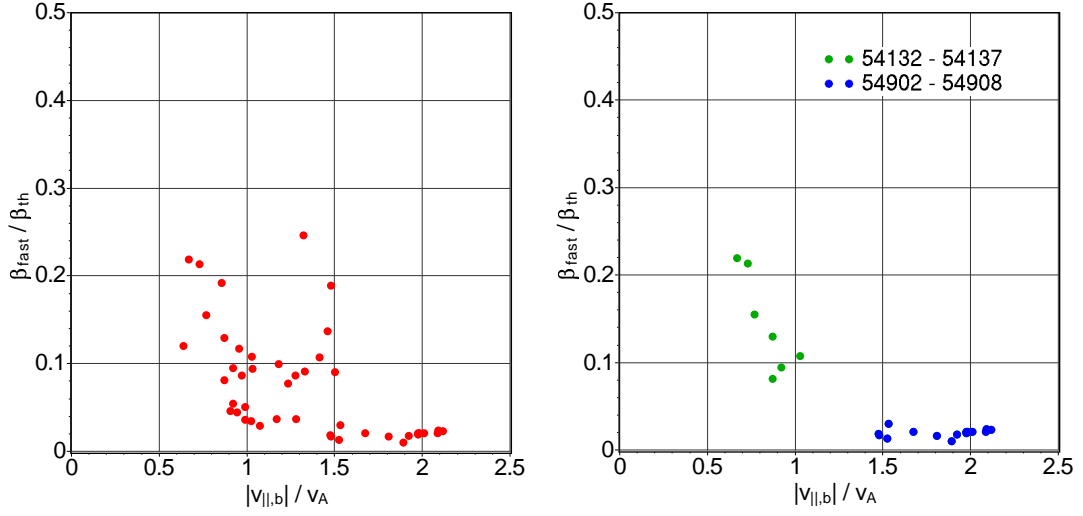


Figure 5.25: Left:  $\beta_{fast}/(\beta_e + \beta_i)$  over  $v_b/v_A$  for all TAEs. All quantities have been evaluated at  $s = s_*$ , the intersection point of the corresponding cylindrical continua. Right: selection of interesting cases.

(2, 1). The GAEs in shot #55003 and #56355 have mode numbers  $(-4, -2)$  and  $(2, 1)$ , respectively, and cause ion losses as shown in Fig. 5.24. In both cases, the ion losses are seen in PMTs #8 and #12 of the EFIP diagnostic which correspond to counterpassing ions with  $\chi \approx 0.9$  and high energies comparable to the NBI injection energy. The correlation times are  $\approx 2 - 4$  ms, cross correlation function values  $> 0.8$  indicate that the losses are indeed caused by resonant wave-particle interaction.

The LGRO code is not yet able to calculate the growth rates of GAEs. But from the sign of the mode numbers it is expected that the diamagnetic drift acts as a stabilizing factor on most of these modes.

### 5.2.2.2 TAEs

The TAEs, listed in detail in Appendix C.2.2, constitute the largest fraction of all successfully identified AEs. They are found in discharges stemming from several experimental campaigns and cover a wider parameter range (Fig. 5.25). TAEs exist in all operational regimes, including high and medium shear discharges, H and D plasmas, low and high magnetic fields. With a few exceptions, the mode numbers were found to be positive, ranging from  $m = 2 \dots 12$  and  $n = 1 \dots 5$ , with frequencies up to 40 kHz.

Strong indications of fast-particle drive were seen in some of the discharges, shown separately in the right diagram of Fig. 5.25. In shots #54132 – #54137, the TAE is observed in a very early stage of the discharge where the NBI power is still being ramped up. An example is given in Fig. 5.26. The amplitude of the TAE increases suddenly, coincident with a step in the NBI heating power. Shortly afterwards, the frequency decreases slightly and the mode decreases. At about the same time, a new

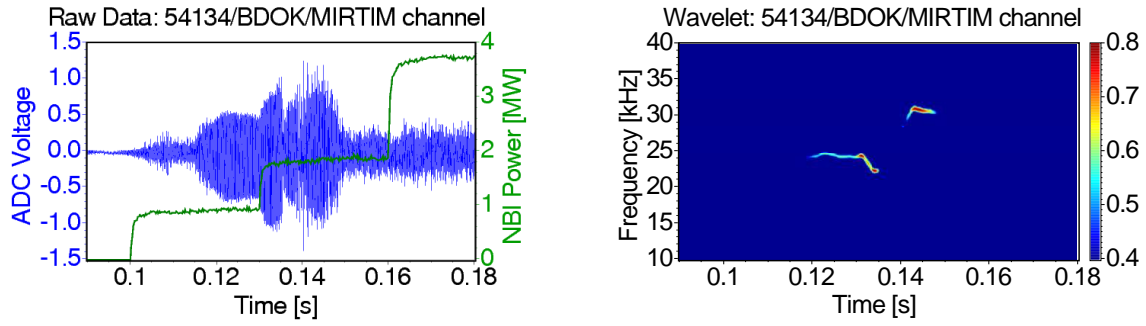


Figure 5.26: Fast particle driven TAE in shot #54134. Left: time traces of Mirnov amplitude  $\sim \dot{B}$  and NBI power, right: wavelet spectrum.

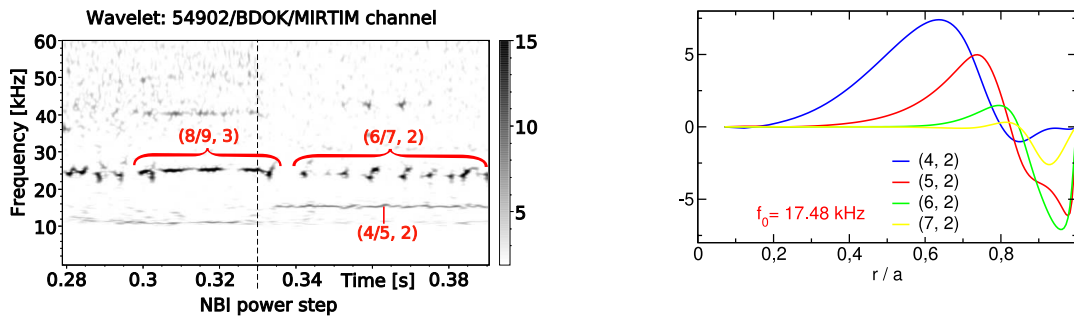


Figure 5.27: TAE spectrum change by NBI power step.

Figure 5.28: Harmonics of a (4/5, 2) TAE calculated using the CAS3D3 code [78, 79] for shot #54906 [84].

eigenmode appears slightly above in frequency that could not be identified because the analysis yields  $m = 0$  as only dominant poloidal harmonic.

The shots #54902 – #54908 belong to a campaign where power scan experiments have been performed. The TAEs were observed in a late stage of the discharges, from  $t = 0.28 \dots 0.39$  s in the stationary high- $\beta$  phase. Due to the low field and the high densities, the Alfvén velocity is rather small, giving ratios  $v_b/v_A > 1$  (Fig. 5.25). In all these discharges, the NBI power has been decreased at  $t = 0.33$  s. This had a negligible effect on the global plasma parameters, the ideal MHD equilibria and the Alfvén continua are comparable. Nevertheless, at  $t \approx 0.33$  s the spectrum of observed unstable TAEs is changed as can be seen from Fig. 5.27. In addition, the mode number spectra of the TAEs in these discharges indicate that a considerable number of dominant harmonics is involved in the formation of the eigenmode. A calculation of the radial eigenfunctions of the harmonics of a TAE at 17 kHz in discharge #54906,  $t = 0.33$  s, performed by Könies using the CAS3D3 code, supports this hypothesis. An excellent agreement between mode numbers and eigenfrequency of the TAE is found.

A different interesting feature is seen in the power scan series in the (6/7, 2) TAE that appears reproducibly in all discharges of that series. As Fig. 5.27 suggests for this activity, it is a bursting mode, where each burst appears twice, slightly shifted upwards in frequency. This behaviour has been termed "frequency splitting", but has not been

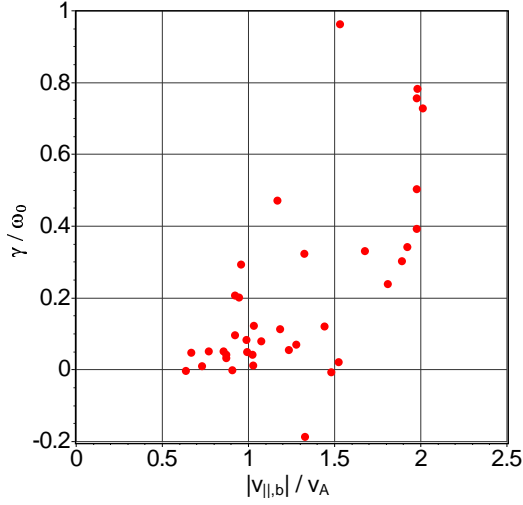


Figure 5.29: Normalized growth rates of the observed TAE instabilities. Most TAEs are predicted to be unstable.

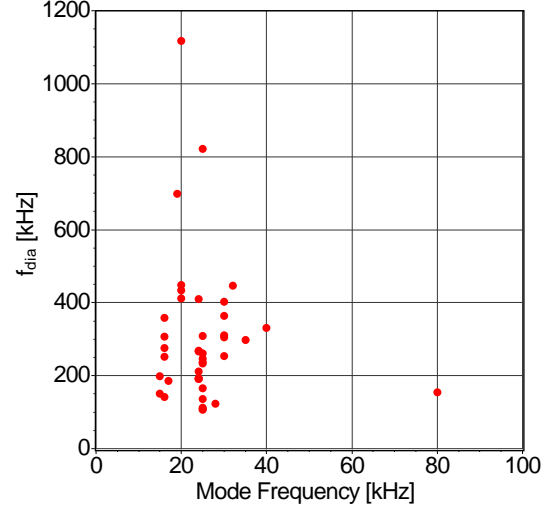


Figure 5.30: Diamagnetic drift frequency of fast ions vs. eigenmode frequency.

further studied.

The sign of the mode numbers suggests that the diamagnetic drift of the fast beam ions drives the modes. The growth rates of all TAEs have been calculated using the LGRO code (Sec. 4.4.4), the results are shown in Fig. 5.29. It can be seen that for some TAEs the growth rates reach magnitudes where it can be expected that the perturbative approach breaks down. The modes with negative mode numbers are predicted to be damped, as expected. In many cases, the density gradient of the thermal ions is sufficiently strong to be slightly destabilizing, the electron Landau damping, however, is always larger than the thermal ion drive. Fig. 5.30 shows the diamagnetic drift frequencies compared to the mode frequencies. The drift frequency,  $f_{dia} = \omega_*/(2\pi)$  has been calculated using the following formula:

$$\omega_* = \frac{v_0^2}{\omega_{ci}} \cdot \frac{1}{r} \frac{d \ln(n_{fast})}{dr}, \quad (5.4)$$

where  $n_{fast} = \int d^3v f_{fast}$ ,  $v_0^2 = n_{fast}^{-1} \int d^3v v^2 f_{fast}$ , and  $\omega_{ci} = eB/m_i$ . All quantities are evaluated at the magnetic surface where the cylindrical continua of the eigenmode harmonics would intersect. Both, the Larmor frequency  $\omega_{ci}$  ( $B < 0$ ) and the density gradient length are negative, which makes  $\omega_* > 0$ . Fig. 5.30 shows that the drive by the diamagnetic drift, which is proportional to  $m\omega_*/\omega_0$  ( $m \approx n/t$  for gap modes) is significantly enhanced by the large ratio  $\omega_*/\omega_0 > 10$ , and the high mode numbers. In contrast to the strong TAE drive by the energetic beam ions, wave-induced fast ion losses were not observed for any TAE.

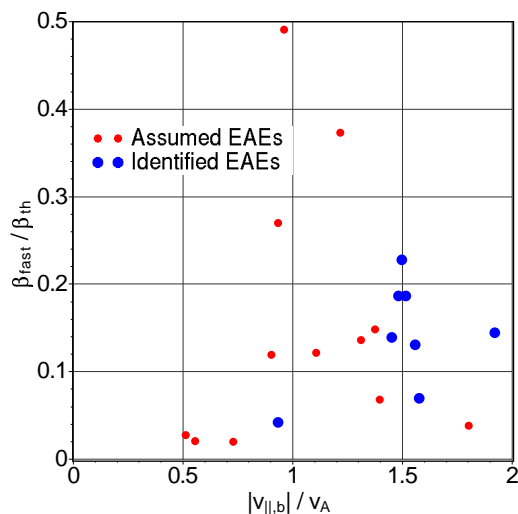


Figure 5.31:  $\beta_{fast}/\beta_{th}$  vs.  $v_b/v_A$  for EAEs.

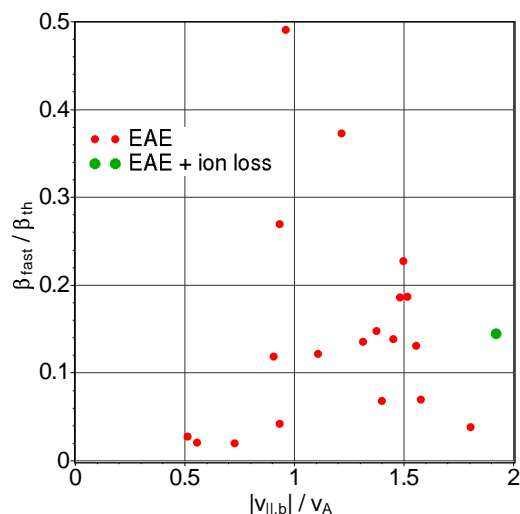


Figure 5.32: EAE for which ion losses are observed.

### 5.2.2.3 EAEs

The number of EAEs that could unambiguously be identified is as low as 8 cases. Additional 13 Alfvén instabilities have frequencies inside the EAE gap but their mode numbers could not be related to couplings in the Alfvén continuum. It is therefore unknown if these modes really constitute EAEs or if they are other instabilities that just coincide with the EAE frequency range. The individual events are listed in Appendix C.2.3, the distribution of dimensionless discharge parameters  $\beta_{fast}/\beta_{th}$  and  $v_b/v_A$  is given in Fig. 5.31. These quantities have been evaluated at  $s = s_*$  for the clearly identified EAEs, in case of the assumed EAEs volume averaged values are given. It should be noted that one half of the assumed EAEs has frequencies that exceed the capabilities of the MIR-1 probe array. Hence, the mode numbers are known only approximately.

The Alfvén continua suggest that the radial localization of the EAEs that could be identified is not in the gradient region, but closer towards the plasma center, roughly at about half the plasma radius. This is consistent with the observation that the amplitudes are relatively small and appear noisy. Six of the well identified EAEs have mode numbers  $m, n < 0$  and are therefore predicted to be stabilized by the ion diamagnetic drift. The remaining EAEs in shots #54151 and #56936 are predicted to marginally unstable with growth rates  $\gamma/\omega_0 \ll 1\%$ . Growth rate calculations for the remaining, assumed EAEs could not be performed. Neither their radial localization nor the dominant harmonics are known.

Although the growth rate calculations suggest that fast particles do not destabilize the EAEs, there is an indication of counterpassing fast ion losses. In shot #54009, a correlation between the EAE amplitude and PMT #13 can be seen, where the ion losses follow the EAE with a time lag of  $\approx 2$  ms. The lost particles correspond to ions with an energy of 35 keV, much larger than the bulk ion temperature, and a pitch of

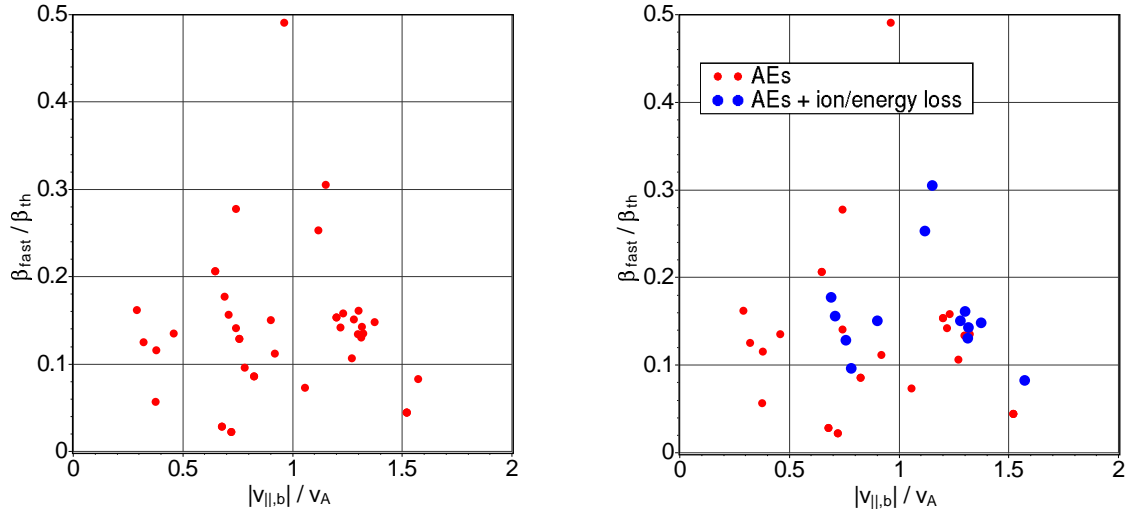


Figure 5.33: Volume averaged  $\beta_{fast}/\beta_{th}$  vs.  $v_b/v_A$ . In the right diagram the cases for which ion or energy losses were observed are highlighted.

$\chi \approx 0.64$  ( $50^\circ$ ). The velocity is  $v/v_b = 0.8$  or  $v_{||}/v_A \approx 1$ . For this shot, the beam velocity was estimated to be  $v_b/v_A \approx 2$ . These observations are consistent with a resonant fast particle loss caused by the EAE. In all other discharges no wave-induced fast ion losses have been identified.

#### 5.2.2.4 Unidentified AEs

There is a number of instabilities that could not be classified. They are listed in Appendix C.2.5, the volume averaged dimensionless parameters  $\beta_{fast}/\beta_{th}$  and  $v_b/v_A$  are plotted in Fig. 5.33. It is seen that, in terms of these parameters, they occupy approximately the same parameter space as the gap modes and GAEs. An exceptionally high number of cases was identified where the Alfvén activity was correlated with significant losses of fast ions or plasma energy. In the right hand side diagram of Fig. 5.33 these cases have been highlighted in a different color. The frequencies of the eigenmodes are shown in Fig. 5.34. The central frequencies of the continuum gaps depend on the plasma parameters via  $\epsilon$  and  $v_A$  (c.f. eq. 3.14) and can vary significantly between discharges. Therefore the frequencies of the instabilities have been normalized to the central TAE gap frequency determined for the discharges from a COBRA run to provide a comparable measure. A range from very low frequency phenomena (well below the TAE, which is the lowest-frequency gap mode) to real high-frequency phenomena (which, if they are gap modes, are stellarator specific HAE or MAE modes) is covered. The central ion densities and temperatures are given in Fig. 5.35. When compared to Fig. 5.17, it is found that the unidentified cases are well spread over the whole parameter range explored in this study. With the exception that losses are only seen for  $v_b/v_A > 0.5$  and from  $f_{TAE} \leq f \leq 5 \cdot f_{TAE}$ , lossy discharges are indistinguishable from ordinary discharges in terms of the presented parameters.

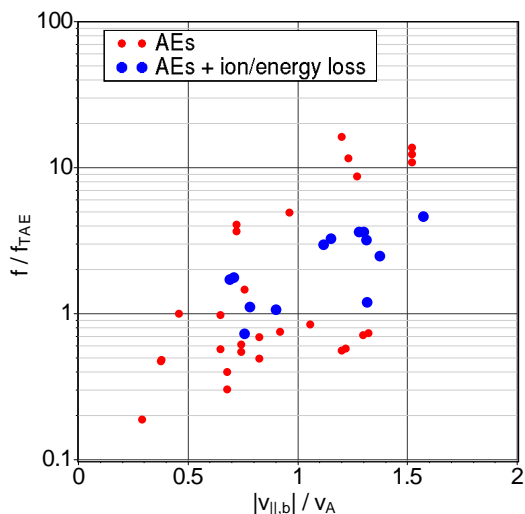


Figure 5.34: Frequencies of the unidentified AEs normalized to the central TAE gap frequency.

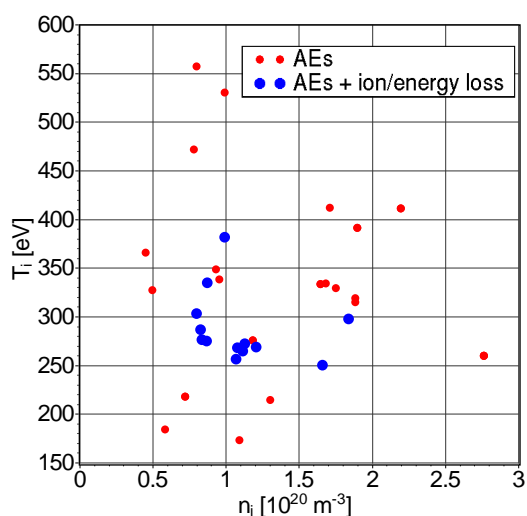


Figure 5.35: Central ion temperatures and densities of discharges with unidentified AEs.

For some cases it is apparent why the AEs have not been identified. The AE burst seen in shots #54128, #54129 and #54138 is very similar in frequency, observation time and mode numbers to instabilities that have been identified as TAEs in #54130 – #54137; the  $(-2, -1)$  peak is likely to alias the  $(11, 4)$  peak. The differences between these discharges is that the edge profile values given by the YAG Thomson scattering diagnostic differ, resulting in changes to the  $t$ - and  $n_i$ -profile in the equilibrium reconstruction that moves the  $(11/12, 4)$  coupling in the Alfvén continua out of the plasma. Consequently, these Alfvén eigenmodes have been classified as unidentified.

In some discharges  $f \geq 70$  kHz and 900 MHz startup heating coincides (e.g. #54903 – #54911  $t = 0.2$  s). The large mode frequency forces to exclude the MIR-1 array from the mode number analysis because of their resonances. The 900 MHz startup heating further leads to strong HF pickup in a part of the MIR-3 array with concomitant data losses. The remaining number of MIR-3 probes together with the MIR-5 array are insufficient to determine the mode numbers even approximately. The different number of probes at the two toroidal positions leads to an unpredictable mode number aliasing spectrum. Besides the missing MIR-1 probe array in that frequency range, the high-frequency modes with  $f/f_{TAE} \gg 1$  (e.g. in #54937, #55049, #55321, #55325 and #56936) are extremely difficult to identify because of yet another reason. The  $B_{\mu\nu}$  spectrum in W7-AS consists of many Fourier coefficients with considerable magnitude. This makes the Alfvén continuum complex at high frequencies. Wide  $HAE_{\mu\nu}$  and  $MAE_{0\nu}$  gaps are aligned side by side, compressing the continuum between them to thin threads. The variation of the central gap frequencies with the plasma parameters has the effect that, at a given frequency, various gaps are found at different radial positions and it is difficult to determine to which gap an observed instability should be associated.

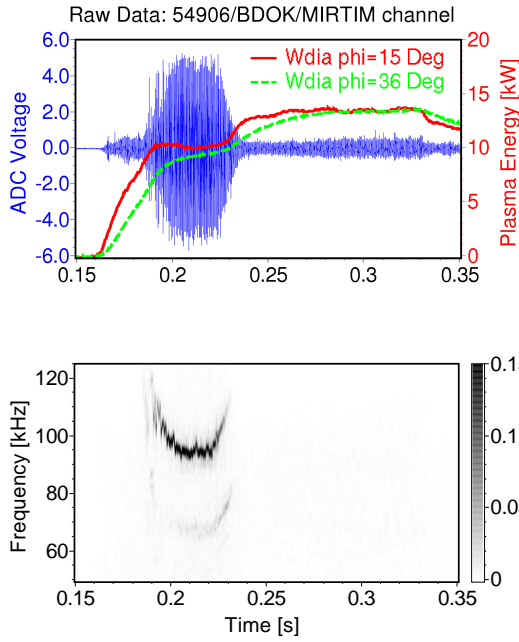


Figure 5.36: Correlation between plasma energy loss and Alfvén activity for shot #54906.

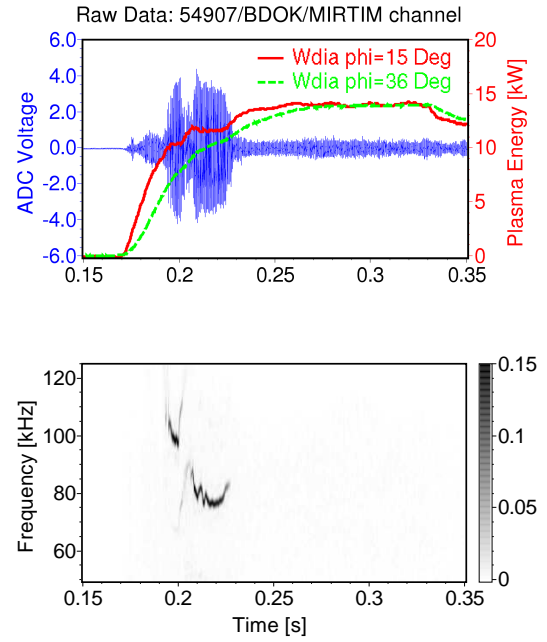


Figure 5.37: Correlation between plasma energy loss and Alfvén activity for shot #54907.

In addition, there are cases where  $m = 0$  was observed as only dominant poloidal harmonic in the mode number spectrum which is likely to be caused by the far-field effect, or where the mode numbers could be determined but not related to expected AEs according to the continuum calculations. This is true for nearly all cases with  $f < f_{TAE}$ . The point with  $f/f_{TAE} \approx 0.18$  belongs to shot #55391, where the central ion density is only  $4.5 \cdot 10^{19} \text{m}^{-3}$  in a full field  $B = -2.5$  T deuterium discharge, resulting in a central TAE gap frequency of  $\approx 160$  kHz. Since no other continuum gaps are located below the TAE gap, the only type of ideal MHD shear Alfvén instability that can be expected at those frequencies are GAEs. The observed mode numbers could not be related to continuum branches that have minima near the observed frequency.

This class, the unidentified AE activities, contains eigenmodes with very different properties. Some might have been wrongly classified here due to uncertainties in the plasma profiles and the equilibrium reconstruction. The remaining instabilities range from very low-frequency phenomena to stellarator specific high-frequency Alfvén eigenmodes, for which the mode numbers remain uncertain with the given probe setup. A few of the modes can be described as stationary and lasting over a long time range, while others show a strongly nonlinear behaviour such as bursting or frequency chirping. Many of the instabilities were reproducibly found in adjacent discharges.

The discharges #54903 – #54907, #54911 show energy losses which are correlated with the observed Alfvén instability. An example showing the correlations is given in Fig. 5.36 for #54906 and in Fig. 5.37 for #54907. The modes always start shortly



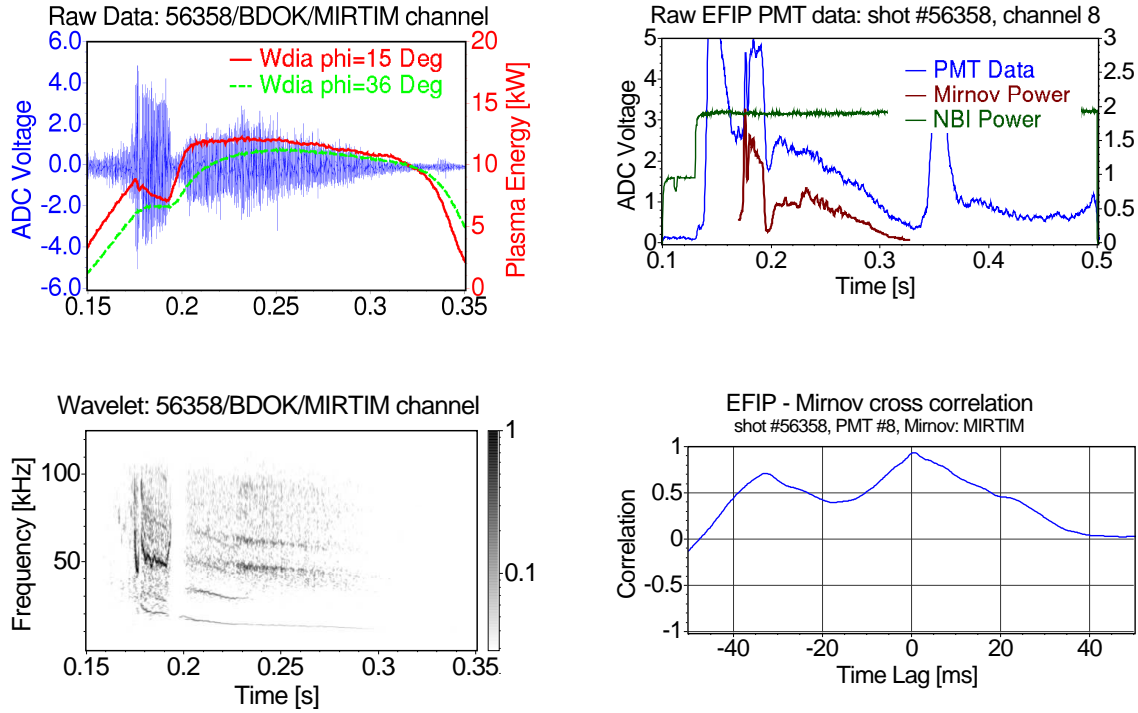


Figure 5.38: Correlation between plasma energy loss, fast ion loss and Alfvén activity for shot #56358.

after an increase of the NBI heating power and sometimes pass through a dithering state until a well-formed eigenmode with sharp frequency and large amplitude develops. In #54908 the eigenmode did not develop out of the dithering state and the plasma energy kept increasing, though at a lower rate. The correlations are observed in the time traces of the fast diamagnetic loop at  $\phi = 15^\circ$ , the diamagnetic loop at  $\phi = 36^\circ$  is too slow to resolve the time dependence. Neither radiation losses in the time traces of the Bremsstrahlung monitor nor a bolometer response were seen, only a slight increase in the  $H_\alpha$  light near the divertor indicates enhanced particle exhaust. The bulk plasma density and temperature, observed by interferometers and SX central electron temperature diagnostic, do not exhibit losses that are sufficiently strong to explain the drop in the plasma energy. It is therefore suggested that energetic particle losses are responsible for the decrease in plasma energy. The losses approximately scale linearly with the Mirnov amplitude which is a strong indication for resonant wave-particle interaction. The fast ion loss probe was positioned at  $z = 33$  cm below the midplane, which is rather far from the plasma, and did not observe significant particle fluxes.

An example showing fast ion losses as well as a significant drop in plasma energy is given in Fig. 5.38. It shows some Alfvén activity that could not be identified to be a gap mode, although it appears to have a frequency inside the TAE gap. The analysis has been performed at  $t \approx 0.18$ s, where the branch near 50 kHz is dominant. The mode number analysis, Fig. 5.39, yields,  $(m, n) = (4, 2)$  as only harmonic with large confidence. The Alfvén continuum suggests, however, that only a GAE with



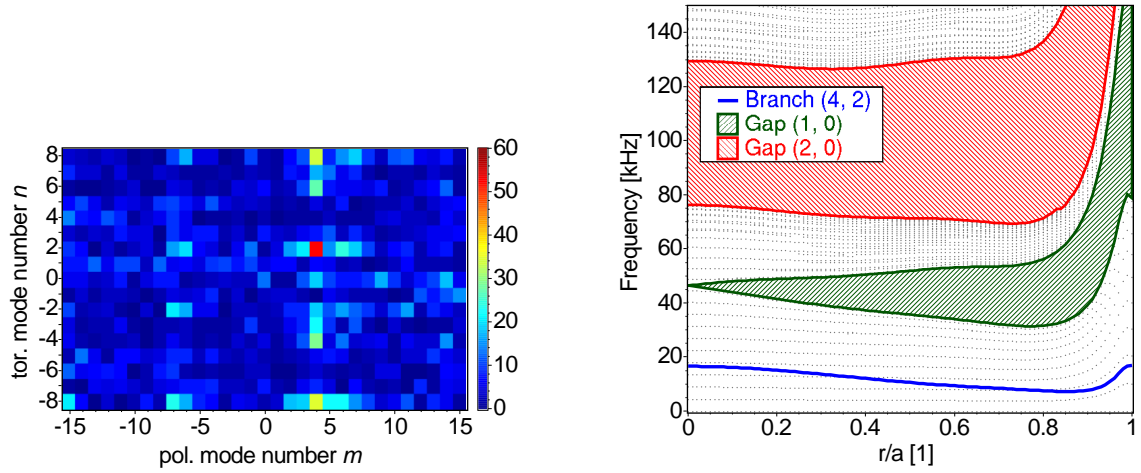


Figure 5.39: Mode number spectrum of the AE activity at  $t \approx 180$ ms, 50 kHz and the corresponding Alfvén continuum for shot #56358, showing the TAE gap and the  $(m, n) = (4, 2)$  branch.

mode numbers  $(4, 2)$  and frequencies well below 10 kHz is expected to be observed at about  $r/a = 0.85$  in experiment. This shot had been subject to previous studies and therefore a set of validated profiles, based on the concept of the integrated data analysis, were available [85] and have been used in the equilibrium reconstruction. The correlation between Mirnov amplitude and ion losses is excellent over a large time, the cross correlation function approaches 1 and peaks at a positive time lag of 2 ms which is comparable to the slowing-down time. This indicates that the Mirnov activity is ahead of the partially slowed down ions that are lost. EFIP PMTs #8 and #13 show the largest signals that exhaust almost the whole dynamic range of the PMT data acquisition setup. These PMTs observe particles that correspond counterpassing ions with medium ( $\approx 15$  keV) and high energies (injection energy 55 keV), respectively, and large pitch  $\chi \approx 0.9$ .

In the remaining discharges for which ion losses could be shown, these occur for counterpassing energetic particles with large pitch  $\chi$  as well. The magnitude of the ion losses is lower and no effect on the diamagnetic energy is seen. All these AE instabilities show strong nonlinearities like frequency chirping or bursting. Discharge #55388 also shows significant fast ion losses, but these were found to be caused by a periodic modulation of the NBI heating power. The bursts of the eigenmode and the ion losses are coincident with NBI bursts, i.e. the cross correlation function peaks at  $\Delta t = 0$ .



# Chapter 6

## Discussion and Conclusions

### 6.1 Equilibrium Reconstruction

The plasma equilibrium is the fundamental building block on which the AE analysis rests. All other steps depend sensitively on the quality of the equilibria which themselves depend on the quality of the spatial profiles of plasma pressure and internal current density. The VMEC/XSTELLOPT toolchain [71–73] has been chosen to solve the ideal MHD equilibrium based on measured pressure profiles and additional constraints.

While the integrated data analysis [81] should be the preferred way to validate the plasma density and temperature profiles obtained from the Nd:YAG Thomson scattering system, it is for now an expensive procedure which is unsuitable to be applied to a larger number of discharges at W7-AS and was only performed for selected shots of special interest. A simplified procedure has been employed that is straightforward to apply to a large number of different discharges.

The pressure profiles in the plasma center are well described by the YAG Thomson scattering system after filtering outliers, and are consistent throughout the discharges of an experimental campaign. The validation of the central densities and temperatures with plasma energy and SX central electron temperature gives sufficient accuracy for a successful quantitative comparison between experimentally observed eigenmode frequencies and the location of the gaps in the Alfvén continuum. Except in very early phases of a discharge, the density profiles are nearly flat in the plasma center and have strong gradients at radii  $r/a \approx 0.7 - 1$ . The temperature profiles are more peaked, the gradient region starts at significantly smaller radii and is less pronounced. Density and temperature values in the edge region are sometimes missing or at least suffer from large uncertainties, although the error estimates given for these points by the Bayesian model for the analysis of YAG Thomson raw data indicate otherwise. Experiments with the incorporation of edge density profiles obtained from the Lithium beam diagnostic have shown that in the discharges of interest, YAG Thomson scattering and

LiBeam give inconsistent results in the important gradient region. This is attributed to the fact that both diagnostics operate at their very limits in the cold and high-density discharges. To be able to proceed, the boundary values of density and temperature were prescribed to be 10% of the central value with a relative error estimate of 30% before fitting the profiles to the profile shape model. These values are roughly expected to be valid outside the LCMS and are consistent with comparable YAG profiles where edge values are determined.

The influence of the internal current density profile has been taken into account only by using a single default profile for all discharges. In addition to the neoclassical bootstrap current, the unbalanced neutral beam injection drives considerable Okhawa currents which were mostly compensated by an Ohmic current to provide net-current free operation. In [86] was studied the influence of the value and the radial profile of  $Z_{eff}$  on the net current densities and the resulting changes to the  $\iota$  profile and the ideal MHD stability. It was found that possible changes to the internal current densities can lower the value of  $\iota$  over large parts of the plasma radius, while it significantly increases the central value of  $\iota$  because both, the ohmic current ( $\sim T^{3/2}$ ) and the Okhawa current ( $\sim P_{NBI}$ ), strongly peak in the center of the discharge. A change in the  $\iota$  profile correspondingly changes the Alfvén continuum. Besides moving couplings between continuum branches (which depend only on  $\iota$ ) into or out of the plasma column, it modifies the variation of AE gap frequencies with the radius and, therefore, can provide enhanced or reduced continuum damping.

The edge magnetic islands that are already present in the vacuum field of W7-AS in the vicinity of a low-order rational transform  $\iota$  near the LCMS also modify the ideal MHD equilibrium considerably. They are required for proper island divertor operation, but destroy the outer magnetic surfaces and thus reduce the available plasma volume and radius. To minimize the influence of the edge islands, only discharges from those experimental campaigns have been studied where the islands are suppressed. This is the case in the high- $\beta$  discharges performed between 2000 and 2002 [82], where the divertor was merely used as limiter. A side effect is that the plasma radius is known, which is a free parameter in the solution of the equilibrium. A constraint imposed on the equilibria is that the last closed magnetic surface extends up to the divertor structures.

Close to the plasma boundary,  $r/a \approx 1$ , the magnetic shear commonly changes sign as seen in Fig. 5.6 at exactly the same position where the curvature of the density profile reverses. This effect is not a physical one, it is introduced by the profile shape model. Consequently, care has to be taken when analyzing eigenmodes that depend on details in this region.

The equilibria that have been calculated are consistent with the observations of Alfvén eigenmodes. In previous studies of Alfvén activity in W7-AS [83, 87] equilibria based on parabolic pressure profiles were used due to the lack of validated pressure profiles. The usability of this approach is limited as seen in Fig. 6.1, which shows a direct comparison between equilibria obtained for a parabolic and a measured flat-top profile. A general

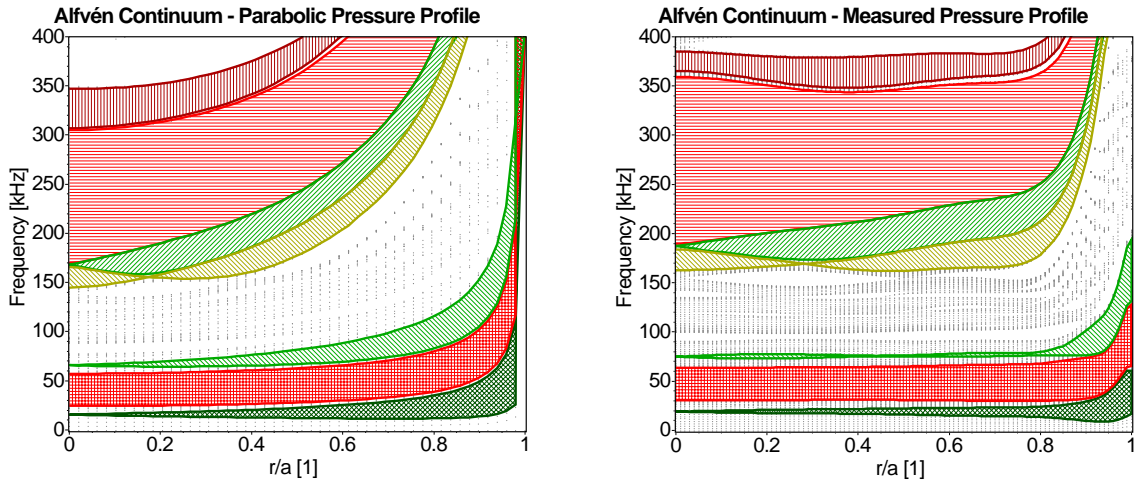


Figure 6.1: Comparison of Alfvén continua obtained from equilibria based on a parabolic and a measured pressure profile, respectively.

observation is that the typical flat-top profile of high- $\beta$  discharges keeps continuum gaps open over much larger plasma regions, especially in the high-frequency region of the continuum. In conjunction with the stronger density gradient this improves the instability of gap modes.

## 6.2 Mirnov Data Analysis

Previous analyses of Alfvén eigenmodes utilizing the Mirnov diagnostic were based on a technique involving Fourier filtering and Singular Value Decomposition (SVD) to separate coexisting features in the spectrum, followed by a phase difference analysis to reconstruct the mode structure [25]. It was found that problems arose due to inadequate poloidal probe positions (vacuum field), too large poloidal mode numbers and a too large distance between plasma and probes. Depending on the radial localization of the eigenmode, the limit in the feasibility to detect poloidal mode numbers  $m$  was found as low as  $m = 3 \dots 5$  using the MIR-1 array.

Two of the problems could be avoided. Firstly, the probe positions are correctly transformed to Boozer coordinates. In these coordinates the harmonics of the eigenmode are assumed to possess a plane wave structure. Secondly, the projection onto a single value of  $m$  or  $n$ , that is inherent in the phase difference analysis, has been avoided. Instead a proper decomposition in orthogonal plane wave basis functions is performed in both, poloidal and toroidal directions simultaneously, comparable to a multidimensional Fourier analysis but suitable for uneven datapoint spacing. More insight gives the equivalent statement that the data is compared to the hypothesis of a  $(m, n, \omega)$ -harmonic, yielding the probability that the harmonic is present in the data. The interpretation in terms of probabilities is permitted by the statistical properties of the Lomb periodogram. Spatial aliasing can thus be recognized by scanning sufficiently

large ranges for  $(m, n)$ , where it should be noted again that the effect of uneven data-point spacing is that different aliasing peaks of the same feature do not necessarily have the same amplitude.

The third problem, the large distance between probes and plasma boundary, can not be circumvented. In fact, the observation of  $m = 0$  features indicates that the strong spatial decay of high multipole orders of the field perturbation imposes a limit on the detectability of Alfvén eigenmodes with high  $(m, n)$ .

In general, the multidimensional Lomb periodogram has proven to be a useful tool that allows the determination of the mode numbers of Alfvén eigenmodes with high accuracy. The statistical interpretation of the spectrum additionally allows to include the Lomb periodogram naturally into the IDA concept [88, 89] for the forthcoming Wendelstein 7-X experiment.

### 6.3 Alfvén Eigenmodes and their Stability

Only ideal MHD shear Alfvén eigenmodes were considered in the eigenmode analysis, kinetic Alfvén waves that exist because of finite parallel electric fields  $\tilde{E}_{\parallel}$  and finite ion gyro-radii have not been looked for. To justify this, it is instructive to look at the "nonideal parameter" [90]:

$$\lambda = \frac{4m\hat{s}\rho_i}{r_m\epsilon^{3/2}} \sqrt{\frac{3}{4} + \frac{T_e}{T_i}},$$

where  $m$  is the poloidal mode number,  $\hat{s} = d \ln(t)/d \ln(r)$  is the magnetic shear,  $\rho_i$  the ion gyro-radius,  $r_m$  is the radius where the mode is localized and  $\epsilon^{3/2} = 5r_m/(2R)$ . It describes the significance of kinetic effects,  $\lambda \ll 1$  corresponds to vanishing importance of non-ideal MHD. This parameter has been calculated for all studied cases and was found to be  $\lambda < 10^{-3}$ , which is a consequence of the small shear in W7-AS and the low temperatures ( $\rho_i$  small). Therefore kinetic Alfvén eigenmodes are not expected to be observed.

Although the studied discharges emerge from a few similar campaigns with low temperatures and high densities, the experimental conditions under which Alfvén instabilities have been analyzed vary considerably in terms of the stability parameters  $\beta_{fast}/\beta_{th}$  and  $v_b/v_A$  because events in the steady-state high- $\beta$  as well as the startup phase  $t < 0.25$ s were used. Under steady-state conditions the eigenmodes usually have low amplitudes and are stationary over large time intervals, while the events observed in the startup phase appear only transiently because they experience a constantly changing background plasma. The typical lifetime of such modes is 50 – 100 ms, depending on the rate of equilibrium changes. Observed eigenmodes appear reproducibly in adjacent discharges of an experimental campaign.

In contrast to previous studies of Alfvén eigenmodes at W7-AS, the identification of instabilities is based on both mode numbers  $(m, n)$  as well as the frequency. This

is made possible by the proper analysis of Mirnov probe data based on the developed multi-dimensional Lomb periodogram, which allows one to obtain reliable mode number spectra even in the case of uneven probe spacing. Eigenmodes are identified by comparing the mode numbers and frequencies to the ideal MHD Alfvén continua. Depending on the mode frequency, uncertainties of 5 – 15 kHz were assumed that describe the combined uncertainties of plasma density and Doppler shift by plasma rotation. Strictly speaking, the restricted number of probes allows the mode number analyses only for low  $(m, n)$  eigenmodes, but significant improvements can be achieved by studying the aliasing in the mode number spectrum. Mode numbers up to  $m = 14$ ,  $n = 7$  have been determined this way using all available probes. The assessment of mode numbers for high-frequency modes was found to be impossible because the characteristics of the MIR-1 probes prohibit their use for frequencies larger than 70 kHz. Gap modes like TAEs or EAEs are identified by frequencies inside the continuum gaps and mode numbers that correspond to couplings between Alfvén continua inside the plasma column. Additionally it is required that the continuum gap is "open" at the mode frequency which means that the mode does not intersect the continuum at some other radial position, otherwise the mode would suffer from continuum damping. A necessary condition for the existence of GAEs is that a Alfvén continuum branch has an off-axis minimum ( $f_{min} > 0$ ). Global Alfvén eigenmodes must have the same mode numbers as the continuum branch and a frequency below, but close to  $f_{min}$ .

Many of the observed instabilities could thereby be identified as one of the ideal MHD Alfvén eigenmodes. Given the uncertainties of density and temperature profiles especially in the gradient region and the unknown current density profile, which all affect the Alfvén continuum, false-positive or false-negative identifications cannot fully be excluded.

### 6.3.1 GAEs

A total of 19 GAEs could be successfully identified. All appeared transiently during the density ramp-up, no GAE was observed in the steady-state phase. Nearly all of them were observed in discharges of a single experimental campaign under comparable conditions, characterized by low values of  $\beta_{fast}/\beta_{th} < 0.1$  and  $v_b/v_A \leq 1/2$ . The remaining GAEs were seen at parameter values not much different. However, due to the low number of cases observed, this behaviour is not necessarily representative. Nearly all the GAEs have mode numbers  $n, m < 0$ . Because the magnetic field is negative, the ions diamagnetic drift is expected to have a stabilizing effect on these modes. The velocity anisotropy term [cf. Eqs. (3.20) and (3.22)] is prefixed with a factor  $m_\alpha \lambda / \mathcal{E}$ , where  $\lambda = 1 - \chi^2$ . Due to the tangential injection, the fast particles are almost aligned to the magnetic field,  $\chi^2 \rightarrow 1$ , which minimizes this term. Significant drive by velocity anisotropy requires that the fast particles have a considerable fraction of their energy perpendicular to the magnetic field. The only possibility for particles to destabilize the mode are positive velocity gradients in the distribution function near the resonant velocities (inverse Landau damping), which requires a loss cone in velocity

space that the beam ions enter during the slowing down. No traces of such losses are seen by the EFIP diagnostic, so the destabilization mechanism of these GAEs remains unclear.

The observation that GAEs appear in low-shear cases close to a low-order rational  $\iota$  but not including it is consistent with earlier observations. It can be explained by the absence of couplings for low mode numbers  $(m, n)$  in the Alfvén continuum that have been avoided by the choice of  $\iota$ . If the shear is sufficiently high to naturally include couplings for low  $(m, n)$ , the GAEs disappear and TAEs constitute the most unstable AE.

### 6.3.2 TAEs

TAEs constitute the major fraction of the studied Alfvén instabilities, observed under a variety of different discharge conditions, transient as well as steady-state. TAEs in high- $\beta$  cases were often found to have a whole range of poloidal mode numbers. This experimental observation is confirmed by a calculation of the mode structure of a typical TAE under high- $\beta$  conditions, which shows that the eigenmode indeed consists of several poloidal harmonics with non-vanishing eigenfunctions near the plasma edge. Having mode numbers  $m, n > 0$ , the fast particle drive of these TAEs is confirmed by growth rate calculations. The main destabilization mechanism is the diamagnetic drift of the fast beam ions. In the studied discharges, thermal ions additionally enhance the growth rate with their diamagnetic drift caused by the strong density gradient near the plasma boundary where the TAEs were found to be localized. But the magnitude of the thermal ion drive is low compared to the fast ion drive because the thermal velocity  $v_{th} \ll v_b$ . In none of the cases the thermal ion drive was sufficiently strong to overcome the electron Landau damping and without the fast particle contribution the mode would be predicted to be stable. In some discharges the fast ion drive was observed directly by an increase of the mode amplitude coincident with an increase of NBI heating power. Another, indirect sign of fast particle drive was seen in the steady-state, high- $\beta$  phase of some discharges where a decrease of NBI heating power, resulting only in small modifications of the plasma equilibrium, caused the spectrum of coexisting unstable TAEs to change.

Fig. 5.25 suggests that there is a threshold in the destabilization of TAEs by fast particles that depends on the ratio of  $v_b/v_A$ . The LGRO code has a mode of operation where it calculates stability diagrams for a given mode by varying the ratio  $v_b/v_A$  and calculating the critical  $\beta_{fast}$  for which  $\gamma = \gamma_e + \gamma_i + \gamma_{fast} = 0$ . Due to the way the code works, it requires that the thermal ions have a damping effect, so the diamagnetic drift of the thermal ions had to be suppressed by assuming a flat density profile. The stability diagram obtained for a selected case using the anisotropic fast particle distribution function is shown in Fig. 6.2 where  $\beta_{fast}/\beta_{th}$  is plotted in logarithmic scale. The same diagram obtained for an isotropic velocity distribution function with equivalent fast particle density and  $\beta_{fast}$  is given in Fig. 6.3. From these figures can be seen that



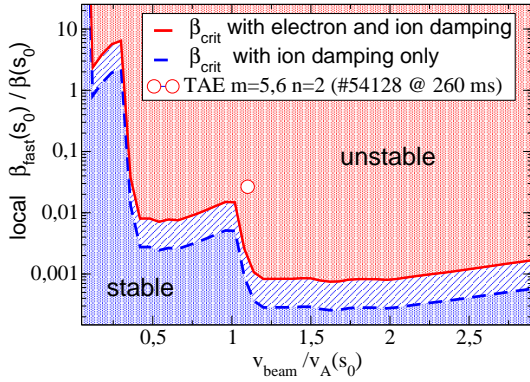


Figure 6.2: LGRO stability diagram for a TAE using the anisotropic energetic ion distribution function.

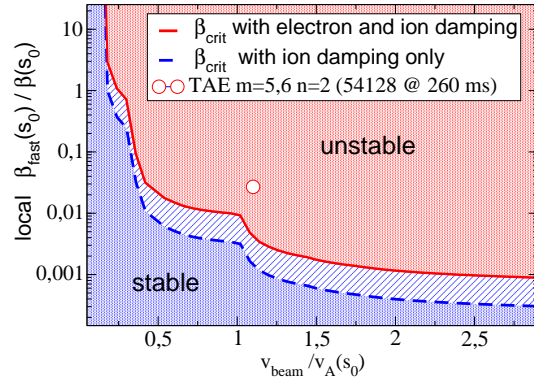


Figure 6.3: LGRO stability diagram for a TAE using an equivalent isotropic fast ion distribution function.

for  $v_b/v_A > 1$  even a perturbatively small population of fast particles is predicted to destabilize the mode. The drive is reduced suddenly by large amounts whenever  $v_{\parallel,b}/v_A$  drops below one of the possible resonance velocities,  $v_{\parallel}^{res}/v_A = 1$  and  $1/3$ , indicated by a larger  $\beta_{crit}$ . It also highlights the importance of electron Landau damping in low-temperature discharges, which increases  $\beta_{crit}$  by a factor of 5 in this example. The comparison between isotropic and anisotropic velocity distribution functions reveals that the main differences occur near the resonance velocities, where isotropy has the effect of smoothing out the strong response of  $\beta_{crit}$  near  $v_{\parallel}^{res}$  and thereby enhances stability at  $v_b \geq v_{\parallel}^{res}$ . The decrease of the instability threshold when  $v_b$  approaches the resonance velocities from above is caused by the pitch angle spread during slowing down, which is correctly described by the fast particle distribution function. Due to the tangential injection, the pitch is  $|\chi| \approx 1$  at the injection energy and the parallel velocity  $v_{\parallel,b} \approx v$ . If the beam velocity is much larger than the Alfvén velocity, particles at resonant velocities are nearly thermalized and isotropic in velocity. As  $v_b \rightarrow v_{\parallel}^{res}$ , the distribution of particles at the resonance velocity becomes localized at the injection pitch angle which effectively increases the number of resonant particles.

The critical  $\beta$  strongly depends on details of the thermal and fast particle distribution functions and the magnitude of the Fourier coefficients of  $|B|$ . For the eigenmodes under consideration, the instability threshold was observed to vary by an order of magnitude between cases. It is therefore not possible to calculate a global stability diagram for all TAEs using the LGRO code. Nevertheless, an instability threshold for the fast particle drive due to electron and ion damping is predicted that qualitatively describes the experimental findings.

### 6.3.3 EAEs and High-Frequency Eigenmodes

Only eight EAEs could clearly be identified. A larger number of eigenmodes was found to have frequencies inside the EAE gap, which can probably be assumed to be EAEs but

could not be identified in terms of their mode numbers. One half of the assumed EAEs has frequencies in excess of 70 kHz which makes the mode number analysis uncertain. Frequencies up to 160 kHz were found to lie inside the EAE gap in cases of low density and high magnetic field. Growth rate calculations were performed for the identified EAEs. Only two of them had mode numbers  $m, n > 0$  and were found to be marginally unstable. The location of the couplings between Alfvén continua suggests that these modes are localized approximately at half the plasma radius, where the density gradient and, consequently, the diamagnetic drift of the fast ions is comparably small. The other cases were strongly damped by the combined effects of electron Landau damping, thermal and energetic ion diamagnetic drifts. For EAEs that were only assumed, the growth rate could not be calculated because neither the mode numbers nor the localization region are known.

High-frequency eigenmodes in W7-AS, that have  $f \gg f_{TAE}$ , can mostly be considered to be stellarator specific HAE or MAE modes due to the structure of the Alfvén continuum which yields that the  $NAE_{\mu 0}$  gaps are small in contrast to the HAE and MAE gaps. The especially wide  $HAE_{21}$  gap is caused by the rotating ellipticity of the plasma cross section in W7-AS, and the stronger magnetic field at both ends of each field period creates a significant  $MAE_{01}$  gap. GAEs are not expected to exist in these frequency ranges because the wide HAE and MAE gaps compress the Alfvén continuum into thin threads so that no continuum branch could possibly form a minimum. The identification of HAEs and MAEs is complicated by the fact that eigenmodes with toroidal coupling numbers  $\nu \neq 0$  involve harmonics with  $n_2 = n_1 \pm N\nu$  where  $N = 5$  is the number of field periods at W7-AS. Such a resolution cannot be obtained with the Mirnov probe setup at W7-AS. The mode number analysis of Mirnov data from the poloidal arrays MIR-3 and MIR-5 results in spectra that show a regular aliasing pattern with  $\Delta m \approx 7$  and  $\Delta n = 2$  where all aliasing peaks are of comparable amplitude. Evidence for the observation of three  $HAE_{21}$ , one  $MAE_{01}$  and one  $NAE_{30}$  eigenmode has been found by comparing the aliasing peaks in the mode number spectrum to couplings in the Alfvén continuum, where one of the harmonics was identified in the correct frequency range. However, this is not significant and could just be by chance.

### 6.3.4 Unidentified Eigenmodes

One third of the events could not be classified to be either gap mode or GAE and is consequently treated as unidentified. Again, approximately one half of these events has frequencies beyond the capabilities of the MIR-1 probe array so that the mode numbers could not be determined with sufficient resolution. Of the remaining low-frequency eigenmodes, three transient eigenmodes have the same characteristics as modes that have been identified as TAEs in other discharges of the same experimental campaign. They have not been identified because the measured density and temperature profile shapes are probably incorrect and result in a modified Alfvén continuum where these modes are not allowed. For most of the remaining low-frequency modes the poloidal mode number  $m = 0$  was found as only dominant harmonic in the mode number

spectrum, which is an indication of far-field effects.

A selection of unidentified Alfvén eigenmodes shows strong non-linear effects like fast frequency chirping or bursting, significant losses of plasma energy or fast ions are observed as well. The frequencies of these modes are often close to, but not inside a continuum gap. Where known, the mode numbers are low-order rationals. Similar characteristics are expected for EPs which are forced oscillations of the plasma in the presence of a resonant fast ion drive that is sufficiently strong to overcome the continuum damping of the modes. EPs should have frequencies that correspond to characteristic frequencies of the driving particle motion, in case of well-circulating fast ions the toroidal transit frequency is expected. In any of these cases the toroidal transit frequency of the most energetic ions,  $v \approx v_b$ , exceeds the mode frequency which means that partially slowed-down beam ions fulfill this condition as well. Volume averaged values of  $v_b/v_A > 0.7$  and  $\beta_{fast}/\beta_{th} > 1\%$  for these discharges, which can easily be exceeded in parts of the plasma, indicate the presence of a strong energetic ion component. A rigorous proof for the observation of EPs in stellarators is currently not possible because the required non-linear simulation tools are not available.

## 6.4 Alfvén Eigenmodes and Fast-Ion Losses

For wave-induced, resonant losses of fast ions it is expected that they scale linearly with the wave amplitude. In addition to causality arguments, this allows one to identify those losses in experiments. Cross correlations between the temporal evolution of the Mirnov amplitude in a spectral band and the photomultiplier time traces of the fast ion loss detector were calculated for this purpose. A distinction between NBI prompt losses and resonant, wave-induced losses is possible by the time lag between wave amplitude and ion loss signal. It is required that the wave amplitude is ahead of the fast ion losses and that the time shift is of the order of the slowing-down time with typical values of 2 – 5 ms. This is close to the detection limit because the photomultipliers were digitized with a frequency of 4 kHz, corresponding to 4 samples/ms. The slowing-down time is an upper limit for the ejection of particles by resonant interaction with AEs. Numerical simulations indicate that energetic particles need a few additional milliseconds to cross the plasma edge region and reach the detector. Larger time lags of the order of the particle confinement time indicate losses by neoclassical transport processes. In cases where the Alfvén eigenmode is excited by an increase of the NBI heating power but does not cause fast ion losses, the time lag at the maximum of the correlation function was found to be negative.

Only three of the identified GAEs and gap modes caused noticeable fast ion losses. Although some of the TAEs were observed to be strongly driven by neutral beam injection, significant particle losses besides the NBI prompt losses could not be seen. In contrast, a considerable fraction of unidentified Alfvén eigenmodes, which are likely to be EPs, could be shown to result in strong losses of plasma energy and/or energetic particles. In discharges #54902 – #54907 and #54911 at  $t \approx 200$  ms fast ion losses

could not be observed directly because the probe was too far away from the plasma. There is, however, a strong anticorrelation between the Mirnov amplitude and the plasma energy measured by the fast diamagnetic loop. The plasma monitor signals suggest escaping fast ions as only explanation for the energy loss. Discharge #56358 shows a similar behaviour of the diamagnetic energy, but in addition the EFIP probe recorded the ion losses as well. There it was shown that the correlation function indeed peaks at  $\Delta t = 2$  ms. The PMTs which observe the losses correspond to small pitch angles and particle energies from the injection energy of 55 keV to medium energies of about 15 keV, which are still much larger than the thermal ion temperature and consistent with the observation of NBI ions expelled from the plasma.

## 6.5 Conclusions

A systematic study of experimentally observed Alfvén instabilities has been performed for a series of discharges taken mostly from high- $\beta$  campaigns at W7-AS, a large number of eigenmodes has been analyzed and compared to theoretical calculations. In these discharges, the eigenmodes are frequently observed during the startup phase of the discharge before the high- $\beta$  phase is reached. Due to the permanently changing bulk plasma in this phase, the eigenmodes appear only transiently.

The ideal MHD equilibrium is one of the most important ingredients in the analysis and all subsequent steps sensitively depend on it. For a successful interpretation of observed Alfvén eigenmodes it is vital that the equilibrium reconstruction is as close to the experimental conditions as possible. This includes the assessment of realistic density and temperature profiles. In the considered discharges at W7-AS the profiles differ significantly from parabolic profiles that were often assumed in previous studies. Qualitative changes of the Alfvén continua, modifying the mode numbers of possible eigenmodes as well as the relevance of continuum damping for these modes, consequently follow. In addition, the equilibrium is required for mapping of Mirnov probe positions to magnetic coordinates, the calculation of the velocity distribution function of energetic neutral beam ions and the determination of growth and damping rates of eigenmodes. The procedure that is used to reconstruct the ideal MHD equilibrium from measured pressure profiles that are made consistent with the measurements of other, independent diagnostics, has resulted in equilibria that are found to be in very good agreement with the observed Alfvén eigenmodes. A small number of exceptions from this general finding is observed and indicates the necessity of high-quality plasma profile diagnostics.

The identification of Alfvén eigenmodes is based on a direct comparison of mode numbers and frequencies to the Alfvén continuum, where only ideal MHD eigenmodes are considered because Kinetic Alfvén Eigenmodes are not expected in the plasma parameter regimes under consideration. The mode numbers were determined from Mirnov probes using the newly developed multi-dimensional Lomb periodogram that is capable of analyzing data of unevenly spaced probes with different sample rates. Limitations of

the Mirnov probes restrict a successful identification of ideal MHD Alfvén eigenmodes to low frequencies. GAEs were found to exist only transiently in the startup phase of low-shear discharges, while TAEs constitute the most frequently observed Alfvén instability, existing in a variety of experimental conditions. They are frequently destabilized the gradient region of the plasma. EAEs have been observed occasionally, a necessary parameter regime for their destabilization is not seen. The identification of high-frequency eigenmodes is difficult due to the complicated structure of the Alfvén continuum and the limitations of the Mirnov probe setup. Strong evidence of the observation of Energetic Particle Modes (EPMs) in the frequency range from 50...120 kHz, which is below the toroidal transit frequency of the most energetic NBI particles in W7-AS, has been found. The higher abundance of gap modes as compared to GAEs is not in contrast to previous studies, but reflects the change in the magnetic configuration in these late discharges.

The fast particle drive of TAEs by energetic ions could be reproduced by growth rate calculations based on a theoretical model that considers strongly localized eigenmodes with two dominant harmonics interacting with well-circulating particles. Despite these simplifications, the model describes the relative magnitudes of the various contributions to growth or damping rates quite well for optimized stellarators like W7-AS, but is expected to underestimate the damping rate due to the neglect of trapped electrons. The thermal ions contribute slightly to the growth rate through their diamagnetic drift which is sufficiently large due to the strong density gradients near the plasma boundary. Electron Landau damping can not be neglected in these cold discharges and provides the only damping mechanism. It was always larger than the drive by thermal ions, and without additional fast particle drive the modes would be stable. The energetic particles strongly destabilize the eigenmode through spatial gradients in their distribution. Velocity anisotropy drive is predicted to be small for well circulating particles and no evidence for positive velocity gradients in the distribution function, which are required for inverse Landau damping, is observed. The instability of GAEs and EAEs can not be explained by fast particle drive because the eigenmodes are found to have the wrong sign of mode numbers. In this case, the spatial gradient in the distribution function acts strongly stabilizing on these modes.

A degradation of the confinement of energetic ions by Alfvén eigenmodes is seen only exceptionally for ideal MHD eigenmodes. Correlations exist in case of two GAEs and one EAE. No losses are observed that are correlated to TAEs, even though strong wave-particle interactions, that provide the drive of the eigenmodes, is both, theoretically predicted and experimentally shown. This stands in contrast to the worst case estimate of ion losses caused by ideal MHD Alfvén eigenmodes as given in Ref. [11], where it was predicted that a significant fraction of energetic ions is radially redistributed and eventually expelled from the plasma by interaction with a TAE. Different from ideal MHD Alfvén eigenmodes, significant drops of plasma energy and severe fast ion losses are frequently observed for presumed EPMS, which are not eigenmodes of the ideal MHD force operator, but can be characterized as forced oscillations of the plasma due to the presence of a non-perturbative fraction of energetic ions.



# Chapter 7

## Summary

In the present thesis, a systematic study of beam driven Alfvén eigenmodes in high-density and low-temperature plasmas of the W7-AS stellarator is performed. The device went out of operation in 2002 and the study is based on stored experimental data. Alfvén instabilities can roughly be divided into ideal MHD Alfvén eigenmodes and those existing due to kinetic effects. The spectrum of ideal MHD Alfvén waves in toroidal fusion devices consists of a continuum of stable waves that are strongly localized. Weakly damped, discrete eigenmodes can exist in gaps of the continuous spectrum which are formed by plasma inhomogeneities and the coupling of Alfvén continua. This allows an identification of ideal MHD Alfvén eigenmodes in terms of their frequency and mode numbers. Kinetic effects can modify this spectrum and cause additional types of eigenmodes, the kinetic Alfvén eigenmodes (KAE) and energetic particle modes (EPM). The goal of this thesis is twofold: (I) identification and description of fast particle driven Alfvén instabilities in W7-AS, and (II) study of energetic particle losses induced by Alfvén instabilities.

The reconstruction of the ideal MHD plasma equilibrium for each discharge with sufficient accuracy is the very foundation of all subsequent steps. This is achieved, based on measured plasma parameter profiles that are further refined by validating them to the measurements of other, independent plasma diagnostics. The applied scheme is inspired by an approach of Integrated Data Analysis (IDA) to combine different diagnostic data and provide combined uncertainties. After mode number analysis and eigenmode identification, the theoretically expected, linear growth rate of the instability is calculated where possible, and the various contributions of the fast particle drive to the instability of the mode are identified.

Alfvénic activity recorded by the Mirnov diagnostic is analyzed, which consists of a set of spatially distributed coils that measure magnetic fluctuations. On W7-AS, the probes are arranged in three poloidal arrays at different toroidal positions. The spacing between the probes is non-equidistant. In addition, the signals of one probe array are digitized with a different sample rate. These characteristics prohibit the straight-forward use of standard tools available for harmonic analysis. Instead, a new

tool has been developed and thoroughly tested. It is a multi-dimensional extension of the Lomb periodogram, able to provide reliable time-resolved frequency and mode number spectra in the case of uneven datapoint spacing. Numerical studies of this periodogram show a good performance with respect to mode number resolution given the low number of available probes, and robustness against perturbations of the signal. Only two of the probe arrays can be used for the analysis of eigenmodes with frequencies  $> 70$  kHz, such that for high-frequency phenomena insufficient information about the mode numbers is available.

A total of 133 different Alfvén eigenmodes is studied in discharges from different experimental campaigns. A restriction to discharges from various high- $\beta$  campaigns with neutral beam heating is required to allow for a realistic reconstruction of plasma equilibrium and velocity distribution functions of energetic particles. The discharges are characterized by high density,  $n_e = 5 \cdot 10^{19} \text{m}^{-3}$  to  $2.5 \cdot 10^{20} \text{m}^{-3}$  at relatively low temperatures of  $T_e = T_i = 150 \dots 600$  eV. Alfvén eigenmodes often appear transiently in the startup phase of these discharges, where density and heating power are being ramped up. Occasionally, Alfvén eigenmodes are seen in the stationary, high- $\beta$  phase in the presence of considerable neutral beam heating.

Most of the Alfvén eigenmodes are successfully classified as ideal MHD eigenmodes. 19 global, 47 toroidicity-induced and 8 ellipticity-induced Alfvén eigenmodes (GAEs, TAEs, and EAEs, respectively) are unambiguously identified by their mode numbers and frequencies. Excellent agreement between experimentally observed mode number spectra and theoretically calculated eigenmode structure is shown for a TAE example. Additional 13 events are found to have frequencies inside the EAE gap and could possibly be EAEs. Evidence for high-frequency Alfvén eigenmodes (mirror- and helicity-induced Alfvén eigenmodes) is seen, but can not be proven rigorously due to uncertain mode numbers and the complexity of the Alfvén continuum. The remaining 41 Alfvén eigenmodes can not be classified to be one of the above cases. Reasons are either high frequencies, mode numbers obscured by far-field effects, or mode numbers that could not be related to ideal MHD Alfvén eigenmodes. A selection of these shows indications of strong non-linear wave-particle interactions and are assumed to be EPs. Kinetic Alfvén eigenmodes are not expected to exist in the experimental conditions that were studied.

The radially resolved velocity distribution function is used to describe the parameter regimes in which the modes are observed in terms of the dimensionless parameters  $v_b/v_A$  (beam velocity normalized to the Alfvén velocity) and  $\beta_{fast}/\beta_{th}$ , where  $\beta$  is the ratio of plasma pressure to magnetic pressure. The first parameter describes through which of the possible resonance velocities particles can interact with the eigenmode. A peculiarity of the fast particle dynamics in fusion devices is that they can resonantly interact with Alfvén eigenmodes through sideband resonances even if  $v < v_A$ . The second parameter describes the energy content of the destabilizing fast particle population compared to the potentially stabilizing thermal plasma component. These parameters contain relevant information about the instability of an eigenmode and such diagrams are given for all observed modes. In addition to that, the expected linear growth rate



of gap modes is calculated based on a theoretical model that extends the ideal MHD by a perturbative, drift-kinetic description of the energy exchange between waves and circulating particles, neglecting the effects of trapped particles. For the discharges under consideration the thermal electron speed is comparable to  $v_A$  and the electrons provide a significant Landau damping contribution. Due to strong density gradients near the plasma boundary in most of the discharges, the thermal ions can provide a small drive via the spatial inhomogeneity which does not overcome the electron damping, however. The drive by spatial inhomogeneity of thermal ions requires a certain propagation direction of the mode and is equally stabilizing for opposite mode numbers. The fast particles also contribute to the growth rate via spatial inhomogeneity, velocity gradients and velocity anisotropy terms are negligible in W7-AS. Most of the observed GAE or EAE modes have negative mode numbers, which correspond to a propagation direction for which the spatial inhomogeneity of thermal and beam ions is predicted to be stabilizing. A fast particle drive of these modes is not confirmed, whereas the TAEs are found to be strongly destabilized by neutral beam injection. The distribution of plasma parameters for discharges showing TAEs in terms of the dimensionless stability parameters suggests an instability threshold that is qualitatively confirmed by an exploration of the parameter space with the theoretical model.

Wave-induced, resonant losses of energetic ions scale linearly with the wave amplitude. To identify them, correlations between ion loss probe signals and wave amplitudes are searched, where correlation times in the order of the slowing-down time of energetic particles are expected. Significant correlations can be established only exceptionally for 3 of the identified ideal MHD Alfvén eigenmodes. Those Alfvén eigenmodes, however, which are assumed to be EPs frequently show severe losses of energetic ions that are visible in the time traces of the plasma energy as well.



# Appendix A

## Differential Geometry – a very small tutorial

### A.1 Reciprocal sets of vectors

An important building block for the description of vectors in curvilinear coordinates is the concept of reciprocal sets of vectors. Two sets of vectors,  $\mathbf{A}, \mathbf{B}, \mathbf{C}$  and  $\mathbf{a}, \mathbf{b}, \mathbf{c}$  are called *reciprocal sets of vectors*, if

$$\begin{aligned}\mathbf{A} \cdot \mathbf{a} &= \mathbf{B} \cdot \mathbf{b} = \mathbf{C} \cdot \mathbf{c} = 1 \\ \mathbf{A} \cdot \mathbf{b} &= \mathbf{A} \cdot \mathbf{c} = \mathbf{B} \cdot \mathbf{a} = \mathbf{B} \cdot \mathbf{c} = \mathbf{C} \cdot \mathbf{a} = \mathbf{C} \cdot \mathbf{b} = 0.\end{aligned}\tag{A.1}$$

This implies that both,  $\mathbf{A}, \mathbf{B}, \mathbf{C}$  and  $\mathbf{a}, \mathbf{b}, \mathbf{c}$  are each comprised of linearly independent vectors and that the respective triple products  $\mathbf{A} \cdot (\mathbf{B} \times \mathbf{C})$  and  $\mathbf{a} \cdot (\mathbf{b} \times \mathbf{c})$  are non-zero. Actually, Eq. (A.1) are necessary and sufficient conditions for both sets of vectors to be reciprocal. To find the vectors of one set  $\mathbf{a}, \mathbf{b}, \mathbf{c}$  in terms of the reciprocal set  $\mathbf{A}, \mathbf{B}, \mathbf{C}$ , we look at the conditions  $\mathbf{a} \cdot \mathbf{B} = \mathbf{a} \cdot \mathbf{C} = 0$ . This means that  $\mathbf{a}$  is perpendicular to both,  $\mathbf{B}$  and  $\mathbf{C}$ . Because  $\mathbf{B}$  and  $\mathbf{C}$  cannot be collinear vectors,  $\mathbf{a}$  must be  $\mathbf{a} = C \cdot (\mathbf{B} \times \mathbf{C})$ . Inserting this into  $\mathbf{a} \cdot \mathbf{A} = C \mathbf{A} \cdot (\mathbf{B} \times \mathbf{C}) = 1$ , one sees that the constant must be  $C^{-1} = \mathbf{A} \cdot (\mathbf{B} \times \mathbf{C})$ . Hence we have the inter-relationship:

$$\mathbf{a} = \frac{\mathbf{B} \times \mathbf{C}}{\mathbf{A} \cdot (\mathbf{B} \times \mathbf{C})} \quad \mathbf{b} = \frac{\mathbf{C} \times \mathbf{A}}{\mathbf{B} \cdot (\mathbf{C} \times \mathbf{A})} \quad \mathbf{c} = \frac{\mathbf{A} \times \mathbf{B}}{\mathbf{C} \cdot (\mathbf{A} \times \mathbf{B})}\tag{A.2}$$

The fact that both sets of vectors consist of linearly independent vectors spanning a non-zero volume can be used to utilize each of the sets as legitimate basis vectors in 3D. Indeed, any vector  $\mathbf{X}$  can be written as

$$\begin{aligned}\mathbf{X} &= (\mathbf{X} \cdot \mathbf{a}) \mathbf{A} + (\mathbf{X} \cdot \mathbf{b}) \mathbf{B} + (\mathbf{X} \cdot \mathbf{c}) \mathbf{C} \quad \text{or} \\ \mathbf{X} &= (\mathbf{X} \cdot \mathbf{A}) \mathbf{a} + (\mathbf{X} \cdot \mathbf{B}) \mathbf{b} + (\mathbf{X} \cdot \mathbf{C}) \mathbf{c}.\end{aligned}\tag{A.3}$$

In cartesian coordinates, the set of unit basis vectors  $\hat{\mathbf{i}}, \hat{\mathbf{j}}, \hat{\mathbf{k}}$  is reciprocal to itself. This implies that in such coordinates the vector  $\mathbf{X}$  can be written as  $\mathbf{X} = (\mathbf{X} \cdot \hat{\mathbf{i}}) \hat{\mathbf{i}} + (\mathbf{X} \cdot \hat{\mathbf{j}}) \hat{\mathbf{j}} + (\mathbf{X} \cdot \hat{\mathbf{k}}) \hat{\mathbf{k}}$ . Relation (A.3) is very important in the upcoming development of curvilinear coordinates.

## A.2 Curvilinear Coordinates

Consider a transformation  $\mathbf{R}(u^1, u^2, u^3)$  that describes any point in 3D space, by means of position vector  $\mathbf{R}$ , as a function of three parameters called (for the moment)  $u^1, u^2, u^3$ . If we expand  $\mathbf{R}$  in cartesian coordinates the transformation reads:

$$\begin{aligned} R(u^1, u^2, u^3) : \quad & x = x(u^1, u^2, u^3) \\ & y = y(u^1, u^2, u^3) \\ & z = z(u^1, u^2, u^3) \end{aligned} \tag{A.4}$$

The transformation is invertible if the functions  $x, y, z$  have continuous partial derivatives with respect to  $u^1, u^2$  and  $u^3$ , respectively, and if the Jacobian of the transformation is not zero. In this case the inverse transform is given by

$$u^1 = u^1(x, y, z), \quad u^2 = u^2(x, y, z), \quad u^3 = u^3(x, y, z) \tag{A.5}$$

This states that any position vector  $\mathbf{R}$  with cartesian coordinates  $(x, y, z)$  can be uniquely described by the independent parameters  $(u^1, u^2, u^3)$  which makes them coordinates as well. The reason for using superscripts will become clear below. The position of the indices is important.

As in every 3D coordinate system, curvilinear coordinates have three naturally occurring families of *coordinate surfaces*, obtained if one coordinate  $u^i$  is kept fixed while the other coordinates are varied continuously. Analogously, three families of *coordinate curves* are obtained by varying one coordinate  $u^j$  continuously while keeping the other coordinates fixed. The direction in which a point on the coordinate curve moves as  $u^j$  is increased is taken to be the positive direction along that coordinate curve. The coordinate system is called *orthogonal* if the coordinate curves intersect at right angles everywhere.

The coordinate system is determined completely only if the coordinate surfaces  $u^i = \text{const.}$  are known. Any coordinate curve  $u^j$  is uniquely determined by the intersection of the coordinate surfaces  $u^i = \text{const.}$  and  $u^k = \text{const.}$  where  $i, j, k$  are a permutation of 1, 2, 3, while it is generally not possible to reconstruct the coordinate surfaces from the coordinate curves alone.

### A.3 Co- and Contravariant Vector Components, Metric Coefficients

It is now possible to define a set of *tangent basis vectors* in point  $P$  described by position vector  $\mathbf{R}$  as any set of vectors  $\mathbf{e}_1, \mathbf{e}_2$  and  $\mathbf{e}_3$  with finite length that point in the positive direction of the coordinate curves. In other words, these basis vectors are tangent vectors to the coordinate curves in point  $P$ . Simple considerations show that  $\partial\mathbf{R}/\partial u^i$  is a tangent vector to the  $u^i$  coordinate curve. Hence the tangent basis vectors are defined by

$$\mathbf{e}_1 = \frac{\partial\mathbf{R}}{\partial u^1}, \quad \mathbf{e}_2 = \frac{\partial\mathbf{R}}{\partial u^2}, \quad \mathbf{e}_3 = \frac{\partial\mathbf{R}}{\partial u^3}. \quad (\text{A.6})$$

This basis is said to be *local* because, in general, the basis vectors vary from point to point. Again, the position of the index is important.

The gradient,  $\nabla u^i$  of a function  $u^i$  is defined so that the differential  $du^i$  is given by

$$du^i = \nabla u^i \cdot d\mathbf{R} = \sum_j \nabla u^i \frac{\partial\mathbf{R}}{\partial u^j} du^j = \nabla u^i \cdot \mathbf{e}_j du^j \quad (\text{A.7})$$

In the last step definition (A.6) has been used as well as the summation convention which says that if a letter appears twice, as sub- and as superscript index, on the same side of the equation, the equation is to be summed over all values of that index. Eq. (A.7) can hold if and only if

$$\nabla u^i \cdot \mathbf{e}_j = \delta_j^i.$$

This relation states that  $\nabla u^i$  and  $\mathbf{e}_j$  form reciprocal sets of vectors defined in (A.1). Therefore we define  $\nabla u^i$  as the *reciprocal basis vectors*

$$\nabla u^i \equiv \mathbf{e}^i \quad \mathbf{e}^i \cdot \mathbf{e}_j = \delta_j^i \quad (\text{A.8})$$

Normally, neither are  $\mathbf{e}^i$  and  $\mathbf{e}_j$  of unit length, nor are they perpendicular. It is important to note that, while  $\mathbf{e}_j$  are tangent vectors to the  $u^j$  coordinate curves, the vectors  $\mathbf{e}^i$  are perpendicular to the  $u^i = \text{const}$  coordinate surfaces. By means of Eq. (A.2) one set of basis vectors can be calculated if the other basis vectors are known.

According to Eq. (A.3), any vector  $\mathbf{D}$  can be written as a linear combination of the vectors of either of the sets of reciprocal sets of vectors:

$$\mathbf{D} = \left( \mathbf{D} \cdot \frac{\partial\mathbf{R}}{\partial u^i} \right) \nabla u^i = (\mathbf{D} \cdot \mathbf{e}_i) \mathbf{e}^i = D_i \mathbf{e}^i. \quad (\text{A.9})$$

which is an expansion of  $\mathbf{D}$  along the reciprocal basis vectors. Analogously,  $\mathbf{D}$  can be written as a linear combination of the tangent basis vectors:

$$\mathbf{D} = (\mathbf{D} \cdot \nabla u^i) \frac{\partial\mathbf{R}}{\partial u^i} = (\mathbf{D} \cdot \mathbf{e}^i) \mathbf{e}_i = D^i \mathbf{e}_i \quad (\text{A.10})$$

This shows that in curvilinear coordinates, there is more than one kind of components of a vector. The coefficients  $D_i$  appearing in (A.9) are called *covariant components* of the vector  $\mathbf{D}$ , while  $D^i$  in (A.10) are called the *contravariant components*.

Of course it's possible to write one set of basis vectors in terms of the other. Rewriting (A.9) and (A.10) with  $\mathbf{D} = \mathbf{e}_i$  and  $\mathbf{D} = \mathbf{e}^j$ , respectively, we get

$$\mathbf{e}_i = (\mathbf{e}_i \cdot \mathbf{e}_j) \mathbf{e}^j = g_{ij} \mathbf{e}^j \quad (\text{A.11a})$$

$$\mathbf{e}^j = (\mathbf{e}^j \cdot \mathbf{e}^k) \mathbf{e}_k = g^{jk} \mathbf{e}_k \quad (\text{A.11b})$$

The dot products of basis vectors are so important that they get their own symbols:

$$g_{ij} = \mathbf{e}_i \cdot \mathbf{e}_j, \quad g^{ij} = \mathbf{e}^i \cdot \mathbf{e}^j, \quad (\text{A.12})$$

they are called *metric coefficients*. From their definition can be seen that the metric coefficients are symmetric:  $g_{ij} = g_{ji}$  and  $g^{ij} = g^{ji}$ . These coefficients contain all relevant information about the metric in a curvilinear coordinate system, hence their name. This can be shown by looking at the differential arc length  $dl$  along a curve

$$(dl)^2 = |d\mathbf{R}|^2 = d\mathbf{R} \cdot d\mathbf{R}.$$

with the differential vector  $d\mathbf{R}$  given by

$$d\mathbf{R} = \frac{\partial \mathbf{R}}{\partial u^1} du^1 + \frac{\partial \mathbf{R}}{\partial u^2} du^2 + \frac{\partial \mathbf{R}}{\partial u^3} du^3 = \mathbf{e}_j du^j$$

so that  $(dl)^2$  is given by

$$(dl)^2 = \sum_{i,j} (\mathbf{e}_i \cdot \mathbf{e}_j) du^i du^j = g_{ij} du^i du^j. \quad (\text{A.13})$$

Expressing the covariant (contravariant) components of a vector in terms of the contravariant (covariant) components is a straightforward matter using the metric coefficients:

$$D_i = \mathbf{D} \cdot \mathbf{e}_i = (D^j \mathbf{e}_j) \cdot \mathbf{e}_i = g_{ji} D^j = g_{ij} D^j \quad (\text{A.14a})$$

$$D^k = \mathbf{D} \cdot \mathbf{e}^k = (D_i \mathbf{e}^i) \cdot \mathbf{e}^k = g^{ik} D_i = g^{ki} D_i \quad (\text{A.14b})$$

There is an interesting relationship between the metric coefficients and the Kronecker delta. Consider Eq. (A.11a),  $\mathbf{e}_i = g_{ij} \mathbf{e}^j$ , dot multiplied with  $\mathbf{e}^k$ :

$$\delta_i^k = \mathbf{e}_i \cdot \mathbf{e}^k = g_{ij} \mathbf{e}^j \cdot \mathbf{e}^k = g_{ij} g^{jk} = g_i^k$$

This relation states that the mixed metric coefficients  $g_i^j$  have the same values, 0 or 1, as the Kronecker delta  $\delta_i^j$ , which originates from the fact that  $\mathbf{e}_i$  and  $\mathbf{e}^j$  are reciprocal sets of vectors.

The metric coefficients  $g_{ij}$  can be used to form a matrix denoted by  $[g_{ij}]$  (similarly for  $g^{kl}$  and  $[g^{kl}]$ ). The product of the matrices  $C = [g_{ij}][g^{kl}]$  equals the identity matrix because of  $C(a, b) = \sum_n g_{an}g^{nb} = g_a^b = \delta_a^b$ . From this immediately follows that  $[g^{kl}]$  is the inverse of  $[g_{ij}]$ . From linear algebra it's known that the determinants satisfy the following relationship:

$$\det[g_{ij}] =: g, \quad \det[g^{kl}] = g^{-1}. \quad (\text{A.15})$$

Now consider the coordinate transform (A.5). The Jacobian  $J$  of the transform is defined as the determinant of the nine partial derivatives  $\partial \mathbf{R}(i)/\partial u^j$ :

$$J = \begin{vmatrix} \partial x/\partial u^1 & \partial x/\partial u^2 & \partial x/\partial u^3 \\ \partial y/\partial u^1 & \partial y/\partial u^2 & \partial y/\partial u^3 \\ \partial z/\partial u^1 & \partial z/\partial u^2 & \partial z/\partial u^3 \end{vmatrix} \quad (\text{A.16})$$

The triple product  $\mathbf{A} \cdot (\mathbf{B} \times \mathbf{C})$  can be written in determinant form with the components  $A_x, A_y, A_z, \dots$  as matrix elements. This allows to write Eq. (A.16) in a more compact form:

$$J = \frac{\partial \mathbf{R}}{\partial u^1} \cdot \frac{\partial \mathbf{R}}{\partial u^2} \times \frac{\partial \mathbf{R}}{\partial u^3} \quad (\text{A.17})$$

The Jacobian of the inverse transform is equally given by the determinant of the matrix of partial derivatives:

$$J^{\text{inv}} = \begin{vmatrix} \partial x/\partial u^1 & \partial x/\partial u^2 & \partial x/\partial u^3 \\ \partial y/\partial u^1 & \partial y/\partial u^2 & \partial y/\partial u^3 \\ \partial z/\partial u^1 & \partial z/\partial u^2 & \partial z/\partial u^3 \end{vmatrix} \quad (\text{A.18})$$

The elements  $\partial u^i/\partial x$ ,  $\partial u^i/\partial y$  and  $\partial u^i/\partial z$  are the cartesian components of  $\nabla u^i$ . Hence,

$$J^{\text{inv}} = \nabla u^1 \cdot \nabla u^2 \times \nabla u^3 \quad (\text{A.19})$$

Starting from (A.19) and substituting  $\nabla u^i = \mathbf{e}^i = \mathbf{e}_j \times \mathbf{e}_k / \mathbf{e}_i \cdot (\mathbf{e}_j \times \mathbf{e}_k) = \mathbf{e}_j \times \mathbf{e}_k / J$ , it can be shown that, as expected because  $\partial \mathbf{R}/\partial u^i$  and  $\nabla u^i$  are reciprocal sets of vectors,  $J^{\text{inv}} = J^{-1}$ .

A relationship between  $g$  and  $J$  can be established by looking at the elements  $g_{ij}$  of the matrix of which  $g$  is the determinant (A.11):

$$g_{ij} = \mathbf{e}_i \cdot \mathbf{e}_j = \frac{\partial \mathbf{R}}{\partial u^i} \cdot \frac{\partial \mathbf{R}}{\partial u^j}.$$

If we write  $x = \mathbf{R}(1)$ ,  $y = \mathbf{R}(2)$ ,  $z = \mathbf{R}(3)$ , then

$$g_{ij} = \sum_n \frac{\partial \mathbf{R}(n)}{\partial u^i} \cdot \frac{\partial \mathbf{R}(n)}{\partial u^j}. \quad (\text{A.20})$$

This relation states that  $[g_{ij}]$  can formally be thought of as the product of two matrices. It is a theorem of linear algebra that the determinant of a product matrix equals the product of the determinants of the factors:

$$g = \det[g_{ij}] = \left( \det \left[ \frac{\partial \mathbf{R}(n)}{\partial u^i} \right] \right) \left( \det \left[ \frac{\partial \mathbf{R}(n)}{\partial u^j} \right] \right) = J^2$$

This yields the important relationship

$$g = J^2 \quad \text{or} \quad J = \sqrt{g}. \quad (\text{A.21})$$

## A.4 Tensors

The most simple introduction to tensors makes use of the dot-product operation between vectors. A *simple second order tensor* or *dyad* is defined via the relation

$$\mathbf{X} \cdot \mathbf{AB} = (\mathbf{X} \cdot \mathbf{A})\mathbf{B} \quad \mathbf{AB} \cdot \mathbf{Y} = \mathbf{A}(\mathbf{B} \cdot \mathbf{Y}) \quad (\text{A.22})$$

The notation for a dyad is a simple juxtaposition,  $\mathbf{AB}$ , of the vectors making up the dyad without any symbol in between. Another notation is  $\mathbf{A} \otimes \mathbf{B}$ ; here  $\otimes$  is called the tensor product or the outer product.

From the definition (A.22), it follows that the order of the vectors making up a dyad is important. It also explains why the dot product of a vector with a dyad is, in general, not commutative:

$$\begin{aligned} \mathbf{X} \cdot \mathbf{AB} &= (\mathbf{X} \cdot \mathbf{A})\mathbf{B} \sim \mathbf{B} \\ \mathbf{X} \cdot \mathbf{BA} &= (\mathbf{X} \cdot \mathbf{B})\mathbf{A} \sim \mathbf{A} \\ \mathbf{AB} \cdot \mathbf{X} &= \mathbf{A}(\mathbf{B} \cdot \mathbf{X}) \sim \mathbf{A} \end{aligned}$$

The vectors  $\mathbf{A}$  and  $\mathbf{B}$  can, as usual, be expanded along a set of basis vectors. This leads to four possible forms of component descriptions of a dyad:

$$\mathbf{AB} = \begin{cases} A_i B_j \mathbf{e}^i \mathbf{e}^j = D_{ij} \mathbf{e}^i \mathbf{e}^j & D_{ij} : \text{covariant components} \\ A^i B^j \mathbf{e}_i \mathbf{e}_j = D^{ij} \mathbf{e}_i \mathbf{e}_j & D^{ij} : \text{contravariant components} \\ A_i B^j \mathbf{e}^i \mathbf{e}_j = D_i^j \mathbf{e}^i \mathbf{e}_j & D_i^j, D_{\cdot j}^i : \text{mixed components} \\ A^i B_j \mathbf{e}_i \mathbf{e}^j = D_{\cdot j}^i \mathbf{e}_i \mathbf{e}^j \end{cases} \quad (\text{A.23})$$

The dot in the indices of the mixed components of the dyad is important to indicate which index comes first. Otherwise,  $D_i^j$  could be interpreted as either the component of  $D_i^j \mathbf{e}^i \mathbf{e}_j$  or as the component of  $D_{\cdot j}^i \mathbf{e}_i \mathbf{e}^j$ . Since the order of vectors making up the dyad matters, these two are generally different. There are nine different combinations of either,  $D_{ij}$ ,  $D^{ij}$ ,  $D_i^j$  and  $D_{\cdot j}^i$ ,  $i, j = 1, 2, 3$  – therefore the component description of a second order tensor is sometimes called the *nonian form*.

Consider now a general second order tensor  $\overleftrightarrow{\mathbf{D}}$  or *dyadic*

$$\overleftrightarrow{\mathbf{D}} = D_{ij} \mathbf{e}^i \mathbf{e}^j = D^{ij} \mathbf{e}_i \mathbf{e}_j = D_i^j \mathbf{e}^i \mathbf{e}_j = D_{\cdot j}^i \mathbf{e}_i \mathbf{e}^j. \quad (\text{A.24})$$



A general second order tensor cannot always be written as a single dyad. It can, however, be written as a sum of three dyads. Let  $\mathbf{A}$ ,  $\mathbf{B}$  and  $\mathbf{C}$  be any three vectors that have a non-zero triple product  $\mathbf{A} \cdot (\mathbf{B} \times \mathbf{C}) \neq 0$ . It's then possible to find three vectors  $\mathbf{X}$ ,  $\mathbf{Y}$  and  $\mathbf{Z}$  such that [91]

$$\overleftrightarrow{\mathbf{D}} = \mathbf{X}\mathbf{A} + \mathbf{Y}\mathbf{B} + \mathbf{Z}\mathbf{C}. \quad (\text{A.25})$$

Calculations including vectors and second order tensors can be done by expansion in appropriate co- and contravariant components and by reminding the relation  $\mathbf{e}_i \cdot \mathbf{e}^j = \delta_i^j$ :

$$\mathbf{X} \cdot \overleftrightarrow{\mathbf{D}} = X_i D^{jk} \mathbf{e}^i \cdot \mathbf{e}_j \mathbf{e}_k = X_i D^{ik} \mathbf{e}_k = Y^k \mathbf{e}_j = \mathbf{Y} \quad (\text{A.26a})$$

$$\overleftrightarrow{\mathbf{D}} \cdot \mathbf{X} = D^{ij} X_k \mathbf{e}_i \mathbf{e}_j \cdot \mathbf{e}^k = D^{ik} X_k \mathbf{e}_i = Z^i \mathbf{e}_i = \mathbf{Z} \quad (\text{A.26b})$$

$$\mathbf{E} \cdot \overleftrightarrow{\mathbf{D}} \cdot \mathbf{F} = E^i D_{jk} F^l \mathbf{e}_i \cdot \mathbf{e}^j \mathbf{e}^k \cdot \mathbf{e}_l = E^i D_{ik} F^k = \text{number} \quad (\text{A.26c})$$

The last relation can be used for the expansion of a general second order tensor in components. Upon substituting  $\mathbf{E}$  and  $\mathbf{F}$  by tangent or reciprocal basis vectors as needed, Eq. (A.26c) gives:

$$\begin{aligned} D_{ij} &= \mathbf{e}_i \cdot \overleftrightarrow{\mathbf{D}} \cdot \mathbf{e}_j, & D^{ij} &= \mathbf{e}^i \cdot \overleftrightarrow{\mathbf{D}} \cdot \mathbf{e}^j, \\ D_{i \cdot j} &= \mathbf{e}_i \cdot \overleftrightarrow{\mathbf{D}} \cdot \mathbf{e}^j, & D^i_{\cdot j} &= \mathbf{e}^i \cdot \overleftrightarrow{\mathbf{D}} \cdot \mathbf{e}_j. \end{aligned} \quad (\text{A.27})$$

As in the case of vectors, conversion between covariant, contravariant and mixed components of a tensor involves metric coefficients, i.e.

$$\begin{aligned} D^{ij} &= \mathbf{e}^i \cdot \overleftrightarrow{\mathbf{D}} \cdot \mathbf{e}^j = \mathbf{e}^i \cdot (D_{kl} \mathbf{e}^k \mathbf{e}^l) \cdot \mathbf{e}^j = D_{kl} \mathbf{e}^i \cdot \mathbf{e}^k \mathbf{e}^l \cdot \mathbf{e}^j = g^{ik} D_{kl} g^{lj} \\ &= \mathbf{e}^i \cdot (D_{\cdot l}^k \mathbf{e}_k \mathbf{e}^l) \cdot \mathbf{e}^j = D_{\cdot l}^k \mathbf{e}^i \cdot \mathbf{e}_k \mathbf{e}^l \cdot \mathbf{e}^j = D_{\cdot l}^i g^{lj} \\ &= \mathbf{e}^i \cdot (D_k^{\cdot l} \mathbf{e}^k \mathbf{e}_l) \cdot \mathbf{e}^j = D_k^{\cdot l} \mathbf{e}^i \cdot \mathbf{e}^k \mathbf{e}_l \cdot \mathbf{e}^j = g^{ik} D_k^{\cdot j} \end{aligned} \quad (\text{A.28})$$

Here eq. (A.27) and  $\mathbf{e}^i \cdot \mathbf{e}_j = \delta_j^i$  have been used.

To complete the short discussion of tensors it is worth noting that the metric coefficients  $g_{ij}$ ,  $g^{kl}$  and  $g_n^m$  are themselves legitimate components of a second order tensor – the so called *metric tensor*  $\overleftrightarrow{\mathbf{g}}$ .

## A.5 Important Vector Identities in Curvilinear Coordinates

**The dot product between vectors** can be "shifted" to dot products between the basis vectors by expanding the vectors in components:

$$\begin{aligned} \mathbf{A} \cdot \mathbf{B} &= A^i B_j \mathbf{e}_i \cdot \mathbf{e}^j = A^i B_j \delta_i^j = A^i B_i \\ &= A_i B^j \mathbf{e}^i \cdot \mathbf{e}_j = A_i B^j \delta_j^i = A_i B^i \\ &= A^i B^j \mathbf{e}_i \cdot \mathbf{e}_j = A^i B^j g_{ij} \\ &= A_i B_j \mathbf{e}^i \cdot \mathbf{e}^j = A_i B_j g^{ij} \end{aligned} \quad (\text{A.29})$$

**The cross product between vectors** can also be expressed by cross products between basis vectors. Care must be taken to expand both vectors along the same basis:

$$\mathbf{A} \times \mathbf{B} = A^i B^j \mathbf{e}_i \times \mathbf{e}_j = A_i B_j \mathbf{e}^i \times \mathbf{e}^j$$

Here, summation over  $i$  and  $j$  is implied. Upon noting that  $\mathbf{e}_k = \epsilon^{ijk} J \mathbf{e}^i \times \mathbf{e}^j$  and  $\mathbf{e}^k = \epsilon_{ijk} J^{-1} \mathbf{e}_i \times \mathbf{e}_j$ , where  $\epsilon_{ijk}$  and  $\epsilon^{ijk}$  are the well known Levi-Civita symbols that evaluate to 1 (−1) for  $i, j, k$  an even (uneven) permutation of 1, 2, 3 and 0 otherwise, this can be rewritten in more compact form:

$$(\mathbf{A} \times \mathbf{B})_k = \epsilon^{ijk} J A_i B_j \quad (\text{A.30a})$$

$$(\mathbf{A} \times \mathbf{B})^k = \epsilon_{ijk} J^{-1} A^i B^j \quad (\text{A.30b})$$

**The Del operator** is a generalization of the *Nabla* operator in cartesian coordinates and is denoted by the same symbol  $\nabla$ . In curvilinear coordinates it can formally be introduced via the relationship  $d\Phi = \nabla\Phi \cdot d\mathbf{R}$ . Observing that  $\mathbf{e}^i \cdot \mathbf{e}_j = \delta_j^i$ ,  $d\Phi$  can be expanded via the chain rule to give:

$$d\Phi = \frac{\partial\Phi}{\partial u^i} du^i = \frac{\partial\Phi}{\partial u^i} \mathbf{e}^i \cdot \mathbf{e}_j du^j = \left( \mathbf{e}^i \frac{\partial}{\partial u^i} \right) \Phi \cdot \mathbf{e}_j du^j = \nabla\Phi \cdot d\mathbf{R}.$$

A comparison of the last two terms shows that  $\nabla$  can be identified with  $\mathbf{e}^i \partial / \partial u^i$ . The Del operator operates on everything on its right, except when brackets indicate otherwise. The *gradient* of a scalar field  $\Phi(u^1, u^2, u^3)$  is obtained by operating  $\nabla$  on  $\Phi$ :

$$\text{grad } \Phi = \nabla\phi = \frac{\partial\Phi}{\partial u^i} \mathbf{e}^i. \quad (\text{A.31})$$

The dot product of the  $\nabla$ -operator with a vector field is called *divergence* of the vector field and is given by:

$$\text{div}\mathbf{A} = \nabla \cdot \mathbf{A} = \frac{1}{J} \frac{\partial}{\partial u^i} (J A^i). \quad (\text{A.32})$$

Different derivations of this formula can be found in many text books about differential geometry. The *curl* of a vector field is obtained as the cross product of the  $\nabla$ -operator with a vector  $\mathbf{A}$ .

$$\begin{aligned} \text{rot}\mathbf{A} &= \nabla \times \mathbf{A} \\ &= \nabla \times (A_j \mathbf{e}^j) = A_j (\nabla \times \mathbf{e}^j) + \nabla A_j \times \mathbf{e}^j = 0 + \frac{\partial A_j}{\partial u^i} \mathbf{e}^i \times \mathbf{e}^j \end{aligned}$$

Here,  $\nabla \times \mathbf{e}^j = \nabla \times \nabla u^j \equiv 0$  and  $\nabla \equiv \mathbf{e}^i \partial / \partial u^i$  were used. This can be further simplified, by using the  $e_i \leftrightarrow e^i$  formalism, to give:

$$(\nabla \times \mathbf{A})_k = \epsilon^{ijk} J^{-1} \frac{\partial A_j}{\partial u^i}. \quad (\text{A.33})$$

**The parallel and perpendicular components of a vector**  $\mathbf{A}$  with respect to the ambient magnetic field  $\mathbf{B}$  are often required and are denoted by  $A_{\parallel}$  and  $\mathbf{A}_{\perp}$ , respectively. The dot product is equivalent to the orthogonal projection of one vector onto the other. Consequently, the parallel component  $A_{\parallel}$  is simply:

$$A_{\parallel} = \frac{\mathbf{A} \cdot \mathbf{B}}{|\mathbf{B}|} = \mathbf{b} \cdot \mathbf{A} \quad (\text{A.34})$$

where  $\mathbf{b}$  is the unit vector along  $\mathbf{B}$ . The component of  $\mathbf{A}$  perpendicular to  $\mathbf{B}$  is given by:

$$\mathbf{A}_{\perp} = -\mathbf{b} \times (\mathbf{b} \times \mathbf{A}). \quad (\text{A.35})$$



# Appendix B

## Boozers magnetic coordinates

### B.1 Covariant B Components

In section 2.1.4 it was shown that the contravariant components of  $\mathbf{B}$  can be related to the magnetic fluxes as follows:  $B^\rho = 0$ ,  $B^\theta = \dot{\Psi}_{pol}^r / 2\pi\sqrt{g_f}$  and  $B^\phi = \dot{\Psi}_{tor} / 2\pi\sqrt{g_f}$ . It is possible to find similar expressions for the covariant  $\mathbf{B}$  components that involve the poloidal and toroidal currents, respectively.

Consider Ampère's law,  $\mu_0 \mathbf{J} = \nabla \times \mathbf{B}$ , which is an inhomogeneous vector differential equation with a source term  $\mu_0 \mathbf{J}$ . The solution of this partial differential equation consists of two terms, the solution  $\mathbf{B}_0$  of the homogeneous equation, and a particular solution  $\mathbf{B}_J$  of the inhomogeneous problem.  $\mathbf{B}_0$  must satisfy  $\nabla \times \mathbf{B}_0 = 0$  which suggests that  $B_0$  can be written as the gradient of a *scalar magnetic potential* in vacuum,  $B_0 = \nabla\Phi$ . This scalar magnetic potential in vacuum is generated completely by exterior currents. Because  $\mathbf{B}_0$  is a physical quantity, it must be single valued. This again can be used to determine the form  $\Phi$  must have:  $\Phi = \Phi' + \tilde{\Phi}$ . Here,  $\tilde{\Phi}$  is periodic in  $(\theta_f, \phi_f)$  and  $\Phi'$  is the secular part. Ampère's law in integral form,  $\oint \mathbf{B} \cdot d\mathbf{l} = \mu_0 \mathbf{I}$ , can be used to determine the secular terms in  $\Phi$ . Any closed integration loop in poloidal direction does not encircle any currents and hence,  $B_{\theta_f} = 0$ . Any closed integration loop that encircles the major axis, however, contains the toroidal field coil currents and therefore  $2\pi B_{\phi_f} = \mu_0 \sum I_{coils}$ . This gives rise to a secular term proportional to  $\phi_f$  in  $\Phi$ :  $\Phi = \mu_0/2\pi \sum (I_{coils})\phi_f + \tilde{\Phi}$ . All coils that wrap around in toroidal direction but stay outside of the torus give rise to a single-valued potential only. The helical windings in classical stellarators carry currents in different directions that cancel in any closed integration path in toroidal direction, giving rise to a periodic potential as well.

In contrast to an ordinary partial differential equation, the particular solution  $\mathbf{B}_J$  must be a correct physical solution because, due to the vector identity  $\nabla \times \nabla\Phi \equiv 0$ , the homogeneous solution vanishes everywhere. The solution to the inhomogeneous

problem,  $\mu_0 \mathbf{J} = \nabla \times \mathbf{B}_J$ , requires knowledge of the contravariant  $\mathbf{J}$  components:

$$J^i = \frac{1}{\mu_0} (\nabla \times \mathbf{B}_J)^i = \frac{1}{\mu_0 \sqrt{g}} \left( \frac{\partial B_k}{\partial u^j} - \frac{\partial B_j}{\partial u^k} \right) \quad (\text{B.1})$$

From the MHD force balance equation,  $\nabla p = \mathbf{J} \times \mathbf{B}$ , one again immediately sees that  $\mathbf{J} \cdot \nabla \mathbf{p} = 0$  which states that  $\mathbf{J}$  lies in the flux surface as well. Hence,  $\mathbf{J} \cdot \nabla \rho = 0$ . Charge conservation yields  $\nabla \cdot \mathbf{J} = 0$ . Similar relations were used for the magnetic field in the last section. Again, it can be shown that the non-vanishing contravariant  $\mathbf{J}$  components are not independent of each other:

$$\frac{\partial}{\partial \theta}(\sqrt{g} J^\phi) + \frac{\partial}{\partial \phi}(\sqrt{g} J^\theta) = 0 \quad (\text{B.2})$$

which allows to introduce a function  $\eta = \eta(\rho, \theta, \phi)$  to write  $\mathbf{J}$  in the same form as the magnetic field:

$$\mathbf{J} = \nabla \rho \times \nabla \eta. \quad (\text{B.3})$$

Again,  $J^\theta$  and  $J^\phi$  are related to  $\eta$  via

$$J^\theta = \frac{-1}{\sqrt{g}} \frac{\partial \eta}{\partial \phi}, \quad J^\phi = \frac{1}{\sqrt{g}} \frac{\partial \eta}{\partial \theta}. \quad (\text{B.4})$$

$\eta$  is subject to similar restrictions with respect to the single-valuedness as  $\nu$ , therefore the most general form for  $\eta$  is

$$\eta(\rho, \theta, \phi) = a(\rho) \theta + b(\rho) \phi + \tilde{\eta}(\rho, \theta, \phi) \quad (\text{B.5})$$

One can now define the poloidal ribbon current and the toroidal current inside the flux surface as:

$$I_{pol}^r = \iint_{S_{pol}} \mathbf{J} \cdot d\mathbf{S} = \iiint_V (\mathbf{J} \cdot \nabla \theta) d^3 R, \quad (\text{B.6a})$$

$$I_{tor} = \iint_{S_{tor}} \mathbf{J} \cdot d\mathbf{S} = \iiint_V (\mathbf{J} \cdot \nabla \phi) d^3 R \quad (\text{B.6b})$$

to obtain  $\eta(\rho, \theta, \phi) = \dot{I}_{tor}(\rho) \theta / 2\pi - \dot{I}_{pol}^r(\rho) \phi / 2\pi + \tilde{\eta}(\rho, \theta, \phi)$ . If  $\tilde{\eta}$  would be constant on the flux surface,  $(\theta, \phi)$  would be *straight current density line* coordinates. Because this is, however, not generally the case, the contravariant  $\mathbf{J}$  components are:

$$J^\rho = 0, \quad J^\theta = \frac{\dot{I}_{pol}^r}{2\pi \sqrt{g}} + \frac{\partial \eta}{\partial \phi}, \quad J^\phi = \frac{\dot{I}_{tor}}{2\pi \sqrt{g}} + \frac{\partial \eta}{\partial \theta}. \quad (\text{B.7})$$

Upon substituting these into (B.1), one sees that the choice

$$(\mathbf{B}_J)_\rho = -\mu_0 \tilde{\eta}(\rho, \theta_f, \phi_f), \quad (\mathbf{B}_J)_{\theta_f} = \frac{\mu_0}{2\pi} \dot{I}_{tor}(\rho), \quad (\mathbf{B}_J)_{\phi_f} = \frac{-\mu_0}{2\pi} \dot{I}_{pol}^r(\rho) \quad (\text{B.8})$$

is a particular solution of the inhomogeneous problem. It must still be checked that this solution is indeed the physical solution. This can be done by applying Ampère's law in integral form on a closed integration path along a coordinate curve. At first this is done along the poloidal coordinate curve:

$$\oint_{\text{along } \theta_f} \mathbf{B} \cdot d\mathbf{l} = \oint B_j \mathbf{e}^j \cdot \mathbf{e}_{\theta_f} d\theta_f = \int_0^{2\pi} B_{\theta_f} d\theta_f = \mu_0 I_{tor}(\rho) \quad (\text{B.9})$$

Doing the same along the  $\phi_f$  coordinate gives the result that  $\int_0^{2\pi} d\phi_f = \mu_0 I_{pol}^{out}(\rho) = \mu_0(I_{pol}^p - I_{pol}^r(\rho))$ . Here,  $I_{pol}^{out}(\rho)$  is the poloidal current outside of the flux surface  $\rho = \text{const.}$  and  $I_{pol}^p$  is the total poloidal plasma current. One sees that an additional integration constant  $\mu_0 I_{pol}^p/2\pi$  is needed to make  $B_{\phi_f}$  a physical quantity.

The homogeneous and the inhomogeneous solution can now be put together. It is convenient to introduce a measure for the total poloidal current made up by the poloidal plasma current and the poloidal current through the external toroidal field coils. This current, denoted  $I_{pol}^d$  is the poloidal current *outside of a flux surface* through a disk touching the magnetic axis. It is given by  $I_{pol}^d = (I_{pol}^p - I_{pol}^r) + \sum I_{coils} = I_{pol}^{out} + \sum I_{coils}$ . By doing so, the scalar magnetic potential becomes purely periodic and the external coil currents are absorbed in the integration constant of the inhomogeneous solution. Finally, the covariant  $\mathbf{B}$  components are:

$$B_\rho = -\mu_0 \tilde{\eta}(\rho, \theta_f, \phi_f) + \frac{\partial \tilde{\Phi}(\rho, \theta_f, \phi_f)}{\partial \rho} \quad (\text{B.10a})$$

$$B_{\theta_f} = \frac{\mu_0}{2\pi} I_{tor}(\rho) + \frac{\partial \tilde{\Phi}(\rho, \theta_f, \phi_f)}{\partial \theta_f} \quad (\text{B.10b})$$

$$B_{\phi_f} = \frac{-\mu_0}{2\pi} I_{pol}^d(\rho) + \frac{\partial \tilde{\Phi}(\rho, \theta_f, \phi_f)}{\partial \phi_f} \quad (\text{B.10c})$$

## B.2 Boozer Coordinates

Boozer uses the freedom provided by (2.20) to make the periodic part of the scalar magnetic potential vanish. This will lead to a new Jacobian that is specifically simple. To find the new *boozer coordinates*  $(\theta_b, \phi_b)$ , one can look at the inverse new Jacobian

$(\sqrt{g_b})^{-1} = \nabla \rho \cdot (\nabla \theta_b \times \nabla \phi_b)$ . Upon substituting (2.20) into this expression,

$$\begin{aligned}
(\sqrt{g_b})^{-1} &= \nabla \rho \cdot [\nabla(\theta_f + \dot{\Psi}_{pol}^r G_b) \times \nabla(\phi_f + \dot{\Psi}_{tor} G_b)] \\
&= \nabla \rho \cdot (\nabla \theta_f \times \nabla \phi_f) + \dot{\Psi}_{pol}^r \nabla \rho \cdot (\nabla G_b \times \nabla \phi_f) \\
&\quad + \dot{\Psi}_{tor} \nabla \rho \cdot (\nabla \theta_f \times \nabla G_b) \\
&= (\sqrt{g_f})^{-1} + \dot{\Psi}_{pol}^r (\nabla \phi_f \times \nabla \rho) \cdot \nabla G_b + \dot{\Psi}_{tor} (\nabla \rho \times \nabla \theta_f) \cdot \nabla G_b \\
&= (\sqrt{g_f})^{-1} + 2\pi \left( \frac{\dot{\Psi}_{pol}^r}{2\pi} \frac{\mathbf{e}_{\theta_f}}{\sqrt{g_f}} \cdot \nabla G_b + \frac{\dot{\Psi}_{tor}}{2\pi} \frac{\mathbf{e}_{\phi_f}}{\sqrt{g_f}} \cdot \nabla G_b \right) \\
&= (\sqrt{g_f})^{-1} + 2\pi \mathbf{B} \cdot \nabla G_b
\end{aligned} \tag{B.11}$$

is obtained. Here, the previously derived expressions for  $B^i$  and  $\mathbf{e}_i = (\nabla u^j \times \nabla u^k) / \sqrt{g}$  were used. An expression for  $\sqrt{g_f}$  and  $\sqrt{g_b}$  can be found by looking at the dot product of  $\mathbf{B}$  with itself:

$$\begin{aligned}
(B)^2 &= \mathbf{B} \cdot \mathbf{B} = B^i B_i \\
&= \frac{\mu_0}{4\pi^2 \sqrt{g_f}} (\dot{\Psi}_{pol}^r I_{tor} + \dot{\Psi}_{tor} I_{pol}^d) + \mathbf{B} \cdot \nabla \tilde{\Phi}.
\end{aligned} \tag{B.12}$$

Solving this for  $\sqrt{g_f}$  yields:

$$\sqrt{g_f} = \frac{\mu_0}{4\pi^2} \frac{\dot{\Psi}_{pol}^r I_{tor} + \dot{\Psi}_{tor} I_{pol}^d}{(B)^2 - \mathbf{B} \cdot \nabla \tilde{\Phi}} \tag{B.13a}$$

$$\sqrt{g_b} = \frac{\mu_0}{4\pi^2} \frac{\dot{\Psi}_{pol}^r I_{tor} + \dot{\Psi}_{tor} I_{pol}^d}{(B)^2} \tag{B.13b}$$

because  $\tilde{\Phi} \equiv 0$  in boozers coordinates. When these Jacobians are substituted into (B.11), the equation can be simplified to

$$\mathbf{B} \cdot \nabla G_b = \frac{2\pi}{\mu_0} \frac{\mathbf{B} \cdot \nabla \tilde{\Phi}}{\dot{\Psi}_{pol}^r I_{tor} + \dot{\Psi}_{tor} I_{pol}^d}. \tag{B.14}$$

This equation has the simple solution

$$G_b = \frac{2\pi}{\mu_0} \frac{\tilde{\Phi}}{\dot{\Psi}_{pol}^r I_{tor} + \dot{\Psi}_{tor} I_{pol}^d}, \tag{B.15}$$

which allows the unique determination of Boozers flux coordinates  $(\theta_b, \phi_b)$ .

For a special choice of the flux label,  $\rho \equiv \Psi_{tor}$ , the Jacobian in boozers coordinates can be further simplified by using the definition of  $\iota$  (2.19):

$$\left( \sqrt{g_b(\Psi, \theta, \phi)} \right)^{-1} = \dot{\Psi}_{tor} \nabla \rho \cdot (\nabla \theta_b \times \nabla \phi_b) = \dot{\Psi}_{tor} \left( \sqrt{g_b(\rho, \theta, \phi)} \right)^{-1}, \tag{B.16a}$$



$$\sqrt{g_b} = \frac{\mu_0}{4\pi^2 \dot{\Psi}_{tor}} \frac{\dot{\Psi}_{pol}^r I_{tor} + \dot{\Psi}_{tor} I_{pol}^d}{(B)^2} = \frac{\mu_0}{4\pi^2} \frac{t I_{tor} + I_{pol}^d}{(B)^2}. \quad (\text{B.16b})$$

The important result is the following. Because  $t$ ,  $I_{tor}$  and  $I_{pol}^d$  are flux surface quantities, on any given flux surface Boozers Jacobian is only a function of  $(B)^2$  :  $\sqrt{g_b} \sim B^{-2}$ . This simple Jacobian and the fact that the boozers coordinates are straight field line coordinates are the reasons why the Boozer coordinates are so commonly used.



# Appendix C

## List of Discharges and AEs

### C.1 Discharges

Shot	$B_{tor}^{36}$ [T]	$B_z$ [T]	Gas	$t_a$	$t_{VMEC}$ [s]	Program
54009	-0.907	-0.020	H2	0.477	0.231	ECRH: – , 900 MHz, NBI high beta
54010	-0.907	-0.020	H2	0.477	0.21	ECRH: – , 900 MHz, NBI high beta
54012	-0.908	-0.020	H2	0.477	0.21	ECRH: – , 900 MHz, NBI high beta
54014	-0.908	-0.020	H2	0.477	0.21	ECRH: – , 900 MHz, NBI high beta
54015	-0.914	-0.019	H2	0.372	0.2	ECRH: – , 900 MHz, NBI high beta
54020	-1.001	-0.019	H2	0.378	0.3	ECRH: – , 900 MHz, NBI high beta
54082	-2.147	-0.020	H2	0.354	0.31	ECRH: 70 GHz, 900 MHz, NBI EBW and X1 current drive
54083	-2.147	-0.020	H2	0.349	0.31	ECRH: 70 GHz, 900 MHz, NBI EBW and X1 current drive
54128	-1.247	-0.017	H2	0.346	0.132, 0.26	ECRH: 70 GHz, NBI high beta
54129	-1.248	-0.017	H2	0.346	0.14	ECRH: 70 GHz, NBI high beta
54130	-1.248	-0.017	H2	0.346	0.132	ECRH: 70 GHz, NBI high beta
54132	-1.248	-0.017	H2	0.346	0.131	ECRH: 70 GHz, NBI high beta

Shot	$B_{tor}^{36}$ [T]	$B_z$ [T]	Gas	$t_a$	$t_{VMEC}$ [s]	Program
54133	-1.249	-0.017	H2	0.346	0.131	ECRH: 70 GHz, NBI high beta with $I_p$
54134	-1.248	-0.018	H2	0.345	0.131	ECRH: 70 GHz, NBI high beta with $I_p$
54135	-1.247	-0.017	H2	0.346	0.14	ECRH: 70 GHz, NBI high beta with $I_p$
54136	-1.248	-0.017	H2	0.346	0.14	ECRH: 70 GHz, NBI high beta with $I_p$
54137	-1.248	-0.017	H2	0.345	0.131	ECRH: 70 GHz, NBI high beta with $I_p$
54138	-1.247	-0.017	H2	0.345	0.15	ECRH: 70 GHz, NBI high beta with $I_p$
54149	-1.244	-0.019	H2	0.342	0.23	ECRH: 70 GHz, NBI high beta with $I_p$
54150	-1.245	-0.019	H2	0.342	0.23	ECRH: 70 GHz, NBI high beta with $I_p$
54151	-1.244	-0.019	H2	0.342	0.23	ECRH: 70 GHz, NBI high beta with $I_p$
54153	-1.244	-0.019	H2	0.342	0.23	ECRH: 70 GHz, NBI high beta with $I_p$
54154	-1.245	-0.019	H2	0.342	0.23	ECRH: 70 GHz, NBI high beta with $I_p$
54155	-1.244	-0.019	H2	0.342	0.21	ECRH: 70 GHz, NBI high beta with $I_p$
54156	-1.243	-0.019	H2	0.303	0.23	ECRH: 70 GHz, NBI high beta with $I_p$
54820	-2.512	-0.010	H2	0.536	0.179, 0.229	ECRH: 140 GHz, H2, NBI transition H-Mode HDH
54821	-2.511	-0.010	H2	0.535	0.179, 0.20	ECRH: 140 GHz, H2, NBI transition H-Mode HDH
54832	-2.501	-0.010	H2	0.520	0.229	ECRH: 140 GHz, H2, NBI transition H-Mode HDH
54840	-2.501	-0.010	H2	0.520	0.2	ECRH: 140 GHz, H2, NBI transition H-Mode HDH
54843	-2.504	-0.010	H2	0.518	0.2	ECRH: 140 GHz, H2, NI transition H-Mode HDH
54844	-2.499	-0.010	H2	0.515	0.2	ECRH: 140 GHz, H2, NI transition H-Mode HDH
54845	-2.498	-0.010	H2	0.522	0.2	ECRH: 140 GHz, H2, NI transition H-Mode HDH
54846	-2.495	-0.010	H2	0.525	0.2	ECRH: 140 GHz, H2, NI transition H-Mode HDH

Shot	$B_{tor}^{36}$ [T]	$B_z$ [T]	Gas	$t_a$	$t_{VMEC}$ [s]	Program
54850	-2.512	-0.010	H2	0.536	0.179, 0.229	ECRH: 140 GHz, H2, NI transition H-Mode HDH
54852	-2.505	-0.010	H2	0.518	0.2	ECRH: 140 GHz, H2, NI transition H-Mode HDH
54853	-2.505	-0.010	H2	0.518	0.2	ECRH: 140 GHz, H2, NI transition H-Mode HDH
54854	-2.505	-0.010	H2	0.518	0.2	ECRH: 140 GHz, H2, NI transition H-Mode HDH
54855	-2.505	-0.010	H2	0.518	0.2	ECRH: 140 GHz, H2, NI transition H-Mode HDH
54856	-2.506	-0.010	H2	0.518	0.2	ECRH: 140 GHz, H2, NI transition H-Mode HDH
54857	-2.503	-0.010	H2	0.518	0.2	ECRH: 140 GHz, H2, NI transition H-Mode HDH
54858	-2.503	-0.010	H2	0.518	0.2	ECRH: 140 GHz, H2, NI transition H-Mode HDH
54902	-0.997	-0.019	H2	0.484	0.329, 0.379	ECRH: 140 GHz, NBI high beta program
54903	-0.992	-0.017	H2	0.491	0.2, 0.328, 0.378	ECRH: 140 GHz, NBI high beta program
54904	-0.995	-0.018	H2	0.488	0.229, 0.329, 0.379	ECRH: 140 GHz, NBI high beta program
54905	-0.994	-0.018	H2	0.488	0.2, 0.328, 0.378	ECRH: 140 GHz, NBI high beta program
54906	-0.993	-0.017	H2	0.491	0.2, 0.328, 0.378	ECRH: 140 GHz, NBI high beta program
54907	-0.998	-0.019	H2	0.484	0.2, 0.328, 0.378	ECRH: 140 GHz, NBI high beta program
54908	-1.001	-0.020	H2	0.481	0.328, 0.378	ECRH: 140 GHz, NBI high beta program
54911	-1.002	-0.021	H2	0.478	0.2	ECRH: 140 GHz, NBI high beta program
54927	-1.249	-0.018	H2	0.626	0.2	ECRH: – , 900 MHz, NBI high beta, iota=5/8
54930	-1.248	-0.018	H2	0.626	0.184	ECRH: – , 900 MHz, NBI high beta, iota=5/8
54937	-1.248	-0.018	H2	0.616	0.36	ECRH: – , 900 MHz, NBI high beta, iota=5/8
54998	-1.807	-0.007	H2	0.565	0.19	ECRH: – , 900 MHz, NBI fluktuations in HDH-Mode
55003	-1.807	-0.007	H2	0.565	0.23	ECRH: – , 900 MHz, NBI density limit at 1.8T

Shot	$B_{tor}^{36}$ [T]	$B_z$ [T]	Gas	$t_a$	$t_{VMEC}$ [s]	Program
55049	-2.503	-0.010	H2	0.518	0.2, 0.23	ECRH: 140 GHz, NBI, transition H-Mode HDH
55056	-2.503	-0.010	H2	0.518	0.19	ECRH: 140 GHz, NBI, transition H-Mode HDH
55288	-1.247	-0.022	D2	0.482	0.232	ECRH: – , 900 MHz, NBI high beta, deuterium NBI
55315	-1.247	-0.022	D2	0.482	0.228	ECRH: 70 GHz, NBI high beta, deuterium NBI
55316	-1.247	-0.022	D2	0.482	0.228	ECRH: 70 GHz, NBI high beta, deuterium NBI
55317	-1.247	-0.022	D2	0.482	0.227	ECRH: 70 GHz, NBI high beta, deuterium NBI
55318	-1.247	-0.022	D2	0.482	0.21	ECRH: 70 GHz, NBI high beta, deuterium NBI
55319	-1.251	-0.021	D2	0.481	0.21	ECRH: 70 GHz, NBI high beta, deuterium NBI
55321	-1.252	-0.021	D2	0.481	0.21	ECRH: 70 GHz, NBI high beta, deuterium NBI
55323	-1.251	-0.021	D2	0.481	0.21	ECRH: 70 GHz, NBI high beta, deuterium NI
55324	-1.253	-0.021	D2	0.481	0.21	ECRH: 70 GHz, NBI high beta, deuterium NI
55325	-1.252	-0.021	D2	0.481	0.21	ECRH: 70 GHz, NBI high beta, deuterium NI
55388	-2.510	-0.010	D2	0.565	0.184	ECRH: 140 GHz, NBI(D) H-mode
55391	-2.511	-0.010	D2	0.537	0.183	ECRH: 140 GHz, NBI(D) H-mode
55413	-1.249	-0.022	D2	0.440	0.18	ECRH: 900 MHz, NBI(D) high beta
55477	-1.520	-0.006	H2	0.562	0.2	ECRH: 140 GHz, 900 MHz, NBI, 3rd harm. OXB, 5/9 config.
55480	-1.521	-0.006	H2	0.563	0.2	ECRH: 140 GHz, 900 MHz, NBI, 3rd harm. OXB, 5/9 config.
55484	-1.520	-0.006	H2	0.563	0.2	ECRH: 140 GHz, 900 MHz, NBI, 3rd harm. OXB, 5/9 config.
55486	-1.520	-0.006	H2	0.563	0.2	ECRH: 140 GHz, 900 MHz, NBI, 3rd harm. OXB, 5/9 config.
55489	-1.521	-0.006	H2	0.562	0.2	ECRH: 140 GHz, 900 MHz, NBI, 3rd harm. OXB, 5/9 config.
55490	-1.520	-0.006	H2	0.563	0.2	ECRH: 140 GHz, 900 MHz, NBI, 3rd harm. OXB, 5/9 config.

Shot	$B_{tor}^{36}$ [T]	$B_z$ [T]	Gas	$t_a$	$t_{VMEC}$ [s]	Program
55493	-1.515	-0.006	H2	0.482	0.2	ECRH 140GHz, 900MHz, NBI, 3rd harm. OXB, 5/9 config.
56355	-1.259	-0.010	H2	0.519	0.2	ECRH: –, 900 MHz, H2, NBI Alfven waves
56358	-1.249	-0.015	H2	0.521	0.186	ECRH: –, 900 MHz, H2, NBI Alfven waves
56370	-1.252	-0.010	H2	0.433	0.3	ECRH: –, 900 MHz, H2, NBI Alfven waves
56380	-1.193	-0.010	H2	0.363	0.19	ECRH: –, 900 MHz, NBI Alven eigenmode studies
56936	-1.277	-0.033	H2	0.494	0.28	ECRH: 70 GHz, H2, NBI high beta

## C.2 Observed Alfvén Instabilities

### C.2.1 GAEs

Shot	t [s]	f [kHz]	(m, n)	Remarks
54820	0.18 - 0.20	33	(-14, -7)	stationary
54821	0.18 - 0.20	33	(-14, -7)	stationary
54832	0.21 - 0.23	24	(-14, -7)	stationary
54840	0.20 - 0.215	25	(-14, -7)	transient
54843	0.20 - 0.215	25	(-14, -7)	transient
54844	0.20 - 0.215	25	(-14, -7)	transient
54845	0.19 - 0.205	25	(-14, -7)	transient
54846	0.18 - 0.19	21	(2, 1)	tail observed
54850	0.18 - 0.19	32	(-14, -7)	tail observed
54852	0.19 - 0.22	24	(-14, -7)	transient
54853	0.20 - 0.215	25	(-14, -7)	transient
54854	0.20 - 0.215	25	(-14, -7)	transient
54855	0.20 - 0.22	25	(-14, -7)	transient
54856	0.195 - 0.21	25	(-14, -7)	transient
54857	0.185 - 0.21	25	(-14, -7)	transient
54858	0.20 - 0.215	25	(-14, -7)	transient
55003	0.19 - 0.21	35	(-4, -2)	transient, ion loss
55480	0.18 - 0.19	30	(2, 1)	dithering
56355	0.19 - 0.23	30	(2, 1)	higher harmonics, ion loss

## C.2.2 TAEs

Shot	t [s]	f [kHz]	(m, n)	Remarks
54010	0.20 - 0.22	28	(10/11, 5)	transient
54012	0.20 - 0.21	30	(10/11, 5)	transient
54014	0.20 - 0.205	30	(10/11, 5)	tail observed
54020	0.27 - 0.37	19	(3/4/5, 1)	bursting
54128	0.25 - 0.31	25	(5/6/7, 2)	stationary
54130	0.12 - 0.135	25	(11/12, 4)	
54132	0.12 - 0.135	25	(11/12, 4)	mode amplitude correlated with NBI power steps
54133	0.12 - 0.135	24	(11/12, 4)	”
54134	0.12 - 0.135	24	(11/12, 4)	”
54135	0.12 - 0.13 0.12 - 0.14	24 35	(11/12, 4) (5/6, 2)	”
54136	0.12 - 0.135	24	(11/12, 4)	”
54137	0.12 - 0.14	24	(11/12, 4)	”
54149	0.21 - 0.25 0.25 - 0.27	20 30	(4/5/6, 1) (5/6/7, 2)	bursting
54150	0.22 - 0.27	30	(7/8, 2)	bursting
54151	0.22 - 0.27	35	(7/8, 2)	bursting
54153	0.22 - 0.27	32	(7/8, 2)	bursting
54154	0.21 - 0.22	35	(5/6/7, 2)	tail observed
54155	0.21 - 0.22	35	(6/7, 2)	tail observed
54156	0.21 - 0.24	30	(6/7, 2)	frequency band
54902	0.29 - 0.33 0.33 - 0.39	25 25 16	(8/9, 3) (6/7/8, 2) (4/5/6/7, 2)	regular bursts bursts, frequency splitting stationary
54903	0.28 - 0.39 0.28 - 0.33	16 25	(5/6/7, 2) (6/7/8, 2)	stationary bursts, frequency splitting
54904	0.28 - 0.33 0.28 - 0.39	16 25	(4/5, 2) (6/7, 2)	stationary bursts, frequency splitting
54905	0.28 - 0.34 0.35 - 0.39	16 25	(4/5/6, 2) (5/6/7, 2)	stationary bursts, frequency splitting
54906	0.28 - 0.33 0.30 - 0.33 0.34 - 0.39	16 25 16	(4/5/6, 2) (6/7/8, 2) (2/3, 1)	stationary bursts, frequency splitting stationary
54907	0.28 - 0.34 0.28 - 0.39	15 25	(4/5/6, 2) (5/6/7, 2)	stationary bursts, frequency splitting
54908	0.30 - 0.33 0.33 - 0.39 0.33 - 0.39	25 17 25	(8/9, 3) (4/5/6, 2) (6/7/8, 2)	regular bursts stationary bursts, frequency splitting



Shot	t [s]	f [kHz]	(m, n)	Remarks
54998	0.19 - 0.194	80	(8/9, 4)	burst, chirping
55315	0.23 - 0.25	19	(7/8, 3)	noisy
	0.22 - 0.25	37	(4/5/6, 2)	noisy
55316	0.20 - 0.25	20	(-9/-8, -4)	noisy
55323	0.21 - 0.24	20	(10/11, 5)	noisy
55324	0.20 - 0.24	37	(4/5/6, 2)	noisy
55325	0.20 - 0.24	20	(-12/-11, -5)	
56380	0.15 - 0.21	40	(2/3, 1)	noisy
56936	0.25 - 0.265	24	(-11/-10, -4)	tail observed

### C.2.3 EAEs

#### C.2.3.1 Successfully Identified EAEs

Shot	t [s]	f [kHz]	(m, n)	Remarks
54009	0.20 - 0.21	32	(-7/-5, -3)	tail observed, ion losses
54151	0.21 - 0.27	32	(5/7, 2)	noisy, frequency splitting
54153	0.21 - 0.27	35	(-9/-7, -3)	noisy, frequency splitting
55316	0.20 - 0.23	49	(-5/-3, -2)	stationary
55317	0.20 - 0.22	49	(-5/-3, -2)	stationary
55318	0.20 - 0.22	49	(-5/-3, -2)	stationary
55319	0.20 - 0.21	49	(-5/-3, -2)	stationary
56936	0.27 - 0.30	50	(1/3, 1)	weak and noisy

#### C.2.3.2 AEs with frequencies inside the EAE gap

Shot	t [s]	f [kHz]	Dominant (m, n)	Remarks
54015	0.20 - 0.205	56	(3, 1) (4, 1)	tail observed
54150	0.21 - 0.27	37	(8, 1) (9, 1)	noisy
54155	0.21 - 0.23	49	(0, -2)	
54820	0.18 - 0.23	$\approx 145$	(3, 2)	
	0.18 - 0.23	$\approx 155$	(-7, -3)	
54821	0.18 - 0.23	$\approx 160$	(-7, -3)	
54850	0.18 - 0.23	$\approx 120$	(-7, -1) (-7, 4)	bursts, frequency chirping
54905	0.38 - 0.34	37	(0, -2)	bursting
54927	0.19 - 0.21	90	(-14, -8) (-12, -8)	bursting
54930	0.19 - 0.205	90	(-2, -2)	bursting
55288	0.235 - 0.245	100	(-1, 0)	transient
55316	0.20 - 0.21	37	(6, 2) (7, 2)	tail observed
56370	0.28 - 0.33	60	$m = -7, 3, \text{ or } 15$	stationary

### C.2.4 NAE, HAE and MAE Modes

It is noted that for the high-frequency modes, where MIR-1 is unavailable, strong mode number aliasing is observed due to the low number of probes remaining. The poloidal mode number  $m$  shows a regular aliasing pattern with  $\Delta m \approx 7$ , while for  $n$  is only known whether it is even or uneven. The aliasing peaks were all of comparable amplitudes. The mode numbers given below are just stated because they appear in the mode number spectrum and correspond to a coupling that is present in the Alfvén continuum. They should not be considered as having unambiguously been determined.

Shot	t [s]	f [kHz]	(m, n)	Remarks
55288	0.23 - 0.235	150	$m = 7, n \text{ even}$	possibly NAE <sub>30</sub>
55315	0.20 - 0.23	370	(-12, -4)?	HAE <sub>21</sub> gap
		450	(-1, -3)?	MAE <sub>01</sub> gap
55323	0.20 - 0.22	330	(6, 5)?	HAE <sub>21</sub> gap
55324	0.20 - 0.22	330	(6, 5)?	HAE <sub>21</sub> gap

### C.2.5 Unidentified Alfvén Eigenmodes

Shot	t [s]	f [kHz]	Dominant (m, n)	Remarks
54082	0.30 - 0.33	30	(-4, -1) (-1, -1)	stationary
54083	0.30 - 0.33	25, 32	(-4, -1) (-4, -3)	have same mode numbers
54128	0.12 - 0.135	27	(-2, -1) (11, 4)	transient
54129	0.12 - 0.135	26	(-2, -1) (11, 4)	transient
54138	0.12 - 0.135	24	(-2, -1) (11, 4)	transient
54903	0.19 - 0.23	110	(-1, 0)	chirping, energy losses
54904	0.19 - 0.21	97	(-1, 0)	chirping, energy losses
54905	0.19 - 0.23	105	(-1, 0)	chirping, energy losses
54906	0.18 - 0.23	95	(-1, 0)	chirping, energy losses
54907	0.19 - 0.23	75	(-1, 0)	chirping, energy losses
54908	0.19 - 0.22	110	(1, 0)	dithering
54911	0.19 - 0.23	70	(1, 1)	stationary, energy losses
54937	0.35 - 0.37	300	(?, ?)	high frequency mode
		340	(?, ?)	high frequency mode
		380	(?, ?)	high frequency mode
55049	0.18 - 0.185	19	(0, 1) (2, 1)	tail observed
	0.18 - 0.20	25	(7, 3) (-7, -4)	transient
	0.22 - 0.23	220		bursts

Shot	t [s]	f [kHz]	Dominant (m, n)	Remarks
55056	0.185 - 0.195	87	(8, 0) (8, 4)	transient
55288	0.245 - 0.25	195	(12, 0) (12, 4)	start observed
55317	0.20 - 0.25	20	(0, -2)	stationary
55318	0.20 - 0.25	20	(0, -2)	stationary
55321	0.20 - 0.21	340	(1, 2)	three bursts
55323	0.20 - 0.24	17	(-4, 3)	ELMy at first
55324	0.20 - 0.24	17	(-4, 3)	ELMy at first
55325	0.20 - 0.21	420	(0, 1) (-12, -6)	two bursts
55388	0.17 - 0.23	40	(-4, $\pm 2$ )	bursting, frequency splitting
55391	0.18 - 0.23	25	(0, -3) (-14, -7)	stationary
55413	0.17 - 0.20	25	(-3, -1)	bursting, ion losses
55477	0.17 - 0.19	40	(-1, -1) (14, 7)	dithering, chirping, ion losses
	0.19 - 0.20	80	(-2, -1) (6, 5)	two bursts
55480	0.20 - 0.21	35	(0, 7) (14, 7)	transient
	0.20 - 0.22	60	(-7, -3) (14, 7)	transient, chirping
55484	0.17 - 0.20	25	m = 0	dithering at first
55486	0.17 - 0.19	35	(-1, -1) (9, 6)	chirping
	0.19 - 0.21	25	(0, -2)	transient
55489	0.185 - 0.195	100	(8, 0) (1, 1)	bursts, ion losses
55490	0.185 - 0.195	100		bursts, ion losses
55493	0.18 - 0.19	50	(5, 2)	chirping, ion losses
56358	0.17 - 0.20	50	(4, 2)	chirping, ion losses
56936	0.26 - 0.30	80 - 220		multiple quasicohherent activity



# Bibliography

- [1] J. Wesson, *Tokamaks*. Clarendon Press, Oxford, 1997.
- [2] H. Alfvén, “On the existence of electromagnetic-hydrodynamic waves,” *Arkiv. Mat. Astron. Fysik*, vol. 29, 1942.
- [3] H. Alfvén, *Cosmical Electrodynamics*. Oxford University Press, New York, 1950.
- [4] H. Grad, “Plasmas,” *Physics Today*, vol. 22, no. 12, p. 34, 1969.
- [5] R. L. Dewar, R. C. Grimm, J. L. Johnson, E. A. Frieman, J. M. Greene, and P. H. Rutherford, “Long-wavelength kink instabilities in low-pressure, uniform axial current, cylindrical plasmas with elliptic cross sections,” *Physics of Fluids*, vol. 17, no. 5, pp. 930–938, 1974.
- [6] C. Kieras and J. Tataronis, “The shear Alfvén continuous spectrum of axisymmetric toroidal equilibria in the large aspect ratio limit,” *Journal of Plasma Physics*, vol. 28, pp. 395–414, 1982.
- [7] C. Z. Cheng and M. S. Chance, “Low- $n$  shear Alfvén spectra in axisymmetric toroidal plasmas,” *Physics of Fluids*, vol. 29, no. 11, pp. 3695–3701, 1986.
- [8] C. Cheng, L. Chen, and M. S. Chance, “High- $n$  ideal and resistive shear Alfvén waves in tokamaks,” *Annals of Physics*, vol. 161, no. 1, pp. 21–47, 1985.
- [9] R. Betti and J. P. Freidberg, “Stability of Alfvén gap mode in burning plasmas,” *Physics of Fluids B*, vol. 4, no. 6, pp. 1465–74, 1992.
- [10] Y. I. Kolesnichenko, V. V. Lutsenko, H. Wobig, Y. V. Yakovenko, and O. Freisenjuk, “Alfvén continuum and high-frequency eigenmodes in optimized stellarators,” *Physics of Plasmas*, vol. 8, no. 2, pp. 491–509, 2001.
- [11] Y. I. Kolesnichenko, V. V. Lutsenko, H. Wobig, and V. Yakovenko, “Alfvén instabilities driven by circulating ions in optimized stellarators and their possible consequences in a helias reactor,” *Physics of Plasmas*, vol. 9, no. 2, pp. 517–528, 2002.
- [12] Y. Li, S. Mahajan, and D. Ross, “Destabilization of global Alfvén eigenmodes and kinetic Alfvén waves by alpha particles in a tokamak plasma,” *Physics of Fluids*, vol. 30, no. 5, pp. 1466–1484, 1987.

- [13] J. Weiland, M. Lisak, and H. Wilhelmsson, "Excitation of global Alfvén modes by trapped alpha particles," *Physica Scripta*, vol. T16, pp. 53–57, 1987.
- [14] W. W. Heidbrink and G. J. Sadler, "The behaviour of fast ions in tokamak experiments," *Nuclear Fusion*, vol. 34, no. 4, pp. 535–615, 1994.
- [15] R. B. White, R. J. Goldston, K. McGuire, A. H. Boozer, D. A. Monticello, and W. Park, "Theory of mode-induced beam particle loss in tokamaks," *Physics of Fluids*, vol. 26, no. 10, pp. 2958–65, 1983.
- [16] D. J. Sigmar, C. T. Hsu, R. White, and C. Z. Cheng, "Alpha-particle losses from toroidicity-induced Alfvén eigenmodes. ii. monte carlo simulations and anomalous alpha-loss processes," *Physics of Fluids B*, vol. 4, no. 6, pp. 1506–16, 1992.
- [17] R. Jaenicke, "Summary of W7-AS results after 14 years of operation," *Proc. 14th Int. Stellarator Workshop (Greifswald)*, 2003. I.Mo1 (13 pages).
- [18] R. Jaenicke, F. Wagner, R. Burhenn, F. Gadelmeier, J. Geiger, M. Hirsch, H. P. Laqua, A. Weller, A. Werner, S. Bäumel, J. Baldzuhn, R. Brakel, A. Dinklage, P. Grigull, M. Endler, V. Erckmann, H. Ehmeler, Y. Feng, R. Fischer, L. Gianone, H. J. Hartfuss, A. Hermann, D. Hildebrandt, E. Holzhauer, Y. Igutkhanov, M. Kick, A. Kislyakov, A. Kreter, J. Kisslinger, T. Klinger, S. Klose, J. P. Knauer, R. König, G. Kühner, H. Maassberg, K. McCormick, D. Naujoks, H. Niedermeyer, C. Nührenberg, E. Pasch, N. Ramasubramanian, N. Rust, E. Sallander, F. Sardei, M. Schubert, H. Thomsen, F. Volpe, U. Wenzel, H. Wobig, E. Würsching, M. Zarnstorff, S. Zoletnik, and the W7-AS Team, "Major results from Wendelstein 7-AS stellarator," *Proc. 19th (IAEA) Fusion Energy Conference (Lyon)*, 2002. OV/2-4 (12 pages).
- [19] C. Görner, A. Weller, M. Anton, J. Geiger, C. Nührenberg, F. P. Penningsfeld, D. Spong, U. Stroth, and the W7-AS Team, "Study of Alfvén eigenmodes in configurations of different shear at Wendelstein 7-AS," *Proc. 1998 ICPP & 25th EPS Conf. on Contr. Fusion and Plasma Phys. (Prague)*, vol. 22, 1998. P1.029 (4 pages).
- [20] A. Weller and D. A. Spong, "Global, toroidal, and helical-induced shear Alfvén instabilities in stellarators," *Proc. 9th Int. Workshop on Stellarators (Garching)*, pp. 554–560, 1993. IAEA TCM on Stellarators and other Helical Confinement Systems.
- [21] A. Weller, D. A. Spong, R. Jaenicke, A. Lazaros, F. P. Penningsfeld, S. Sattler, and the W7-AS Team, "Neutral beam driven global Alfvén eigenmodes in the Wendelstein W7-AS stellarator," *Phys. Rev. Lett.*, vol. 72, no. 8, pp. 1220–1223, 1994.
- [22] A. Weller, M. Anton, J. Geiger, C. Görner, R. Jaenicke, C. Konrad, F. P. Penningsfeld, N. Rust, D. A. Spong, C. Y. Teo, the W7-AS Team, the NBI Team,

- and the ECRH Group, "Correlation between MHD-activity, energetic particle behaviour and anomalous transport phenomena in Wendelstein 7-AS," *Proc. 24th EPS Conf. on Contr. Fusion and Plasma Phys. (Berchtesgaden)*, vol. 21A, no. IV, pp. 1649–1652, 1997.
- [23] A. Weller, M. Anton, R. Brakel, J. Geiger, C. Görner, H. J. Hartfuss, M. Hirsch, R. Jänicke, C. Nührenberg, S. D. Pinches, D. A. Spong, S. Zoletnik, the W7-AS Team, the NBI Group, and the ECRH Group, "Investigation of equilibrium, global modes and microinstabilities in the stellarator W7-AS," *Proc. 17th IAEA Fusion Energy Conference*, 1998. EX2/1 (8 pages).
- [24] C. Y. Teo, A. Weller, C. Konrad, the W7-AS Team, and the NBI Team, "Further observations of neutral beam driven global Alfvén eigenmodes in Wendelstein W7-AS," *Nuclear Fusion*, vol. 38, no. 3, pp. 409–417, 1998.
- [25] M. Anton, R. Jaenicke, A. Weller, J. Geiger, the W7-AS Team, the NBI Team, and the ECRH Group, "Analysis of W7-AS Mirnov data using SVD and correlation techniques," *Proc. 24th EPS Conf. on Contr. Fusion and Plasma Phys. (Berchtesgaden)*, vol. 21A, no. IV, pp. 1645–1648, 1997.
- [26] R. Balescu, *Equilibrium and Nonequilibrium Statistical Mechanics*. Wiley Press, New York, 1975.
- [27] K. Whiteman, "Invariants and stability in classical mechanics," *Reports on Progress in Physics*, vol. 40, no. 9, p. 1033, 1977.
- [28] A. H. Boozer, "Plasma equilibrium with rational magnetic surfaces," *Physics of Fluids*, vol. 24, no. 11, pp. 1999–2003, 1981.
- [29] U. Stroth, "Transport in toroidal plasmas," in *Lecture Notes in Physics* (A. Dinklage, T. Klinger, G. Marx, and L. Schweikhard, eds.), Springer Verlag Berlin Heidelberg, 2005.
- [30] J. A. Elliot, "Plasma kinetic theory," in *Plasma Physics: an Introductory Course* (R. Dendy, ed.), Cambridge University Press, 1996.
- [31] J. Freidberg, *Ideal Magnetohydrodynamics*. Plenum Press, New York, 1987.
- [32] S. M. Mahajan, "Spectrum of Alfvén waves, a brief review," *Physica Scripta*, vol. T60, pp. 160–170, 1995.
- [33] L. Chen and A. Hasegawa, "Plasma heating by spatial resonance of Alfvén wave," *Physics of Fluids*, vol. 17, p. 1399, 1974.
- [34] L. Chen and F. Zonca, "Theory of shear Alfvén waves in toroidal plasmas," *Physica Scripta*, vol. T60, pp. 81–90, 1995.
- [35] G. V. F. Zonca and S. Briguglio, "Dynamics of Alfvén waves in tokamaks," *Rivista del Nuovo Cimento*, vol. 22, no. 7, pp. 1–97, 1999.

- [36] J. P. Goedbloed, "Plasma-vacuum interface problems in magnetohydrodynamics," *Physica D*, vol. 12, pp. 107–132, 1984.
- [37] A. G. Shalashov, E. V. Suvorov, L. V. Lubyako, H. Maassberg, and the W7-AS team, "NBI-driven ion cyclotron instabilities at the W7-AS stellarator," *Plasma Physics and Controlled Fusion*, vol. 45, pp. 395–412, 2003.
- [38] Y. I. Kolesnichenko, S. Yamamoto, K. Yamazaki, V. V. Lutsenko, N. Nakajima, Y. Narushima, K. Toi, and Y. V. Yakovenko, "Interplay of energetic ions and Alfvén modes in helical plasmas," *Physics of Plasmas*, vol. 11, no. 1, pp. 158–169, 2004.
- [39] A. Könies, "A kinetic magnetohydrodynamic energy integral in three dimensional geometry," *Physics of Plasmas*, vol. 7, no. 4, pp. 1139–47, 2000.
- [40] A. Könies, "Growth and damping rates of Alfvén eigenmodes in stellarators using kinetic MHD," in *Theory of Fusion Plasmas – Proceedings of the Joint Varenna-Lausanne International Workshop* (J. W. Connor, O. Sauter, and E. Sindoni, eds.), pp. 297–302, Società Italiana di Fisica, 2004.
- [41] R. Marchand, W. M. Tang, and G. Rewoldt, "Two-dimensional analysis of trapped-ion eigenmodes," *Physics of Fluids*, vol. 23, no. 6, pp. 1164–81, 1980.
- [42] S. Pinches, *Nonlinear Interaction of Fast Particles with Alfvén Waves in Tokamaks*. PhD thesis, University of Nottingham, 1996.
- [43] S. Pinches *et al.*, "The HAGIS self-consistent nonlinear wave-particle interaction model," *Computer Physics Communications*, vol. 111, pp. 133–149, 1998.
- [44] W. Park, E. V. Belova, G. Y. Fu, X. Z. Tang, H. R. Strauss, and L. E. Sugiyama, "Plasma simulation studies using multilevel physics models," *Physics of Plasmas*, vol. 6, no. 5, pp. 1796–1803, 1999.
- [45] H. R. Strauss, L. E. Sugiyama, G. Y. Fu, W. Park, and J. Breslau, "Simulation of two fluid and energetic particle effects in stellarators," *Nuclear Fusion*, vol. 44, pp. 1008–1014, 2004.
- [46] A. Hasegawa and L. Chen, "Kinetic process of plasma heating due to Alfvén wave excitation," *Physical Review Letters*, vol. 35, no. 6, pp. 370–73, 1975.
- [47] R. R. Mett and S. M. Mahajan, "Kinetic theory of toroidicity-induced Alfvén eigenmodes," *Physics of Fluids B*, vol. 4, no. 9, pp. 2885–2893, 1992.
- [48] O. P. Fesenyuk, Y. I. Kolesnichenko, V. V. Lutsenko, H. Wobig, and Y. V. Yakovenko, "Kinetic mirror-induced Alfvén eigenmodes in Wendelstein-type stellarators," *Plasma Physics and Controlled Fusion*, vol. 46, pp. 89–104, 2004.
- [49] F. Zonca and L. Chen, "Theory of toroidal Alfvén modes excited by energetic particles in tokamaks," *Physics of Plasmas*, vol. 3, no. 1, pp. 323–43, 1996.



- [50] H. L. Berk, D. N. Borba, B. N. Breizman, S. D. Pinches, and S. E. Sharapov, "Theoretical interpretation of Alfvén cascades in tokamaks with nonmonotonic  $q$  profiles," *Physical Review Letters*, vol. 87, no. 18, p. 185002, 2001.
- [51] F. Zonca, S. Briguglio, L. Chen, S. Dettrick, G. Fogaccia, D. Testa, and G. Vlad, "Energetic particle mode stability in tokamaks with hollow  $q$ -profiles," *Physics of Plasmas*, vol. 9, no. 12, pp. 4939–56, 2002.
- [52] F. Zonca and L. Chen, "Destabilization of energetic particle modes by localized particle sources," *Physics of Plasmas*, vol. 7, no. 11, pp. 4600–08, 2000.
- [53] L.-J. Zheng, L. Chen, and R. A. Santoro, "Numerical simulations of toroidal Alfvén instabilities excited by trapped energetic ions," *Physics of Plasmas*, vol. 7, no. 6, pp. 2469–76, 2000.
- [54] J. Hofmann *et al.*, "Stellarator optimization studies in W7-AS," *Plasma Physics and Controlled Fusion*, vol. 38, no. 12A, p. A193, 1996.
- [55] R. Fischer, C. Wendland, A. Dinklage, V. D. S. Gori, and the W7-AS team, "Thomson scattering analysis with the bayesian probability theory," *Plasma Physics and Controlled Fusion*, vol. 44, no. 8, pp. 1501–1519, 2002.
- [56] S. Besshou, C. Thomas, T. Ohba, A. Iiyoshi, and K. Uo, "Diamagnetism and beta in beam heated currentless plasmas of Heliotron E," *Nuclear Fusion*, vol. 26, no. 10, pp. 1339–48, 1986.
- [57] H. J. Gardner, "Modelling of the behaviour of the magnetic field diagnostic coils on the W VII-AS stellarator using a three-dimensional equilibrium code," *Nuclear Fusion*, vol. 30, no. 8, pp. 1417–24, 1990.
- [58] A. Weller, C. Görner, and D. Gonda, "X-ray diagnostics on WENDELSTEIN 7-AS," *Review of Scientific Instruments*, vol. 70, no. 1, pp. 484–488, 1999.
- [59] D. S. Darrow, A. Werner, and A. Weller, "Energetic ion loss diagnostic for the Wendelstein 7-AS stellarator," *Review of Scientific Instruments*, vol. 72, no. 7, pp. 2936–2942, 2001.
- [60] N. R. Lomb, "Least-squares frequency analysis of unequally spaced data," *Astrophysics and Space Science*, vol. 39, pp. 447–462, 1976.
- [61] J. van den Berg, *Wavelets in Physics*. Cambridge University Press, England, 1999.
- [62] D. B. Percival and A. T. Walden, *Wavelet Methods for Time Series Analysis*. Cambridge University Press, England, 2000.
- [63] I. Daubechies, *Ten Lectures on Wavelets*. Society of Industrial and Applied Mathematics, Philadelphia, 1992.

- [64] P. Goupillaud, A. Grossmann, and J. Morlet, "Cycle-octave and related transforms in seismic signal analysis," *Geoexploration*, vol. 83, no. 1, pp. 85–102, 1984.
- [65] A. Grossmann and J. Morlet, "Decomposition of Hardy functions into square integrable wavelets of constant shape," *Siam Journal on Mathematical Analysis*, vol. 15, no. 4, pp. 723–736, 1984.
- [66] P. D. Welch, "Use of fast fourier transform for estimation of power spectra - a method based on time averaging over short modified periodograms," *IEEE Transactions on Audio and Electroacoustics*, vol. AU15, no. 2, pp. 70–73, 1969.
- [67] R. I. Shrager, "On a three-term variant of the lomb periodogram," *Astrophysics and Space Science*, vol. 277, pp. 519–530, 2001.
- [68] W. H. Press, S. A. Teukolsky, W. T. Vetterling, and B. P. Flannery, *Numerical Recipes in C*. Cambridge University Press, 1992.
- [69] J. D. Scargle, "Studies in astronomical time series analysis. ii. statistical aspects of spectral analysis of unevenly spaced data," *The Astrophysical Journal*, vol. 263, pp. 835–853, 1982.
- [70] J. H. Horne and S. L. Baliunas, "A prescription for period analysis of unevenly sampled time series.," *The Astrophysical Journal*, vol. 302, no. 2, pp. 757–763, 1986.
- [71] S. Hirshman and D. Lee, "Momcon: a spectral code for obtaining three-dimensional magnetohydrodynamic equilibria," *Computer Physics Communications*, vol. 39, no. 2, pp. 161–172, 1986.
- [72] S. Hirshman, W. van Rij, and P. Merkel, "Three-dimensional free boundary calculations using a spectral green's function method," *Computer Physics Communications*, vol. 43, no. 2, pp. 143–155, 1986.
- [73] D. Strickler, S. Hirshman, D. Spong, M. Cole, J. Lyon, B. Nelson, D. Williamson, and A. Ware, "Development of a robust quasi-poloidal compact stellarator," *Fusion Science and Technology*, vol. 45, no. 1, pp. 15–26, 2004.
- [74] <http://www.ipp.mpg.de/~stel/mapping/mapping.html>.
- [75] Y. Turkin. private communication.
- [76] A. Werner. private communication.
- [77] H. Maassberg. private communication.
- [78] C. Nührenberg, "Compressional ideal magnetohydrodynamics: Unstable global modes, stable spectra, and Alfvén eigenmodes in Wendelstein 7-X-type equilibria," *Physics of Plasmas*, vol. 6, no. 1, pp. 137–147, 1998.

- [79] C. Nührenberg, “Computational ideal MHD: Alfvén, sound and fast global modes in W7-AS,” *Plasma Physics and Controlled Fusion*, vol. 41, pp. 1055–1070, 1999.
- [80] A. Könies. private communication, 2005.
- [81] R. Fischer, A. Dinklage, and E. Pasch, “Bayesian modelling of fusion diagnostics,” *Plasma Physics and Controlled Fusion*, vol. 45, pp. 1095–1111, 2003.
- [82] J. Geiger, A. Weller, M. Zarnstorff, C. Nührenberg, A. Werner, Y. I. Kolesnichenko, and the W7-AS TEAM, “Equilibrium and stability of high- $\beta$  plasmas in Wendelstein 7-AS,” *Fusion Science and Technology*, vol. 46, no. 1, pp. 13–23, 2004.
- [83] A. Weller *et al.*, “Survey of magnetohydrodynamic instabilities in the advanced stellarator Wendelstein 7-AS,” *Physics of Plasmas*, vol. 8, no. 3, pp. 931–956, 2001.
- [84] CAS3D3 calculation provided by A. Könies, IPP, 2006.
- [85] A. Dinklage and A. Werner. private communication, 2005.
- [86] J. Geiger, N. B. Marushchenko, H. Maassberg, A. Dinklage, A. Werner, the NBI Group, and the W7-AS-Team, “Analysis of high- $\beta$  equilibria with toroidal net-current densities for W7-AS,” in *Proceedings of the 30th EPS Conference on Controlled Fusion and Plasma Physics*, 2003. P-1.3.
- [87] Y. I. Kolesnichenko, V. V. Lutsenko, V. S. Marchenko, A. Weller, A. Werner, H. Wobig, Y. Yakovenko, and K. Yamazaki, “Fast-ion confinement and fast-ion-induced effects in stellarators,” *Fusion Science and Technology*, vol. 46, no. 1, pp. 54–63, 2004.
- [88] R. Fischer and A. Dinklage, “Integrated Data Analysis of fusion diagnostics by means of the Bayesian probability theory,” *Review of Scientific Instruments*, vol. 75, no. 10, pp. 4237–39, 2004.
- [89] J. Svensson, A. Dinklage, J. Geiger, A. Werner, and R. Fischer, “Integrating diagnostic data analysis for W7-AS using Bayesian graphical models,” *Review of Scientific Instruments*, vol. 75, no. 10, pp. 4219–4221, 2004.
- [90] P. Lauber, S. Günter, and S. D. Pinches, “Kinetic properties of shear Alfvén eigenmodes in tokamak plasmas,” *Physics of Plasmas*, vol. 12, p. 122501, 2005.
- [91] W. D. D’haeseleer, W. N. G. Hitchon, J. D. Callen, and J. L. Shohet, *Flux Coordinates and Magnetic Field Structure*. Springer Verlag, 1991.